Analytical, Numerical and Experimental Developments to Investigate the Dynamics of Flexible Bodies Rocking on Deformable Support Media



Zheng-You Zhang
St Hugh's College
University of Oxford

A thesis submitted for the degree of
Doctor of Philosophy

Trinity 2025

Acknowledgements

First and foremost, I owe my deepest intellectual debt to my supervisors, Prof. Sinan and Prof. Manolis, whose guidance has shaped not only the trajectory of this thesis, but also my understanding of what it means to be a good researcher.

Each of them profoundly inspired me. Prof. Sinan consistently encouraged me to cultivate intuitive insights from mathematical models. His practical, hands-on approach grounded and balanced the theoretical depth of our discussions. Prof. Manolis, with his meticulous attention to detail, taught me to think and learn with precision and depth. His patient, Socratic questioning continually challenged me to reflect on my thoughts and to develop a more rigorous intellectual posture. These lessons are ones I will never forget and will carry with me throughout my academic life.

Together, their joint supervision has been a model of intellectual partnership from which I have benefited immensely. Without them, I would not have achieved what I have today. Put metaphorically, Prof. Sinan is a lighthouse in the ocean, Prof. Manolis is an ocean of knowledge, and I am the small boat navigating those waters in search of new lands; and whenever I found myself lost in that vast ocean, the lighthouse always guided me back to the course. There were many moments when our discussions became extremely detailed—so much so that I lost both direction and familiarity with the concepts involved. In those moments, Prof. Sinan would redirect us toward the broader perspective, while Prof. Manolis would then provide deep and insightful explanations of the essential ideas, allowing me to regain my footing and fully benefit from the conversation. At other times, when the pace of explanation moved too quickly for me to follow, Prof. Sinan would interject with clarifying questions to bring me back into the flow. In summary, because of Prof. Manolis's vast knowledge I could always obtain insightful answers and broaden my understandings; and because of Prof. Sinan's steady oversight of the big picture, I never drifted away from central problems.

I'm also deeply grateful for their extraordinary dedication: for the weekly meetings maintained over the years despite their demanding schedules; for their constant

encouragement and remarkably prompt responses—even during holidays or inconvenient hours; for the careful supervision reports that Manolis never once forgot (though I often did); and for the countless occasions when a short discussion naturally unfolded into a long and enriching meeting. In addition, their commitment extended far beyond the research itself. Over the years, they provided guidance not only for my academic development but also for research philosophy and long-term career planning—advice that will continue to influence my future endeavours. Their willingness to share their experiences, aspirations, and reflections offered invaluable insights into navigating academic life.

Ultimately, it has been a privilege to learn from supervisors who exemplify the ideals of teaching, guidance, and intellectual generosity—echoing the traditional Chinese conception of an educator: "A teacher is one who imparts philosophy, instructs in knowledge, and resolves doubts" (*Shi Shuo*, Hanyu (AD 802)). Their example is one I will strive to follow. It has also been a joy to witness their life milestones—becoming husbands and fathers—quiet celebrations that have accompanied many chapters of my doctoral journey.

Secondly, I would like to express my sincere gratitude to my friends in Room 11—Miles, Jing, Jiaxu, Huanian, Kutsi, Janet, Yilong, Jiayao, Jorge, Markella, Cathy, and Sanjeev—as well as to my college friends Hannan, Yvhang, Jiaxing, Hanyu, and Sirui, and to the friends I met through the Oxford Chinese Drama Society. Their emotional support and the colour they brought to my everyday life have been invaluable throughout this journey. I am also grateful to Clive for his technical support in the lab, without which I could not have completed my work on time.

Finally, I wish to extend my deepest thanks to my parents. They have supported me financially throughout twelve years of study abroad and have never doubted my decisions. Their trust—expressed not through control or instruction but through the freedom they afforded me to choose my own path—is especially meaningful in a time when society often pressures young people toward immediate employment and when international education places a heavy financial burden on families. I am profoundly grateful for their sacrifices and unwavering belief in me.

Abstract

The study of rocking behaviour in earthquake engineering has evolved from simple rigid blocks to flexible structures with various contact conditions. Understanding the dynamics of such rocking systems is essential for safe and efficient design. However, to the author's knowledge, studies addressing the combined effects of rocking-body flexibility, support deformability, and sliding motion on rocking response—particularly regarding stability and contact force behaviour—remain limited. To bridge this gap, this thesis proposes and integrates analytical, numerical, and experimental approaches to examine the coupled influence of structural flexibility, support deformability, and sliding motion on rocking response. An analytical model, termed the *Flexible Rocking Model on Concentrated Springs (FRMCS)*, is first developed to qualitatively investigate these effects. Stability analyses indicate that the influence of structural flexibility and support deformability is clearly frequency-dependent, while sliding enhances stability across most of the frequency range. Response spectra show that impacts can generate large contact forces, that a soft support medium effectively reduces them, that lateral flexibility can amplify them, and that small amounts of sliding substantially decrease lateral force demand. A generalised numerical framework capable of capturing a wide range of structural configurations and the complex stress states arising in the contact zone is then proposed. The framework successfully reproduces the experimental results of an uplifting steel frame, and numerical studies reveal that beam models, though adequate for stability analysis, significantly underestimate stress demands near contact zones. The complex interaction between rocking-body deformability and contact stress response is also observed. Finally, an experimental setup, utilising high-speed digital image correlation systems and accelerometers, along with a novel non-contact method for estimating total contact forces are used to investigate the influence of lateral flexibility, support deformability, and sliding motion. The experimental results verify the qualitative findings from the FRMCS model and provide valuable data for quantifying these influences.

Contents

1 Introduction **1**

1.1 Research background 1

1.2 Motivations and objectives 4

1.3 Organisation of this thesis 5

2 Literature review **6**

2.1 Review of analytical modelling of rocking problems 6

2.2 Review of numerical modelling of rocking problems 9

2.3 Review of experimental studies of rocking problems 12

2.4 Conclusions 17

3 The Dynamic Behaviour of Flexible Oscillators Rocking and Sliding on Concentrated Springs **19**

3.1 Introduction 19

3.2 Model introduction 20

3.2.1 Equations of motion 21

3.2.2 Constitutive relation and numerical implementation 23

3.2.3 Definition of base shear, axial force and moment quantities . . 25

3.3 Model parameter normalisation 25

3.4 Model comparison for effectively rigid support media 26

3.4.1 Review of FRM 27

3.4.2 Free vibration comparison 28

3.4.3 Stability analysis comparison 31

3.5 Influence of support medium stiffness and μ on the dynamic response 32

3.5.1 Time history evaluation 32

3.5.2 Response spectra evaluation 36

3.5.3 Case one (stiff-stiff) 37

3.5.4 Case two (soft-stiff) 40

3.5.5 Case three (stiff-soft) . . . 41
3.5.6 Case four (soft-soft) . . . 43
3.5.7 Case five (Case four with sliding) . . . 44
3.6 Conclusion . . . 47

4 A Generalised Framework for Modelling the Rocking Response of Flexible Structures on Deformable Media 49
4.1 Introduction . . . 50
4.2 Modelling framework . . . 51
4.2.1 The floating frame of reference formulation . . . 52
4.2.2 The Craig-Bampton reduction . . . 54
4.3 Structure configurations . . . 56
4.4 Numerical implementation . . . 57
4.5 Procedures to obtain the reduced order model . . . 60
4.6 Model comparison for effectively rigid rocking body . . . 62
4.7 Influence of Euler beam assumption on the rocking response . . . 63
4.8 Influence of the structure flexibility on the rocking response . . . 67
4.8.1 Free vibration evaluation . . . 67
4.8.2 Single cycle pulse evaluation . . . 69
4.8.3 Stability analysis . . . 71
4.8.4 Sliding case demonstration . . . 72
4.9 Modelling of complex structures . . . 73
4.10 Capability for three-dimensional rocking response . . . 75
4.11 Conclusion . . . 76

5 Experimental investigations of the stability and the contact force response of flexible body rocking and sliding on deformable media 78
5.1 Introduction . . . 78
5.2 Experimental setup . . . 79
5.2.1 The rocking specimen . . . 79
5.2.2 The support condition . . . 81
5.3 Instrumentation . . . 82
5.3.1 3D high speed DIC system . . . 83
5.3.2 Accelerometers . . . 84
5.3.3 Time synchronization between the DIC system and the accelerometers . . . 85
5.3.4 Measurement noise quantification . . . 86

5.4 Experimental procedure . . . 86
5.4.1 Pulse excitation test . . . 87
5.4.2 Stability test . . . 88
5.5 Introduction to the new unscented Kalman filter . . . 88
5.5.1 The augmented nonlinear model . . . 88
5.5.2 Initialization of the filter . . . 89
5.5.3 General unscented transformation . . . 90
5.5.4 Time update . . . 90
5.5.5 Measurement update . . . 91
5.6 Numerical verification of the filter . . . 91
5.6.1 The FRMCS model introduction . . . 92
5.6.2 Generation of benchmark states . . . 93
5.6.3 Generation of benchmark measurements . . . 94
5.6.4 Generation of sampled noise measurements . . . 95
5.6.5 Filter setup . . . 95
5.6.6 Filter performance with only DIC and DIC with accelerometer data . . . 97
5.7 Experimental stability test results . . . 98
5.8 Experimental pulse test results . . . 101
5.8.1 Results of Soft-Stiff-Rough under 8 Hz pulse . . . 101
5.8.2 State and force comparisons between all rough surface configurations under 8 Hz pulse . . . 104
5.8.3 State and force comparisons between all rough surface configurations under 3 Hz pulse . . . 106
5.8.4 State and force comparison between rough and semi-slippery surface configurations . . . 107
5.8.5 Sliding amount estimation for the semi-slippery surface test . . . 109
5.9 Comparisons between FRMCS predictions and experimental results . . . 112
5.10 Conclusion . . . 114

6 Conclusions **116**
6.1 Research contributions . . . 116
6.2 Summary of findings . . . 117
6.3 Recommendations for future work . . . 120

A Supplementary Results **121**

A.1 Stiff-Stiff-Rough under 8 Hz pulse 121

A.2 Stiff-Soft-Rough under 8 Hz pulse 123

A.3 Soft-Soft-Rough under 8 Hz pulse 124

A.4 Stiff-Stiff-Rough under 3 Hz pulse 126

A.5 Stiff-Soft-Rough under 3 Hz pulse 127

A.6 Soft-Stiff-Rough under 3 Hz pulse 129

A.7 Soft-Soft-Rough under 3 Hz pulse 130

A.8 Soft-Soft-Semi-slippery under 3 Hz pulse 132

Bibliography **134**

List of Figures

1.1 Configuration of some rocking structural systems. Reproduced from [13]. 2
1.2 Crushed corners of a rocking precast concrete wall specimen. Reproduced from [10]. 2
1.3 (a). Free-standing obelisk of Queen Hatshepsut (29 meters tall) reproduced from [20]. (b). A marble horse statue from Aphrodisias on display reproduced from [21]. (c). Overturned cabinet in Mexico earthquake reproduced from [22]. 3
1.4 (a). Schematic illustration of a rocking masonry wall. (b). A collapsed masonry wall due to out-of-plane rocking. Reproduced from [29]. . . 4

2.1 Analytical model of **(a)** rigid body rocking on rigid support [1], **(b)** rigid body rocking on deformable support considering sliding motion [35], **(c)** flexible body rocking on rigid support [36] and **(d)** flexible body rocking on rigid support considering sliding motion [37]. All sub-figures reproduced from the respective references. 7
2.2 Stability plot comparison of **(a)** rigid body rocking on different support deformability [35], **(b)** rocking body with different lateral flexibilities on rigid support [36] and **(c)** flexible body rocking on rigid support with different coefficients of friction [37] (FRM represents no sliding scenario). All sub-figures reproduced from the respective references. . 8
2.3 Demonstrations of **(a)** simplified contact approximation reproduced from [55] and **(b)** advanced contact approximation reproduced from [54]. 11
2.4 Stability analysis comparison between different modelling approaches. Reproduced from [54]. 12
2.5 Rocking angle comparison of rigid block rocking on different support material (AR5_C for concrete support, AR5_R4 for rubber support and AR5_T for timber support). Reproduced from [61]. 13

2.6 **(a)** Recorded acceleration of a rigid block under pure rocking due to a base harmonic acceleration, and **(b)** filtered acceleration with a high-pass Butterworth filter (10th order). Reproduced from [58]. 14
2.7 Free vibration response comparison of a flexible oscillator rocking on rigid support with different coefficients of friction (Test 35 on sandpaper and Test 45 on PTFE sheet). Reproduced from [64]. 15
2.8 Free vibration comparison between a flexible and a stiff frame rocking on stiff support. Reproduced from [69]. 16

3.1 (a) Schematic drawing and (b) displaced configuration of FRMCS. . . 21
3.2 Free body diagrams of (a) the top mass and (b) the bottom mass. . . 22
3.3 Illustrations of (a) Coulomb friction model and (b) elastic-predictor and plastic-corrector scheme for implementing the friction model. . . 23
3.4 Free body diagram of the base section. 25
3.5 (a) Displaced configuration of FRM and (b) Impulses during impact. 27
3.6 Free body diagram for the initial condition. 30
3.7 Free vibration response comparisons for (a) Case A ($\omega_n = 9.8225p$), (b) Case B ($\omega_n = 4.9599p$) and (c) Case C ($\omega_n = 2.4313p$) from FRMCS and FRM simulations. 31
3.8 Stability plots for (a) stiff body rocking on rigid support and (b) soft body rocking on rigid support. 32
3.9 Pulse excitation response comparisons for Case two ($\omega_n = 2.431p$, $\omega_v = 563.865p$) and Case four ($\omega_n = 2.431p$, $\omega_v = 56.387p$). 34
3.10 Pulse excitation response comparisons for Case four ($\omega_n = 2.431p$, $\omega_v = 56.387p$) and Case five (Case four with μ=0.14). 35
3.11 Response spectrum for Case one ($\omega_n = 9.822p$, $\omega_v = 563.865p$). 38
3.12 Maximum normalised pre-impact $\dot{\theta}$ vs (a) maximum normalised internal and external forces and (b) maximum normalised shear forces. . . 39
3.13 Response spectrum for Case two ($\omega_n = 2.431p$, $\omega_v = 563.865p$). 40
3.14 Response spectrum for Case three ($\omega_n = 9.822p$, $\omega_v = 56.387p$). . . . 41
3.15 Maximum M_{norm} vs Maximum N_{norm} for (a) Case three and (b) Case one. 42
3.16 Response spectrum for Case four ($\omega_n = 2.431p$, $\omega_v = 56.387p$). 43
3.17 Response spectrum comparison for different values of μ ($\omega_n = 2.431p$, $\omega_v = 56.387p$). 46

3.18 Comparison of stability plots for (a) Cases one to four and (b) Cases four and five. 47

4.1 A schematic representation of the kinematics in FFR. *YOX* is the global inertia reference frame, *Y'O'X'* the FFR. 53
4.2 A schematic representation of the kinematics in the Craig-Bampton method. 55
4.3 Approximation of $\boldsymbol{\delta}_r^I$ with selected mode shapes $\boldsymbol{\phi}^N$ and the corresponding coordinates $\boldsymbol{p}^N$. 56
4.4 (a) Column geometry, (b) rigid corner feet position and (c) points for time history demonstration. 58
4.5 (a) Finite element representation of the column (11172 dofs) and (b) Rigid corner feet on bottom surface shown in deep blue. 59
4.6 Comparison of rocking angle response between different reduced order models. 61
4.7 Comparison of normal stress response at point P9 (9m high) between different reduced order models. 61
4.8 Comparison of stability plots between the highly stiff elastic column and the rigid analytical model. 62
4.9 Comparison of global response of Case B modelled with different elements. 64
4.10 Comparison of stress response of Case B modelled with different elements. 65
4.11 Cross-sectional normal stress distribution at different heights at an examined time instance. The semi-transparent surface is the Euler beam stress distribution; the purple line represents the examined time instant of 0.6472s. 66
4.12 Comparison of global free vibration response of Case A (stiff), Case B (intermediate stiff), Case C (soft) and Case D (rigid) column. 67
4.13 Comparison of stress response in free vibration of Case A (stiff), Case C (soft) and Case D (rigid) column. 68
4.14 Comparison of single cycle pulse response of Case A (stiff), Case B (intermediate stiff) and Case C (soft) column. 70
4.15 Comparison of stability plots for three different cases. 71
4.16 Comparison of global response on high-grip surfaces to low-grip surfaces. 72
4.17 The tested steel frame and its Simulink model. 74

4.18 Comparison of displacement response between the Simulink prediction and the experiment result. . . . 75
4.19 Response of Case B to pulse type ground acceleration with a 30° attack angle . . . 76

5.1 The rocking specimen. . . . 80
5.2 Different support conditions (condition A is not shown because photo was not taken). . . . 82
5.3 The experiment setup. . . . 82
5.4 The placement of DIC speckles. . . . 84
5.5 The placement of accelerometers. . . . 85
5.6 (a) Schematic drawing showing the parameters and (b) states and contact forces of FRMCS. . . . 93
5.7 (a) Schematic drawing showing the states and (b) the free body diagram of the simplified model for time update. . . . 96
5.8 Comparison between the estimated displacement states and the benchmark. . . . 98
5.9 Comparison between the estimated velocity states and the benchmark. 99
5.10 Comparison between the estimated force states and the benchmark. . 99
5.11 Experimental stability test results with the shake table acceleration limit. . . . 100
5.12 Specimen 2 on support condition A: Comparison between the estimated accelerations and the measurements at different points, indicated in Figure 5.5, on the bottom mass. . . . 101
5.13 Specimen 2 on support condition A: Comparison between the estimated displacements and the measurements at different points on the bottom mass. . . . 102
5.14 Specimen 2 on support condition A: Comparison of the estimated accelerations and displacements with the measurements of the top oscillator. . . . 102
5.15 Estimated displacement states and forces. . . . 104
5.16 Comparison of estimated displacement responses across all cases under 8 Hz pulse. . . . 105
5.17 Comparison of estimated contact force responses across all cases under 8 Hz pulse. . . . 106

5.18 Comparison of estimated displacement responses across all cases under 3 Hz pulse. 108
5.19 Comparison of estimated contact force responses across all cases under 3 Hz pulse. 108
5.20 Comparison of estimated displacement responses between rough and semi-slippery surface cases under 3 Hz pulse. 109
5.21 Comparison of estimated contact force responses between rough and semi-slippery surface cases under 3 Hz pulse. 110
5.22 Measured vertical acceleration at P for stiff-soft-rough configuration under 3 Hz excitation. 110
5.23 Time windows for calculating sliding amount at different corners. . . 113
5.24 Comparison between experimental displacement estimations and FRMCS predictions for the soft–soft–rough case under the 8 Hz pulse. 114
5.25 Comparison between experimental force estimations and FRMCS predictions for the soft–soft–rough case under an 8 Hz pulse. 114

A.1 Comparison between the estimated accelerations and the measurements at various points on the bottom mass. 121
A.2 Comparison between the estimated displacements and the measurements at various points on the bottom mass. 122
A.3 Comparison of the estimated accelerations and displacements with the measurements of the top oscillator. 122
A.4 Comparison between the estimated accelerations and the measurements at various points on the bottom mass. 123
A.5 Comparison between the estimated displacements and the measurements at various points on the bottom mass. 123
A.6 Comparison of the estimated accelerations and displacements with the measurements of the top oscillator. 124
A.7 Comparison between the estimated accelerations and the measurements at various points on the bottom mass. 124
A.8 Comparison between the estimated displacements and the measurements at various points on the bottom mass. 125
A.9 Comparison of the estimated accelerations and displacements with the measurements of the top oscillator. 125
A.10 Comparison between the estimated accelerations and the measurements at various points on the bottom mass. 126

A.11 Comparison between the estimated displacements and the measurements at various points on the bottom mass. 126
A.12 Comparison of the estimated accelerations and displacements with the measurements of the top oscillator. 127
A.13 Comparison between the estimated accelerations and the measurements at various points on the bottom mass. 127
A.14 Comparison between the estimated displacements and the measurements at various points on the bottom mass. 128
A.15 Comparison of the estimated accelerations and displacements with the measurements of the top oscillator. 128
A.16 Comparison between the estimated accelerations and the measurements at various points on the bottom mass. 129
A.17 Comparison between the estimated displacements and the measurements at various points on the bottom mass. 129
A.18 Comparison of the estimated accelerations and displacements with the measurements of the top oscillator. 130
A.19 Comparison between the estimated accelerations and the measurements at various points on the bottom mass. 130
A.20 Comparison between the estimated displacements and the measurements at various points on the bottom mass. 131
A.21 Comparison of the estimated accelerations and displacements with the measurements of the top oscillator. 131
A.22 Comparison between the estimated accelerations and the measurements at various points on the bottom mass. 132
A.23 Comparison between the estimated displacements and the measurements at various points on the bottom mass. 132
A.24 Comparison of the estimated accelerations and displacements with the measurements of the top oscillator. 133

Chapter 1

Introduction

1.1 Research background

When subjected to ground motions, objects lacking sufficient tensile strength at their base connections may undergo rotational motions, characterized by repeated separation, impact, sliding, and re-contact with their supports. This behaviour is commonly referred to as rocking.

In the attempt to explain the stability of rocking objects during earthquakes, Housner published his pioneering paper in 1963 [1] then the earthquake engineering community started a series of studies about the rocking dynamics. To date, studies of rocking behaviour mainly aim at addressing three types of research questions:

a. **The enhancement of seismic performance of buildings and bridges.**

   The study subjects often are bridge piers (e.g., [2, 3, 4]), seismic frames (e.g., [5, 6, 7]) or walls (e.g., [8, 9]) that are designed to rock during earthquakes; their stability is ensured by additional structural elements that prevent overturning (e.g., Figure 1.1). The idea is to use the rocking motion as a designed mechanism for earthquake isolation and to reduce the residual story drift. These rocking structural components could be tall and slender, so their lateral flexibility cannot be ignored. In addition, experimental studies (e.g., [10, 11, 12]) have shown that the force and stress response at the rocking corner can be large and cause local damage (Figure 1.2); these large stresses may further alter the contact surface geometry, thereby affecting the overall rocking response. Consequently, quantifying these forces and stresses is crucial.

b. **The stability analysis of important unanchored objects.**

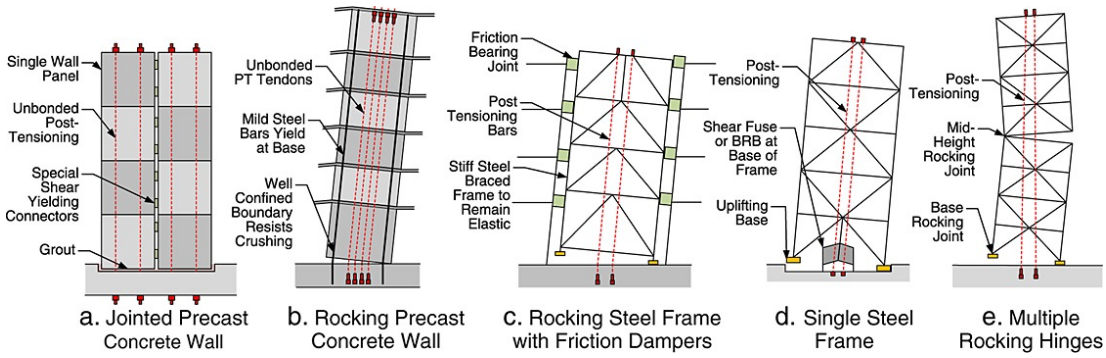


Figure 1.1: Configuration of some rocking structural systems. Reproduced from [13].

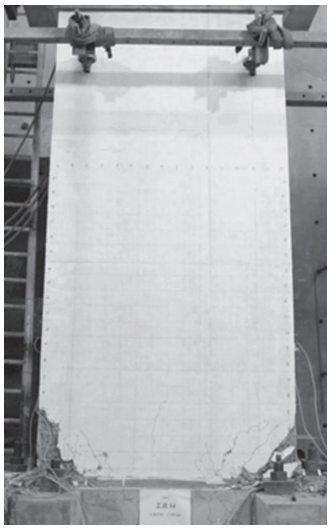


Figure 1.2: Crushed corners of a rocking precast concrete wall specimen. Reproduced from [10].

The study subjects include historical remains, such as tall and slender Obelisks Figure 1.3.(a), or short and stocky tombstones; artistic assets such as statues, museum displays Figure 1.3.(b); unanchored non-structural components in critical facilities such as electrical cabinets resting freely in a power plant Figure 1.3.(c), and valuable stacked ship containers. It can be seen that these objects feature different geometries and for some of them, the flexibility cannot be ignored. The stability of these objects is often of interest (e.g., [14, 15, 16, 17]). To evaluate their susceptibility to overturning under dynamic loads, large displacements and hence geometric nonlinearity must be considered. Furthermore, experimental studies (e.g., [18, 19]) have shown that sliding motion and support deformability noticeably affect the stability.



Figure 1.3: (a). Free-standing obelisk of Queen Hatshepsut (29 meters tall) reproduced from [20]. (b). A marble horse statue from Aphrodisias on display reproduced from [21]. (c). Overturned cabinet in Mexico earthquake reproduced from [22].

c. **The seismic assessment of masonry structures.**

The study subjects are often masonry walls, as it is well established that under strong out-of-plane seismic excitations, masonry walls lacking box-type structural behaviour are susceptible to detachment from the main structure, followed by rocking, sliding, and potentially overturning Figure 1.4. This rocking response is one of the most recurrent out-of-plane failure modes and therefore, the stability analysis of the masonry walls is important for seismic assessment (e.g., [23, 24, 25, 26, 27]). Moreover, masonry walls located within a building and supported at elevated levels, such as on floor diaphragms with different

stiffness, can also exhibit rocking behaviour [28]. In such cases, the characteristics of the supporting system are different from those of ground-supported walls.

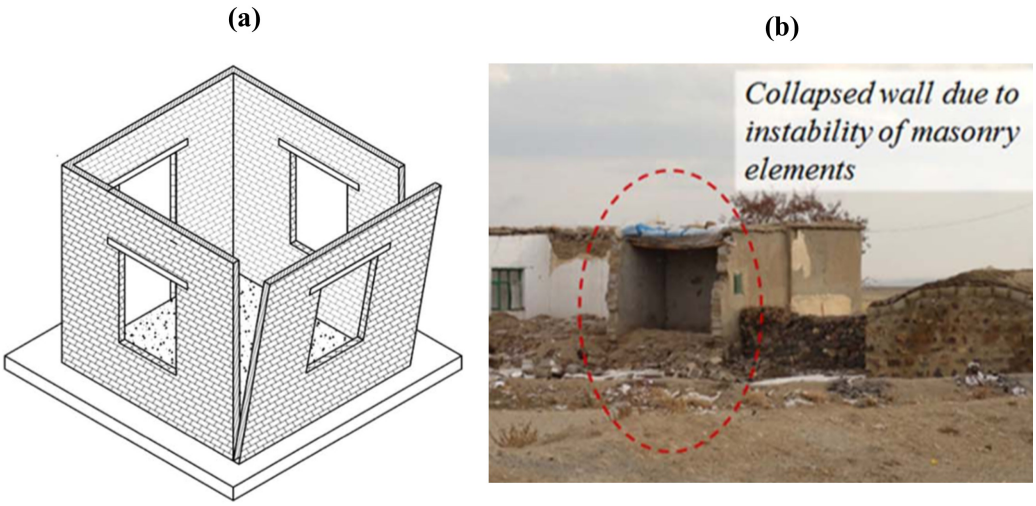


Figure 1.4: (a). Schematic illustration of a rocking masonry wall. (b). A collapsed masonry wall due to out-of-plane rocking. Reproduced from [29].

1.2 Motivations and objectives

It can be seen from the previous section that the study of rocking dynamics encompasses not only stiff bodies but also flexible structures, and frequently involves complex phenomena such as sliding motions and varying support conditions; also that such analyses should address the stability of the rocking bodies to evaluate how prone they are to overturning, and the contact force and stress response during rocking. A comprehensive literature review presented in **Chapter** 2 highlights significant research gaps in the current analytical, numerical, and experimental studies on the stability and the contact response of flexible structures rocking on deformable supports. To address these gaps, the present study is dedicated to the systematic examination of flexible bodies rocking on deformable supports, with the objectives to:

- propose an analytical model that considers the sliding motions, geometric nonlinearities for stability analysis, and allows for contact force investigations.
- propose a computationally efficient numerical model that considers stress concentration near the rocking corners, sliding motions and geometric nonlinearities.

- investigate experimentally the influence of flexibility and support deformability on the rocking response, with a focus on the force response during impact.

1.3 Organisation of this thesis

A detailed review of research on the analytical, numerical and experimental studies of rocking problems is presented in **Chapter** 2. The research gaps are identified and, the proposed methods to overcome them are detailed in the following **Chapters** 3-5.

Chapter 3 presents an analytical model developed to qualitatively investigate the influence of superstructure flexibility and support deformability on the rocking response, incorporating sliding motions and geometric nonlinearities. The superstructure flexibility is represented by a point-mass oscillator, while the contact behaviour (i.e., impact and frictional behaviour) is modelled using discrete elements comprising springs and dampers. This modelling approach enables the evaluation of contact force responses and will be employed for contact stress analysis within the numerical framework proposed in **Chapter** 4.

Chapter 4, a generalised numerical framework for modelling the rocking, free flight, sliding motion of flexible structures on deformable support is proposed. The contact behaviour is modelled with discrete elements. Isoparametric finite elements in a floating frame of reference are used to model the superstructure; this general representation can capture a wide range of structural configurations, including rocking columns and rocking frames, and allows for modelling the complex stress states which arise in the contact zone. To achieve computationally efficient models, the Craig-Bampton reduction method is used to represent the superstructure finite element model on the basis of a limited number of natural vibration modes.

In **Chapter** 5, an experimental setup is employed to investigate the influence of structural flexibility, support deformability and sliding motion on the rocking response. The contact force response is estimated from displacement and acceleration measurements using a modified Unscented Kalman Filter (UKF). The setup includes a high-speed Digital Image Correlation (DIC) system, accelerometers, a deformable support with different surface conditions, and a rocking specimen designed to replicate the analytical model proposed in **Chapter** 3.

Important findings from analytical, numerical, and experimental studies of flexible structures rocking on deformable support in **Chapters** 3-5 are summarised in **Chapter** 6, and suggestions for further work are identified.

Chapter 2

Literature review

2.1 Review of analytical modelling of rocking problems

The first study on the rocking dynamics of rigid bodies was conducted by Housner [1] in 1963 to explain the unexpected stability of tall, slender structures under seismic excitation. It was motivated by observations in the 1960 Chilean earthquake, where elevated "golf-ball-on-a-tee" water tanks and other slender structures survived strong shaking, while reinforced-concrete tanks suffered severe damage. Housner showed that tall, slender, large-scale rocking structures are more stable against overturning than static analysis predicts and identified a scale effect, where geometrically similar but larger structures are inherently more stable than smaller ones. To describe this behaviour, he proposed the inverted pendulum model (IPM) (shown in Figure 2.1 (a)), representing a rigid body rocking on a flat base with one rotational degree of freedom. Energy dissipation occurs through inelastic impacts at the contact points, quantified by an energy reduction ratio. Subsequent studies [30, 31, 32, 33, 34] expanded Housner's work by incorporating additional motion phases. Ishiyama [30] classified six types of motion and derived governing equations for each. Shenton and Jones [31] developed a unified formulation encompassing sliding, rocking, slide–rock, and free-flight motions. Lipscombe and Pellegrino [34] conducted free-rocking tests on steel blocks with different aspect ratios and proposed improved analytical models. Pompei et al. [32] established criteria distinguishing sticking, slipping, and separation modes under horizontal excitation. Collectively, these studies showed that different motion phases significantly influence impact energy loss and overall stability. However, these models were not capable of considering combined effects of geometric nonlinearities, ground deformability, sliding, and uplift. To overcome this, Chatzis and Smyth [35]

proposed a new model (shown in Figure 2.1 (b)) where the support deformability was modelled with CSM or Winkler models that follow Coulomb frictional behaviour. They conducted a stability analysis using their models to investigate the influence of support deformability. In such analyses, a rocking body is subjected to horizontal ground accelerations in the form of single-cycle pulses with varying magnitudes and frequencies. The magnitude-frequency pairs that cause overturning are then recorded to generate a stability plot. They found that support deformability significantly affects the stability of the rocking body (shown in Figure 2.2 (a)) by influencing both stiffness and energy dissipation, and sliding provides a form of hysteretic damping that affects the stability conditions.

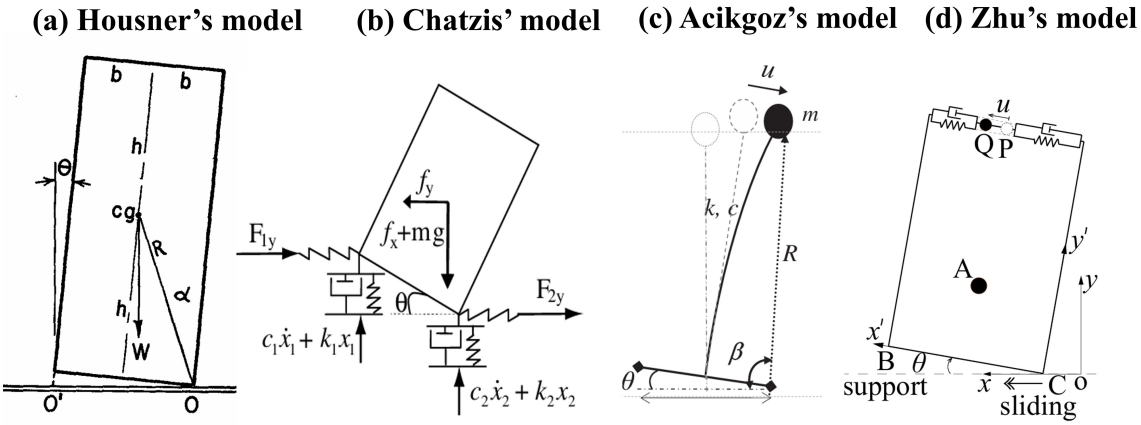


Figure 2.1: Analytical model of **(a)** rigid body rocking on rigid support [1], **(b)** rigid body rocking on deformable support considering sliding motion [35], **(c)** flexible body rocking on rigid support [36] and **(d)** flexible body rocking on rigid support considering sliding motion [37]. All sub-figures reproduced from the respective references.

Research on flexible rocking began with Beck and Skinner [38], who examined the feasibility of allowing bridge piers to rock as an economical alternative. Their work was motivated by advances in reinforced-concrete technology that made tall concrete bridges more economical than steel ones, but their greater mass generates higher seismic inertia forces, requiring costly solutions such as heavy reinforcement or high ductility. Huckelbridge and Clough [5] later tested rocking steel frames and developed analytical models, and noticed that the response changed significantly after changing the stiff support to a neoprene impact pad. Yim et al. [39] analysed the feasibility of foundation uplift. These early studies mainly aimed to demonstrate the seismic advantages of allowing rocking in different structural components. Psycharis [40] was first to clarify the dynamics of flexible rocking. He modelled the superstructure as an n-degree-of-freedom shear system with viscous damping and the foundation with

spring–damper elements to represent impact energy loss. He found that uplift and rocking strongly affect the first vibration mode, while higher modes remain largely unaffected. Recognizing the limitations of small-displacement assumptions in the previous studies, Oliveto et al. [41] developed a nonlinear formulation for large displacements and showed that linearized models underestimate displacements and internal forces in response spectra. Acikgoz and DeJong [36] used the same model (shown in Figure 2.1 (c)) with improved impact treatment and considered pulse type excitations. They identified an "uplifted resonance" phenomenon where elastic–rocking coupling amplifies responses, and flexibility influences overturning stability (shown in Figure 2.2 (b)) through a "shrinking and sinking" effect. To address the excessive or unrealistic energy loss in earlier studies, Zhu et al. [42] proposed a new impact model and a new flexible rocking model. The same authors [37] later incorporated sliding motion (shown in Figure 2.1 (d)), noting its long-neglected but important role. They found that for slender, flexible structures on low-friction surfaces, sliding can induce unexpected overturning even after a purely sliding phase and, the sliding motion can enhance the overturning stability for flexible rocking body compared to no sliding scenario (shown in Figure 2.2 (c))).

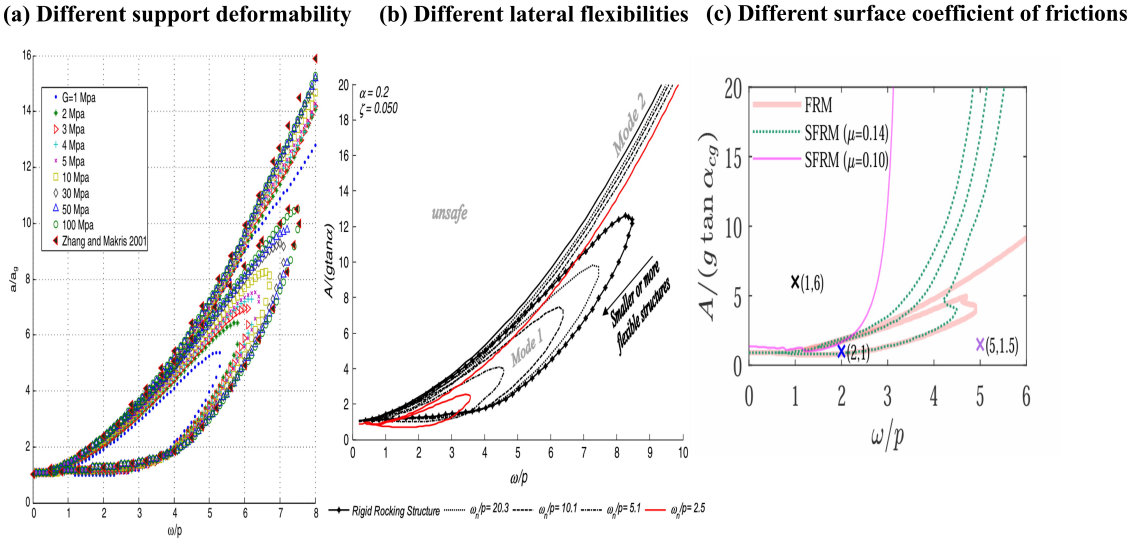


Figure 2.2: Stability plot comparison of **(a)** rigid body rocking on different support deformability [35], **(b)** rocking body with different lateral flexibilities on rigid support [36] and **(c)** flexible body rocking on rigid support with different coefficients of friction [37] (FRM represents no sliding scenario). All sub-figures reproduced from the respective references.

Overall, the literature review shows that analytical studies of rocking cover both rigid and flexible bodies, with supports modelled as either rigid (using impact mod-

els) or deformable (using spring–damper elements). Studies on flexible bodies with deformable supports (e.g., [39, 5]) focused mainly on demonstrating seismic benefits rather than the coupled effects of structural flexibility and foundation deformability. Moreover, although experiments and analyses [32, 31, 35, 37] have shown that sliding greatly affects rocking behaviour, no study has yet examined the combined influence of structural flexibility, support deformability, and sliding on the rocking response.

2.2 Review of numerical modelling of rocking problems

With the growing adoption of rocking mechanisms in structural systems, numerous numerical modelling approaches have been developed to simulate rocking behaviour. However, because rocking involves complex nonlinear, impact and sliding phenomena, full-scale finite element modelling is highly challenging and has typically been limited to analysing individual rocking columns under monotonic quasi-static loading (e.g., [43]). To make dynamic analysis more practical, researchers have proposed a wide range of methods, from simplified models developed for computational efficiency to high-fidelity formulations capable of capturing detailed nonlinear response.

Many studies have simplified the representation of the contact interface between a rocking body and its support. Spieth et al. [44], Palermo et al. [3], Marriott et al. [45], and Wang et al. [46] used a series of zero-length, compression-only, two-node contact elements distributed along the joint interface (an example is shown in Figure 2.3 (a2)). This approach is conceptually straightforward but requires a large number of elements to capture the contact-force distribution accurately, compromising its computational efficiency. Vassiliou et al. [47] proposed a nonlinear elastic, viscously damped, zero-length rotational spring model to represent the contact interface (an example is shown in Figure 2.3 (a3)). While being computationally efficient, it cannot capture sliding motions and the abrupt changes in contact force that occur during impact.

Other researchers [48, 49, 50, 51] employed flexibility-based or force-based (FB) beam–column elements. In these models, the rocking member is represented by a single FB element, and the contact interface is simulated using a single cross-section or fibres with compression-only material response (an example is shown in Figure 2.3 (a1)). However, these elements enforce the plane-cross-section assumption due to the use of beam-column elements, which is not valid near the contact region ([52]). Avgenakis and Psycharis [53] developed a macroelement formulation for rocking members

that captures the nonlinear stress distribution at the contact interface and allows both sliding and upthrow motion.

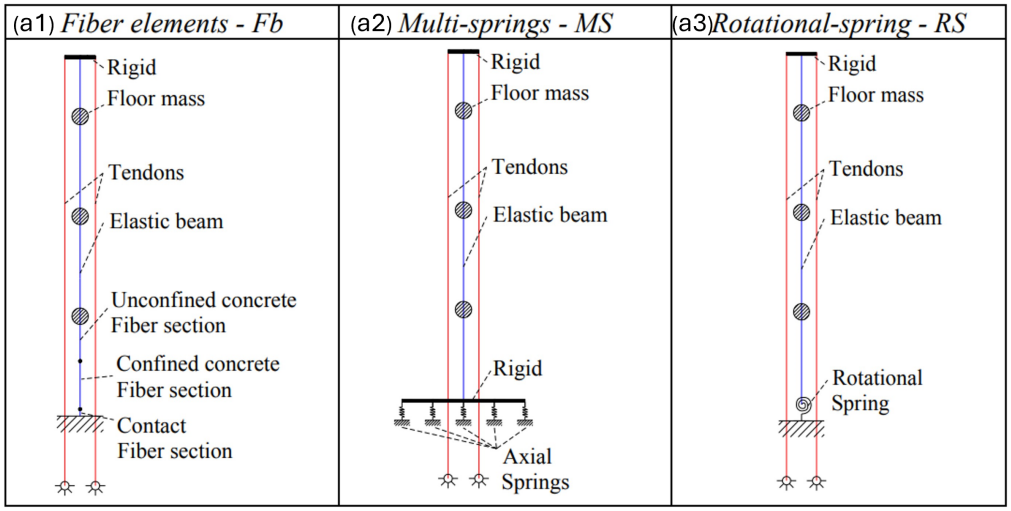
It should be noticed that, however, the previously mentioned methods, except for the model of [47], are based on small-displacement assumptions. These assumptions limit their use in problems involving large rotations or stability analysis.

More advanced methods overcome the limitations of simplified models. Emmanouil et al. [54] proposed a high-fidelity approach based on the material point method (MPM) illustrated in Figure 2.3 (b) to model both the rocking body and support media. Their model accounts for geometric nonlinearity, the deformability of both the rocking body and the support, and sliding motion. This formulation can capture complex impact and contact behaviour with high accuracy. Although it offers significant improvements over traditional full-scale finite element methods, the computational cost remains considerable. In addition, they conducted stability analysis, using different modelling approaches, on a rigid body rocking on stiff support, the configuration of which is shown in Figure 2.4 (a), and the results are shown in Figure 2.4 (b). It can be seen that the MPM model demonstrates a very good agreement with the WM (Winkler spring model), which is a Winkler spring model counterpart of the concentrated spring model (Figure 2.2 (b)) additionally proposed in [35]. Based on this, they argued that the simplified concentrated spring model can produce stability analysis results in good agreement with the MPM model as well for a body rocking on feet.

In summary, the literature review shows that existing modelling strategies demonstrate a trade-off between accuracy and computational efficiency. Simplified approaches are easy to implement but rely on assumptions that restrict their applicability (e.g., precluding stability analysis) and neglect potentially important aspects (i.e., sliding and nonlinear stress distribution) in rocking problems. High-fidelity methods, while capable of representing geometric nonlinearity and impact effects in detail, remain computationally demanding and hence impractical for large systems. Consequently, there is a need for a practical numerical method that accounts for large displacements, variable deformability of both the rocking body and its support, and the nonlinear stress distribution near the contact zone.

.

(a) Rocking modelling with simplified contact approximation



(b) Rocking modelling with advanced contact approximation

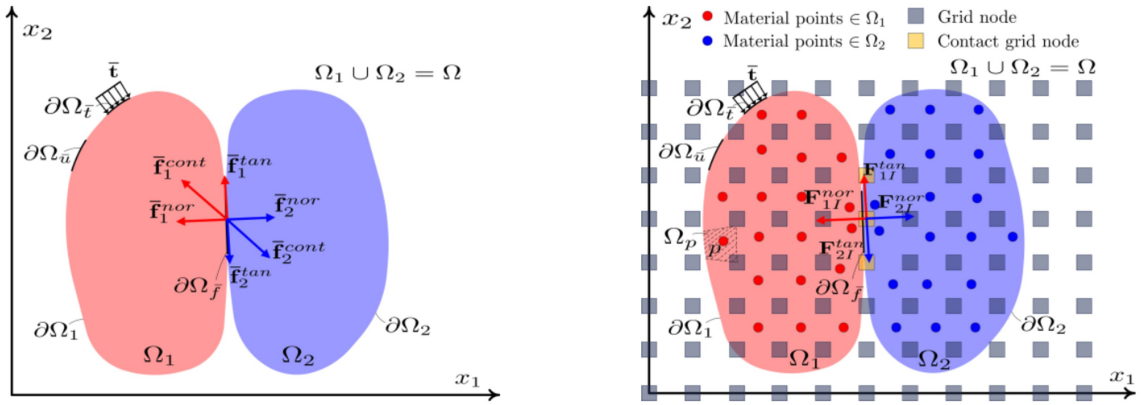


Figure 2.3: Demonstrations of **(a)** simplified contact approximation reproduced from [55] and **(b)** advanced contact approximation reproduced from [54].

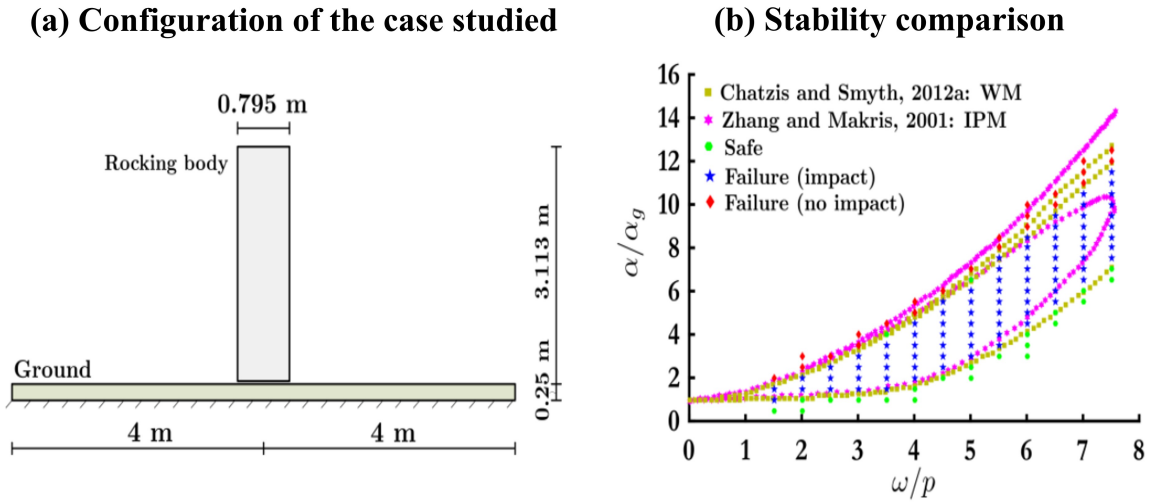


Figure 2.4: Stability analysis comparison between different modelling approaches. Reproduced from [54].

2.3 Review of experimental studies of rocking problems

One of the first experimental investigations of rigid body rocking was conducted by Priestley et al. [56]. Their research, inspired by the work of Housner [1], aimed to explore the potential seismic benefits of allowing structures to rock and to develop a simple design method for predicting rocking displacements. Since then, experimental studies on rigid body rocking have primarily focused on validating theoretical models, quantifying energy dissipation during impacts (on both rigid and deformable supports), examining overturning stability, and investigating non-planar rocking behavior (e.g., [34, 57, 18, 58, 59]).

Importantly, Taniguchi [60] conducted experiments on rigid blocks rocking on flat surfaces with different coefficients of friction and found that sliding significantly influences both the onset and magnitude of rocking. ElGawady et al. [61, 18] performed experiments on concrete blocks rocking on supports with varied base materials. They observed that different support material influenced the free rocking response as shown in Figure 2.5. In addition, they noticed that softer base materials reduced impact accelerations and increased energy losses per impact, and reported energy exchange between the rocking body and rubber supports, leading to altered rocking responses compared with stiff supports. Furthermore, Baratta et al. [58] reported that, in experiments on rigid blocks rocking on stiff supports, applying a high-pass Butterworth filter (10th order) to the acceleration data removed the peak accelerations at impact

as shown in Figure 2.6, indicating that impact energy spreads across a wide range of frequencies.

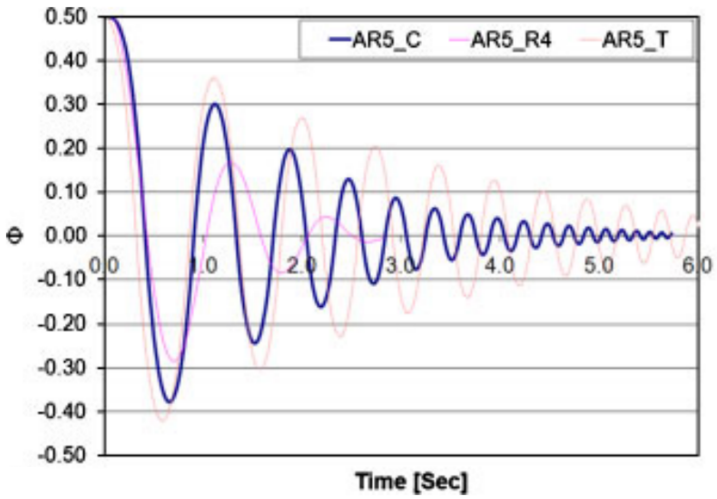


Figure 2.5: Rocking angle comparison of rigid block rocking on different support material (AR5_C for concrete support, AR5_R4 for rubber support and AR5_T for timber support). Reproduced from [61].

On the other hand, experimental investigations involving flexible rocking systems remain relatively scarce. Truniger et al. [62] conducted rocking tests on laterally flexible cantilevers to validate energy dissipation models during impact. Acikgoz et al. [63] performed experiments using modular flexible rocking columns and confirmed that lateral vibration is coupled with rocking motion. In these experiments, sliding was deliberately minimized in an attempt to remove its influence on the response. In addition, although both displacements and accelerations data were recorded, the data post-processing method usually treated them separately, preventing the potential benefits by integrating the two types of data to improve the estimation of the velocity states, which is important for coefficient-of-restitution-based impact models. To overcome these limitations, Zhu et al. (under review) [64] subsequently proposed an experimental setup that allows modular change of lateral flexibility and surface coefficient of friction, allowing the study of sliding motion. The data were recorded with a digital image correlation (DIC) system and the accelerometers, and post-processed with a data fusion method to obtain improved estimates of unmeasured velocity information. The results provided data for impact model verification and, showed that sliding accelerates the decay of rocking motion and affects overall stability (an example is shown in Figure 2.7). However, the sampling frequency of the DIC system

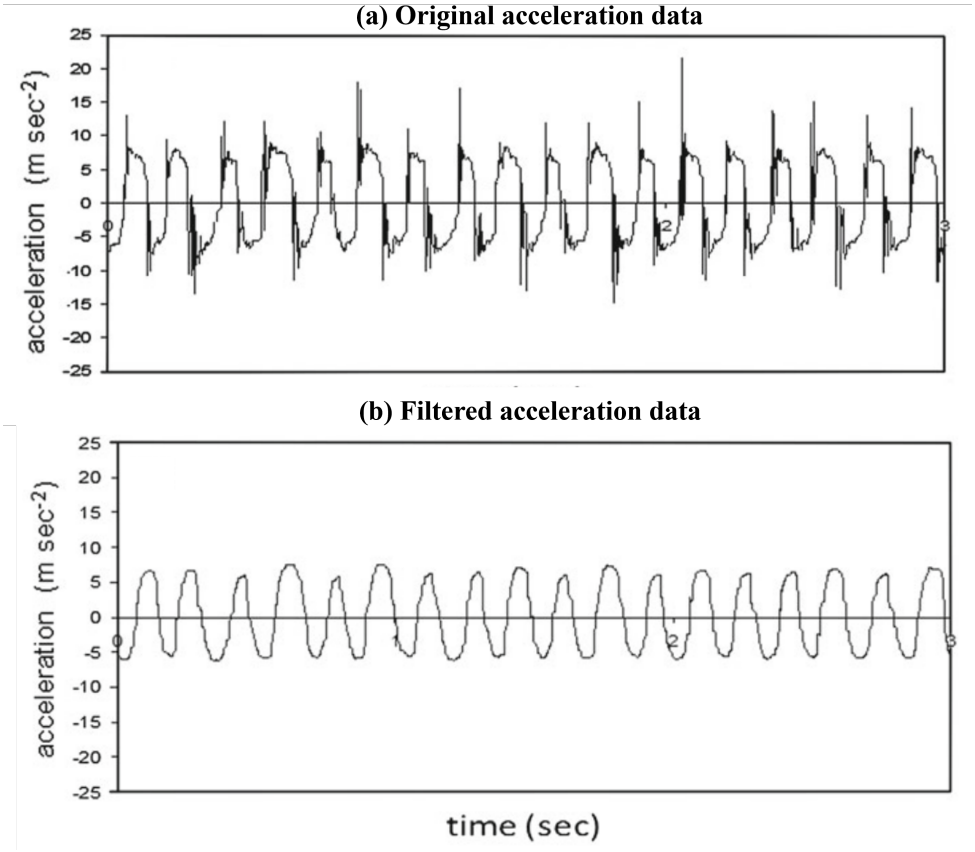


Figure 2.6: **(a)** Recorded acceleration of a rigid block under pure rocking due to a base harmonic acceleration, and **(b)** filtered acceleration with a high-pass Butterworth filter (10th order). Reproduced from [58].

was 100 times smaller than that of the accelerometers, which could compromise the quality of the velocity estimation using data fusion.

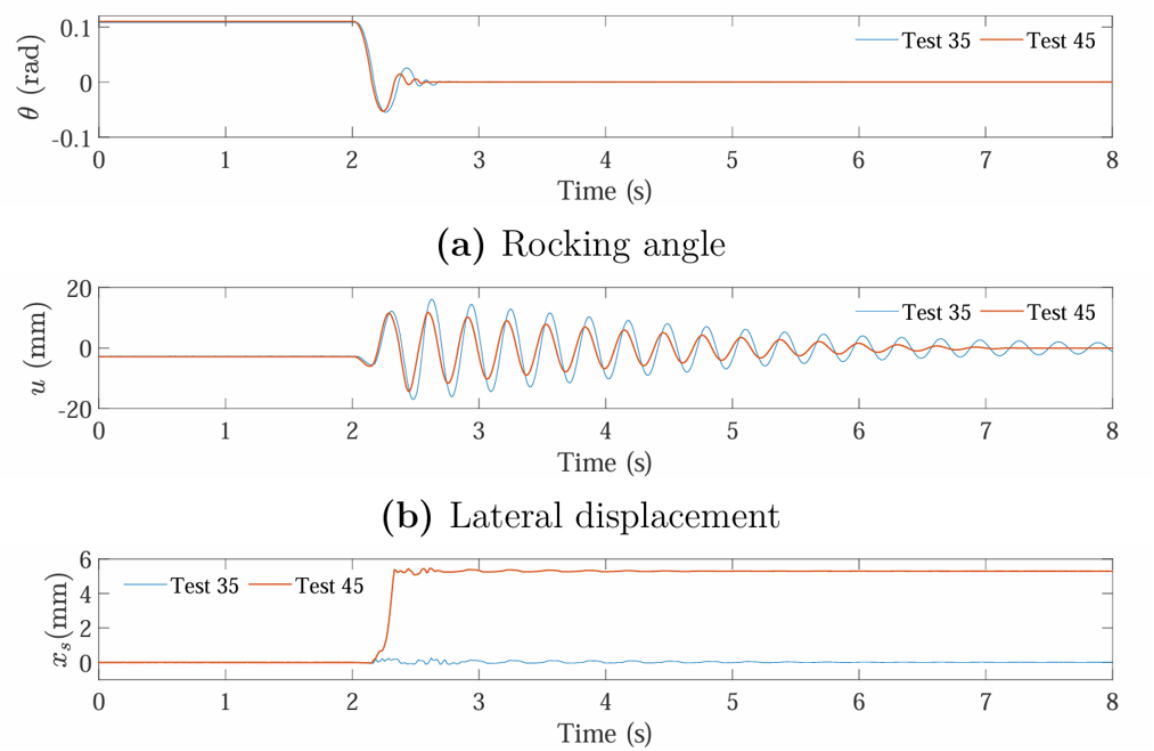
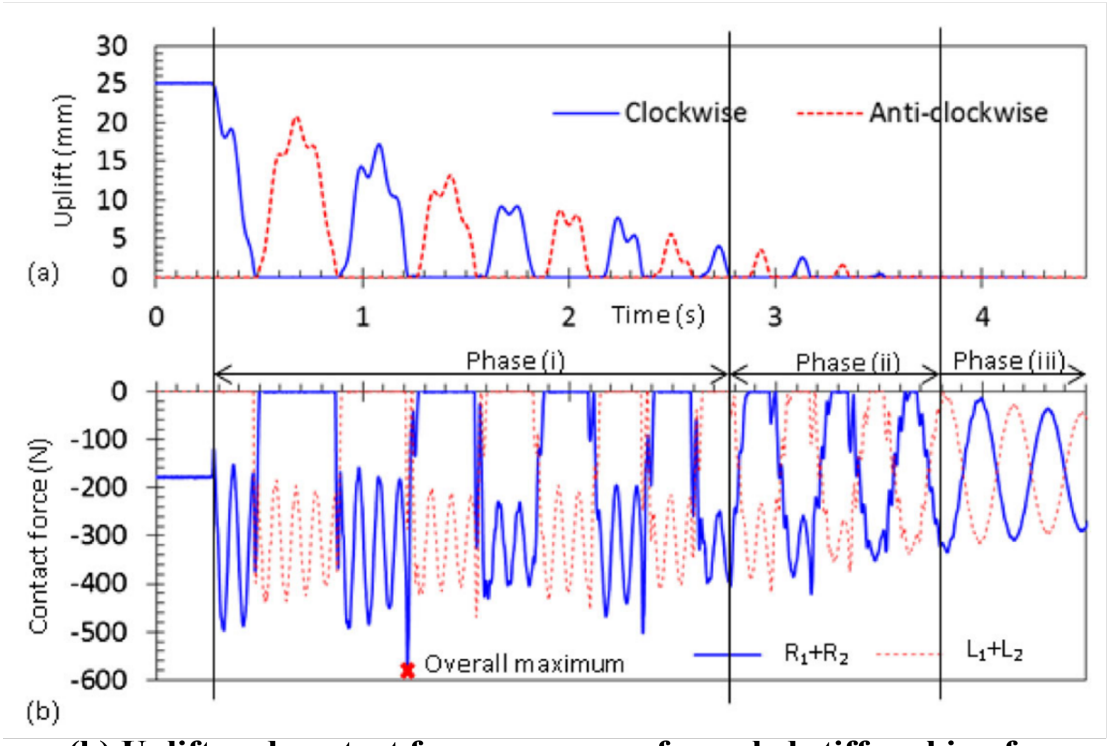


Figure 2.7: Free vibration response comparison of a flexible oscillator rocking on rigid support with different coefficients of friction (Test 35 on sandpaper and Test 45 on PTFE sheet). Reproduced from [64].

In addition, several experimental studies that aimed to prove the concept of rocking isolation using scaled models of real structures [10, 65, 66, 67, 68] showed that while rocking effectively reduced structural deformation, it also caused crushing of the rocking corners, indicating the presence of large contact forces. Quantifying these forces is essential for better design of rocking interfaces; however, such forces were not recorded in those experiments. Chen et al. [69] employed load cells to experimentally assess the contact forces between the footing of a rocking bridge pier and a stiff support. Their results indicated that bridge pier flexibility significantly affected both the magnitude of the contact force and the amplitude of rocking angle as shown in Figure 2.8. Nevertheless, the compliance of the load cells was found to influence the interface properties, thereby altering the system response

.

(a) Uplift and contact force response of a scaled flexible rocking frame



(b) Uplift and contact force response of a scaled stiff rocking frame

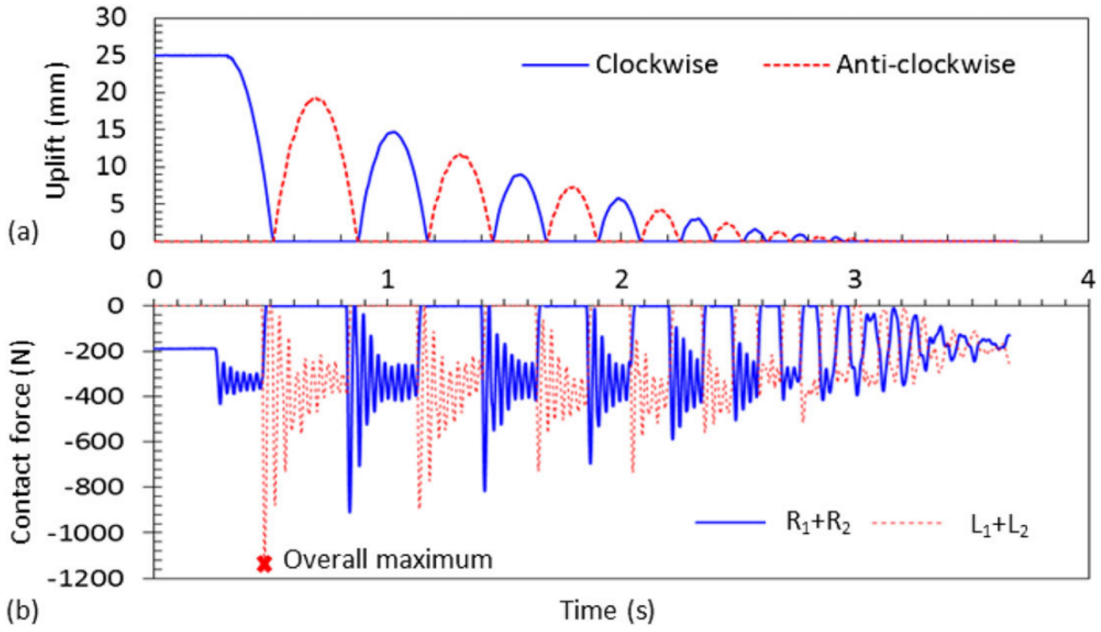


Figure 2.8: Free vibration comparison between a flexible and a stiff frame rocking on stiff support. Reproduced from [69].

Collectively, the literature demonstrates that both the subject matter and the experimental methods used to study rocking problems have advanced substantially; the subject matter progresses from early, simplified cases to recent investigations that account for more realistic factors and applications, and from methods based on separate analysis of recorded data to modern data fusion approaches. However, although existing studies show that lateral flexibility, support deformability, and sliding motion each significantly affect the rocking response, no experimental research has yet examined their combined effects. The literature also indicates that impact-induced energy is distributed over a wide frequency range, and that contact-based force measurements can inadvertently alter interface properties. Consequently, there is a clear need for (i) experiments that investigate the coupled effects of lateral flexibility, support deformability, and sliding motion on rocking behaviour, (ii) advanced signal-processing techniques capable of analysing data with minimal frequency cutoff, and (iii) non-contact force measurement methods that preserve the original interface characteristics.

2.4 Conclusions

This chapter has reviewed the existing analytical, numerical, and experimental studies on the rocking problems. Analytical investigations have established the fundamental understanding of rocking dynamics, beginning with Housner's inverted pendulum model and extending to flexible systems with deformable supports. These studies have demonstrated that lateral flexibility, support deformability, and sliding motion each have a pronounced influence on overturning stability and energy dissipation. However, most analytical models either neglect one or more of these factors or treat their interactions in a simplified manner, leaving the coupled effects insufficiently understood.

Numerical modelling studies have made substantial progress in capturing the nonlinear behaviour of rocking systems, but they reveal a persistent trade-off between computational efficiency and physical fidelity. Simplified models are efficient but mostly rely on small-displacement assumptions and oversimplified contact representations, while high-fidelity formulations accurately capture geometric nonlinearity and impact phenomena at the cost of significant computational expense. A practical yet sufficiently accurate numerical method that considers geometric nonlinearity, sliding motions, deformability of both the rocking body and the supports, and the nonlinear stress distribution near the contact interface remains to be developed.

Experimental studies have provided validation of analytical and numerical predictions, confirming the sensitivity of rocking response to surface friction, support stiffness, and structural flexibility. Nevertheless, previous experiments have generally examined these effects in isolation. The combined influence of flexibility, support deformability, and sliding motion has not been experimentally characterised. Moreover, conventional contact-based force measurement techniques have been shown to alter the interface properties, while signal processing of acceleration data remains challenging due to that the impact energy spreads across a wide range of frequencies.

To address the identified research gaps, **Chapters** 3–5 present the corresponding analytical, numerical, and experimental methods developed in this study to overcome them.

Chapter 3

The Dynamic Behaviour of Flexible Oscillators Rocking and Sliding on Concentrated Springs

3.1 Introduction

To address the research gap identified in **Chapter** 2.1—namely, the absence of studies examining the combined effects of lateral flexibility, support deformability, and sliding motion on rocking response—this chapter proposes a new analytical model, termed the *Flexible Rocking Model on Concentrated Springs* (FRMCS). In this model, concentrated vertical springs and viscous dampers are employed to simulate the contact forces from the support medium at the corners of the body; the tensionless vertical contact element behaves linearly in compression. Horizontal concentrated springs and linear viscous dampers are used to represent the frictional behaviour at the corners, where the constitutive law of the springs accounts for both elastic deformations and sliding in accordance with Coulomb friction law. Incorporating the deformability of the support medium also enables direct evaluation of the contact forces.

The proposed FRMCS model is presented in detail in **Section** 3.2. Following model parameter normalisation in **Section** 3.3, the FRMCS model is compared with the *Flexible Rocking Model* (FRM) developed by Zhu *et al.* [42] in **Section** 3.4. This comparison considers the response of a slender body on a high-grip, stiff support medium—conditions under which the effects of sliding and free flight are minimal—to verify whether FRMCS can produce results consistent with FRM given that the two models incorporate different energy dissipation mechanisms.

Subsequently, **Section** 3.5 investigates two rocking configurations representing

soft oscillators with either stiff or soft support media, together with a third configuration focusing on the effect of sliding. These configurations are subjected to sinusoidal pulse excitations to preliminarily explore the influences of support deformability, lateral flexibility, and sliding on rocking response. To generalise the findings, **Section** 3.5 further considers two additional configurations involving stiff oscillators with either stiff or soft support media, resulting in a total of five configurations. These are subjected to a wide range of sinusoidal pulse excitations, and their force and displacement response spectra are examined. The main findings are summarised in **Section** 3.6.

3.2 Model introduction

A schematic drawing for FRMCS is shown in Figure 3.1(a). The model consists of a top point mass m_p and a rigid bottom body of mass m with a centre of mass located at point B and a mass moment of inertia about B, I_g. The bottom mass can take any shape that is bilaterally symmetric and to simplify the figure, it is represented as a box. The top mass m_p is connected to the bottom mass through springs and dampers, and is constrained to move laterally, in a direction parallel to the line defined by the two bottom corners ZY. When the spring is undeformed, the top mass is located at point P. The width of the bottom body is denoted as b, height as h. Its centre of mass is located at height h_b. The centre of mass of the whole body is located at point C when the body is at rest at height h_{cg}. The slenderness of the top mass, the bottom mass and the whole system are described with α_p ($\tan\alpha_p = b/(2h)$), α ($\tan\alpha = b/(2h_b)$) and α_{cg} ($\tan\alpha_{cg} = b/(2h_{cg})$) respectively. R_p, R_{cg} and R is the distance from points P, C, B to either of the bottom corners. FRMCS can be used to represent rocking structures with lateral flexibility. For example, a tall rocking bridge pier can be idealised with FRMCS where the top mass would be the supported mass in the deck and the bottom mass the bridge foundation mass. The bridge pier mass can be distributed to the top and bottom masses. Since the bottom mass represents structural components above the rocking interface, it may be located at a non-zero height. It should be noted that FRMCS is a simplified representation, because structures normally have more than one lateral mode but FRMCS possesses only one lateral degree of freedom.

Figure 3.1(b) shows the deformed position of the system. In this chapter, this will largely be due to the influence of horizontal $\ddot{x}_g$ and vertical $\ddot{y}_g$ ground excitations. The FRMCS has five degrees of freedom: x, y, θ, u and $\boldsymbol{F_{fs}}$. x and y are the $\boldsymbol{IJ}$

coordinates of the centre of mass of the bottom body with respect to an absolute frame with origin, O, located on the undeformed ground surface. u is elongation of the lateral spring and describes the $\vec{i}$ coordinate of the body in the rotating $\boldsymbol{ij}$ coordinate system with the origin at B. The rotation of the bottom body is described by θ. $\boldsymbol{F_{fs}}$ is the frictional spring force that has to be tracked to describe current states of the model; it is introduced in depth in **Section** 3.2.2. The positive sign convention is demonstrated with the unit vector pairs shown in Figure 3.1(b).

Contact elements at the corners consist of a spring (k_v) and a damper (c_v) in the vertical direction. In the horizontal direction, a spring (k_f) and a damper (c_f) are used to model horizontal ground deformability and sliding behaviour according to Coulomb law of friction. The springs and dampers are illustrated in Figure 3.1.

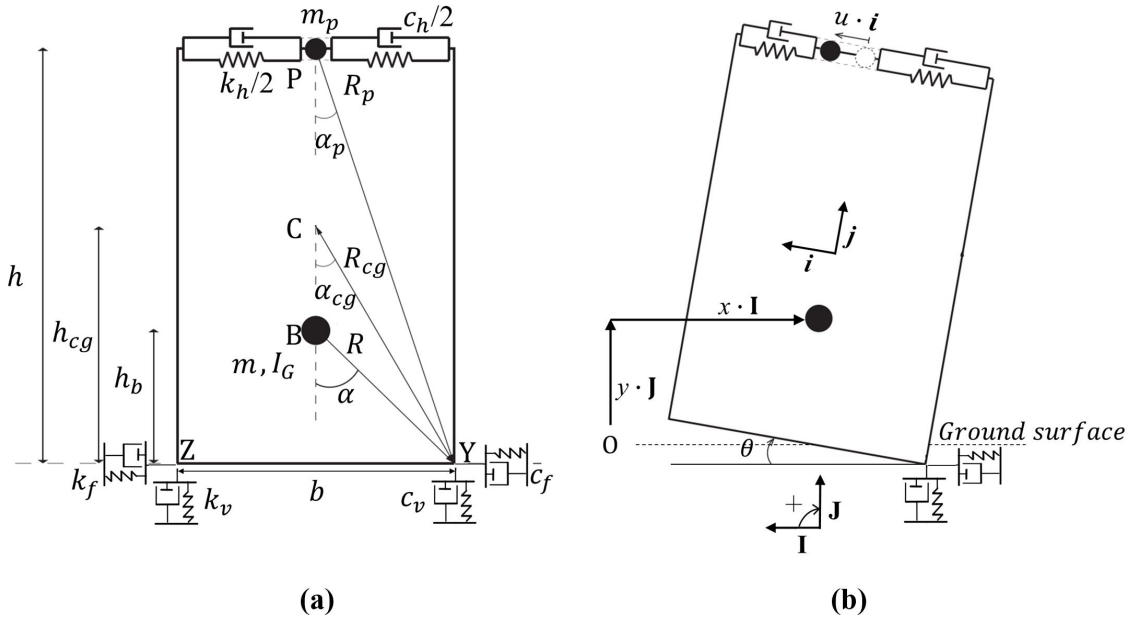


Figure 3.1: (a) Schematic drawing and (b) displaced configuration of FRMCS.

3.2.1 Equations of motion

The free-body diagrams of the top mass and the bottom body are shown in Figure 3.2.

F_s and F_c represent the total forces due to the springs and dampers acting on the top mass, respectively. F_n represents the normal reaction force between the top and the bottom mass that constrains the top mass to move in the u direction. F_{Z1} and F_{Y1} ('1' refers to the horizontal direction in the inertial reference frame) are the horizontal contact forces at the two corners due to the frictional springs and dampers,

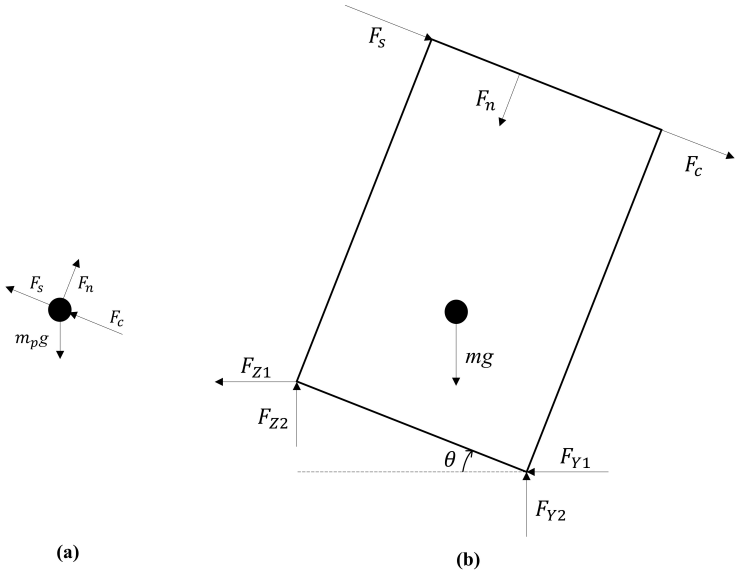


Figure 3.2: Free body diagrams of (a) the top mass and (b) the bottom mass.

and F_{Z2} and F_{Y2} ('2' refers to the vertical direction in the inertial reference frame) are the vertical contact forces due to the ground springs and dampers at the two corners. The vertical and horizontal contact forces become zero when the support spring goes into tension. The equations of motion of the top mass are given by:

$$m_p\Big((\ddot{x}_g + \ddot{x})\cos\theta + (\ddot{y}_g + \ddot{y})\sin\theta + \ddot{u} - u\dot{\theta}^2 - (h - h_b)\ddot{\theta}\Big) = F_s + F_c - m_p g\sin\theta \quad (3.1)$$

$$m_p\Big(-(\ddot{x}_g + \ddot{x})\sin\theta + (\ddot{y}_g + \ddot{y})\cos\theta + u\ddot{\theta} + 2\dot{u}\dot{\theta} - (h - h_b)\dot{\theta}^2\Big) = F_n - m_p g\cos\theta \quad (3.2)$$

$$m(\ddot{x}_g + \ddot{x}) = F_{Z_1} + F_{Y_1} + (-F_s - F_c)\cos\theta + F_n\sin\theta \quad (3.3)$$

$$m(\ddot{y}_g + \ddot{y}) = -mg + F_{Z_2} + F_{Y_2} + (-F_s - F_c)\sin\theta - F_n\cos\theta \quad (3.4)$$

$$I_G\ddot{\theta} = F_{Z_1R}\cos(\alpha + \theta) + F_{Z_2R}\sin(\alpha + \theta) + F_{Y_1R}\cos(\alpha - \theta) - F_{Y_2R}\sin(\alpha - \theta) - F_n\,u + (F_s + F_c)(h - h_b) \quad (3.5)$$

Equations (3.1) and (3.2) are the equations of motion of the top mass along the directions of the rotating vectors $\vec{i}$ and $\vec{j}$ respectively. Equations (3.3)-(3.5) are those of the bottom body along $\vec{I}$, $\vec{J}$ and θ respectively.

3.2.2 Constitutive relation and numerical implementation

The vertical contact forces F_{Z2} and F_{Y2} are exerted by the vertical support springs and dampers, as follows:

$$F_{Z2} = \begin{cases} 0, & \text{if } y_Z > 0 \\ -k_v y_Z - c_v \dot{y}_Z, & \text{elsewhere} \end{cases} \tag{3.6}$$

$$F_{Y2} = \begin{cases} 0, & \text{if } y_Y > 0 \\ -k_v y_Y - c_v \dot{y}_Y, & \text{elsewhere} \end{cases} \tag{3.7}$$

where y_Z and y_Y are the vertical coordinates of the corners Z and Y respectively in the inertial reference frame. If either of the coordinates are larger than zero, then the corresponding corner is above the ground surface (refer to Figure 3.1(b)) and there is no contact force. The horizontal contact forces F_{Z1} and F_{Y1} are the sum of the horizontal spring and damper forces at each corner. They are defined using the Coulomb friction model, illustrated in Figure 3.3(a), where F_{nc} is the normal contact force (i.e., F_{Z2} for the left corner and F_{Y2} for the right corner) and μ is the coefficient of friction. The horizontal force in a contact spring is generically described as $\boldsymbol{F_{fs}}$ in the figure; it refers to F_{Z1} if the computation is done for the left corner and F_{Y1} for the right corner.

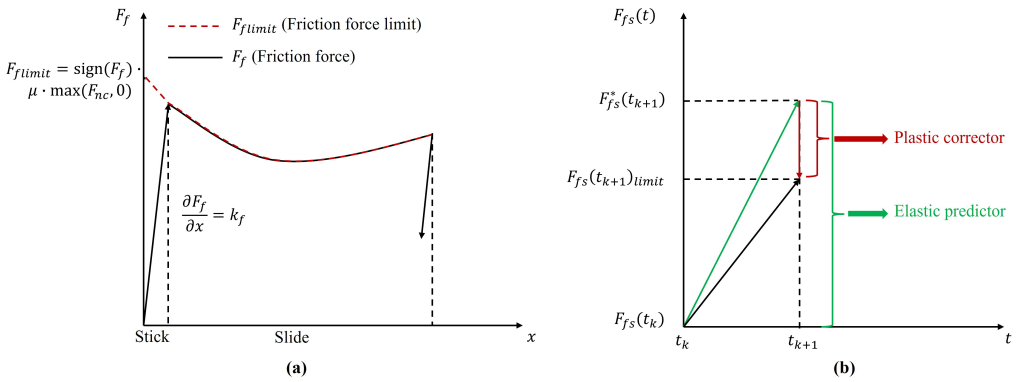


Figure 3.3: Illustrations of (a) Coulomb friction model and (b) elastic-predictor and plastic-corrector scheme for implementing the friction model.

Figure 3.3(b) illustrates the elastic-predictor and plastic-corrector scheme employed in the numerical implementation of the model. To calculate the corner friction

force (i.e., F_{Z1} and F_{Y1}) governed by the Coulomb friction model at each time step, the frictional spring force ($\boldsymbol{F_{fs}}$) is treated as an additional state; it is tracked and corrected using the elastic-predictor and plastic-corrector scheme:

$$F_f(t_{k+1})_{limit} = \mu \cdot \max(F_{nc}(t_{k+1}), 0) \tag{3.8}$$

$$F^*_{fs}(t_{k+1}) = F_{fs}(t_k) + \int_{t_k}^{t_{k+1}} k_f \dot{x}(t_{k+1}) dt \tag{3.9}$$

$$F^*_f(t_{k+1}) = F^*_{fs}(t_{k+1}) + c_f \dot{x}(t_{k+1}) \tag{3.10}$$

$$F_f(t_{k+1}) = \begin{cases} F^*_f(t_{k+1}), & \text{if} |F^*_f(t_{k+1})| \leq |F_f(t_{k+1})_{limit}| \\ sign[F^*_f(t_{k+1})] F_f(t_{k+1})_{limit}, & \text{if} |F^*_f(t_{k+1})| > |F_f(t_{k+1})_{limit}| \end{cases} \tag{3.11}$$

$$F_{fs}(t_{k+1})_{limit} = F_f(t_{k+1}) - c_f \dot{x}(t_{k+1}) \tag{3.12}$$

$$F_{fs}(t_{k+1}) = \begin{cases} F^*_{fs}(t_{k+1}), & \text{if} |F^*_{fs}(t_{k+1})| \leq |F_{fs}(t_{k+1})_{limit}| \\ F_{fs}(t_{k+1})_{limit}, & \text{if} |F^*_{fs}(t_{k+1})| > |F_{fs}(t_{k+1})_{limit}| \end{cases} \tag{3.13}$$

where * symbol indicates a trial quantity which will be corrected if it violates Coulomb friction limit. $\boldsymbol{F_{fs}}$ is the tracked frictional spring force and $\dot{x}$ is the horizontal velocity of each corner (e.g., $\dot{x}_Z$ and $\dot{x}_Y$). Equation (3.9) represents the elastic-predictor step and Equation (3.13) the plastic-corrector step. They are graphically illustrated in Figure 3.3(b) for better understanding.

Numerical simulations were carried out in MATLAB for this study. ode45 was chosen as the numerical solver and had been modified to include the aforementioned elastic-predictor and plastic-corrector scheme for the implementation of penalty Coulomb friction model. Relative tolerance and absolute tolerance are modified so that the simulation results are not sensitive to them. However, they cannot be too small otherwise they would reach the computational hardware limit and errors would happen. For soft support springs (defined in **Section** 3.5), error tolerance in the order of e-06 returned converged results; while for stiff support springs, it was in the order of e-10. The stricter requirement of error tolerance for stiff support springs is a consequence of solving a numerically stiffer differential equations compared to the soft support springs ones. In addition, event function was used to switch between different governing equations, which accounted for the different states of the $\boldsymbol{F_{fs}}$; for example, $\boldsymbol{F_{fs}}$ will be zero if the body is in air and hence disappear from the state variables.

3.2.3 Definition of base shear, axial force and moment quantities

The positive directions of the base shear force (S), axial force (N) and moment (M) are illustrated in Figure 3.4. These are computed using the contact forces:

$$S = \cos\theta(-F_{Y_1} - F_{Z_1}) - \sin\theta(F_{Y_2} + F_{Z_2}) \tag{3.14}$$

$$N = \sin\theta(F_{Y_1} + F_{Z_1}) - \cos\theta(F_{Y_2} + F_{Z_2}) \tag{3.15}$$

$$M = \sin\theta(-F_{Y_1} + F_{Z_1})b/2 + \cos\theta(F_{Y_2} - F_{Z_2})b/2 \tag{3.16}$$

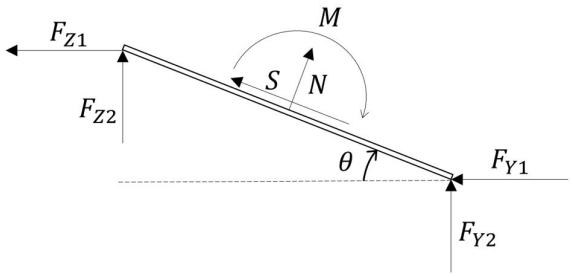


Figure 3.4: Free body diagram of the base section.

3.3 Model parameter normalisation

In this chapter, horizontal pulses are used to examine the response of FRMCS to earthquakes. These pulses can be used to approximate the ground motions recorded in near-field earthquake and may lead to overturning [70, 71, 72, 73]. To present the model input parameters in a more compact way, dimensional analysis is utilised to obtain dimensionless groups. The model governing equation can be re-written to the following mathematical form:

$$\begin{aligned}\boldsymbol{f}\big(x, y, \theta, u, \boldsymbol{F_{fs}}, m, m_p, I_G, g, b, \omega_n, \zeta_n, \omega_v, \zeta_v,\\ \omega_f, \zeta_f, \omega, A, \mu, t, \alpha, \alpha_{cg}\big) = \mathbf{0}\,.\end{aligned} \tag{3.17}$$

where A and ω are the magnitude and the frequency of the horizontal acceleration pulse respectively. $\zeta_n = c_h/(2\sqrt{k_h m_p})$ is the damping ratio associated with the top lateral spring if the bottom body was fixed, while $\zeta_v = c_v/(2\sqrt{k_v(m_p+m)})$ and $\zeta_f = c_f/(2\sqrt{k_f(m_p+m)})$ are the ground damping ratio of the system of two masses rigidly

moving in the vertical and horizontal direction respectively. μ is the coefficient of friction. ω_n, ω_v and ω_f are frequency parameters for the SDOF systems that would correspond to the isolated movements of: the top mass in lateral direction, and the two masses rigidly moving together in the vertical and horizontal direction respectively. A larger value of those frequency parameters implies a stiffer spring. They are defined by the following equations:

$$\omega_n = \sqrt{\frac{k_h}{m_p}} \quad (3.18) \qquad \omega_v = \sqrt{\frac{2k_v}{m_p + m}} \quad (3.19) \qquad \omega_f = \sqrt{\frac{2k_f}{m_p + m}} \quad (3.20)$$

Aside from the output parameters x,y, θ, u and $\boldsymbol{F_{fs}}$, there are 17 independent input parameters and according to the Buckingham's π theorem they can be expressed in terms of 14 dimensionless groups using three repeating variables. The choice of repeating variables is not unique as long as themselves do not form a dimensionless group. In this chapter, m_p, g and p are chosen as the repeating variables, where p is the rocking frequency parameter ($p = \sqrt{(m + m_p)gR_{cg}/(I_G + m_pR_p^2 + mR^2)}$). The 17 input parameters are expressed in terms of the 14 dimensionless groups. The resulting dimensionless groups are adjusted by conducting algebraic and trigonometric operations to achieve a new set of more intuitive dimensionless parameters. The final set of dimensionless parameters are listed in Table 3.1.

Table 3.1: Input Π groups.

Π groups	Π_1	Π_2	Π_3	Π_4	Π_5	Π_6	Π_7	Π_8	Π_9	Π_{10}	Π_{11}	Π_{12}
Expression	m/m_p	ω_n/p	ζ_n	ω_v/p	ζ_v	ω_f/p	ζ_f	ω/p	$A/(g\tan\alpha_{cg})$	μ	tp	$I_G/(mR^2)$

A clarification is necessary for the dimensionless groups Π_2, Π_4, Π_6 and Π_8. The unit of ω terms in these dimensionless groups is rad/s while that of p is $1/s$.

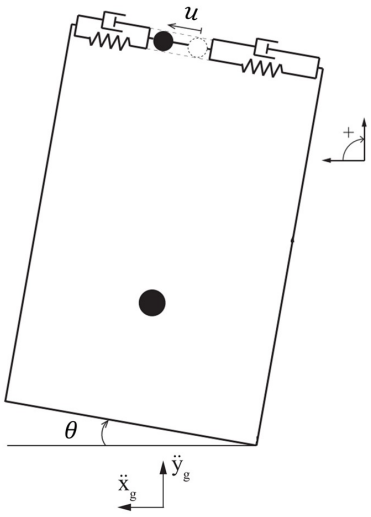
3.4 Model comparison for effectively rigid support media

In this section, FRMCS simulations are compared to those from the flexible rocking model (FRM). A brief review of the flexible rocking model (FRM) is presented in

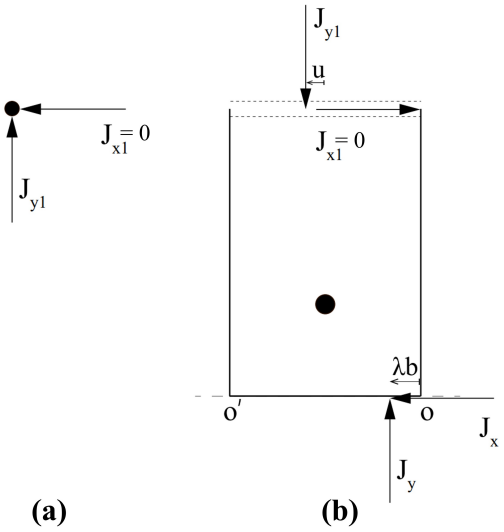
Section 3.4.1. Free vibration tests and stability analysis under pulse excitations are conducted in **Section** 3.4.2 and **Section** 3.4.3 respectively.

3.4.1 Review of FRM

The flexible rocking model (FRM) was proposed by Zhu et al. [42] to describe the rocking of laterally flexible oscillators on a rigid support medium. It consists of a top mass and bottom rigid body, similar to the FRMCS. However, sliding and free flight are not accounted for in the FRM. To enable comparisons, the geometric parameters of FRM have been adopted to be compatible with FRMCS. Figure 3.5a shows the displaced configuration of FRM, with the ground excitation $\ddot{x_g}$ and $\ddot{y_g}$. The model has two degrees of freedom: u and θ. u is the relative displacement of the top mass and θ is the rotation of the bottom mass. The positive sign convention is shown on the top right of the Figure 3.5a.



(a) Displaced configuration of FRM.



(b) (a) Impulses during impact for the top mass and (b) the bottom mass from Zhu et al. [42].

Figure 3.5: (a) Displaced configuration of FRM and (b) Impulses during impact.

Due to the rigid treatment of the support medium in FRM, the impact between the bottom mass and the support medium has an infinitesimal duration. This gives rise to a vertical impulsive force J_{y1} between the top mass and the bottom body, and vertical J_y and horizontal J_x impulsive forces between the bottom body and the support medium during impact.

Zhu et al. [42] argued that there cannot be a horizontal impulse between the top mass and the bottom body during an infinitesimal duration impact. The lateral force that can be exerted by springs and dampers during an infinitesimal duration impact is either zero or a finite value; therefore the corresponding horizontal impulse J_{x1} (shown in Figure 3.5b(a)) is zero. The horizontal position of the vertical support medium impulse J_y can be anywhere between the future rocking corner and the midpoint of the base. The horizontal location of J_y is described by λb and illustrated in Figure 3.5b(b). A value of λ must be assumed in FRM. Zhu et al. [42] investigated a bottom body with feet at the corners, where λ can be reasonably assumed as zero.

3.4.2 Free vibration comparison

In this section, the free vibration responses from FRMCS and FRM are compared for a case where the support medium is practically undeformable and, the effects of sliding and free-flight are minimal. The common parameters that describe the geometry, lateral flexibility and damping ratio of models are presented in Table 3.2. To enable a like-for-like comparison, the vertical spring stiffness (k_v), the viscous damping factor (c_v), the frictional spring stiffness (k_f), the horizontal viscous damping factor (c_f) and the coefficient of friction (μ) of the support media should be taken such that: i) the contact is effectively rigid, ii) the effects of sliding and free flight are minimal. The parameters were obtained by gradually increasing the magnitude from initial guesses until responses stopped changing in a noticeable manner (i.e., when $k_v = 2.414 \cdot 10^{11} N/m$, $c_v = 1.460 \cdot 10^{8} N/(m/s)$, $k_f = 10^{12} N/m$, $c_f = 2.5023 \cdot 10^{8} N/(m/s)$ and $\mu = 0.8$). It is noteworthy that the large value of coefficient of friction minimizes the effects of sliding, but small amounts of sliding always occur in FRMCS as the normal contact force tends to zero.

Table 3.2: Values of the common parameters.

Parameter	**Value**	**Parameter**	**Value**	**Parameter**	**Value**
h (m)	8.2933	h_b (m)	3.4250	h_{cg} (m)	6.7263
R_p (m)	8.3534	R (m)	3.5680	R_{cg} (m)	6.8003
α_p (rad)	0.1200	α (rad)	0.2841	α_{cg} (rad)	0.1476
b (m)	2.0000	I_G (kg $\cdot$ m^2)	1.1297e05	p (s^{-1})	1.1143
m_p (kg)	3.3173e04	m (kg)	1.5746e04	ζ_n	0.0500

Three bodies, each with a different lateral spring stiffness (Case A: $\omega_n = 9.8225p$, Case B: $\omega_n = 4.9599p$, Case C: $\omega_n = 2.4313p$), were examined as in Zhu et al. [42].

These values of ω_n represent lateral vibration frequency values for stiff, intermediately stiff and flexible structures in this study. For all three bodies, the free vibration motion is initiated with $\theta_0 = 0.8\alpha_{cg}$. For the FRM, the initial values $\dot{u_0}$, $\dot{\theta_0}$ and u_0 are set to zero. The FRMCS adopts the same initial parameters but also requires the application of external forces to ensure static equilibrium. The force F_1 is applied at the corner of the body above the support medium, and an external horizontal force F_2 is applied to the corner of the body embedded in the ground so that the bottom body is in static equilibrium. The free body diagram is shown in Figure 3.6. The initial rotation θ_0 is taken as positive and hence, F_1 and F_2 are applied to the left and right corner respectively. The release of F_1 and F_2 initiates the movement of the body. F_{Y2_0} is the initial support vertical spring force. F_{n_0} is the initial normal force exerted on the bottom mass by the top mass, which is the component of the top mass weight that is normal to the top surface. Because u_0 and $\dot{u_0}$ are set to zero, there is no lateral force on the bottom mass due to the top springs and dampers. F_{Y2_0}, F_1 and F_2 are found by setting the body at static equilibrium with θ_0 and assuming that the frictional springs are undeformed. Mathematically, this leads to:

$$F_1 + F_{Y2_0} - mg - F_{n_0}\cos\theta_0 = 0 \tag{3.21}$$

$$F_2 + F_{n_0}\sin\theta_0 = 0 \tag{3.22}$$

$$F_1 b\cos\theta_0 - mgR\sin(\alpha - \theta_0) - F_{n_0} b/2 = 0 \tag{3.23}$$

The initial vertical displacement of the right corner, y_{y0}, then can be solved using the obtained value of F_{Y2_0}. Finally, x_0 and y_0 are obtained with θ_0 and y_{y0} using the following kinematics relationships:

$$x_0 = R\sin(\alpha - \theta_0) - b/2 \tag{3.24}$$

$$y_0 = R\cos(\alpha - \theta_0) + y_{y0} \tag{3.25}$$

The free vibration time history plots are presented in Figure 3.7. In each column, the normalised rotation (θ/α_{cg}), normalised top mass relative elastic displacement

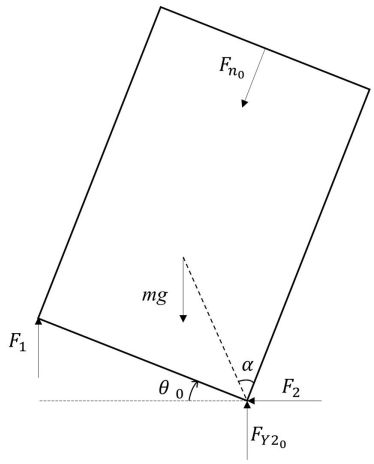


Figure 3.6: Free body diagram for the initial condition.

(u/u_{cr}) and normalised energy (E/E_{ref}) are presented for a specific lateral spring configuration; in each sub-figure, the responses obtained from both FRMCS and FRM are plotted. E is the total energy and E_{ref} is the potential energy difference between the unstable and stable equilibrium location of a rigid rocking block with similar geometric characteristics, as defined in Acikgoz and DeJong [36]. u_{cr} is defined as the top mass displacement for which uplift would be expected to occur for a structure with zero bottom mass height ($h_b = 0$) and no damping ($u_{cr} = gb[\frac{m_p+m}{m}]/(2\omega_n^2 h)$).

It can be seen from Figure 3.7 that the responses from the FRMCS and FRM are in excellent agreement. In FRM, pre-impact state variables and the impulse-momentum equations are used to define the post-impact parameters. For the free vibration simulations shown in Figure 3.7, Zhu et al. [42] assumed that the vertical impulse occurs at the future-rocking corner, similar to Housner's IPM. The proposed FRMCS does not require appropriate definition of impulsive force location to define energy loss at impact. Instead, energy is dissipated through viscous damping at contact elements. Therefore, the agreement between these two fundamentally different models is instructive. It demonstrates that the Zhu et al. [42] assumptions concerning impulse transmission through the springs and support medium force concentration at the edges are consistent with the FRMCS predictions for effectively rigid support media. The excellent agreement between the time histories indicates that the assumptions hold for small and large rocking motion and for different lateral flexibility values. Considering that the FRM yields equivalent results to IPM for effectively rigid bodies, it can also be concluded that FRMCS also can produce equivalent results to IPM. This aspect was examined numerically by the authors but is not presented for brevity.

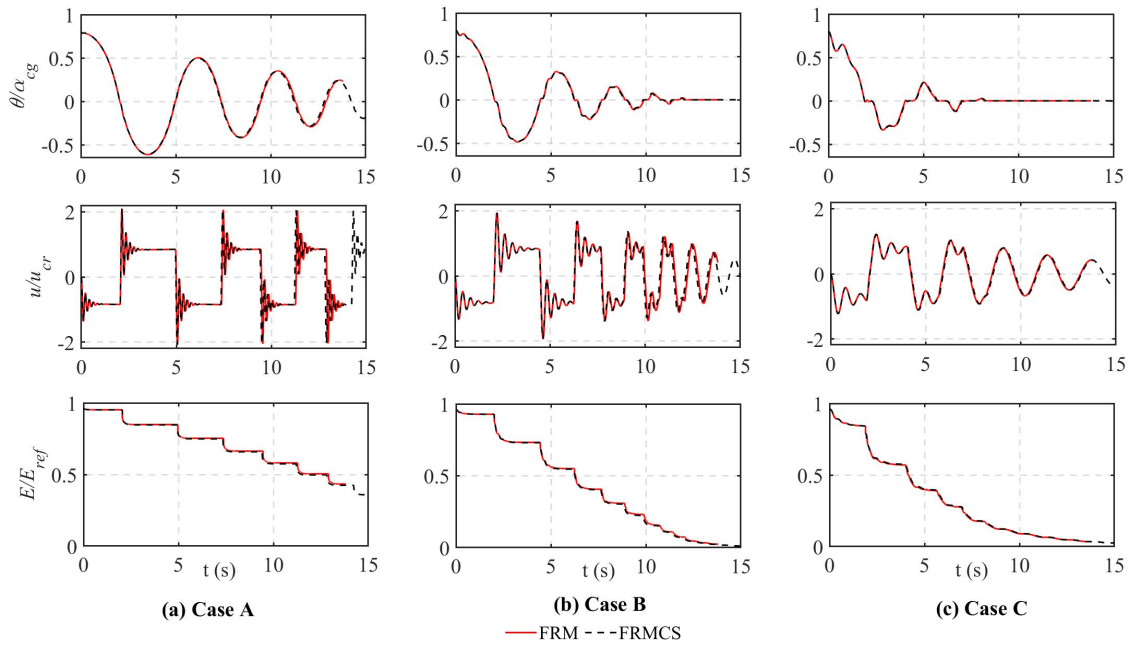


Figure 3.7: Free vibration response comparisons for (a) Case A ($\omega_n = 9.8225p$), (b) Case B ($\omega_n = 4.9599p$) and (c) Case C ($\omega_n = 2.4313p$) from FRMCS and FRM simulations.

3.4.3 Stability analysis comparison

In stability analysis, a rocking body is subjected to horizontal ground accelerations in the form of single cycle pulses with different magnitudes and frequencies. Magnitude and frequency pairs which cause overturning are recorded. In this study, the overturning event is recognized when θ is equal to ninety degrees. In general, three areas can be observed in a stability plot for symmetric rocking bodies subjected to single cycle horizontal acceleration pulses when sliding and free flight are neglected. Taking Figure 3.8(a) for example, typically, the uppermost line in the diagram corresponds to the minimum value of pulse magnitude for a specific frequency ω for which the body will overturn without experiencing any impacts. Above this line, overturning occurs without impact; this is referred to as Mode II failure area. Below the Mode II impact boundary, Mode I failures may be encountered, where the body overturns after experiencing impacts. Areas outside Mode I or II failures are safe.

Cases A (stiff) and C (flexible) from previous free vibration comparison are used for the stability analysis. The results are presented in Figure 3.8; the black line represents the FRMCS response and the red line the FRM. In Figure 3.8(a), it can be seen that the FRMCS is in excellent agreement with the FRM for Case A. There is a small region of disagreement around ω/p equal to 9.5. Similar observations can be

made for Figure 3.8(b), which examines a more flexible oscillator. The small regions of disagreement are due to the finite values adopted for the support medium flexibility and numerical simulation errors. Furthermore, because the FRMCS uses physical elements (i.e., the discrete contact springs and dampers) to model contact, it can be regarded as a higher-fidelity model compared to the FRM which relies on energy loss assumptions to govern contact behaviour. Therefore, the excellent agreement between the FRMCS and FRM stability plots serves to validate the FRM.

Comparing Figure 3.8(a) and (b), it can be seen that the Mode I overturning area shrinks and sinks with increasing lateral flexibility, reproducing earlier observations from Acikgoz and DeJong [36]. The combined influence of the lateral spring and the support medium deformability is investigated next.

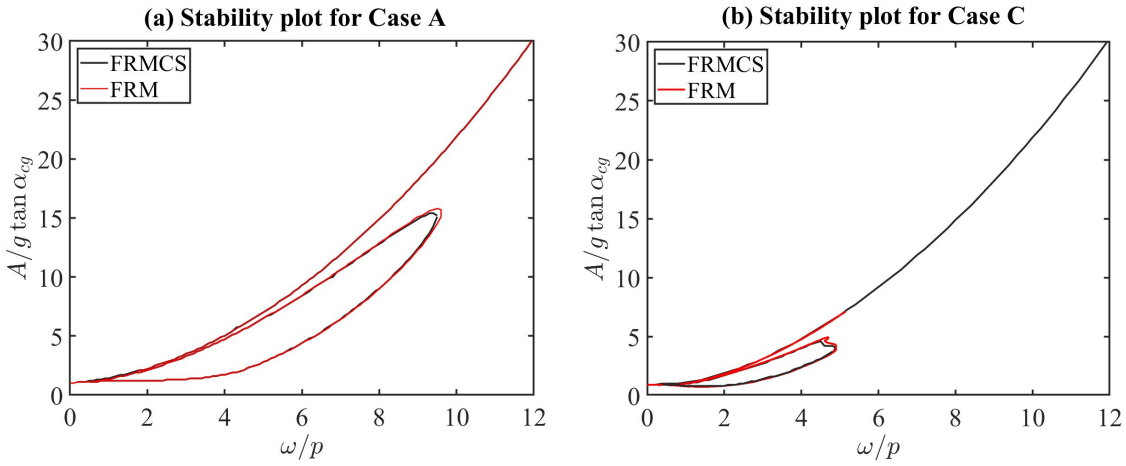


Figure 3.8: Stability plots for (a) stiff body rocking on rigid support and (b) soft body rocking on rigid support.

3.5 Influence of support medium stiffness and μ on the dynamic response

3.5.1 Time history evaluation

To understand the influence of support medium deformability and the coefficient of friction on the structural response, five configurations in total are studied. The values of the common dimensionless groups of the five rocking configurations are presented in Table 3.3 while the case-specific groups are reported in Table 3.4. First, high grip surfaces with either soft or stiff lateral spring and vertical contact elements are

considered (Cases one to four). The influence of a lower surface grip is then examined by reducing the horizontal support spring coefficient of friction (Case five).

Table 3.3: Common dimensionless groups for Cases one to five.

Π groups	Π_1	Π_3	Π_5	Π_6	Π_7	Π_8	Π_9	Π_{11}	Π_{12}	Π_{13}	Π_{14}
Expression	m/m_p	ζ_n	ζ_v	ω_f/p	ζ_f	ω/p	$A/(g\tan\alpha_{cg})$	tp	$I_G/(mR^2)$	α	α_{cg}
Value	0.475	0.05	0.8	25662	0.8	$[0.2, 12]$	$[0.2, 30]$	$[0, (25+2\pi/\omega)p]$	0.564	0.284	0.148

Table 3.4: Unique dimensionless groups for Cases one to five

	$\Pi_2(\omega_n/p)$	$\Pi_4(\omega_v/p)$	$\Pi_{10}(\mu)$
Case one	9.822	563.865	0.8
Case two	2.431	563.865	0.8
Case three	9.822	56.387	0.8
Case four	2.431	56.387	0.8
Case five	2.431	56.387	0.3 or 0.14

The pulse excitation time histories of some of the configurations in Table 3.4 are comparatively examined in this section to obtain an intuitive understanding of response. These are soft(lateral spring)-stiff(support spring) (Case two), soft-soft (Case four) and Case five. Case five is the same as Case four except that it uses a low-grip surface with $\mu = 0.14$. This is defined as a low-grip surface since $\mu < \alpha_{cg}$, where sliding is expected to be dominant. Π_2 is 2.431 for the soft lateral spring; Π_4 is 563.865 and 56.387 for the stiff and soft support spring configurations. The three configurations share the same geometric properties presented in Table 3.2. It should be noticed that the Π_4 value adopted for the stiff support spring configuration is five times smaller than the values used in **Section** 3.4, which were meant to simulate rigid support media.

The three configurations are subjected to a single cycle sinusoidal acceleration pulse with Π_8 and Π_9 equal to six and three respectively. Figure 3.9 compares the response of Case two (soft-stiff) and Case four (soft-soft) configurations. Time history responses of θ, u and vertical support forces at two corners are shown. The black, the blue and the red lines represent Cases two, four and five respectively.

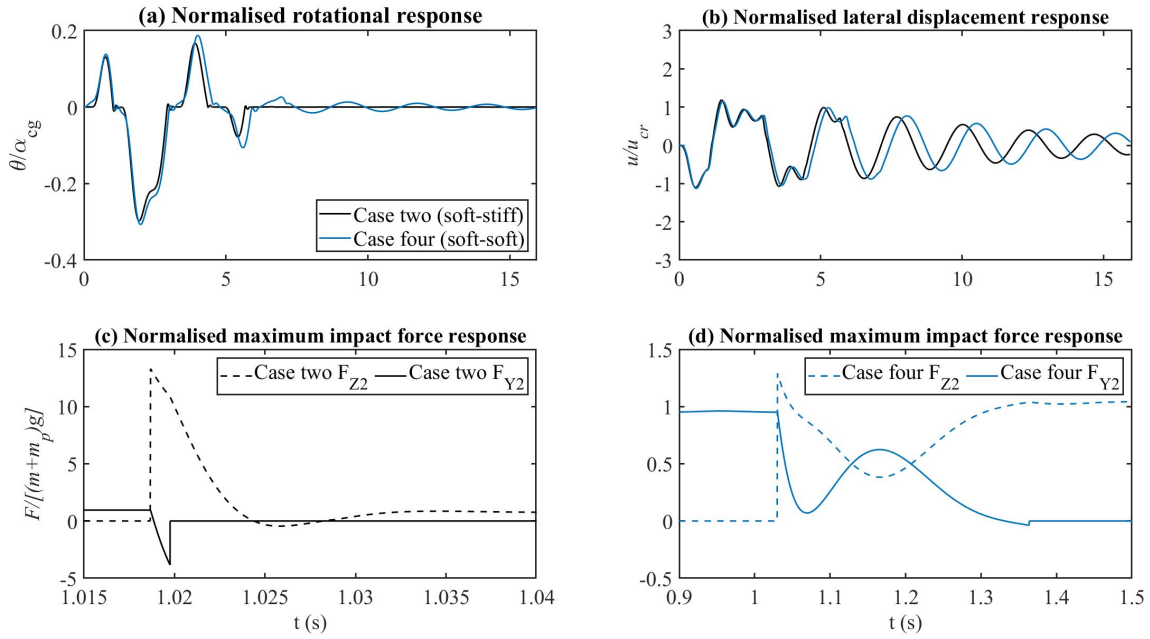


Figure 3.9: Pulse excitation response comparisons for Case two ($\omega_n = 2.431p$, $\omega_v = 563.865p$) and Case four ($\omega_n = 2.431p$, $\omega_v = 56.387p$).

In Figure 3.9(a) and (b), the rocking and lateral elastic displacement responses of Cases two and four appear to be relatively similar. However, the forces exerted by the support media on the structures are very different. Figure 3.9(c) and (d) present the contact forces at the impacting corner following the first major rocking cycle, around t=1s. This brief time window describes when maximum vertical contact forces are experienced by both bodies. However, the maximum vertical force for Case two is almost ten times that of Case four. This observation indicates how the support stiffness may have a significant influence on the contact forces while having no apparent effects on the maximum displacement response. It is noteworthy that an increase in contact force is likely to indicate an increase in base force and moment demands in the structure (see **Section** 3.2.3); this aspect will be examined in detail in **Section** 3.4.2.

In Figure 3.9, impact can be assumed to initiate when the future-rocking corner hits the support (i.e., when F_{Z2} starts to compress). It ends when the opposite corner is in the air (i.e., when F_{Y2} is zero) and the vertical velocity of the future-rocking corner becomes zero. This corresponds to the interval 1.01858-1.03924 seconds in Figure 3.9(c). The impulses due to normal contact forces at points Y and Z can be calculated as the integral of force over the impact duration. The ratio of the magnitude of left corner (i.e. future rocking corner) impulse to the right corner

impulse is equal to 23. Ratios of similar orders of magnitude are observed for other impacts. Similarly to Zhu et al. [42] and Chatzis and Smyth [35], this indicates that for bodies which can be modelled using the CSM, e.g. those that have feet at their bottom corners, the vertical impulse is practically concentrated at the future rocking corner for stiff support media when the effects of sliding and free flight are small. However, a similar impulse concentration is not observed for Case four, where the support medium is soft. Using the same definition of impact and assuming that it lasts from 1.02874 to 1.49571 seconds, a future to past rocking corner impulse ratio of 3.856 is obtained. Ratios of similar order of magnitude are observed for other impacts. Such smaller ratios indicate that for soft support media, impulses cannot be assumed to be concentrated at the future rocking corner.

The following Figure 3.10 presents a similar comparison between Case four (soft-soft) and Case five. This figure additionally examines the base axial force N and base shear force S responses.

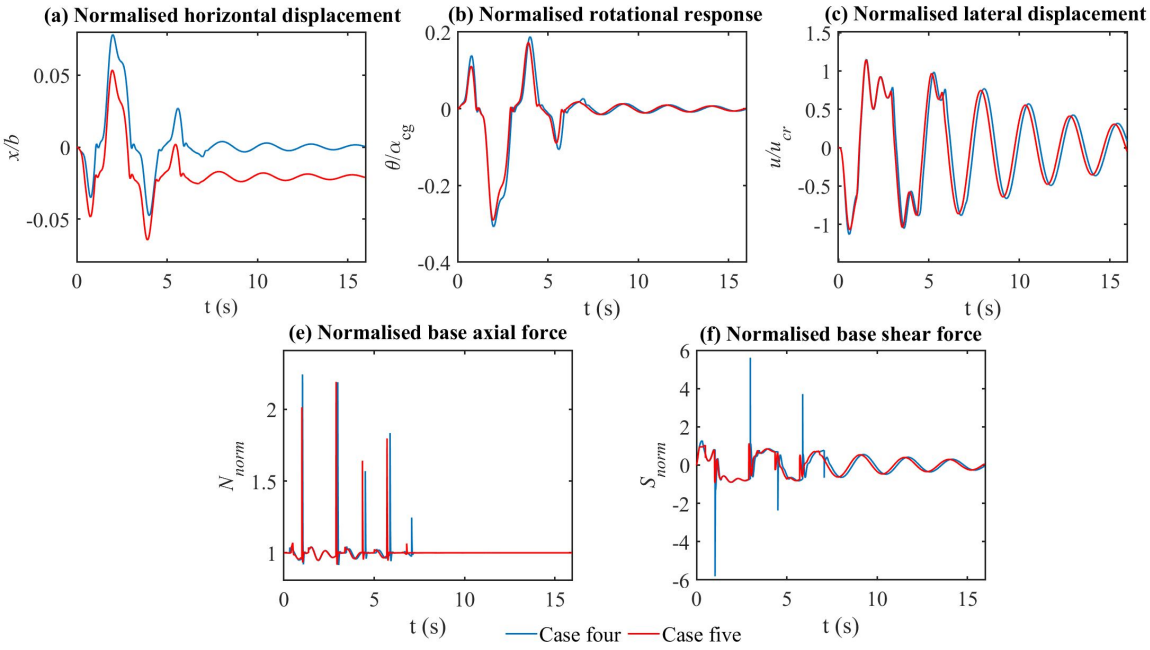


Figure 3.10: Pulse excitation response comparisons for Case four ($\omega_n = 2.431p$, $\omega_v = 56.387p$) and Case five (Case four with μ=0.14).

Figure 3.10 compares the time history responses of Cases four (soft-soft with high-grip, examined already in Figure 3.9) and five (soft-soft with low-grip). Figure 3.10(a) shows the horizontal position x of the centroid of the bottom body. At the end of the time history, a residual displacement was observed for Case five due to sliding of the

body. Despite the sliding, Figures 3.10(b) and (c) show that the rotational response θ and the lateral displacement response u are similar between the two cases.

The impact of sliding on the contact forces is examined in Figure 3.10(e-f). The base axial force N is normalised with respect to the weight of the structure. The base shear force S is normalised with respect to the static horizontal force needed at the center of mass to uplift an equivalent rigid rocking body.

$$N_{norm} = \frac{N}{(m + m_p)g} \tag{3.26}$$

$$S_{norm} = \frac{S}{(m + m_p)g \tan \alpha_{cg}} \tag{3.27}$$

In Figure 3.10(e), the axial force response patterns and maximum peak values are similar for the two cases. However, sliding has a significant influence on the base shear force response. Figure 3.10(f) shows that the maximum shear force response decreased by almost six times in Case five compared to Case four.

It is useful to summarise the observations from the examined time histories: (a) the support spring stiffness has a significant effect on the maximum vertical support force response (and consequently base force and moment demands in the structure); (b) for bodies with feet at the bottom corners the vertical impulses from the support medium concentrate at the future rocking corner when the support medium is stiff, while this may not be true for soft support media; and (c) sliding between the structure and support medium can significantly reduce the maximum base shear force demand in the structure.

3.5.2 Response spectra evaluation

Previous time history studies are based on three rocking configurations subjected to a pulse excitation of specific amplitude and frequency. A more exhaustive investigation is conducted in this section to see if the observed trends are applicable to other configurations and single cycle excitations with different amplitudes and frequencies. To achieve this, different values of dimensionless groups are used in the following sections to investigate a wide range of support and lateral spring stiffness. Therefore, in addition to Cases two, four and five from the previous section, another two cases are examined below: stiff(lateral spring)-stiff(support spring) (Case one) and stiff-soft (Case three) configurations (see Tables 3.3 and 3.4).

3.5.3 Case one (stiff-stiff)

In this section, response spectra referring to various quantities are presented in Figure 3.11(a)-(e). These spectra report the maximum magnitudes of the examined quantities under different single cycle sinusoidal acceleration pulses. The spectra are plotted for varying pulse frequency in the horizontal axis and pulse amplitude in the vertical while indicating the maximum values of the quantity of interest using colours as indicated by colour bars. The stability diagram is also plotted in red in Figure 3.11(a) for ease of reference. The response spectra for pairs of frequency and amplitudes that would lie within the Mode II failure are not of interest and so the corresponding regions are left uncoloured in the figures.

The non-dimensional pre-impact rotational velocity parameter $\dot{\theta}/p$ is obtained using the maximum rotational velocity in the time history, just before the rocking body hits the support medium. The discretised contours in Figure 3.11(a) refer to this parameter. Figure 3.11(b) presents the spectra for the normalised base moment M_{norm}. The parameter is normalised by the base moment needed to uplift a rigid assembly of the two masses statically:

$$M_{norm} = \frac{2M}{(m + m_p)gb} \tag{3.28}$$

Normalised base axial force in Figure 3.11(c) was introduced earlier in Equation (3.26). The lateral displacements in Figure 3.11(d) are normalised with respect to u_{cr} similar to earlier sections to obtain u_{norm}.

Figure 3.11(e) represents the lateral moment, M_L. M_L is calculated as the product of the top shear force F_p (sum of F_s and F_c) and the bottom body height h. This represents the part of the base moment demand caused by the lateral springs and dampers. In Figure 3.11(f), the maximum normalised pre-impact rotational velocity is plotted against the maximum N_{norm} or S_{norm} from different time analyses. To relate various force demands in the system, Figure 3.12(a) presents the ratio between the maximum internal forces (i.e., the base axial and shear force) to the maximum ground forces (i.e., the vertical and the horizontal support force) from the same excitation. During this specific numerical experiment, it was noted that the maximum internal force and the maximum external force occurred at the same time instance, therefore this ratio qualitatively shows whether the maximum internal force occurs during impact. For example, if it occurs during impact then θ is close to zero and hence the ratio should be close to 1; if it occurs outside the impact time window, the ratio

will not be 1 according to equations in **Section** 3.2.3. Figure 3.12(b) presents the graphical relationship between the maximum pre-impact rotational velocity and the maximum shear forces applied between the two masses and at the base of the bottom mass. The top shear force F_p is calculated as the negative sum of the lateral spring force (F_s) and the lateral damper force (F_c).The lateral moment M_L and the top shear force F_p are normalised in the same way as M and S to obtain $M_{L_{norm}}$ and $F_{p_{norm}}$.

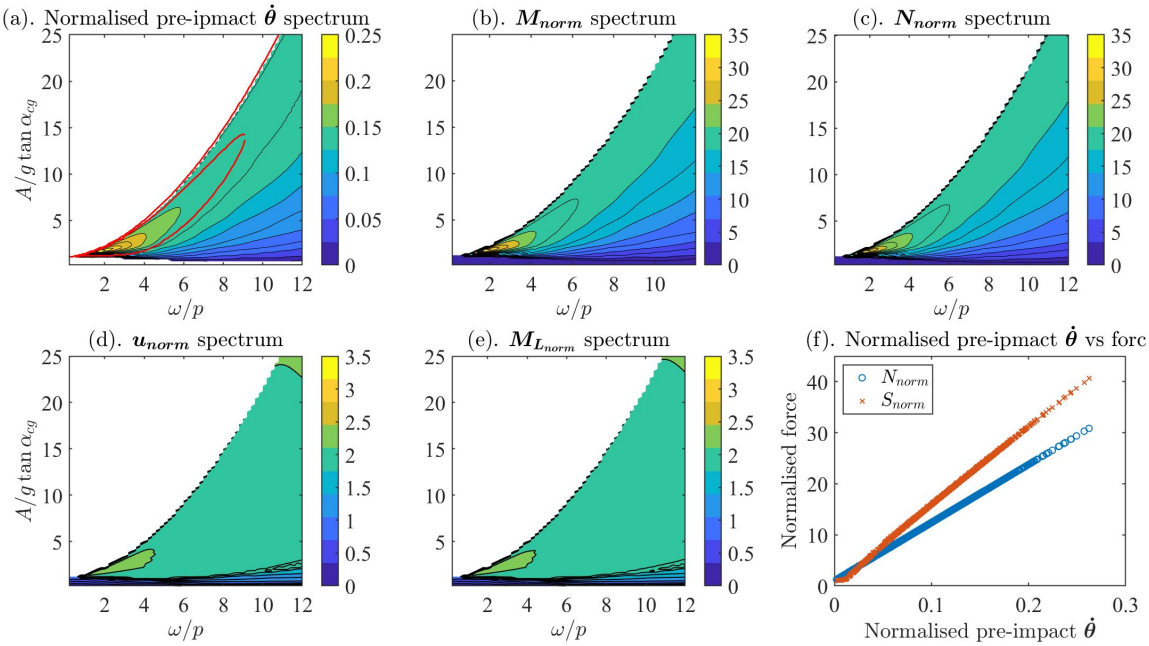


Figure 3.11: Response spectrum for Case one ($\omega_n = 9.822p$, $\omega_v = 563.865p$).

Figure 3.11(a) has two white areas, one above the coloured contour map and one below. The white area above the coloured contour map is the area of overturning without impact and hence the pre-impact $\dot{\theta}$ is undefined; the white area below the map represents the area where uplifting from ground did not occur and hence the pre-impact $\dot{\theta}/p$ is undefined either. Figure 3.11(a) shows that the maximum pre-impact $\dot{\theta}$ increased with the single cycle pulse amplitude given a fixed pulse frequency outside the overturning zone. However, inside the overturning zone (Mode I failure zone, coloured area enclosed by the red line), the maximum pre-impact $\dot{\theta}$ first increased and then decreased with pulse amplitude for pulse frequency ranging from 0.2p to 5p. The base moment and the base axial force spectra (Figure 3.11(b),(c)) demonstrate similar response trends to those of the pre-impact rotational velocity (Figure 3.11(a)). In areas where overturning is not experienced, forces and moments appear to increase with increasing pulse amplitude and decreasing pulse frequency. However, highest

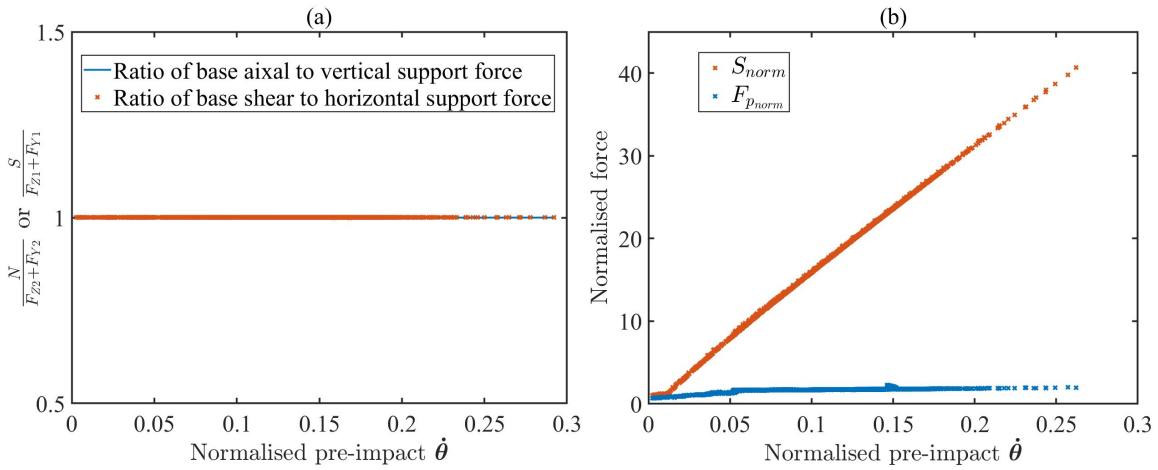


Figure 3.12: Maximum normalised pre-impact $\dot{\theta}$ vs (a) maximum normalised internal and external forces and (b) maximum normalised shear forces.

force and moment demands coincide with regions of Mode I failure as can be seen from the yellow area. Figure 3.11(f) reveals that there is an almost linear relationship between the maximum pre-impact rotational velocity and the maximum base forces. Figure 3.12(a) shows that the maximum internal forces (i.e., the base shear and the base axial force) are the same as the maximum external forces (i.e., the vertical and the horizontal support force) for all of the excitations. This demonstrates that the maximum base forces occur around impact where the base is almost horizontal. Earlier, **Section** 3.4.3 showed that for Case A (stiff-stiff case) the vertical impulse at impact concentrates at the future-rocking corner. Therefore, the maximum base moment should be approximately equal to the product of maximum base axial force and half the base width. This explains the similarity between Figures 3.11(c) and (b).

Figure 3.11(d) shows that the lateral displacement of the top mass does not vary significantly across a wide range of pulse excitations. Correspondingly, the top shear force in Figure 3.12(b) does not linearly increase with the maximum pre-impact rotational velocity and features a plateau. Similar observations were made by Yim and Chopra [74], Psycharis [75] and Acikgoz and DeJong [76]. However, Figure 3.12(b) highlights that the maximum top shear force is in general much smaller than the maximum base shear force. Similarly, it can be seen that the lateral moment M_L is also much smaller than the base moment M by comparing Figures 3.11(b) and (e). This shows that the maximum lateral displacement alone is not an indicator of reducing the applied moments on the base of the body. These observations emphasise the need for caution when interpreting the reduction of base shear force and moment demands

that can be achieved with a rocking system by judging top shear forces only. For the investigated body, the maximum base axial force can reach 30 times the system self weight; the maximum base shear force can reach 40 times the static uplifting force and the maximum base moment can reach 30 times the moment needed to uplift the structure statically.

3.5.4 Case two (soft-stiff)

The following Figure 3.13 presents the same type of response spectra for the soft (lateral spring)-stiff (support spring) configuration to those presented in Figure 3.11.

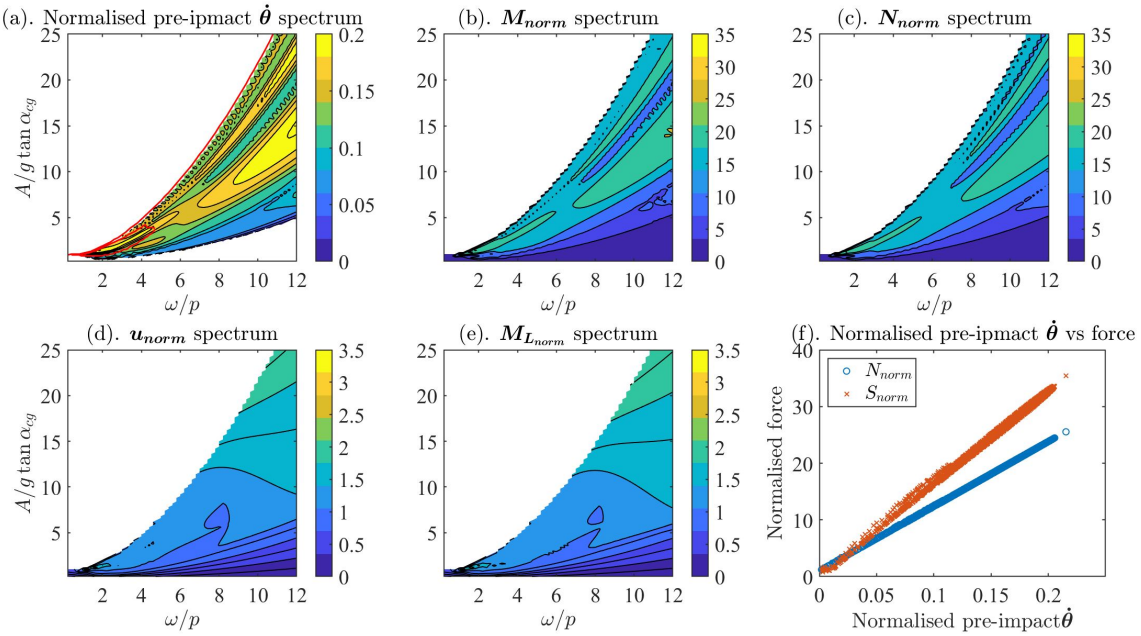


Figure 3.13: Response spectrum for Case two ($\omega_n = 2.431p$, $\omega_v = 563.865p$).

Figure 3.13 shows that the spectra of the pre-impact normalised $\dot{\theta}$, N_{norm}, S_{norm}, and M_{norm} parameters are still correlated. This is evident in Figure 3.13(f) where a linear relationship is observed between maximum normalised pre-impact $\dot{\theta}$ and maximum normalised base forces. However, due to the interaction between the lateral vibrations of the top mass and the rocking motion, the response spectra appear to be more irregular in Figure 3.13 than in Figure 3.11. For example, in Figure 3.13(a) the rocking motion amplitudes (and consequently the maximum pre-impact rotational velocities) do not tend to increase with increasing pulse amplitude and decreasing pulse frequency as in Figure 3.11(a). As a result, in areas where overturning is not experienced, the maximum forces and moments do not necessarily increase with increasing

pulse amplitude and decreasing pulse frequency. Furthermore, the highest force and moment demands do not coincide with regions of Mode I failure as can be seen that the green area also appeared outside the Mode I failure zone as well. In the u_{norm} spectrum in Figure 3.13(d) the contour lines appear to be more evenly scattered, highlighting a more uniform dependence on the excitation amplitude and frequency. The normalised lateral moment $M_{L_{norm}}$ shown in Figure 3.13(e) is much smaller compared to the normalised base moment M_{norm} in Figure 3.13(b), highlighting again the need for caution when interpreting the force reduction effect that can be achieved with rocking systems. Additionally, it is noteworthy that the normalised maximum force and the normalised moment response magnitudes are similar in Figure 3.11 and 3.13, despite an increase in structural flexibility in the latter case.

3.5.5 Case three (stiff-soft)

The following Figure 3.14 plots results for the stiff(lateral spring)-soft(support spring) configuration.

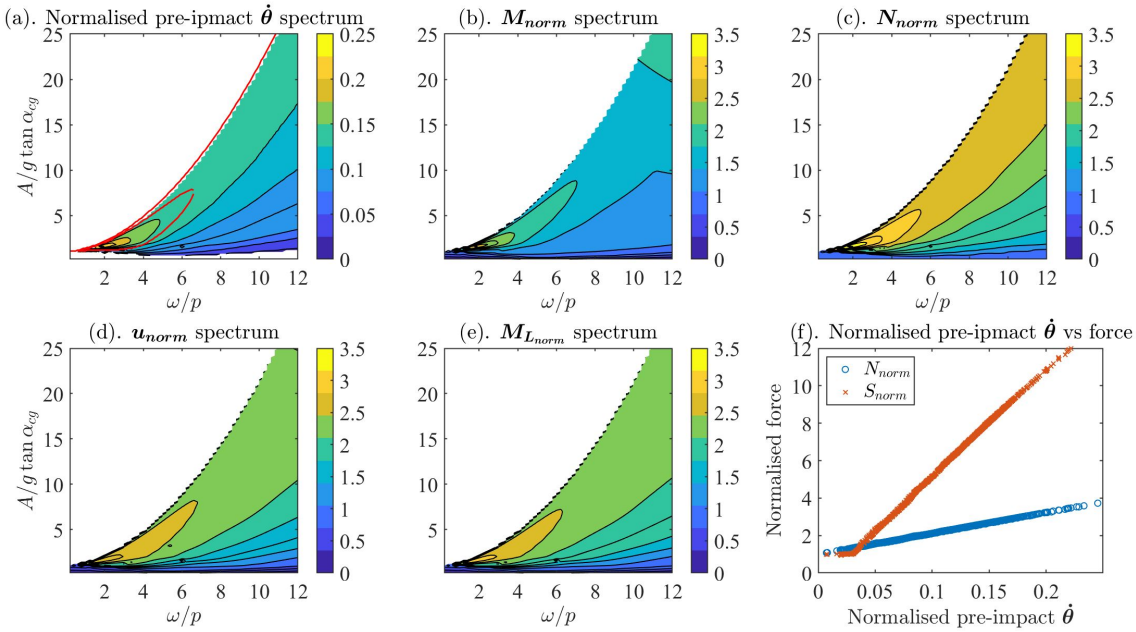


Figure 3.14: Response spectrum for Case three ($\omega_n = 9.822p$, $\omega_v = 56.387p$).

From Figure 3.14(f) it can be seen that the strongly linear relationship between the maximum normalised pre-impact $\dot{\theta}$ and the maximum normalised base forces also holds for the soft support medium. Secondly, Figure 3.14(a) shows that while the response range for the maximum normalised pre-impact $\dot{\theta}$ is the similar to Cases 1 and 2 shown in Figure 3.11(a) and 3.13(a), the maximum normalised force and

moment magnitudes in Figures 3.14(b-c) and (f) are significantly reduced. More specifically, the maximum N_{norm} and M_{norm} response are reduced by ten times and the S_{norm} by three times in comparison to corresponding values in Figures 3.11(b) and (f), demonstrating that the support spring stiffness can significantly reduce the maximum base force and moment demands when the lateral spring is stiff. In addition, because of the significant reduction in M_{norm} the difference between $M_{L_{norm}}$ and M_{norm} becomes smaller compared to the previous two cases. Thirdly, by comparing Figure 3.14(d) and Figure 3.11(d), it can be seen that when the lateral spring is stiff, the reduction of the stiffness of the support results in slightly larger maximum top mass displacement. Lastly, the similarity of response patterns between N_{norm} and M_{norm}, e.g. previously observed in Figure 3.11, is not present in Figure 3.14. The differences between axial force and moment demand patterns are to be expected as the net support reaction forces are not concentrated near the future-rocking corner for soft support media.

To verify this argument, N_{norm} is plotted against M_{norm} in Figure 3.15(a) for Case three, and Figure 3.15(b) for Case one.

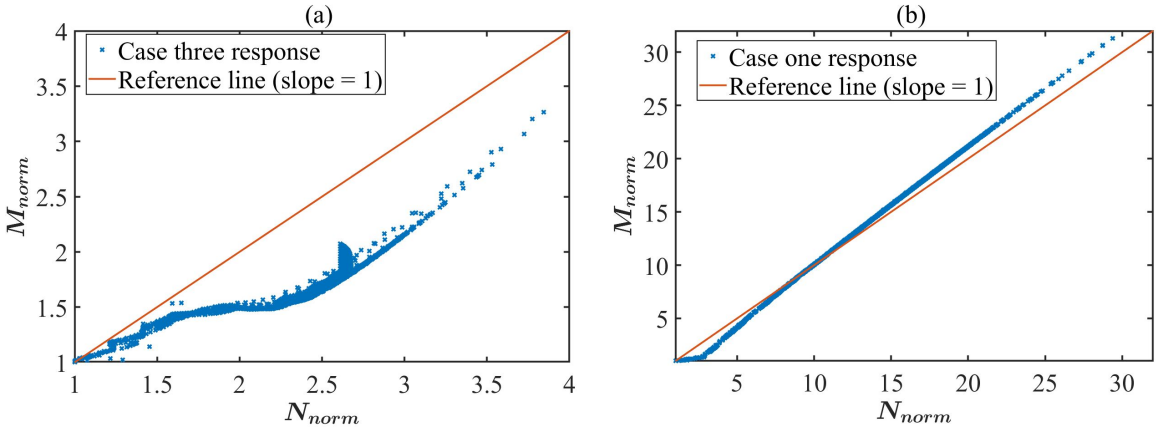


Figure 3.15: Maximum M_{norm} vs Maximum N_{norm} for (a) Case three and (b) Case one.

A reference line with slope of one and passing through point (1,1) is also plotted. During impact, if the net reaction force is concentrated at the future-rocking corner, then the base moment should be equal to the product of the axial force (i.e., the net vertical support force) and half the base width (1m). This corresponds to the slope of one for the reference line. It can be seen from Figure 3.15(b) that the blue line follows closely to the reference line for Case one. It falls slightly below the reference line when the maximum axial force is small then goes slightly above as the maximum axial force

increases. In contrast, it can be clearly seen in Figure 3.15(a) that in the soft support rocking case, the blue markers are located significantly below the reference line. This supports the argument that even for a body with feet placed at its bottom corners that during impact the net vertical support force is not concentrated near the future rocking corner when the support medium is softer.

3.5.6 Case four (soft-soft)

The following Figure 3.16 presents the results for the soft(lateral spring)-soft(support spring) configuration.

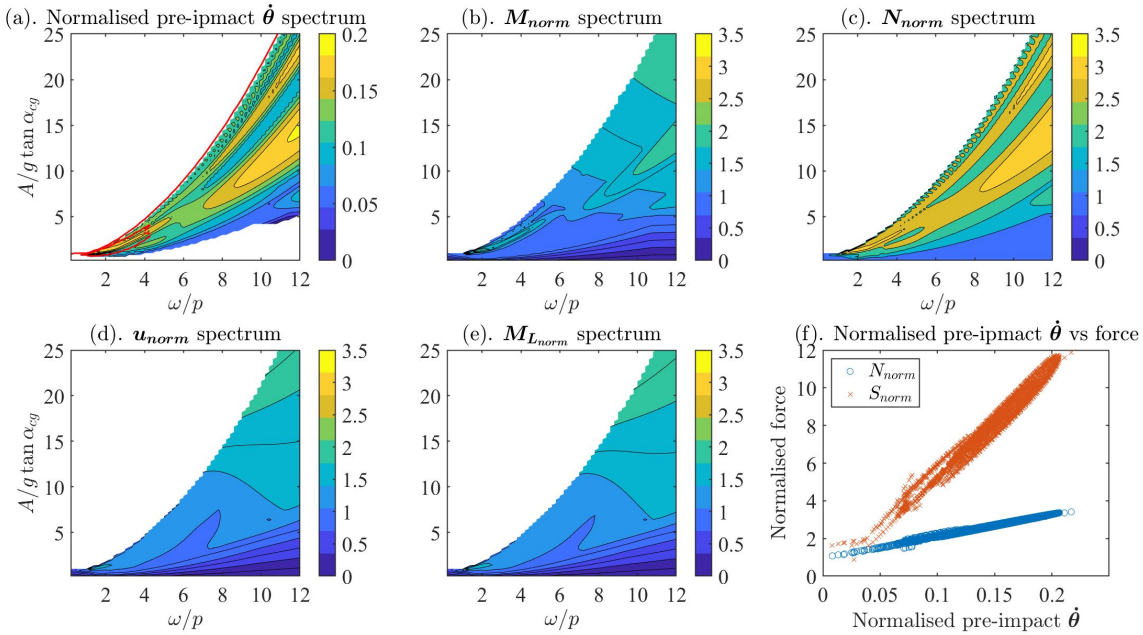


Figure 3.16: Response spectrum for Case four ($\omega_n = 2.431p$, $\omega_v = 56.387p$).

As can be seen in Figure 3.16(f), a strong linear trend between the maximum normalised pre-impact $\dot{\theta}$ and the maximum normalised base forces is still observed. It is likely that this linear trend applies to other (e.g. intermediate lateral spring and support stiffness) configurations that have not been examined in this chapter. Similar to Case three, trends observed in M_{norm} and N_{norm} spectra (Figures 3.16(b) and (c)) do not mirror one another, as the support forces at impact are not concentrated in one corner.

As can be seen in Figures 3.16(b) and (c), the range of the maximum normalised response indicates that the soft lateral spring slightly reduces the maximum response of N_{norm} and M_{norm} compared to Case three (stiff-soft). However, this force reduction

effect is smaller than the reduction achieved by softening the support medium between Case two (soft-stiff) and Case one. A similar observation was qualitatively made with time history investigations in **Section** 3.5.

In terms of the normalised top mass displacement u_{norm}, it can be seen in Figure 3.16(d) that the soft support spring does not result in any noticeable change (an increase of 3.0%) under different pulse excitations by comparing Figure 3.16(d) and Figure 3.13(d). A similar observation was made in **Section** 3.5. However, earlier, a noticeable increase of 23.4% in the maximum u_{norm} response was observed when comparing Cases one and three. This shows that the effect of the compliance of the support medium on increasing the maximum u_{norm} may become more or less pronounced depending on the stiffness of the lateral spring. In addition, the same trends highlighted in Figure 3.12(a) and Figure 3.12(b) are also observed across all the four cases, although the corresponding figures were not shown for Cases two to four for brevity. Therefore, it is likely that for all different rocking configurations, the maximum base forces happen during impact and that the maximum top shear force is smaller than the maximum base shear force.

3.5.7 Case five (Case four with sliding)

Case five investigates the influence of sliding on a soft lateral spring and soft support medium by adopting Case four geometry and material properties but using two lower values of coefficient of friction μ. The sliding x_{ts} is defined by combining sliding displacements at each support spring using the following equations:

$$x_{Zs} = (x_Z - x_{Zinitial}) - x_{Zel} \tag{3.29}$$

$$x_{Ys} = (x_Y - x_{Yinitial}) - x_{Yel} \tag{3.30}$$

$$x_{ts} = x_{Zs}H(-y_Z) + x_{Ys}H(y_Z) \tag{3.31}$$

where x_{Zs} and x_{Ys} are the sliding, i.e., the inelastic parts of the displacement of corners Z and Y, illustrated as the 'slide' part in Figure 3.3(a); x_{Zel} is the elastic deformation of the frictional spring at corner Z (i.e., $x_{Zel} = F_{Zfs}/k_f$); $x_{Zinitial}$ is the initial horizontal coordinate of corner Z and H is the Heaviside function (notice y_Z will never be exactly equal to zero in numerical simulations so the Heaviside function

is well defined). x_{ts} uses the information from the spring in contact with the ground, which experiences negligible translational motion due to rocking motion of the body.

Figure 3.17 shows response spectra under different values of μ. In the spectra, x_{ts} is normalised by the base width (2 m). Spectra exclude the unsafe area (i.e., Mode I and II areas) where large sliding is often experienced as the rocking angle tends to $\pi/2$. This sliding near collapse becomes less of interest as the body would tend to fail anyway by overturning and hence the associated sliding that occurs before failure will not be examined in the chapter. In Figure 3.17, decreasing μ from 0.8 to 0.3 leads to some, albeit small magnitude, sliding . This is accompanied by a 50% reduction in the maximum S_{norm} and negligible change in the maximum N_{norm} and the maximum u_{norm}. It is also noteworthy that the white area, where overturning happens, shrinks in the high frequency region (i.e., around Π_8 larger than 7). These observations suggest that, in addition to increasing support flexibility, allowing a small amount of sliding can notably reduce the maximum base shear force demand. A similar observation was qualitatively made with time history investigations in **Section** 3.5.

The response spectra for $\mu = 0.14$, which are shown in Figures 3.17(c),(f),(i),(l), feature a distinct overturning region compared to the other examples. The presence of an overturning failure area although μ is smaller than $tan(\alpha_{cg})$ of 0.15 is instructive - for a similar rigid body rocking on a rigid surface, no overturning would be expected, as the body would experience pure sliding when subjected to pulse excitation. As Greenbaum [59] showed for rigid bodies on deformable supports and Zhu et al.[42] showed for flexible oscillators on rigid support media, not only uplift but even overturning can be observed for situations where a rigid body on a rigid ground would only be predicted to experience pure sliding, when deformability of the support medium or the structure are considered . Figure 3.17(i) indicates a drastic increase in x_{ts}; sliding displacements in the order of metres can be observed. The accompanying maximum base shear force also decreases. Due to the significant interaction with sliding, the maximum top mass displacement demand also reduces noticeably. The results appear to suggest that, for this type of excitation, adopting very low grip support media may help to reduce the force and the displacement responses at the expense of increasing sliding.

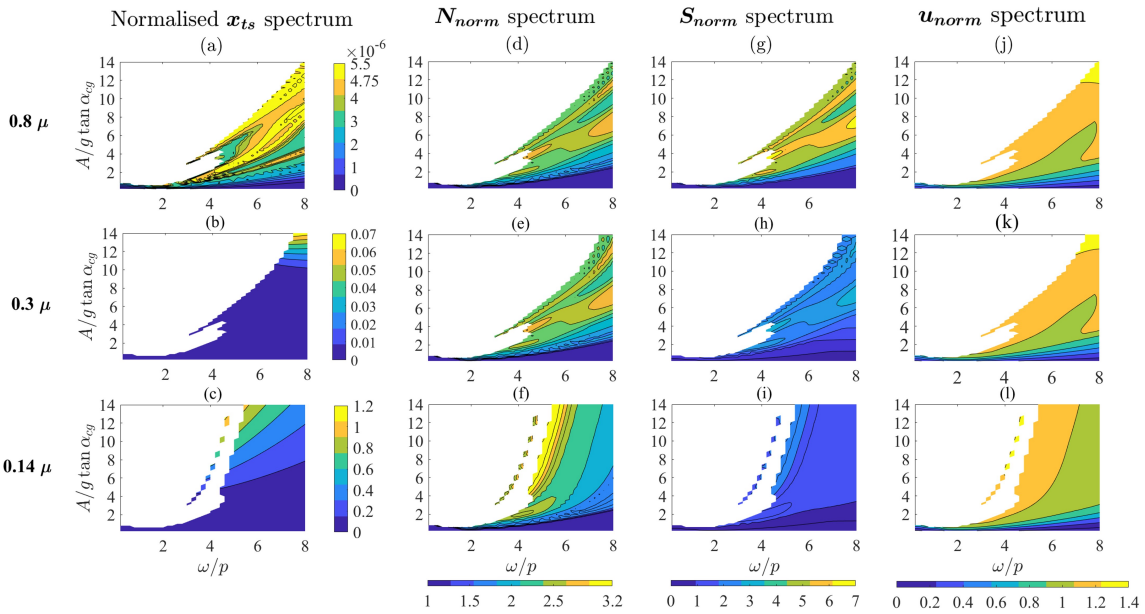


Figure 3.17: Response spectrum comparison for different values of μ ($\omega_n = 2.431p$, $\omega_v = 56.387p$).

Finally, the stability diagrams of the five cases are plotted in the following Figure 3.18. As can be seen in Figure 3.18(a), the Mode II collapse boundary is not significantly affected by the support medium and the lateral spring stiffness for large pulse frequencies; however, for small pulse frequencies ranging from 0.2p to 2p, softer lateral spring decreased the pulse amplitude needed to overturn the structure as can be seen from the observation that the purple line is below the blue line and, the red line is below the green line. Mode I is more strongly affected. Comparison of Case one and Case two lines shows that when the support medium spring is stiff, reducing the lateral spring stiffness can reduce the Mode I overturning area while also causing it to extend to the low frequency and low amplitude excitation region. The same effect was observed in [36] and was described as the 'shrinking and sinking' of the Mode I area. A similar 'shrinking and sinking' effect can also arise due to increasing support flexibility, compare stability diagrams for the Cases three and four.

The stability plots of Case four and Case five (0.3 μ) in Figure 3.18(b) indicate that small amount of sliding slightly increases the Mode I overturning area but shrinks the Mode II overturning area in the high frequency excitation range (i.e., around Π_8 larger than 7). With more sliding (see Case five (0.14 μ)), the Mode II area decreases starting from Π_8 equal to 3 but slightly increases in the low frequency excitation range (Π_8 = 0.4-1). At the same time, the Mode I area enlarges from around Π_8 equal to 3.5. In summary, sliding has both positive and negative effects on the rocking stability depending on the pulse frequency.

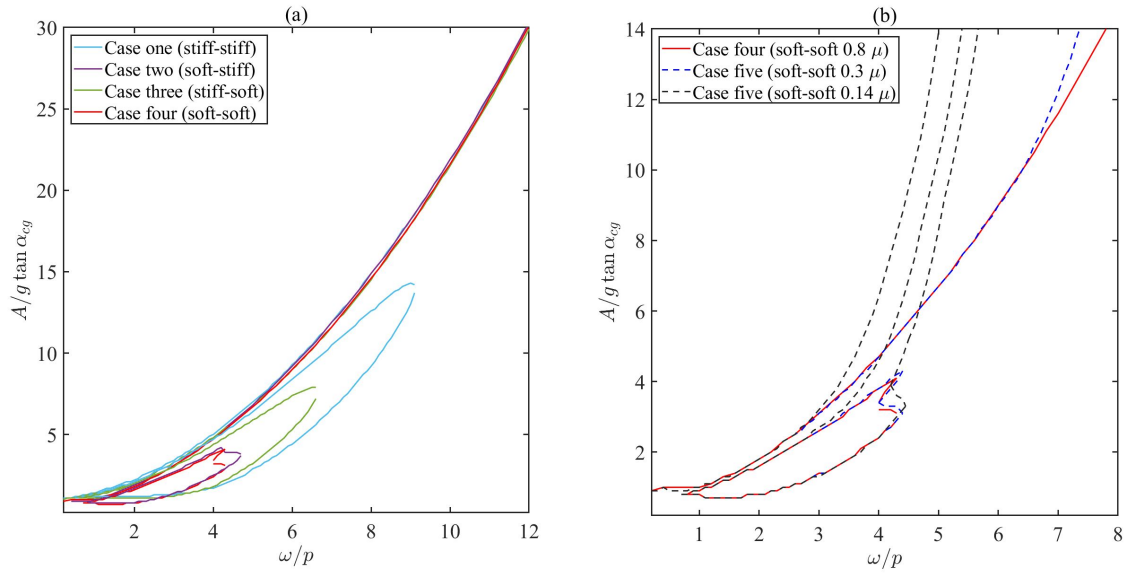


Figure 3.18: Comparison of stability plots for (a) Cases one to four and (b) Cases four and five.

3.6 Conclusion

This chapter developed a new analytical model, the Flexible Rocking Model on Concentrated Springs (FRMCS), to qualitatively investigate the dynamic behaviour of laterally flexible oscillators rocking and sliding on deformable supports. The model represents the support medium using concentrated vertical and horizontal spring–damper elements that capture compression-only contact, sliding governed by Coulomb friction, and free-flight motion. Incorporating support flexibility allows the evaluation of contact forces transmitted from the deformable foundation to the structure during impact.

The FRMCS exhibited excellent agreement with the earlier Flexible Rocking Model (FRM) for rocking on effectively rigid supports, confirming its robustness under limiting conditions and validating the FRM. Stability analyses showed that softer lateral springs and more deformable supports reduce stability at low frequencies but enhance it at higher frequencies, while sliding improves stability across almost the entire frequency range, though excessive sliding may lead to failure. Response force spectra demonstrated that impact can generate contact forces exceeding 35 times the self-weight of the structure; maximum base forces increase proportionally with pre-impact rotational velocity. A soft support medium effectively reduces peak base forces, lateral flexibility could amplify them, and small amounts of sliding substan-

tially decrease lateral force demand with minimal effect on vertical one.

Chapter 4

A Generalised Framework for Modelling the Rocking Response of Flexible Structures on Deformable Media

Nomenclature specifically for this chapter

$\boldsymbol{R}$,$\boldsymbol{\theta}$	position vector and rotation of the floating frame of reference in a global inertial reference frame
$\boldsymbol{\delta}$	Vector of small displacements relative to a body reference
$\boldsymbol{m}$,$\boldsymbol{c}$,$\boldsymbol{k}$	inertia or mass, damping, stiffness matrix
$\bar{\boldsymbol{Q}}_{\boldsymbol{R}}$,$\bar{\boldsymbol{Q}}_{\boldsymbol{\theta}}$,$\bar{\boldsymbol{Q}}_{\boldsymbol{\delta}}$	Generalised external forces at global coordinates, elastic coordinates
$\boldsymbol{\delta}^C$	Vector of small displacements from initial position to constraint position
$\boldsymbol{\delta}^N$	Vector of small displacements from constraint position to final position
$\boldsymbol{\delta}^B$,$\boldsymbol{\delta}^I$	Vector of small displacements at interface, non-interface nodes from initial position to final position
$\bar{\boldsymbol{\phi}}^C$	Matrix of constraint modes
$\boldsymbol{\phi}^N$	Matrix of retained normal modes with all interfaces fixed
$\boldsymbol{p}^N$	Vector of generalised coordinates for the retained normal modes
$\boldsymbol{\delta}_r^B$,$\boldsymbol{\delta}_r^I$	Small displacements at interface, non-interface nodes from constraint position to final position
$\boldsymbol{m}^R$,$\boldsymbol{c}^R$,$\boldsymbol{k}^R$	mass, damping, stiffness matrix after Craig-Bampton transformation

4.1 Introduction

Existing modelling strategies demonstrate a trade-off between accuracy and computational efficiency. Simplified approaches are easy to implement but rely on assumptions (e.g., small displacements assumption) that restrict their applicability (e.g., precluding stability analysis) and neglect potentially important aspects (i.e.,sliding and nonlinear stress distribution) in rocking problems. High-fidelity methods, while capable of representing geometric nonlinearity and impact effects in detail, remain

computationally demanding and hence impractical for large systems. Consequently, this chapter presents a generalized numerical framework for modelling the rocking of flexible structures on deformable support media, accounting for large displacements, sliding and free-flight phases. The literature review indicated that the concentrated spring model (CSM) provides stability predictions consistent with those from the advanced material point method; therefore, the same contact modelling approach used in the FRMCS model is adopted here for computational efficiency. Small elastic deformations of the superstructure are modelled using finite elements in a floating frame of reference. This general representation captures a wide range of structural configurations and the complex stress states that arise in the contact zone. To maintain computational tractability, the Craig–Bampton method is employed to represent the superstructure using a limited number of natural vibration modes. The chapter outlines the underlying theory, describes the proposed framework, and demonstrates its potential through representative examples that highlight key aspects of system behaviour.

Section 4.2 introduces the modelling framework implemented in Simulink. **Section** 4.6 verifies the implementation and evaluates its performance through the stability analysis of a stiff elastic column. **Section** 4.7 compares two models of the same rocking column: one using Euler–Bernoulli beam elements and the other employing tetrahedral elements with Craig–Bampton model reduction. This comparison clarifies the influence of the Euler–Bernoulli assumption on key response parameters such as the stability plot and stress distribution. Subsequently, free-vibration (**Section** 4.8.1) and pulse-excitation (**Section** 4.8.2) simulations are performed on columns of varying stiffness to examine the effect of structural flexibility on the rocking response. An additional case study of a column rocking on a low-friction surface demonstrates the framework's ability to capture sliding motion. In **Section** 4.9, the framework is applied to simulate an experimental rocking steel frame [77], illustrating its capability to model structures with complex geometries. Finally, **Section** 4.10 demonstrates the framework's extension to 3D rocking problems, and the findings are summarized in **Section** 4.11.

4.2 Modelling framework

The deformable medium is modelled with tensionless concentrated springs and viscous dampers in the vertical direction. In the horizontal direction, concentrated nonlinear

springs that follow the Coulomb friction law are used so that sliding motion is considered; these are paired with linear viscous dampers. The details of these elements can be found in the previous work by the authors [78]. The flexible superstructure is modelled with isoparametric linear tetrahedral elements with 4 nodes. Although the elements are formulated for small deformations, they are placed in a floating frame of reference, which enables the consideration of geometric nonlinearities due to large rigid body translations and rotations. The Craig-Bampton method is used to reduce the size of the finite element representation of the superstructure and hence the computational cost. This new framework can be implemented through Simulink.

While Simulink provides many relevant libraries for the simulation, some further additions and modifications over the base version were implemented. Those are described in the following lines. An in-house developed library, OXcontact, was used for implementing the contact elements. The corresponding blocks allow for implementing the same constitutive model behaviour of the springs as that defined in [78] and [35]. The Matlab built-in function for Craig-Bampton reduction was modified to allow for producing a reduced order model by using selected modes rather than truncating frequencies that fall outside a range of interest. As discussed later in **Section** 4.5 that was important for a robust representation of the system. Codes to reconstruct the full order response from the reduced order response after Simulink simulations were developed.

The following sections briefly introduce the floating frame of reference formulation and the Craig-Bampton reduction method.

4.2.1 The floating frame of reference formulation

During the response of a typical rocking body, the total lateral displacement of the body is composed of large rigid body translations and rotation and a small proportion of elastic deformations. A floating frame of reference (FFR) formulation is used to separate these components of motion, as will be briefly introduced herein.

In the FFR kinematics, two types of coordinates are used: reference coordinates and elastic coordinates. The reference coordinates define the pose of the body and the coordinates that its points would have if the body were completely undeformed (i.e., the body reference position). They hence provide a description of the rigid body movement of the body. The elastic coordinates describe the deformation of the body relative to the body reference position. A schematic representation of the FFR kinematics is shown in Figure 4.1, using a discretized beam component as an example for ease of presentation. In the case of the beam example, the reference coordinates

describe the body reference position using global displacements and rotations of the beam's neutral axis, and the elastic displacements describe the beam deformations relative to the body reference position. The floating frame of reference ($Y'O'X'$) is fixed to the middle node of the beam; $\boldsymbol{u}^i$ is the position vector of a beam node in the global inertial reference frame (YOX); $\boldsymbol{u}_0^i$ the position vector of the node in the FFR on the body reference position; $\boldsymbol{\delta}^i$ are the coefficients of the elastic displacement of the node expressed in terms of the floating frame of reference. It should be noted that, as is also the case in this chapter, the theory and the developed model are not restricted to beam -type elements and can be applied to more general deformable bodies. For a more abstract and fundamental understanding, readers can refer to [79] for more details.

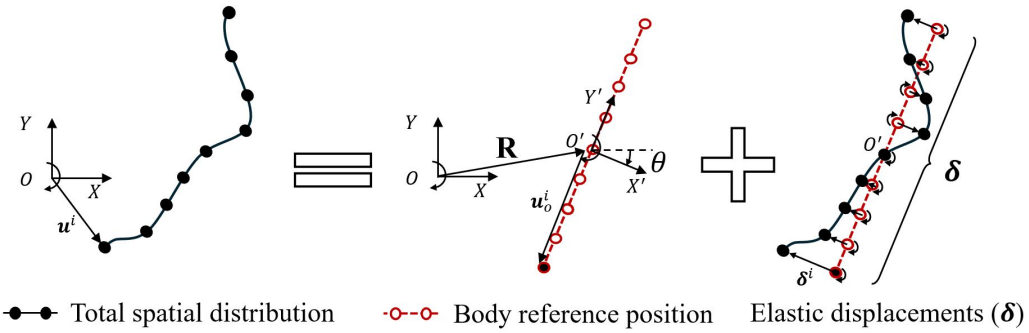


Figure 4.1: A schematic representation of the kinematics in FFR. YOX is the global inertia reference frame, $Y'O'X'$ the FFR.

The position vector ($\boldsymbol{u}^i$) expressed using FFR kinematics is given by:

$$\boldsymbol{u}^i = \boldsymbol{R}^i + \mathbf{A}\boldsymbol{u}_0^i + \mathbf{A}\boldsymbol{\delta}^i \tag{4.1}$$

$$\mathbf{A} = \begin{bmatrix} \cos\theta & -\sin\theta \\ \sin\theta & \cos\theta \end{bmatrix} \tag{4.2}$$

Using the FFR kinematics and assuming viscous damping, the equation of motion of a body that experiences large rigid body motion and small deformations can be written as:

$$\begin{bmatrix} \boldsymbol{m}_{RR} & \boldsymbol{m}_{R\theta} & \boldsymbol{m}_{R\delta} \\ \boldsymbol{m}_{R\theta} & \boldsymbol{m}_{\theta\theta} & \boldsymbol{m}_{\theta\delta} \\ \boldsymbol{m}_{R\delta} & \boldsymbol{m}_{\theta\delta} & \boldsymbol{m}_{\delta\delta} \end{bmatrix} \begin{bmatrix} \ddot{\boldsymbol{R}} \\ \ddot{\boldsymbol{\theta}} \\ \ddot{\boldsymbol{\delta}} \end{bmatrix} + \begin{bmatrix} 0 & 0 & 0 \\ 0 & 0 & 0 \\ 0 & 0 & \boldsymbol{c}_{\delta\delta} \end{bmatrix} \begin{bmatrix} \dot{\boldsymbol{R}} \\ \dot{\boldsymbol{\theta}} \\ \dot{\boldsymbol{\delta}} \end{bmatrix} + \begin{bmatrix} 0 & 0 & 0 \\ 0 & 0 & 0 \\ 0 & 0 & \boldsymbol{k}_{\delta\delta} \end{bmatrix} \begin{bmatrix} \boldsymbol{R} \\ \boldsymbol{\theta} \\ \boldsymbol{\delta} \end{bmatrix} = \begin{bmatrix} \bar{\boldsymbol{Q}}_{\boldsymbol{R}} \\ \bar{\boldsymbol{Q}}_{\boldsymbol{\theta}} \\ \bar{\boldsymbol{Q}}_{\boldsymbol{\delta}} \end{bmatrix} \tag{4.3}$$

The origin of the reference coordinates does not need to be on the body as long as a unique body reference is defined with it. On the left-hand side of Equation (4.3),

only the sub-matrix in the mass matrix that is related to the rotational reference coordinates $\boldsymbol{\theta}$ (i.e., $\boldsymbol{m}_{R\theta}$, $m_{\theta\theta}$ and $\boldsymbol{m}_{\theta\delta}$) and the term $\boldsymbol{m}_{R\delta}$ change with time, the rest is constant. Therefore, re-write the last row of Equation (4.3) by moving the time changing parts on the left-hand side to the right-hand side:

$$\boldsymbol{m}_{\delta\delta}\ddot{\boldsymbol{\delta}} + \boldsymbol{c}_{\delta\delta}\dot{\boldsymbol{\delta}} + \boldsymbol{k}_{\delta\delta}\boldsymbol{\delta} = \bar{\boldsymbol{Q}}_{\delta} - \ddot{\boldsymbol{R}}\boldsymbol{m}_{R\delta} - \ddot{\boldsymbol{\theta}}\boldsymbol{m}_{\theta\delta} \tag{4.4}$$

Equation (4.4) with constant mass, damping and stiffness matrices describing the small deformations relative to the body reference is hence obtained.

4.2.2 The Craig-Bampton reduction

Because the mass, damping and stiffness matrices in Equation (4.4) are constant, model order reduction method for linear systems like the Craig-Bampton method can be applied for computational efficiency. The following introduction of the method is based on the work of Hurty[80] and, Craig and Bampton[81].

Kinematically, the Craig-Bampton method treats the elastic displacement at each node ($\boldsymbol{\delta}$) as the summation of a constraint displacement ($\boldsymbol{\delta}^C$) and a relative displacement, $\boldsymbol{\delta}^N$, to the constraint displacement:

$$\boldsymbol{\delta} = \boldsymbol{\delta}^C + \boldsymbol{\delta}^N \tag{4.5}$$

The displacement vector ($\boldsymbol{\delta}$) can then be partitioned into displacements at the interface nodes ($\boldsymbol{\delta}^B$) and at the non-interface nodes($\boldsymbol{\delta}^I$), i.e., $\boldsymbol{\delta} = [\boldsymbol{\delta}^B, \boldsymbol{\delta}^I]$. It should be noted that in the Craig-Bampton transformation: (a) the physical coordinates at the interface nodes ($\boldsymbol{\delta}^B$) are retained; (b) the component of $\boldsymbol{\delta}^I$ in $\boldsymbol{\delta}^C$ is assumed to relate to $\boldsymbol{\delta}^B$ through the Guyan reduction matrix[82]; and (c) the component of $\boldsymbol{\delta}^I$ in $\boldsymbol{\delta}^N$, $\boldsymbol{\delta}^I_r$, is approximated with an incomplete set of relative normal modes ($\boldsymbol{\phi}^N$) and corresponding generalised coordinates ($\boldsymbol{p}^N$) for model order reduction. Therefore, Equation (4.5) can be re-written as the following:

$$\begin{bmatrix} \boldsymbol{\delta}^B \\ \boldsymbol{\delta}^I \end{bmatrix} = \begin{bmatrix} \boldsymbol{I} & \boldsymbol{0} \\ \bar{\boldsymbol{\phi}}^C & \boldsymbol{\phi}^N \end{bmatrix} \begin{bmatrix} \boldsymbol{\delta}^B \\ \boldsymbol{p}^N \end{bmatrix} \tag{4.6}$$

Hence, the Craig-Bampton transformation matrix ($\boldsymbol{T}_{CB}$) is defined as follows:

$$\boldsymbol{T}_{CB} = \begin{bmatrix} \boldsymbol{I} & \boldsymbol{0} \\ \bar{\boldsymbol{\phi}}^C & \boldsymbol{\phi}^N \end{bmatrix} \tag{4.7}$$

Continuing with the last figure in Figure 4.1, a schematic representation of Equations (4.5) and (4.6) is shown in Figure 4.2 for an intuitive understanding. In the Craig-Bampton kinematics, the body first moves from its initial position to the constraint position with displacements described by $\boldsymbol{\delta}^C$, then it moves to the final position from the constraint position through displacements described by $\boldsymbol{\delta}^N$

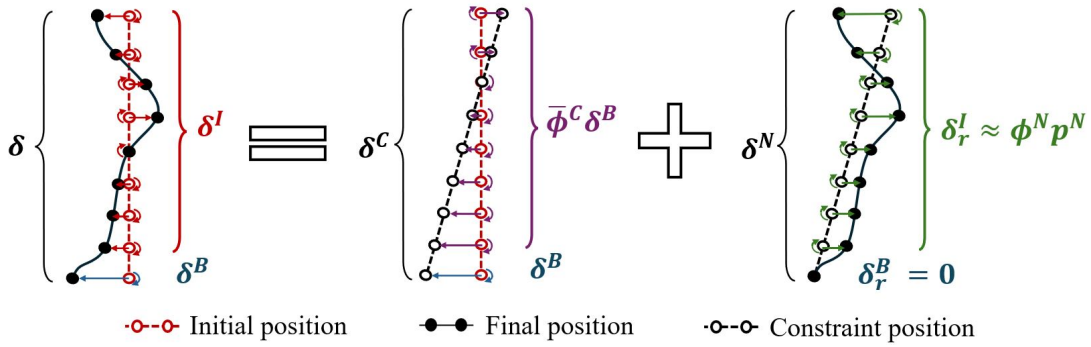


Figure 4.2: A schematic representation of the kinematics in the Craig-Bampton method.

The details regarding the reduction of model order and the equations defining $\bar{\boldsymbol{\phi}}^C$ and $\boldsymbol{\phi}^N$ are provided in the later appearing equations (4.13) and (4.14). Grouping the right-hand side terms into one and omitting the matrices subscripts in Equation (4.4) lead to:

$$\boldsymbol{m}\ddot{\boldsymbol{\delta}} + \boldsymbol{c}\dot{\boldsymbol{\delta}} + \boldsymbol{k}\boldsymbol{\delta} = \boldsymbol{F} \tag{4.8}$$

Partitioning Equation (4.8) in terms of the interface nodes and the non-interface nodes; then, substituting in Equation (4.6) and premultiplying with the transpose of $\boldsymbol{T}_{CB}$, one would obtain:

$$\begin{aligned}\boldsymbol{T}_{CB}^T \begin{bmatrix} \boldsymbol{m}^{BB} & \boldsymbol{m}^{BI} \\ \boldsymbol{m}^{IB} & \boldsymbol{m}^{II} \end{bmatrix} \boldsymbol{T}_{CB} \begin{bmatrix} \ddot{\boldsymbol{\delta}}^B \\ \ddot{\boldsymbol{p}}^N \end{bmatrix} + \boldsymbol{T}_{CB}^T \begin{bmatrix} \boldsymbol{c}^{BB} & \boldsymbol{c}^{BI} \\ \boldsymbol{c}^{IB} & \boldsymbol{c}^{II} \end{bmatrix} \boldsymbol{T}_{CB} \begin{bmatrix} \dot{\boldsymbol{\delta}}^B \\ \dot{\boldsymbol{p}}^N \end{bmatrix} \\ + \boldsymbol{T}_{CB}^T \begin{bmatrix} \boldsymbol{k}^{BB} & \boldsymbol{k}^{BI} \\ \boldsymbol{k}^{IB} & \boldsymbol{k}^{II} \end{bmatrix} \boldsymbol{T}_{CB} \begin{bmatrix} \boldsymbol{\delta}^B \\ \boldsymbol{p}^N \end{bmatrix} = \boldsymbol{T}_{CB}^T \begin{bmatrix} \boldsymbol{F}^B \\ \boldsymbol{F}^I \end{bmatrix}\end{aligned} \tag{4.9}$$

The transformed mass matrix ($\boldsymbol{m}^R$), damping matrix ($\boldsymbol{c}^R$) and stiffness matrix ($\boldsymbol{k}^R$) are hence defined:

The following describes how $\bar{\boldsymbol{\phi}}^C$ and $\boldsymbol{\phi}^N$ in the transformation matrix are obtained, and to reduce the model order. Firstly, $\bar{\boldsymbol{\phi}}^C$ in the Craig-Bampton transformation ($\boldsymbol{T}_{CB}$) is calculated as:

$$\bar{\boldsymbol{\phi}}^C = -\boldsymbol{k}^{II^{-1}}\boldsymbol{k}^{IB} \tag{4.13}$$

$$\boldsymbol{m}^R = \boldsymbol{T}_{CB}^T \begin{bmatrix} \boldsymbol{m}^{BB} & \boldsymbol{m}^{BI} \\ \boldsymbol{m}^{IB} & \boldsymbol{m}^{II} \end{bmatrix} \boldsymbol{T}_{CB} \tag{4.10}$$

$$\boldsymbol{c}^R = \boldsymbol{T}_{CB}^T \begin{bmatrix} \boldsymbol{c}^{BB} & \boldsymbol{c}^{BI} \\ \boldsymbol{c}^{IB} & \boldsymbol{c}^{II} \end{bmatrix} \boldsymbol{T}_{CB} \tag{4.11}$$

$$\boldsymbol{k}^R = \boldsymbol{T}_{CB}^T \begin{bmatrix} \boldsymbol{k}^{BB} & \boldsymbol{k}^{BI} \\ \boldsymbol{k}^{IB} & \boldsymbol{k}^{II} \end{bmatrix} \boldsymbol{T}_{CB} \tag{4.12}$$

Each column vector in $\bar{\boldsymbol{\phi}}^C$ can be interpreted as the displacement at all nodes due to a unit displacement at one specific interface node while holding other interface nodes fixed and the non-interface nodes are free to move. It should also be noticed that Equation (4.13) is the Guyan reduction expression for the static problem of Equation (4.8), and hence $\bar{\boldsymbol{\phi}}^C$ can be seen as a transformation matrix that relates the displacements at the interface node ($\boldsymbol{\delta}^B$) to those at the non-interface node ($\boldsymbol{\delta}^I$). In other words, it shows what the displacements are at the non-interface node given an identity matrix of $\boldsymbol{\delta}^B$.

Secondly, $\boldsymbol{\phi}^N$ in $\boldsymbol{T}_{CB}$ consists of a selection of modes of the component with all interface nodes fixed and damping ignored during free vibration:

$$\boldsymbol{m}^{II}\ddot{\boldsymbol{\delta}}_r^I + \boldsymbol{k}^{II}\boldsymbol{\delta}_r^I = \boldsymbol{0} \tag{4.14}$$

$\boldsymbol{\delta}_r^I$ can then be approximated in terms of $\boldsymbol{\phi}^N$ and the corresponding generalised coordinates ($\boldsymbol{p}^N$) as graphically shown in Figure 4.3. And, the number of non-interface dofs reduces from $\boldsymbol{\delta}^I$ to $\boldsymbol{p}^N$ as suggested in Equation (4.6).

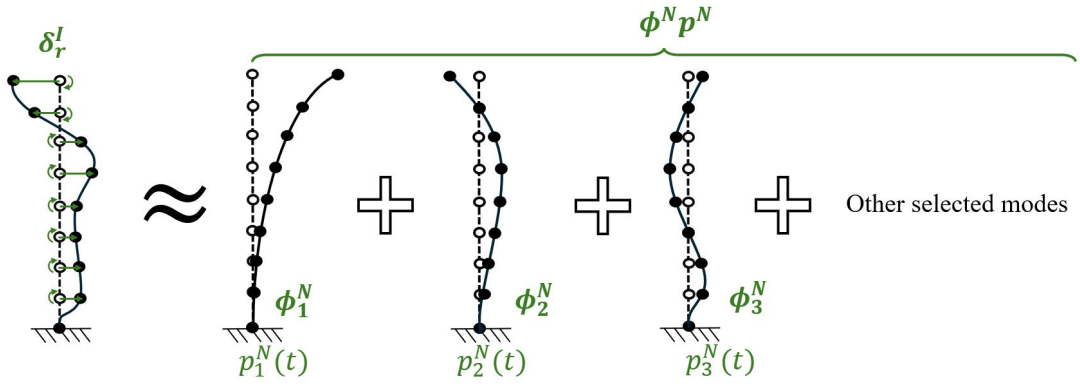


Figure 4.3: Approximation of $\boldsymbol{\delta}_r^I$ with selected mode shapes $\boldsymbol{\phi}^N$ and the corresponding coordinates $\boldsymbol{p}^N$.

4.3 Structure configurations

Four structure configurations are considered in this study. The basic configuration, called Case B, is a solid marble column with four rigid corner feet standing on a high grip, stiff support medium; the height of the corner feet is considered to be negligible.

This marble column is considered as an intermediate stiff superstructure in the study. Its geometry is shown in Figure 4.4. Figure 4.4.(c) shows six different points marked on the column; they locate in the middle of the column surface at various heights and are used to demonstrate stress time history studies in the following sections. Compared to Case B, Case A represents a stiffer column, while Case C represents a more deformable one; they are obtained by varying the material Young's modulus (E) of Case B. The last case, Case D, represents a perfectly rigid column that shares the same mass and geometry properties as those of Case B. For Cases A to C, a uniform modal damping model with all modal damping ratios being set equal to $\zeta = 0.05$ is applied to the free-free superstructure after the Craig-Bampton reduction. In terms of the support medium modelling, the stiffness of the vertical springs is defined so that the vertical natural frequency (f_v) of the system that would correspond to a the rigid mass moving purely vertically is 60 Hz; i.e., $\sqrt{\frac{4k}{m}} = 2\pi f_v$, where k is the stiffness of each support spring and m is the mass of the column. This stiffness is considered to represent a reasonably stiff medium. The viscous damping ratio of each vertical damper (ζ_v) is chosen so that the corresponding damping ratio of the pure vertical vibration of the rigid body would be 0.5; i.e., is defined as $\zeta_v = c/\sqrt{km} = 0.5$, where c is the damping coefficient of each support damper. The stiffness and damping coefficient for the horizontal frictional elements are the same as those of the vertical ones. And, the coefficient of friction (μ) is assumed to be 0.8 to simulate a high grip support medium. The values of the key parameters for the four cases are summarised in Table 4.1, where T_n is the fixed-end first mode period for a more intuitive demonstration of different column flexibilities, I_{cg} is the moment of inertia of the rigid body with the same geometry and p is the rocking frequency parameter ($p = \sqrt{\frac{mgh}{(2\cos(\alpha_{cg})I_{cg}}}$).

Table 4.1: Values of the common parameters.

	E (GPa)	T_n (s)	f_v (Hz)	ζ	ζ_v	μ	b (m)	d (m)	h (m)	α_{cg} (rad)	ρ (kg/m^3)	p (1/s)	I_{cg} (kg·m^2)
Case A	48.828	0.146	60	0.05	0.5	0.8	1	1.05	10	0.08	2256.86	2.418	1.995×10^5
Case B	5.425	0.440	60	0.05	0.5	0.8	1	1.05	10	0.08	2256.86	2.418	1.995×10^5
Case C	1.085	0.980	60	0.05	0.5	0.8	1	1.05	10	0.08	2256.86	2.418	1.995×10^5
Case D	Rigid	N/A	60	0.05	0.5	0.8	1	1.05	10	0.08	2256.86	2.418	1.995×10^5

4.4 Numerical implementation

The size of the linear tetrahedron elements and the integration step size need to satisfy two necessary conditions: the Courant–Friedrichs–Lewy (CFL) condition, and

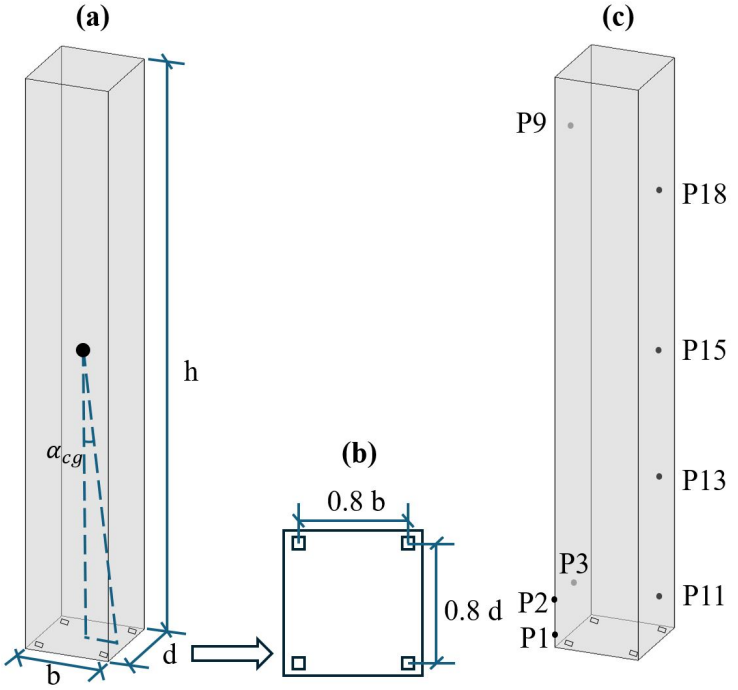


Figure 4.4: (a) Column geometry, (b) rigid corner feet position and (c) points for time history demonstration.

the wavelength to element size condition.

$$\frac{v_x\,\Delta t}{\Delta x} + \frac{v_y\,\Delta t}{\Delta y} + \frac{v_z\,\Delta t}{\Delta z} \leq C_{\max} \tag{4.15}$$

$$\frac{\lambda}{\Delta x, y, z} \geq N_{min} \tag{4.16}$$

where v_x,v_y,v_z are the elastic axial wave speed in x,y,z direction, respectively; Δx,Δy,Δz are the element size in x,y,z direction respectively; λ is the wavelength and Δt is the integration step size. The CFL condition is necessary to ensure the convergence of explicit integration schemes; the wavelength to element size condition is necessary to accurately capture elastic wave propagation. In this study, C_{max} is taken as 1 according to the CFL condition, and N_{min} as 10 according to the related literature [83]. The two conditions are used as a starting guide and the final mesh size is determined by convergence analysis as detailed in **Section** 4.5.

As a result, the meshed column with 11172 dofs is shown in Figure 4.5. The dark blue surfaces in Figure 4.5(b) are constrained to act as flat rigid surfaces using the multipoint constraint functionality in Simulink. The rocking angle in this study is defined as the relative rotation between the bottom left rigid contact surface in Figure

4.5(b) and the ground surface. In the following analyses, the rigid surfaces shown in Figure 4.5(b) remain practically parallel to each other at all times, even though this is not explicitly imposed so the choice of the contact surface used for measuring the rocking angles had a minimal effect. The motion of each rigid surface is described using six degrees of freedom, the translations of the central node and the rotations of the surface. Those dofs are the interface dofs that are retained in the Craig-Bampton reduction. Those are also the interfaces to be connected to the contact elements used to model the interaction of the support medium with the feet of the body. This means point contact loads are applied to the deformable superstructure through these rigid surfaces. In addition, the six degrees of freedom associated with the bottom left rigid surface are chosen as the floating frame of reference (FFR) to define the body reference.

Finally, Runge-Kutta (4,5) pair is chosen as the numerical solver. The relative tolerance and absolute tolerance are chosen as 1e-5 after convergence analysis.

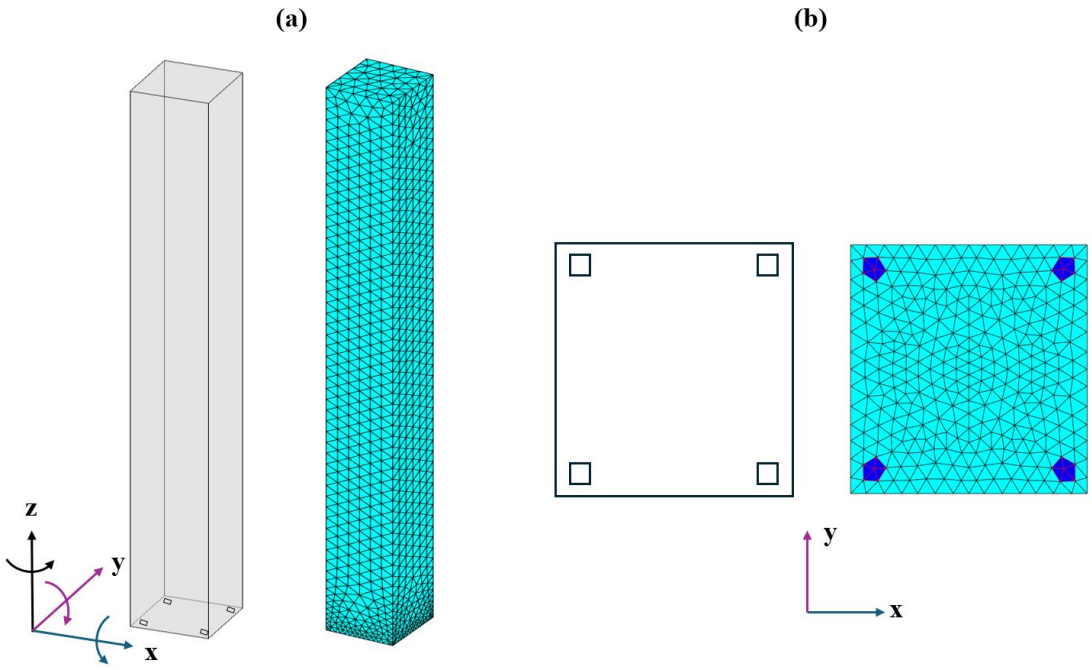


Figure 4.5: (a) Finite element representation of the column (11172 dofs) and (b) Rigid corner feet on bottom surface shown in deep blue.

4.5 Procedures to obtain the reduced order model

As introduced in **Section** 4.2.2, one needs to decide what fixed-interface modes to include in the Craig-Bampton method for an accurate reduced order model. In general, the decision procedure includes two steps: first, use prior knowledge to make a reasonable initial guess on what modes should be included; second, verify the reduced order model by comparing the response with a full order model.

In this study, a general procedure is employed. First, to obtain a pseudo 'full' order model, the reduced order model is subjected to a ground excitation along the width, b, of the column, and the response of different numbers of fixed-interface modes is compared. The pseudo 'full' order model is obtained when the response does not practically change when further fixed-interface modes are included in the analysis. Then, the reduced order model is obtained by including fewer modes than the 'full' order model while maintaining good accuracy. It was found that (i) local stress response should be the tested for convergence rather than global response parameters like rocking angle because the latter converges much earlier, and (ii) including sufficient axial dominant modes, in addition to other relatively low frequency modes, seems to be an important requirement of convergence in rocking problems. These axial modes ensure that the self weight stresses are correctly accounted for.

Case B is used for demonstration. The rocking angle response of the reduced order model, that includes 10, 20, and 40 modes starting from the first mode, subjected to pulse excitation of $3p$ and $1.2g\tan(\alpha_{cg})$ are compared in Figure 4.6. It can be seen that the rocking angle responses of the three reduced order models are nearly identical. Therefore, the rocking angle appears to have converged after 10 fixed-interface modes. However, the normal stress in the vertical direction (σ_{zz}) response indicates a different trend. Figures 4.7.(a) to (c) compare the normal stress response at point P9, which best illustrates the difference compared to other points studied, (see Figure 4.4.(c) for the location of this point) of reduced order models that include 10, 20, 40, and 60 fixed-interface modes. Figure 4.7.(a) clearly showed that the stress time histories require a significant number of modes to be kept before convergence is reached: Figures 4.7.(b) to (c) indicate that the response stops varying between 40 and 60 modes, and hence 40 modes can be considered as the 'full' order model. The time histories of σ_{zz} at other points across the body also converge, but these are not shown for conciseness.

By observing Figure 4.7.(b), one can see that the self-weight normal stress at time zero of the 20 modes reduced-order model is different from the 'full' order model. Six

extra axial-dominant modes are hence added on top of the 20 modes, and the response comparison is shown in Figure 4.7.(d). It can be seen that the response is now much more similar to the 'full' order model. Figure 4.7.(d) is chosen as the reduced order model, due to its limited degrees of freedom. After the Craig-Bampton reduction, the total number of modes decreases from 11172 to 50 (26 non-interface dofs and 24 interface dofs) for Case B. The same procedure is applied to Case A and Case C.

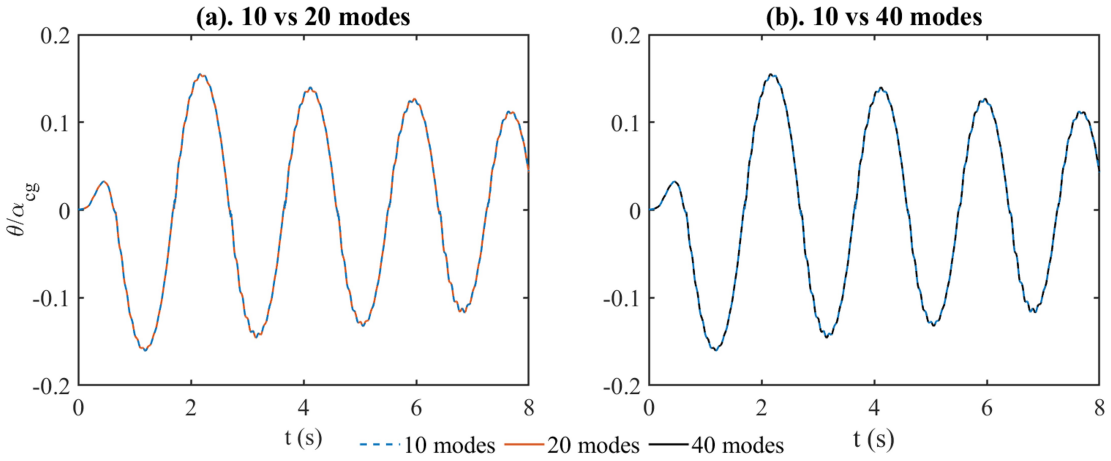


Figure 4.6: Comparison of rocking angle response between different reduced order models.

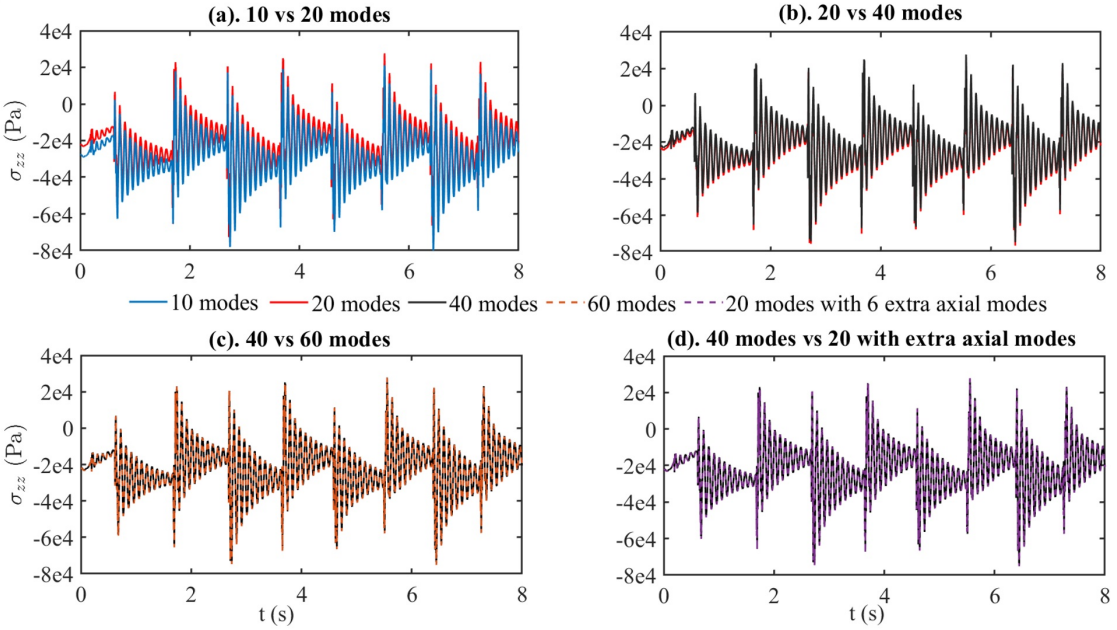


Figure 4.7: Comparison of normal stress response at point P9 (9m high) between different reduced order models.

4.6 Model comparison for effectively rigid rocking body

To verify the Simulink implementation of the new library OXcontact and evaluate the performance of the proposed framework, Case D is modelled using both the analytical model FRMCS [78] and the proposed numerical framework. The resulting stability plots are compared for verification. In the proposed framework, two modelling approaches are considered for the rocking body. First, the rocking body is modelled as a perfectly rigid body. Second, it is represented using finite elements with a high stiffness material, where the Young's modulus is set to be 100 times larger than that of Case B. It is hence expected that the flexibility of the body has a negligible effect on the rocking response.

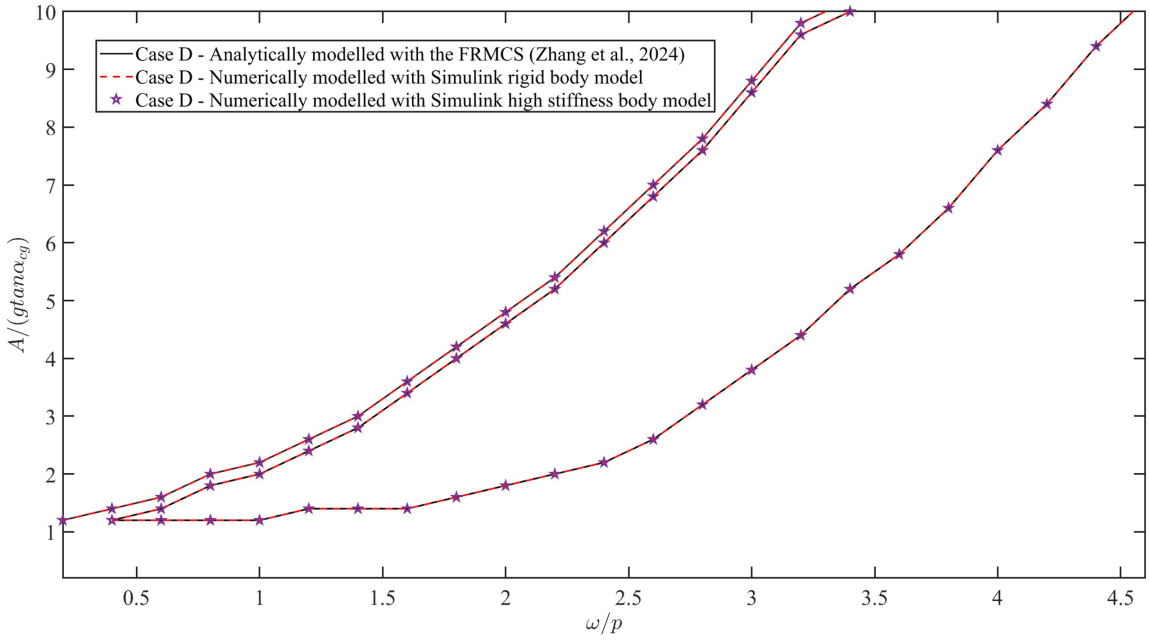


Figure 4.8: Comparison of stability plots between the highly stiff elastic column and the rigid analytical model.

Figure 4.8 shows the comparison of stability plots. Ground excitations with magnitude above $10g \tan \alpha_{cg}$ (i.e., $0.8g$) are relatively rare and not considered. For the range considered, it can be seen that the stability plots obtained using the FRMCS and two different Simulink modelling approaches are in excellent agreement. In particular, the agreement between the FRMCS and the Simulink perfectly rigid body model verifies the proper implementation of the Oxcontact library; the agreement between the finite elements Simulink model and the perfectly rigid Simulink model

shows that the proposed numerical framework works properly in cases where the rocking body is stiff. From hereon, all simulations are carried out using the proposed framework implemented in the Simulink environment.

4.7 Influence of Euler beam assumption on the rocking response

The tetrahedral finite elements used for Cases A, B, and C do not enforce the usual Euler-Bernoulli beam theory assumption of all cross sections of the beam remaining plane after deformation. While this is expected to still largely manifest for standard pinned or fixed boundary conditions of the columns, in a rocking specimen the response of the cross sections may deviate substantially from this idealization. The fact that the base is in partial contact with the support during rocking, is expected to lead to a nonlinear stress zone near the contact area. Secondly, the impacts during rocking will induce stress waves whose propagation within the beam will not necessarily conform to the assumed distribution of normal stresses. Both pose challenges to the standard assumptions of Euler-Bernoulli beam theory. In this section, the influence of Euler–Bernoulli beam assumption is investigated using Case B. The response of the system is compared when two different types of finite elements are used to model the super-structure: beam macro-elements versus linear tetrahedral elements.

The following Figure 4.9 presents the comparison of the time histories for the rotation angle and vertical contact force responses between the beam and the tetrahedron models.

In Figure 4.9, the definition of the rotation angle is provided in **Section** 4.4 and it is normalised by α_{cg} (0.08) of the superstructure. The frequency and the amplitude of the single cycle sinusoidal pulse used for excitation are shown at the bottom of the Figure 4.9. Sub-figure (a) demonstrates that the beam model rotation response follows closely that of the tetrahedron model until after the first impact; then it starts to diverge. The divergence becomes more apparent with each rocking cycle. However, Figure 4.9.(b) shows that when there are fewer impacts, the beam model rotation angle response in general follows closely the tetrahedron model. This suggests that using beam elements to model the superstructure could be sufficient for single cycle pulse stability analysis where there is one or less impact before overturning. This will also be investigated by examining the corresponding stability diagram which is done in the later **Section** 4.8.3. In Figures 4.9.(c) and (d), both the beam and the tetrahedron model show that the vertical contact force at the left front foot reaches

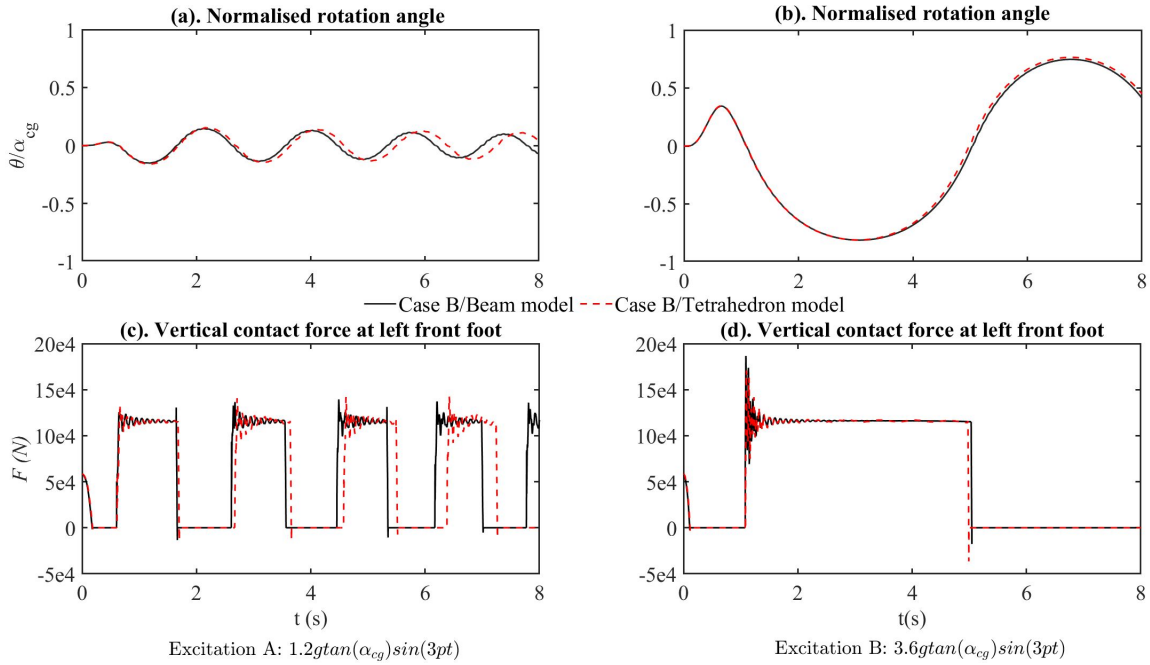


Figure 4.9: Comparison of global response of Case B modelled with different elements.

its maximum values during impacts. Here, larger rotation angles before impact result in larger contact forces. These observations qualitatively agree with the findings from the analytical model FRMCS [78]. Furthermore, the maximum contact force predicted by the two models is in good agreement.

Figure 4.10 shows the comparison of the normal stress (σ_{zz}) time history evaluated at locations P1 and P2, when the system is subjected to the ground acceleration shown as Excitation A in Figure 4.9. Figure 4.10 further shows, as was the case for the maximum force in Figure 4.9, that the occurrence of the maximum stress in magnitude coincides consistently with impact, i.e., around intervals for which the rotation is close to zero in Figure 4.9.(a).

Figure 4.10.(a) shows for point P1 that the model that uses Euler-Bernoulli beam elements severely underestimated the maximum stress response by 145.3% as well as the initial stress response near the bottom of the superstructure. The initial stress response (at zero time) predicted by the beam model is equal to the weight of the superstructure above 0.3 m height, divided by the cross-sectional area. This is notably different from the tetrahedron model stress, where stress localisation is evident, due to the presence of the rocking feet.

The vertical stress response at point P2, 1 m high from the base, is shown in Figure 4.10.(b). Here, the beam model predicted the same initial stress response as the tetrahedron model did, and the stress magnitude is equal to the weight of the su-

perstructure above 1 m divided by the cross-sectional area. Furthermore, contrary to the large discrepancies observed at P1, the beam model now overestimates the maximum response only by 6.5%. Lastly, by comparing the tetrahedron model response in Figures 4.10.(a) and (b), one can see that the maximum stress magnitude at P1, 0.3 m away from the contact feet, is 2.47 times larger than that at, P3. The stresses near the contact zone, as predicted by the tetrahedral elements, vary in a way that cannot be captured by Euler-Bernoulli theory. However, for areas sufficiently away from the contact zone (e.g. above 1m height), the Euler-Bernoulli assumptions yield more consistent predictions with the tetrahedral models.

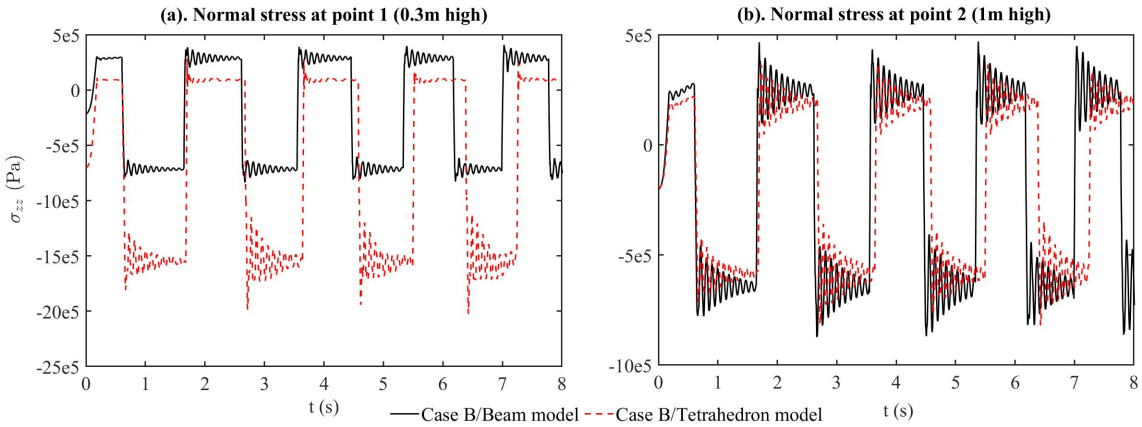


Figure 4.10: Comparison of stress response of Case B modelled with different elements.

To understand the noticeable prediction difference at different heights as well as the large decrease of stress response between 0.3 m and 1 m, the cross-section normal stress distribution at 0.3 m, 1 m and 4.6 m heights during impact, are presented in Figure 4.11. The coloured surfaces represent the tetrahedron model response, while the semi-transparent black surfaces represent the beam model response. For the ease of presentation a colour bar is also used to further indicate the stresses of the tetrahedron-based model. Firstly, Figure 4.11.(d) shows the global states near the examined time instance for the tetrahedral model. The vertical purple line highlights the examined time instant. At this instant, the left corner foot starts to contact with the support medium with the contact force sharply increasing from zero. At the same time, the right corner foot starts to leave the support but is still in contact since the contact force is not zero yet. These observations indicate that the examined response occurs during the impact window, where the contact forces are large. Secondly, Figure 4.11.(a) demonstrates the normal stress distribution at the height of 0.3 m. It clearly shows that the cross-section normal stress distribution is nonlinear near the base

where contact happens. Large compressive stress concentrates around the impacting left feet. This stress concentration, and the inability of the Euler-Bernoulli beam theory to describe such a phenomenon within a cross-section, explains why the beam model underestimates stresses as was observed in Figure 4.10. (a). Then, Figure 4.11.(b) shows the stress distribution at 1 m height. It can be seen that the stress distribution within a cross-section has a planar shape. This confirms that the depth of the nonlinear stress zone is confined within the first meter from the contact surface along the height of the body. Finally, when reaching the vertical distance of 4.4 m from the contact surface, the cross-section starts to warp. The warping is most evident at 4.6 m high as presented in Figure 4.11.(c). The warping likely indicates the presence of elastic stress waves during impact. In summary, while it was shown in Figure 4.9, that it is sufficient to use the beam model for stability analysis, it is not conservative to use beam models for an analysis that tries to predict the maximum stresses occurring within the body, which are expected to occur, as in this example, near the contact surface. While this was perhaps expected, what should further be noticed is that there is a significant area of the column for which the stresses cannot be sufficiently described using Euler-Bernoulli beam theory. Therefore, tetrahedra elements rather than beam elements are used in the following investigations.

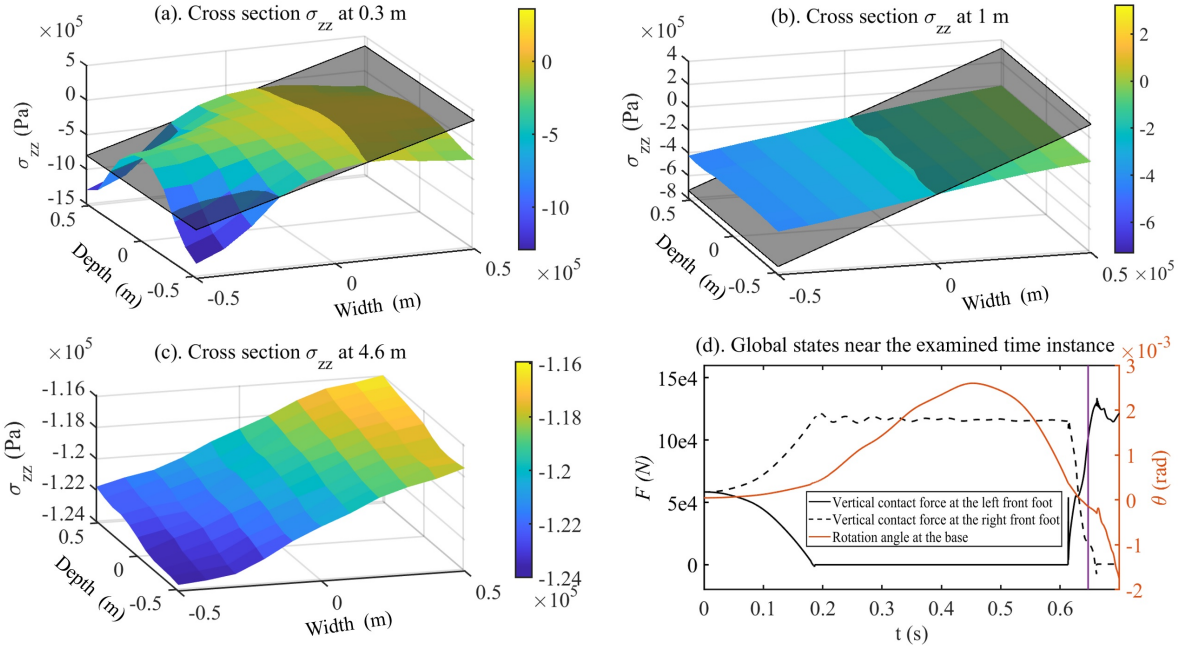


Figure 4.11: Cross-sectional normal stress distribution at different heights at an examined time instance. The semi-transparent surface is the Euler beam stress distribution; the purple line represents the examined time instant of 0.6472s.

4.8 Influence of the structure flexibility on the rocking response

4.8.1 Free vibration evaluation

Free vibration tests are conducted with Case A (stiff column), Case B (intermediate stiff) and Case C (soft column) to investigate the influence of the flexibility of the structure on the rocking response. The column is right above the ground surface, and displaced to 0.03 rads (1.72 degrees) about the left contact corner while all the elastic states are zero (i.e., zero contact spring deformation and zero column deformation). In this way, the three cases have the same potential energy at the instance of release. The column is then released from the initial condition and the response is recorded. In addition, one extra test is conducted on Case D to see the difference in response between a rigid column and a stiff column. The results are shown in Figure 4.12 and Figure 4.13.

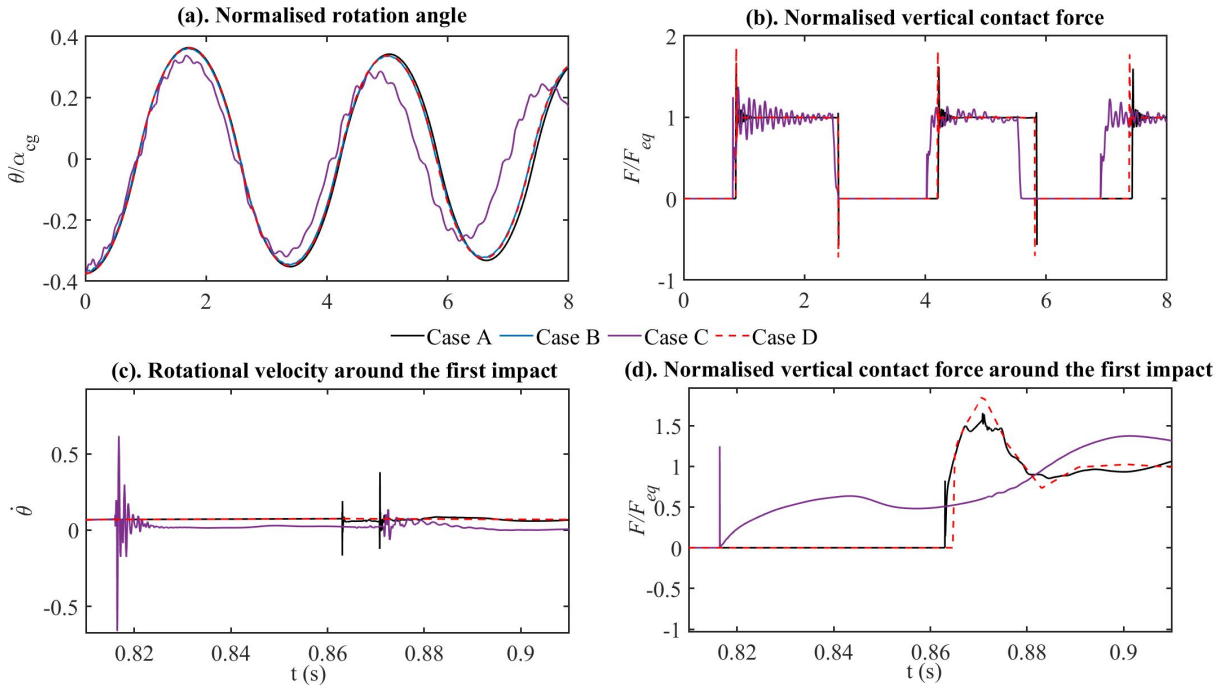


Figure 4.12: Comparison of global free vibration response of Case A (stiff), Case B (intermediate stiff), Case C (soft) and Case D (rigid) column.

Figure 4.12 shows the global response of the three configurations. Figure 4.12.(a) demonstrates that the intermediate stiff, the stiff and the rigid column share very similar rotation angle response, but the response of the soft column is noticeably smaller.

This observation clearly suggests that the column flexibility has non-negligible influence on the rotation angle response. Figure 4.12.(b) presents the vertical contact force response at the right bottom foot in Case A, Case C and Case D. The force is normalised to the static vertical contact force at each corner when the structure is in the unstable equilibrium position; mathematically, $F_{eq} = mg/2$. This figure shows that the maximum vertical contact force occurs during impact. The contact force varies significantly depending on the column flexibility: the softer the structure is, the smaller the maximum vertical contact force is. In their previous study [78], the authors observed that the maximum vertical contact force is linearly proportional to the pre-impact rotational velocity when sliding is negligible. Therefore, the force reduction effect observed for the more flexible structure may be partially due to its different pre-impact rotational velocity . To see if this is the case, the rotational velocity and the vertical force response are examined around the first impact in Figures 4.12.(c) and (d). It can be seen from Figure 4.12.(c) that the three cases share very similar pre-impact rotational velocities before the first impact. Despite that, Figure 4.12.(d) shows that the soft column experiences the smallest vertical contact force during impact, followed by the stiff and the rigid column. Therefore, the force reduction effect observed in Figure 4.12.(b) can be attributed to the influence of different superstructure flexibilities.

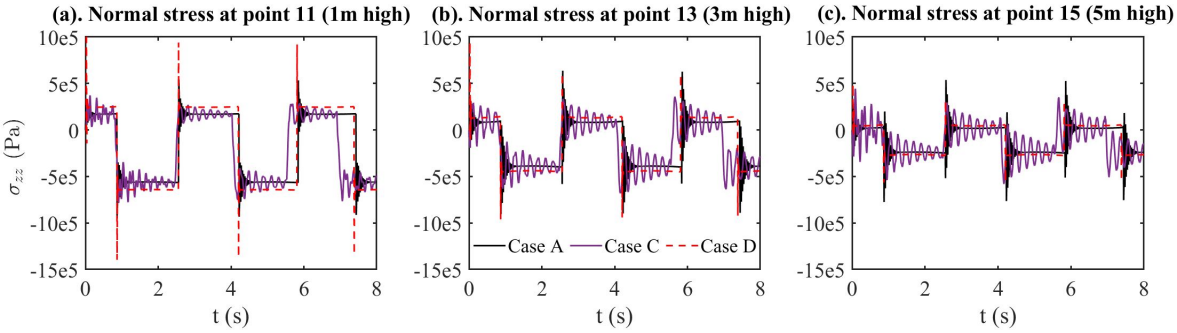


Figure 4.13: Comparison of stress response in free vibration of Case A (stiff), Case C (soft) and Case D (rigid) column.

Figure 4.13 shows the normal stress, σ_{zz} , response at three points in Case A, Case C and Case D. They are all in the middle of the right surface but located at different heights (i.e., P11, P13, P15 and P18) as shown in Figure 4.4. The stress distribution in Case D (rigid column) is approximated using the Euler–Bernoulli beam theory, given by:

$$\sigma_{zz} = \frac{N}{A} + \frac{My}{I},$$

where N is the axial force, M is the bending moment, A is the cross-sectional area, I is the moment of inertia, and y is the distance from the neutral axis. Firstly, Figures 4.13.(a) to (c) clearly show that the stress changes during impact. Furthermore, the maximum stress magnitudes are observed during impact for all columns, which agrees with earlier free vibration observations. In addition, it can be seen that the maximum magnitude of the normal stress decreases as the distance along the z axis from the contact surface increases; the further away from the base, the smaller the stress magnitude is. Secondly, Figures 4.13.(a) and (b) show that the magnitude of the maximum stress decreased for a softer column when compared to the stiffer column, which again agrees with the earlier observation on the maximum vertical contact force. This suggests that the superstructure flexibility has influence on the stress response and a softer superstructure may result in a smaller maximum stress response (however, this reduction effect could be compromised by complex superstructure behaviour induced by pulse excitations as presented in the following pulse excitation studies). Finally, it is worth noting that in Figure 4.13.(c), the magnitude of the maximum stress of the rigid column is on par with that of a soft column, and they are both smaller than that of the stiff column. This suggests that the superstructure flexibility has influence on the decay rate of the maximum stress along the height.

4.8.2 Single cycle pulse evaluation

Compared to the free vibration scenario, ground acceleration input is likely to excite more noticeable structure lateral deformation before impact and hence exposing the influence of structure flexibility on the rocking response under more complex structure behaviour, which will be shown to be different from what observed in the previous free vibration section. Two single cycle pulse horizontal ground accelerations with the same frequency, but different amplitudes are applied to Cases A to C. The results are presented in Figure 4.14.

The first column of Figure 4.14 ((a) and (c)) shows the response under a large amplitude pulse excitation, while the second column ((b) and (d)) under a small amplitude excitation. In particular, Figure 4.14.(a) shows that the soft column has the smallest rocking angle among all cases, which is in line with what was observed in the free vibration tests. However, the intermediate stiff column response is noticeably smaller than the stiff column response, which is not seen in the free vibration test. Considering all the cases, Figure 4.14.(a) suggests that a softer column could result in a smaller maximum rotation angle response under large pulse excitation and hence

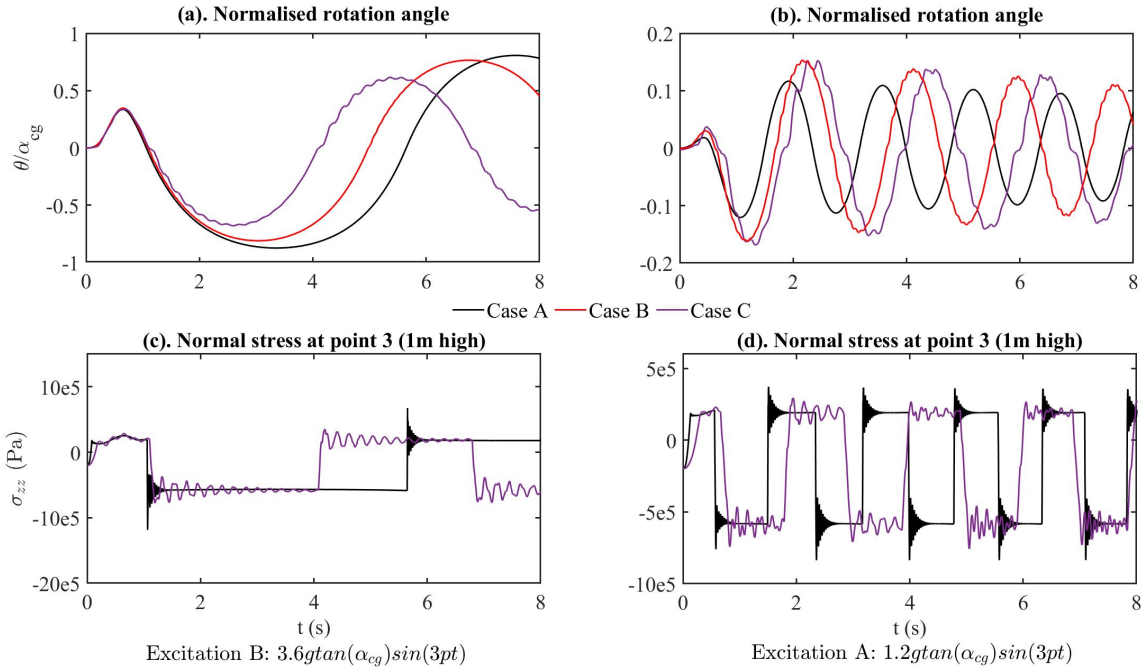


Figure 4.14: Comparison of single cycle pulse response of Case A (stiff), Case B (intermediate stiff) and Case C (soft) column.

be more stable. This inference will be checked later in **Section** 4.8.3 with stability diagrams. However, under the small amplitude excitation, Figure 4.14.(b) shows that the stiff column has the smallest maximum rotation, followed by the intermediate stiff and the soft column cases. This trend is exactly opposite to what observed under the large amplitude excitation and in the free vibration scenario.

Figure 4.14.(c) shows that the soft column in general has a smaller stress response than the stiff column. More specifically, the maximum stress of the soft column is 1.5 times smaller than that of the stiff column. These observations are in line with those made in the free vibration scenario. Although this trend still holds under small amplitude excitation as shown in Figure 4.14.(d), the difference in the maximum stress between the two cases is much smaller; especially around the first impact, the soft column has almost identical maximum stress as the stiff column does. To explore the reason, readings on the rotational velocity response are checked and, it is found that right before the first impact, the rotational velocity of the soft column is 1.32 times larger than that of the stiff column. Based on this, a possible explanation for the very similar maximum stress response is that while a softer column itself has the tendency to reduce the stress response as suggested by the free vibration tests, the larger pre-impact velocity has the tendency to increase, together resulting in a competing effect.

4.8.3 Stability analysis

The stability comparison plots are shown in Figure 4.15, where the horizontal axis corresponds to the frequency of a single cycle sinusoidal pulse acceleration and the vertical axis the amplitude. The range of the single cycle pulse ($A\sin\omega t$) considered is: $A = [0.2-10]g\tan(\alpha_{cg})$ and $\omega = [0.2-4.4]p$. Three cases are considered: Case B, Case C and Case B modelled with beam elements. Comparing between the three cases are insightful: (i) the comparison between Case B and Case C reveals the influence of the column flexibility on the stability, and (ii) the comparison between Case B modelled with tetrahedral elements and Case B modelled with beam elements shows the influence of different modelling approaches on the stability.

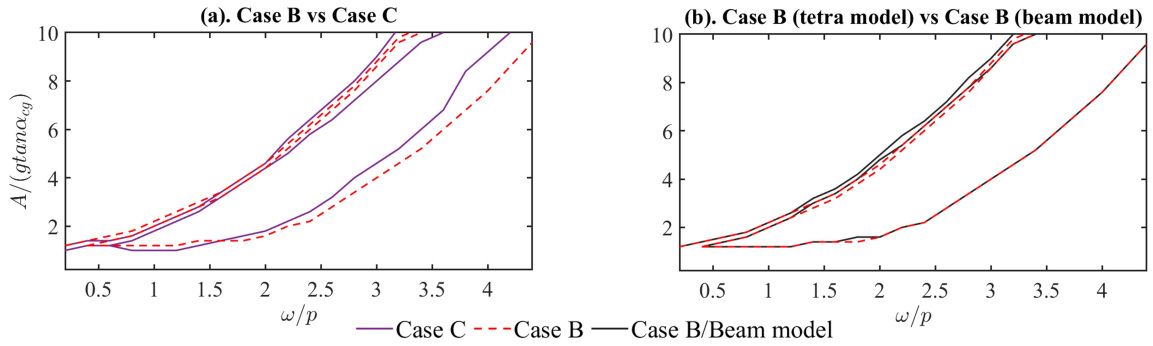


Figure 4.15: Comparison of stability plots for three different cases.

Figure 4.15.(a) shows that the soft column has a smaller Mode I overturning area than the intermediate stiff column, which agrees with the observation from previous single cycle pulse studies. However, earlier Mode I overturning also occurs in the low frequency and low amplitude region for the soft column. These observations are in line with the findings from Acikgoz and DeJong [36]'s analytical singe mass oscillator model, and the FRMCS analytical model [78]. The Mode II overturning boundary of the soft column appears earlier in the low frequency region, then as the frequency becomes larger, it appears later than the intermediate stiff one does. Figure 4.15.(b) shows that the beam model can well reproduce the Mode I overturning zone of the tetrahedron model, but a small region of unconservative results is present between pulse frequencies from 1.5p to 2p. This result generally complies with the observations made in **Section** 4.7. On the contrary, the beam model overestimates the Mode II overturning boundary for a wide range of pulse frequencies.

4.8.4 Sliding case demonstration

To demonstrate the ability of the framework to incorporate the effects of sliding in the response, Case B and Case B on a low-grip surface ($\mu = 0.15$) are subjected to sinusoidal pulse Excitation A (amplitude of $1.2g \tan \alpha_{cg}$, $\omega = 3p$), and the global response is compared in this section.

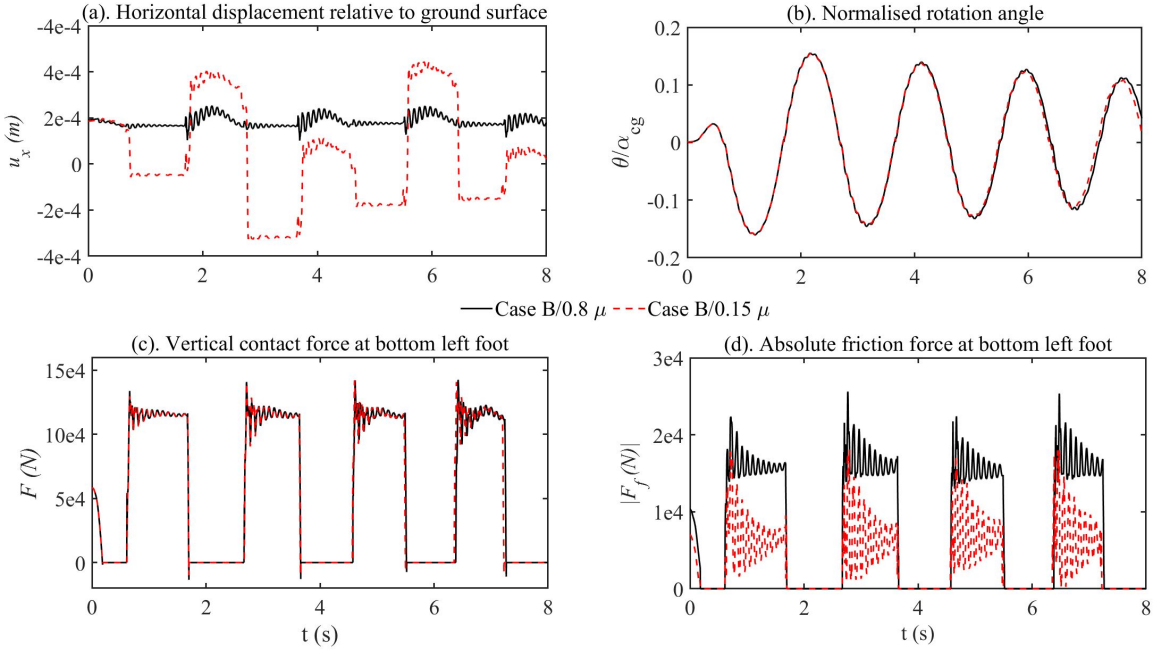


Figure 4.16: Comparison of global response on high-grip surfaces to low-grip surfaces.

The results are shown in Figure 4.16. Figure 4.16.(a) presents the horizontal displacement of the bottom left rigid surface relative to the ground surface. It shows that there were sudden and relatively large changes in the displacement magnitude on a low-grip surface, suggesting intervals during which the corner is sliding. By contrast, the displacement response on a high grip surface shows a consistent oscillatory pattern and, no sudden change in the displacement was observed. This demonstrates the capability of the proposed framework to capture sliding motion, although the sliding is not significant in the case studied. Figure 4.16.(b) compares the rotation angle response. First, it can be seen that the difference between the two responses are negligible. This suggests that, the present amount of sliding did not noticeably influence the rotation angle. Secondly, by considering Figure 4.16.(a) and Figure 4.16.(b) together, one can see that the sliding occurred every time when the rotation angle is around zero, where the corner foot is about to contact with or leave the support. A similar observation was made in the previous studies using the analytical model

FRMCS. Figures 4.16.(c) and (d) compare the support force response; the absolute friction force in Figure 4.16.(d) is the magnitude of the total friction force, consisting of one in the x direction and another one in the y direction. Figure 4.16.(c) shows that the vertical contact force response on the two surfaces are very similar. In contrast, it can be seen from Figure 4.16.(d) that the friction force response on the low-grip surface is generally smaller than that on the high-grip surface; more specifically, the maximum response decreases by 30%. These observations agree well with the earlier FRMCS finding that a small amount of sliding has negligible influence on the vertical contact force response but can lead to a large reduction in the horizontal contact force response.

4.9 Modelling of complex structures

In this section, the experiment steel frame tested on a shake table by Clough and Huckelbridge [77], which was allowed to uplift, is examined. The test frame is modelled using the generalised framework to demonstrate its ability to consider more complex structures than the ones examined earlier.

The test frame used in the Clough and Huckelbridge experiment was a single-bay, three-story steel frame built from rolled A36 steel. A photo of the test frame is shown in Figure 4.17.(a). The height of the test frame is 17'5" (5.31 m), the bay width is 12' (3.66 m) and the distance between two frames is 6' (1.83 m). An 8000 lbs (3628.74 kg) weight is placed on each floor to model the dead load. These details and the size of different components in the test frame can be found in Figure 4.17. (b). The uplift mechanism is placed around the column base. It included vertical roller bearings to prevent horizontal displacements, while providing negligible resistance to uplift motion, and neoprene impact pads underneath the column to protect the contact face.

Using the generalised framework, the test frame is modelled with beam elements and the contact is modelled with the discrete elements. Craig-Bampton reduction is not applied, to remove its effects from the results of this section. The beam elements have the same properties as the physical girders and the columns; a uniform modal damping ratio of 5% is assumed and applied to each component. For contact elements, the vertical contact spring stiffness is 7×10^6 N/m to match that of the impact pads, while the damping coefficient is calibrated to 9.9×10^4 N/(m/s) to match the test results. The stiffness, the damping coefficient and the coefficient of friction of the horizontal contact elements are calibrated to 2.9×10^8 N/m, 1.05×10^6 N/(m/s)

and artificially as high as 10^{10}, respectively, to prevent sliding as much as possible to approximate the horizontal constraint at the column base. The Simulink model of the test frame is shown in Figure 4.17. (c). The discrete contact elements are attached to the column base (which are not shown in the figure). The input signal, which is along the width of the frame, for simulations is obtained by digitalisation from the acceleration time history graph of the shake table provided in the paper, which approximated the amplified N-S component of the 1940 El Centro earthquake with a PGA of 0.71g.

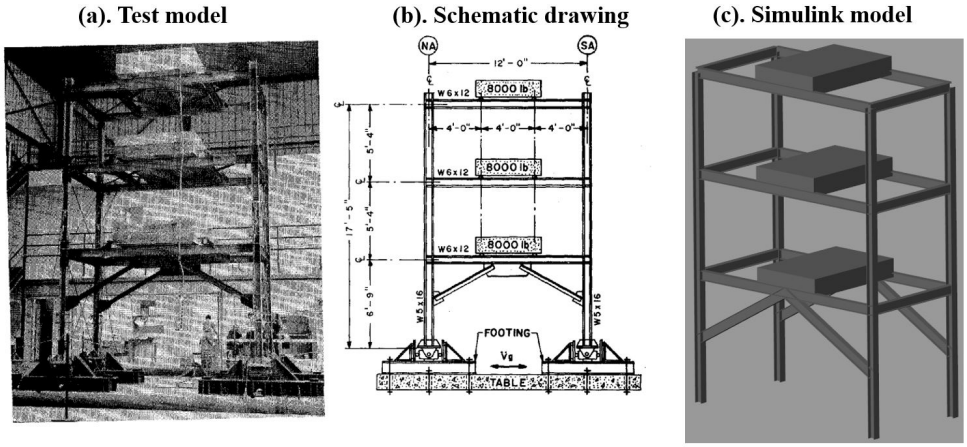


Figure 4.17: The tested steel frame and its Simulink model.

Figure 4.18 shows the comparison between the simulation and the experiment results. The comparison of the vertical displacement of the column relative to its static equilibrium position is shown in Figure 4.18.(a) and, the comparison of the horizontal displacement of the third floor relative to the shaking table is shown in Figure 4.18.(b). Despite efforts to prevent horizontal motions to approximate the uplift mechanism, the last two seconds in Figure 4.18.(b) showed there is an 1.1 in (0.028 m) residual displacement, which could be due to sliding despite the efforts, in the simulation. This not surprising since the Columb friction law employed in the contact elements requires normal forces to develop friction force. The vertical contact spring and damper cannot develop normal forces instantly at the moment when the column base contacts the support, so a small amount of sliding is inevitable. Aside from that, it can be seen from Figure 4.18 that the simulation well reproduced the trend of the experiment results. It is expected that with better known contact properties and input signal, the model should produce results in more agreement with the experimental ones.

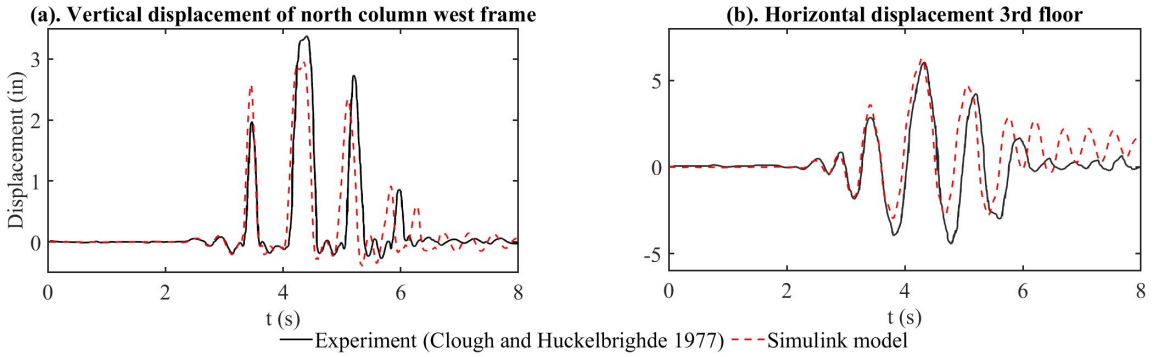


Figure 4.18: Comparison of displacement response between the Simulink prediction and the experiment result.

4.10 Capability for three-dimensional rocking response

In the previous numerical studies, the ground accelerations are along the direction of the width of the superstructure (i.e., along the x direction in the coordinate system defined in Figure 4.5), and this results in responses that exhibit 2D behaviour. However, it should be noticed that the proposed framework does not impose any kinematic constraint on the states, and therefore it can handle cases where the systems response is three-dimensional. To demonstrate the capability, a single cycle sinusoidal pulse-type ground acceleration with frequency of $3p$ and amplitude of $3g \tan \alpha_{cg}$ is applied at an attack angle of 30° to the Case B configuration. The bottom face of the column is modelled as rigid to reduce computational cost, because the stress concentration due to contact near the bottom surface is not the focus. In addition, the top surface is modelled as rigid as well for the ease of presenting experiment results. The global displacement response relative to the ground surface of the top surface and the local deformational response of the centre point on the top surface are presented in Figure 4.19. It was found that 75 fixed-interface modes are needed for the deformational response of the centre point to converge, which is much more than what was needed for the two-dimensional like response (i.e., 26 fixed-interface modes for stress convergence). However, because the bottom surface is modelled as rigid, the overall computational cost is not high; each analysis can be completed in a few minutes. Definitions of coordinate direction can be found in Figure 4.5, and the rotations are reported in extrinsic Euler angles with the order of X-Y-Z.

The first two rows of Figure 4.19 show that the six global responses of the top surface. It can be seen that all six degrees of freedom are clearly mobilised, demon-

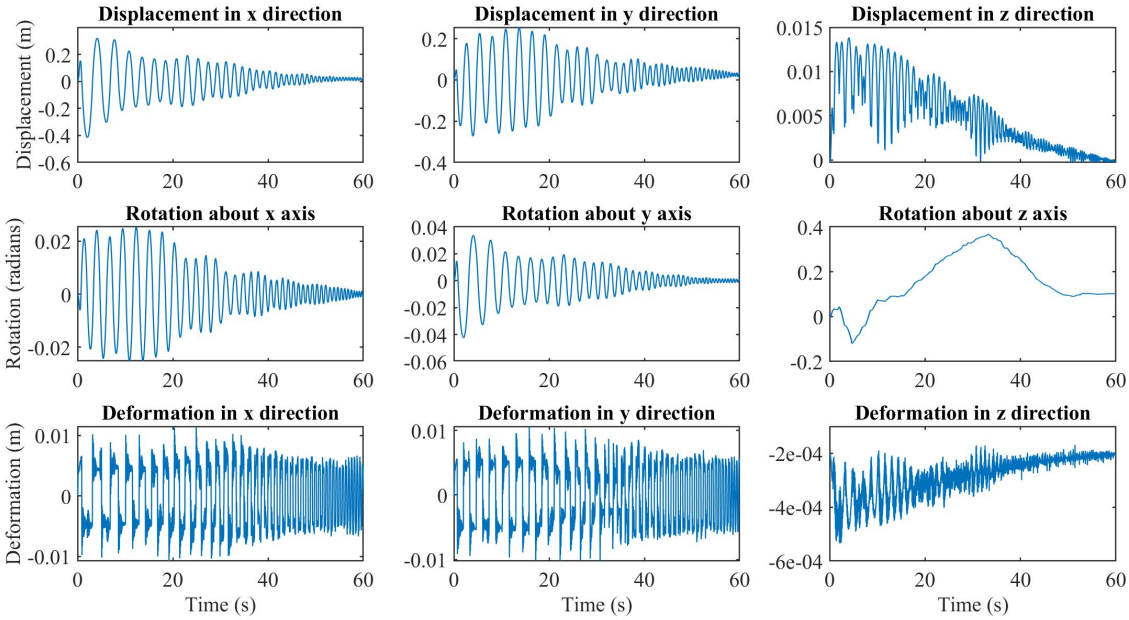


Figure 4.19: Response of Case B to pulse type ground acceleration with a 30° attack angle

strating the three-dimensional nature of the response. In fact at the end of the response, there is a permanent twist of the body with respect to the vertical axis z of 0.1 rad. The last row shows the local deformational response of the centre point relative to the body reference, which in this case is the rigid body configuration defined by the orientation and movement of the bottom surface where the FFR is placed. It can be seen clearly that the deformational responses are non-zero. This demonstrates the flexibility of the superstructure and shows that deformations occurred during the rocking response. Therefore, this example shows that the framework is able to handle three-dimensional rocking problems for flexible rocking body.

4.11 Conclusion

This chapter developed a generalised framework for modelling the rocking of flexible structures on deformable support media, implemented in SIMULINK.The contact interface is represented with concentrated springs, whose constitutive relationships allow for modelling the response of the rocking body without neglecting the contributions of sliding and free flight. Finite elements in a floating frame of reference are used to model the small elastic deformations of the superstructure while considering geometric nonlinearity. This representation allows for modelling the stress in the

contact zone and a range of structural configurations. The Craig-Bampton reduction method is used to represent the superstructure to improve computational cost.

Stability analyses using the framework showed excellent agreement with the analytical FRMCS model under stiff-support conditions. Subsequent analyses demonstrated that beam-element model reproduces the stability diagram but substantially underestimate stresses near contact zones compared to a tetrahedral-element model for a flexible column-like structure, and the stress response far from the contact zone is also different. Numerical results of the tetrahedral-element model revealed that softer columns reduce the Mode I overturning area, yet tend to overturn earlier at low frequencies, consistent with analytical observations. A softer column also reduces stress demand during free vibration but could experience larger pre-impact velocities during pulse excitation, partially offsetting the stress reduction. Allowing limited sliding was shown to decrease frictional force demand markedly, while having little influence on the normal contact forces. Finally, the framework successfully reproduced the experimental response of an uplifting steel frame and was shown to handle fully three-dimensional rocking motions, confirming its versatility and capability to model a wide range of flexible rocking structures.

Chapter 5

Experimental investigations of the stability and the contact force response of flexible body rocking and sliding on deformable media

5.1 Introduction

The literature review indicates that the experimental studies conducted to date have shown that lateral flexibility, support deformability, and sliding motion each have a significant influence on the rocking response. However, no experimental work has yet examined their combined effects. In addition, measuring complete states, including velocities, is important for understanding impact behaviour, particularly in relation to the coefficient-of-restitution-based impact models commonly adopted for stiff support media. Furthermore, several experiments have reported damage to rocking corners due to contact forces during impact. Measuring these forces remains challenging because contact-based sensors can alter interface properties and thus modify the system response. Finally, the investigations in **Chapter** 3 using the proposed analytical model predict large contact forces during impact. Experimental measurement of these forces is therefore essential for validating the model's findings.

To address these limitations, this chapter experimentally investigates the influence of support deformability, rocking-body lateral flexibility, and sliding on the rocking response. An experimental setup incorporating a high-speed digital image correlation system operating at 3000 Hz and accelerometers sampling at 18,000 Hz was used to obtain high-frequency measurements. A new non-contact method based on an unscented Kalman filter is proposed to estimate total contact forces during rocking without altering the contact interface. The approach was verified numerically and

showed the necessity of combining DIC and accelerometer data to avoid noise amplification. Stability tests were performed on flexible slender specimens with varying support deformability and surface conditions, and pulse excitation tests were conducted on stocky configurations with varying lateral flexibility, support deformability and surface conditions.

Section 5.2 presents the experimental setup, including the rocking specimen, the support and surface conditions, and the measurement systems that will be used, as well as the details of the excitation schemes and testing programme. **Section** 5.3 describes the instrumentation and data acquisition systems, focusing on the high-speed DIC system, accelerometers, and their synchronization. **Section** 5.4 outlines the experimental procedure, detailing the pulse and stability tests. **Section** 5.5 introduces the proposed unscented Kalman filter used for estimating contact forces, followed by **Section** 5.6, which numerically verifies the filter using synthetic data generated by the FRMCS model. **Section** 5.7 presents the experimental stability test results, while **Section** 5.8 reports the pulse test results, including analyses of rocking, sliding, and contact force behaviour under different configurations. **Section** 5.9 compares the experimental estimations with the FRMCS predictions to evaluate model accuracy and damping representation. Finally, **Section** 5.10 summarises the key findings and discusses their implications in flexible rocking systems.

5.2 Experimental setup

The experimental setup comprises a rocking specimen, variable support conditions, and measurement system consisting of accelerometers and a Digital Image Correlation (DIC) system. This set up is based on the setup developed by Zhu et al. (under review) [64], the detailed design of which is provided in the same paper. Modifications to the original setup include the addition of newly designed support conditions, and an upgraded high-speed DIC system. Each component in the setup is described in detail in the following sections.

5.2.1 The rocking specimen

The rocking specimen is shown in Figure 5.1(b); the x-y reference frame indicates the default orientation of the specimen. The specimen was deliberately designed to correspond to the parametric representation illustrated in Figure 5.1(a), which follows the analytical model proposed in [42]. A schematic drawing of the specimen is presented in Figure 5.1(c). The specimen comprises a top mass–spring–rail assembly

(highlighted in red in Figure 5.1) and a stiff shelf structure. The top assembly can be positioned at different elevations on the shelf structure, allowing variation in slenderness, and is equipped with interchangeable stiffness modules to adjust its lateral flexibility.

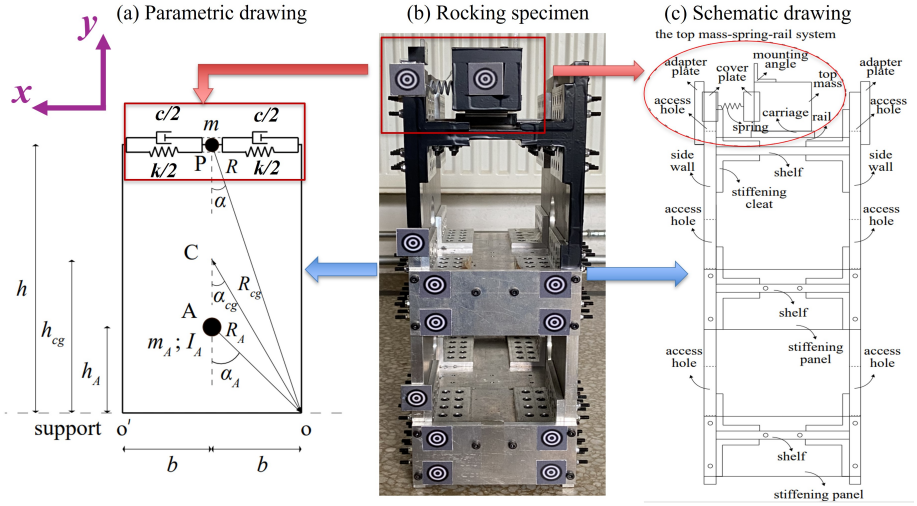


Figure 5.1: The rocking specimen.

Three specimen configurations were examined in the experiments: 1. the top mass with a stiff rod placed on the first shelf; 2. the top mass with a soft spring placed on the first shelf; and 3. the top mass with a soft spring placed on the third shelf. The corresponding parameter values for these configurations are summarized in Tables 5.1 and 5.2. The details of how the spring stiffness and damping coefficient are determined can be found in [64].

Table 5.1: Parameter values of configuration 1 and 2.

Parameter	**Value**	**Parameter**	**Value**	**Parameter**	**Value**
h (m)	0.0944	h_A (m)	0.1966	h_{cg} (m)	0.1648
R (m)	0.1163	R_A (m)	0.2082	α (rad)	0.6245
α_A (rad)	0.3353	α_{cg} (rad)	0.3939	p (s^{-1})	7.2803
b (m)	0.068	I_A (kg·m^2)	0.0766	k (N/mm)	Rigid* | 4.51
m (kg)	6.0245	m_A (kg)	13.3581	c (N·s/mm)	N.A.* | 0.0185

Note: * denotes configuration 1 where the spring on the top mass is replaced by a stiff rod.

Table 5.2: Parameter values of configuration 3.

Parameter	**Value**	**Parameter**	**Value**	**Parameter**	**Value**
h (m)	0.3844	h_A (m)	0.2019	h_{cg} (m)	0.2586
R (m)	0.3903	R_A (m)	0.2130	α (rad)	0.1751
α_A (rad)	0.3249	α_{cg} (rad)	0.2572	p (s^{-1})	5.8754
b (m)	0.068	I_A (kg·m^2)	0.0412	k (N/mm)	4.51
m (kg)	6.0245	m_A (kg)	13.3581	c (N·s/mm)	0.0185

5.2.2 The support condition

Two types of support materials and three types of contact surfaces were used in the experiments. The two support materials included a stiff medium-density fibreboard (MDF) panel, representing a rigid support medium, and a Sorbothane rubber mattress, representing a soft support. The rubber mattress originally measured 30.5 cm × 30.5 cm × 1.5 cm and was cut into various shapes for experimental use.

Contact surfaces are placed over the support materials. The three contact surface types considered in this study are: (1) 60-grit sandpaper, representing a high-friction surface; (2) a poly-tetrafluoroethylene (PTFE) sheet, representing a low-friction surface; and (3) a composite surface combining both sandpaper and PTFE layers to produce a mixed-friction interface.

Together, the different support materials and contact surfaces defined four support conditions examined in the experiments: A. rigid support with rough surface; B. soft support with rough surface; C. soft support with smooth surface; and D. soft support with combined surface. Support condition A was previously developed in [64], while the new support conditions B-D are illustrated in Figure 5.2. Support condition D features a semi-slippery surface and was used to investigate the influence of sliding on the rocking response. Support condition C was not adopted in the pulse tests because these tests were conducted on rocking configuration 2, representing a stocky and flexible rocking body. During preliminary experiments, it was found that for such stocky, flexible specimens, achieving simultaneous rocking and sliding motion with condition C (a low-friction surface) was difficult—the specimen tended to slide without observable rocking. Therefore, a semi-slippery surface (condition D) was selected to enable both rocking and sliding motion.

The final experimental setup is illustrated in Figure 5.3. The rocking specimen is mounted on variable support conditions, which are anchored to the shake table. The system is subjected to excitations applied along the x-direction. Displacements and

(a) Support condition B (b) Support condition C (c) Support condition D

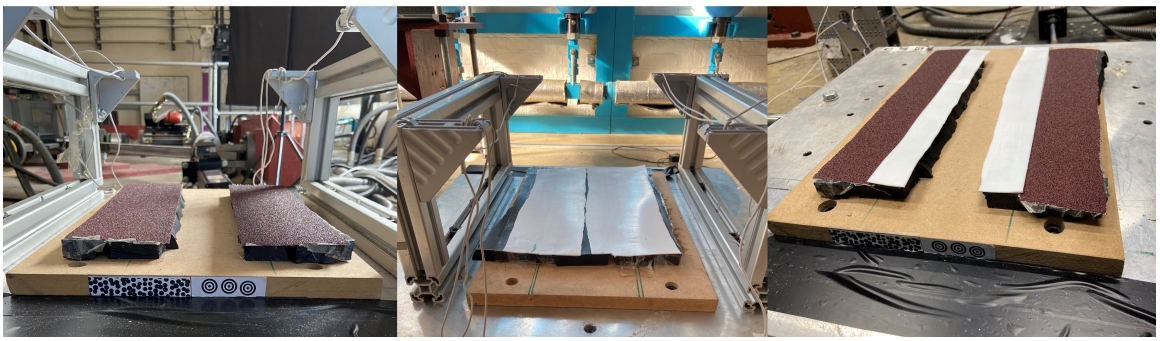


Figure 5.2: Different support conditions (condition A is not shown because photo was not taken).

accelerations are captured using the DIC system and accelerometers, respectively. The instrumentation details for them are provided in the following sections.

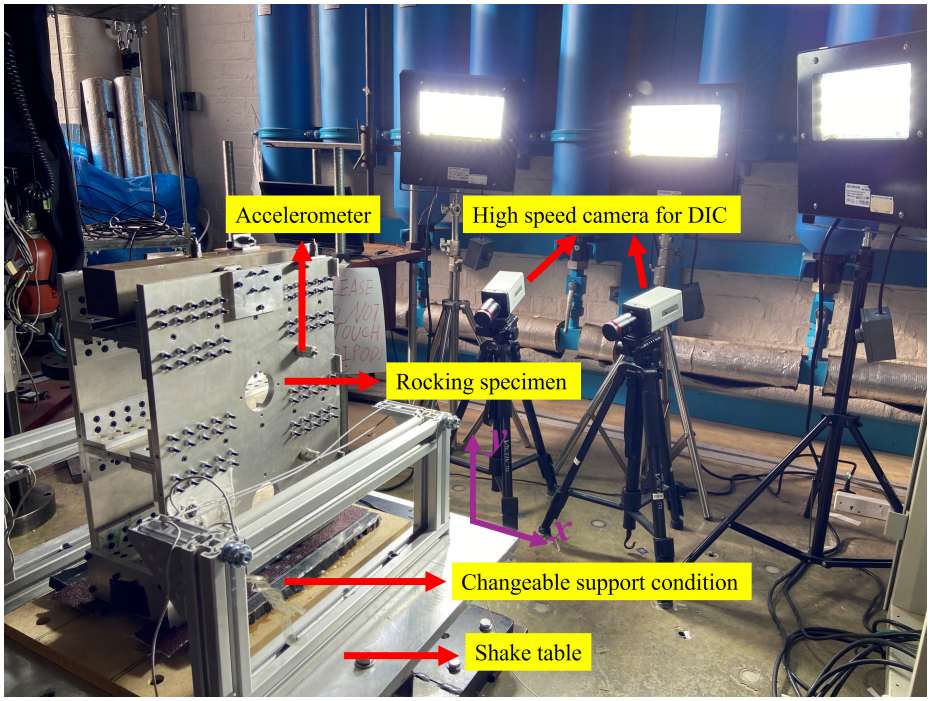


Figure 5.3: The experiment setup.

5.3 Instrumentation

High speed cameras and accelerometers were used to record the rocking specimen response at high sampling rates. In particular, local Digital Image Correlation (DIC) algorithms were used to measure 3D displacements in specific regions of interest on

the rocking body, while the accelerometers were used to measure uniaxial and triaxial responses at various points. The high sampling rates were necessary to investigate the impact response of the investigated rocking body.

When used alone, the DIC system is susceptible to high-frequency noise amplification, while the accelerometers are prone to low-frequency drifts. Therefore, the DIC system and accelerometers were employed complementarily in this study to overcome the individual limitations. The following sections introduce the instrumentation for the DIC system and the accelerometers. As will be demonstrated later, this combination enables reliable derivation of quantities of interest such as the velocity of the rocking body and total contact force.

5.3.1 3D high speed DIC system

The high-speed stereo DIC system hardware consisted two high-speed IX cameras equipped with Kowa LM25XC 25 mm lenses, external LED light sources, and speckle patterns for target tracking. The hardware was controlled using the MatchID High-Speed Grabber software. Five regions of interest on the specimen and one region on the MDF board were selected and marked with inkjet printed speckle patterns, as shown in Figure 5.4. The dot diameter on the speckle patterns covered 6-10 pixels. The displacement of the centroid of each region was determined with respect to a stationary reference image and used for further analysis. The number of regions on the specimen were chosen to ensure that sufficient measurement information is available for state and force estimation, which will be introduced later in **Section** 5.5. The measurements were oriented such that the horizontal direction is defined along the excitation direction of the shake table whilst the vertical direction is perpendicular to the shake table horizontal plane.

A reduced field of view of 1024 $\times$ 520 pixels was adopted for the cameras. This setting allowed tracking the regions of interest during experiments while maintaining a relatively high sampling frequency of 3000 Hz. The LED light intensity was set to 80% of its maximum, to prevent over- or underexposure. The master camera was positioned perpendicular to the specimen surface with a stand-off-distance (SOD) of 0.47 m and the slave camera was angled at 26.14°. The lens aperture was set to f/5.6 and, the focus was adjusted to ensure that both the specimen and the MDF speckle planes were positioned approximately in the middle of the depth of field. To eliminate potential movement of the camera supports due to impact-induced vibrations, the camera tripods were affixed to the laboratory strong floor.

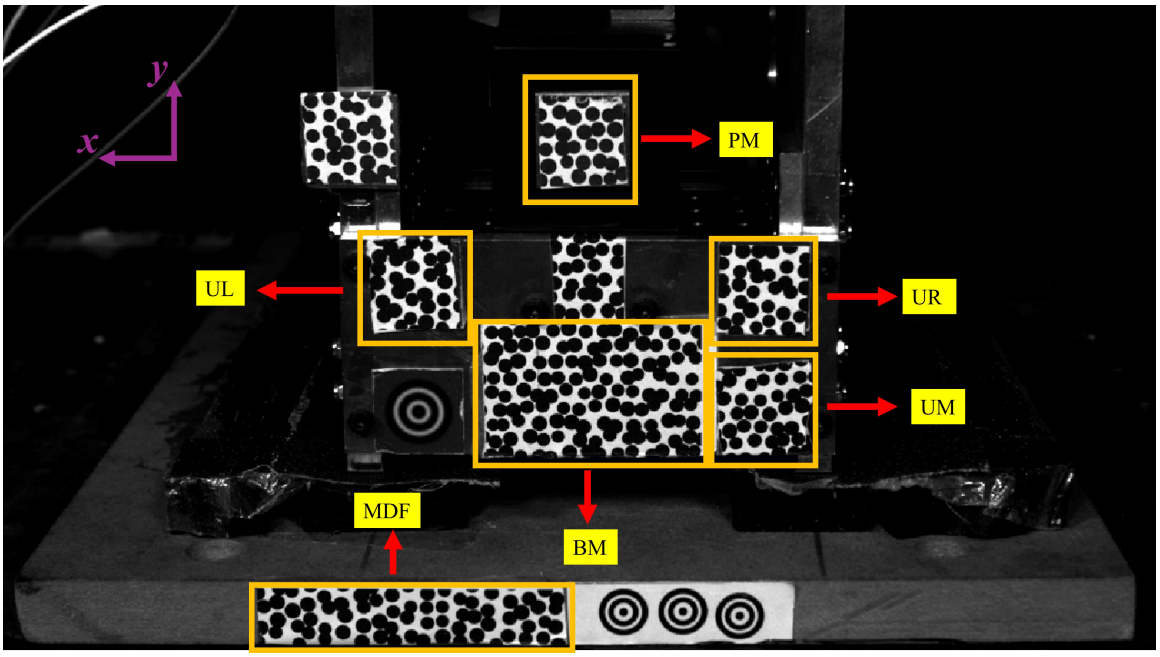


Figure 5.4: The placement of DIC speckles.

The calibration of the stereo system was performed on approximately 200 images of a standard 9 by 12 dot (diameter of 15 mm) grid calibration plate and processed with MatchID Calib, following a full-bundle technique. DIC was performed using MatchID Stereo with subset and step size set to 22 pixels and 3 pixels, respectively.

5.3.2 Accelerometers

Piezoelectric accelerometers manufactured by PCB Piezotronics and Dytran were used for the measurements. The accelerometers had sensitivities of approximately 100 mV/g or 1000 mV/g, and the sampling rate during the experiments was set to 18 000 Hz. They measured the total acceleration that is horizontal or vertical relative to the rocking specimen. In total, nine accelerometers were stud-mounted onto the specimen, as labelled in Figure 5.5. Among them, accelerometers P1 and P2 were mounted on the top mass assembly, the rest were on the bottom shelf structure.

Data acquisition was performed using a National Instruments PXIe-4492 module housed within a PXIe-1082 chassis. A custom LabVIEW virtual instrument (VI) was developed to configure the PXIe-4492 module for data collection. Within the VI, a DAQ Assistant was implemented to define the measurement type, physical channel configuration, accelerometer sensitivities, and sampling rate, along with other acquisition parameters. The VI was programmed to acquire, process, display, and

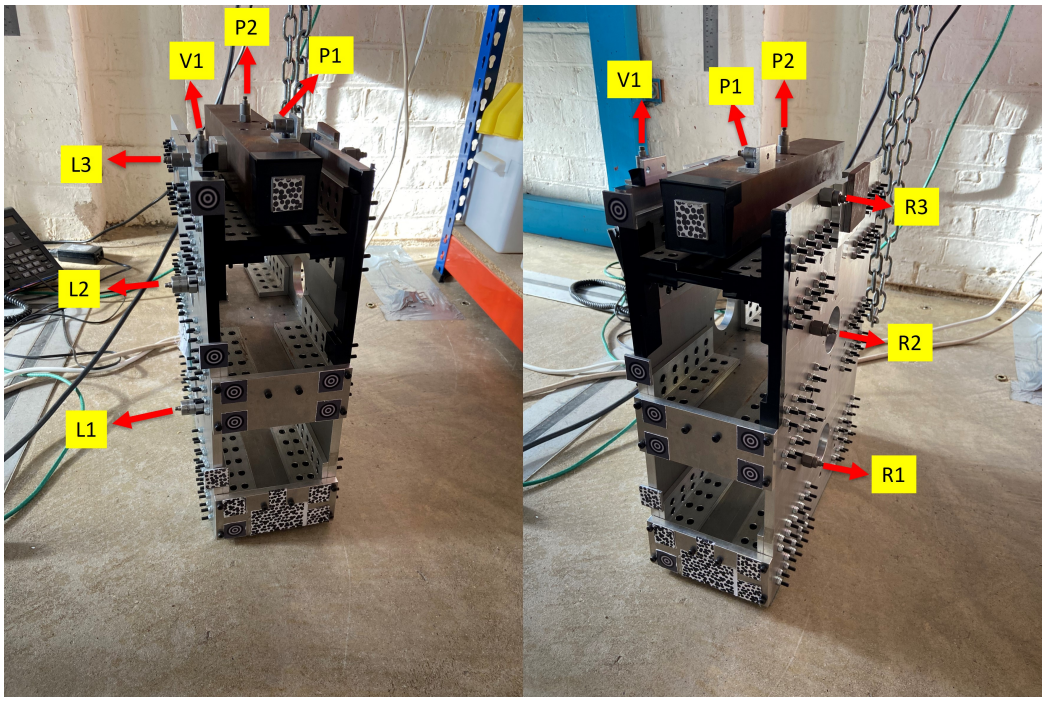


Figure 5.5: The placement of accelerometers.

store the acceleration data. Using this setup, all recorded acceleration signals shared the same sampling frequency and were fully synchronized.

5.3.3 Time synchronization between the DIC system and the accelerometers

Two issues arise when synchronizing the DIC system and the accelerometers. First, the sampling frequency of the DIC system is lower than that of the accelerometers. Second, the accelerometers begin recording earlier and continue recording longer than the DIC system. However, to apply the new Unscented Kalman Filter, the two datasets must be synchronized such that they share the same time step and have identical starting and ending time.

To accomplish this, an SCB-68A screw terminal block was used to connect the master camera of the DIC system to the PXIe-4492 module, which acquires the acceleration data. When the physical trigger of the DIC system was activated, DIC recording began, and the master camera transmitted a camera-synchronization signal at the same rate as the camera sampling frequency to the slave camera.

This synchronization signal was simultaneously transmitted to the PXIe-4492 via the SCB-68A terminal to enable starting time alignment between the two systems. A

DAQ Assistant, embedded within the same LabVIEW VI used for accelerometer acquisition, was configured to perform edge counting on this signal. The edge-counting sampling frequency was set to 100 kHz to ensure accurate capture of the synchronization signal. By aligning the timestamp of the first detected edge, indicating the onset of DIC recording, with the corresponding accelerometer timestamp, a new time zero for the acceleration data was established first, thereby aligning the starting time of the DIC and the accelerometer measurements. Then, the DIC data was linearly interpolated to match the time step of the accelerometer measurements. Finally, the acceleration data outside the recorded time length of the interpolated DIC measurements was discarded to align the ending time.

5.3.4 Measurement noise quantification

To apply the Kalman filter, the noise characteristics of both the DIC system and the accelerometers must be quantified. Noise measurements were therefore collected over a one-second interval during which the specimen was subjected to no external excitation. This procedure yielded 3000 data points for each DIC region and 18 000 data points for each accelerometer, which was deemed sufficient for reliable noise characterization. The resulting noise distributions were found to be Gaussian with zero mean. Although the noise profile is simplistic (e.g. it neglects the spatial cross-correlation in the DIC measurements and the charge leak in the piezoelectric accelerometers), it was considered sufficient for proof-of-concept testing. The estimated variances for the DIC system and the accelerometers are reported in Tables 5.3 and 5.4, respectively. The variance of the shake table (i.e., region MDF in Figure 5.4) DIC measurement is not recorded because it is not needed in the filter.

Table 5.3: Variance of DIC horizontal and vertical measurements at different centre points.

Centre point of	**BM**	**PM**	**UL**	**UR**	**UM**
Horizontal variance $(\mu\text{m})^2$	22.64	25.82	26.96	33.52	39.52
Vertical variance $(\mu\text{m})^2$	26.12	30.64	30.27	40.56	44.92

5.4 Experimental procedure

2D rocking behaviour was considered in the experiments. Therefore, the external excitation is applied along the width of the specimen. The experimental program

Table 5.4: Variance of accelerometers at different locations.

Point	**R1**	**R2**	**R3**	**L3**	**L2**	**L1**	**V1**	**P1**	**P2**
Variance $(\mathrm{m} \cdot \mathrm{m/s^2})^2$	2.69	2.18	2.37	2.45	9.27×10^{-4}	8.64×10^{-4}	2.56	2.79	2.51

consisted of two parts: (1) single-cycle sinusoidal pulse excitation, during which both displacement and acceleration responses were recorded, and (2) a stability test, in which only the frequency and amplitude of the overturning pulses were recorded. The excitations were applied using an ANCO shake table with a platform size of 600 × 600 mm. The table was driven by two Exlar Tritex linear actuators, each with a load capacity of 2 kN. During the experiment, the actuator in the out-of-plane direction was disconnected and clamped to ensure unidirectional input motion. The actuators provided a maximum stroke length of 254 mm (10 in.) and a maximum velocity of 1 m/s.

Because the shake table operates under displacement control, a displacement time history corresponding to the desired single-cycle sinusoidal pulse acceleration was used as the input command to the table. The displacement function adopted in the experiments was discussed in an earlier study by Zhu et al. (under review) [64]. In each test, the shake table remained stationary at its neutral position for 7 seconds before initiating motion according to the prescribed displacement time history that generated the target pulse acceleration. Following the excitation, the table was held stationary for an additional 10 seconds to allow all rocking motion to cease, after which it gradually returned to the neutral position in preparation for the subsequent test.

5.4.1 Pulse excitation test

A total of nine tests were conducted. The first four tests employed an 8 Hz single-cycle sinusoidal pulse acceleration with an amplitude of 2.249 g, applied to four experimental configurations: (1) specimen configuration 1 (no lateral flexibility, low slenderness) supported on condition A (stiff support with rough surface); (2) specimen configuration 1 supported on condition B (soft support with rough surface); (3) specimen configuration 2 (high lateral flexibility, low slenderness) supported on condition A; and (4) specimen configuration 2 supported on condition B.

The remaining five tests used a 3 Hz single-cycle sinusoidal pulse acceleration with an amplitude of 0.5 g, applied to the same four configurations and, additionally, to (5)

specimen configuration 2 supported on condition D (soft support with semi-slippery surface). In each test, both displacement and acceleration responses were recorded and later processed using the Kalman filter to estimate the displacement, velocity states, and total contact force.

5.4.2 Stability test

In the stability tests, the rocking specimen was subjected to horizontal ground accelerations in the form of single-cycle pulses with varying magnitudes and frequencies. The combinations of pulse magnitude and frequency that resulted in overturning were recorded. Three experimental configurations were examined: (1) specimen configuration 3 (high lateral flexibility and high slenderness) supported on condition A; (2) specimen configuration 3 supported on condition B; and (3) specimen configuration 3 supported on condition C (soft support with slippery surface).

The frequency ratio range (ω/p) of the input pulses varied from 2 to 7, with an increment of 0.2. The amplitude increment was adjusted as needed to accurately capture the overturning threshold.

5.5 Introduction to the new unscented Kalman filter

An observability-inspired unscented Kalman filter is employed in this study to estimate the total contact forces during the experiments. The filter introduces a new parameter, L, defined as the number of time steps between the occurrence of an unmeasured input and the point at which it becomes observable and can be accurately estimated. Accordingly, the filter uses measurements until L time steps later to update the estimations L time steps earlier.

The following sections present the algorithm for the case where $L = 0$, to describe the basic principles for input estimation (i.e., the total contact force). For details on the implementation and formulation of the non-zero L case, readers can refer to Chatzis et al.[84].

5.5.1 The augmented nonlinear model

Assume a discrete-time nonlinear system is given by:

$$
\begin{aligned}
\mathbf{x}_{k+1} &= f(\mathbf{x}_k, \mathbf{F}_k, t_k) + \mathbf{w}_k \\
\mathbf{y}_k &= h(\mathbf{x}_k, \mathbf{F}_k, t_k) + \mathbf{v}_k \\
\mathbf{w}_k &\sim (0, \mathbf{Q}_k) \\
\mathbf{v}_k &\sim (0, \mathbf{R}_k)
\end{aligned}
\tag{5.1}
$$

where $f(\mathbf{x}_k, \mathbf{F}_k, t_k)$ is the state transition function that predicts the states of a dynamic system. For example, equations of motion that describe the time evolution of the DoFs of a rigid body; $h(\mathbf{x}_k, \mathbf{F}_k, t_k)$ is the measurement function that maps the states of the system to the measured outputs. For example, the kinematic relationship that maps the DoFs of a rigid body to the movement of an arbitrary point on the rigid body. $\mathbf{x}_k$ is the state vector of the system, $\mathbf{y}_k$ is the output vector to be measured of the system, $\mathbf{F}_k$ is the input force vector to be identified, $\mathbf{w}_k$ and $\mathbf{v}_k$ are the process noise and the observation noise with zero mean and covariance matrices of $\mathbf{Q}_k$ and $\mathbf{R}_k$, respectively.

By treating the force vector $\mathbf{F}_k$ as part of the state with process noise $\mathbf{j}_k$ of zero mean and covariance matrix of $\mathbf{J}_k$, the discrete-time nonlinear system is augmented and becomes:

$$
\begin{aligned}
\mathbf{x}^a_{k+1} = \begin{bmatrix} \mathbf{x}_{k+1} \\ \mathbf{F}_{k+1} \end{bmatrix} &= \begin{bmatrix} f(\mathbf{x}^a_k, t_k) \\ \mathbf{F}_k \end{bmatrix} + \begin{bmatrix} \mathbf{w}_k \\ \mathbf{j}_k \end{bmatrix} \\
\mathbf{y}_k &= h(\mathbf{x}^a_k, t_k) + \mathbf{v}_k \\
\mathbf{j}_k &\sim (0, \mathbf{J}_k)
\end{aligned}
\tag{5.2}
$$

5.5.2 Initialization of the filter

The following operation is based on the augmented nonlinear model, and for simplicity the superscript 'a' in the $\mathbf{x}^a_k$ is omitted. Assume the process noise between different states is independent, the filter is initialized as:

$$
\begin{aligned}
\hat{\mathbf{x}}^+_0 &= \mathbb{E}[\mathbf{x}_0] \\
\mathbf{P}^+_0 &= \mathbb{E}[(\mathbf{x}_0 - \hat{\mathbf{x}}^+_0)(\mathbf{x}_0 - \hat{\mathbf{x}}^+_0)^\top]
\end{aligned}
\tag{5.3}
$$

the $_0$ subscript denotes the initial values, the hat symbol $\hat{}$ indicates that the quantity is an estimate. The superscripts $^+$ and $^-$ (the latter superscript to be introduced soon) denote the state posterior to and prior to the measurement update, respectively. Their roles in the filter will become clear later in the presentation. $\mathbf{x}_0$ is the initial value of the state vector, and $\mathbf{P}^+_0$ is the initial state covariance matrix, which represents the uncertainty in the initial estimates of the state ($\hat{\mathbf{x}}^+_0$).

5.5.3 General unscented transformation

There are different forms of unscented transformation to obtain the sigma points, $\mathbf{x}^{(i)}$. These points are used to provide temporal updates (prediction) for the states, the measurements and the covariance.

In this study, the general unscented transformation is used. Assume the size of the augmented state vector at time k-1, $\mathbf{x}_{k-1}$, is n, then there will be $2n$+1 sigma points and they are generated by:

$$\begin{aligned}
\hat{\mathbf{x}}_{k-1}^{(0)} &= \hat{\mathbf{x}}_{k-1}^{+} \\
\hat{\mathbf{x}}_{k-1}^{(i)} &= \hat{\mathbf{x}}_{k-1}^{+} + \left(\sqrt{(n+\lambda)\mathbf{P}_{k-1}^{+}}\right)_{i}^{\top}, \quad i = 1, \ldots, n \\
\hat{\mathbf{x}}_{k-1}^{(n+i)} &= \hat{\mathbf{x}}_{k-1}^{+} - \left(\sqrt{(n+\lambda)\mathbf{P}_{k-1}^{+}}\right)_{n+i}^{\top}, \quad i = 1, \ldots, n
\end{aligned} \tag{5.4}$$

where again the hat symbol $\hat{}$ indicates that the quantity is an estimate. The subscript i indicates the ith row of the matrix square root.

The weight of each sigma point is given by:

$$\begin{aligned}
W_m^{(0)} &= \frac{\lambda}{n+\lambda} \\
W_c^{(0)} &= \frac{\lambda}{n+\lambda} + \left(1 - \alpha^2 + \beta\right) \\
W_m^{(i)} &= W_c^{(i)} = \frac{1}{2(n+\lambda)}, \quad i = 1, \ldots, 2n \\
\lambda &= \alpha^2(n+\kappa) - n
\end{aligned} \tag{5.5}$$

W_m denotes the weight factors used for the state and measurement means, while W_c represents the corresponding weights for the covariance. The parameters α and κ control the spread of the sigma points around the state mean, and β specifies the incorporation of prior knowledge about the state distribution. α ranges from 0 to 1 and for highly nonlinear problems, it is a common practice to use large value of α (e.g., larger than 0.1). κ is normally set either to 0 or to $3 - n$. A value of $\beta = 2$ is optimal when the state distribution is Gaussian, which is normally the case for problems using Kalman filter.

5.5.4 Time update

For each sigma point $\mathbf{x}^{(i)}$, the predicted states $\hat{\mathbf{x}}^{(i)}$ and predicted measurements $\hat{\mathbf{y}}^{(i)}$ can be obtained using the nonlinear model:

$$\hat{\mathbf{x}}_k^{(i)} = \begin{bmatrix} f(\hat{\mathbf{x}}_{k-1}^{(i)}, t_{k-1}) + \mathbf{w}_{k-1} \\ \mathbf{F}_{k-1} + \mathbf{j}_{k-1} \end{bmatrix} \tag{5.6}$$

$$\hat{\mathbf{y}}_k^{(i)} = h(\hat{\mathbf{x}}_k^{(i)}, t_k) + \mathbf{v}_{k-1} \tag{5.7}$$

This data is then used to obtain the time update of the state estimate, the measurement estimate, and the state covariance:

$$\begin{aligned} \hat{\mathbf{x}}_k^- &= \sum_{i=0}^{2n} W_m^{(i)}\, \hat{\mathbf{x}}_k^{(i)} \\ \hat{\mathbf{y}}_k &= \sum_{i=0}^{2n} W_m^{(i)}\, \hat{\mathbf{y}}_k^{(i)} \\ \mathbf{P}_k^- &= \sum_{i=0}^{2n} W_c^{(i)} \left(\hat{\mathbf{x}}_k^{(i)} - \hat{\mathbf{x}}_k^-\right) \left(\hat{\mathbf{x}}_k^{(i)} - \hat{\mathbf{x}}_k^-\right)^\top \end{aligned} \tag{5.8}$$

5.5.5 Measurement update

After the time update, the predicated state estimate and covariance will be updated using the actual measurements, $\mathbf{y}_k$, at the current step to obtain a posterior state estimate and covariance:

$$\begin{aligned} \mathbf{P}_y &= \sum_{i=0}^{2n} W_c^{(i)} \left(\hat{\mathbf{y}}_k^{(i)} - \hat{\mathbf{y}}_k\right) \left(\hat{\mathbf{y}}_k^{(i)} - \hat{\mathbf{y}}_k\right)^\top \\ \mathbf{P}_{xy} &= \sum_{i=0}^{2n} W_c^{(i)} \left(\hat{\mathbf{x}}_k^{(i)} - \hat{\mathbf{x}}_k^-\right) \left(\hat{\mathbf{y}}_k^{(i)} - \hat{\mathbf{y}}_k\right)^\top \\ \mathbf{K}_k &= \mathbf{P}_{xy}\, \mathbf{P}_y^{-1} \\ \hat{\mathbf{x}}_k^+ &= \hat{\mathbf{x}}_k^- + \mathbf{K}_k \left(\mathbf{y}_k - \hat{\mathbf{y}}_k\right) \\ \mathbf{P}_k^+ &= \mathbf{P}_k^- - \mathbf{K}_k\, \mathbf{P}_y\, \mathbf{K}_k^\top \end{aligned} \tag{5.9}$$

It can be seen from Equation (5.9) that the force to be identified is treated as a state in the filter, and it is estimated during the measurement update process through the $\mathbf{K}(\mathbf{y} - \hat{\mathbf{y}})$ term.

5.6 Numerical verification of the filter

Synthetic data test is conducted to verify the filter numerically. The FRMCS model [78] is used to generate the measurements because it resembles the experiments, and

another model similar to the FRMCS model, but without contact modelling, is used in the filter for the time update. The identified force and state are compared with the benchmark results at the end of this section. The following sections elaborate the details of the numerical test.

5.6.1 The FRMCS model introduction

The FRMCS model was proposed by the authors to study the influence of support media on the rocking response of a flexible body while considering geometric nonlinearities and all motion phases during rocking, including sliding motion.

The parameters of the model are shown in the schematic drawing in Figure 5.6(a). The model consists of a top-mass oscillator of mass m_p and a rigid bottom body of mass m with a centre of mass located at point B and a mass moment of inertia about B, I_g. The bottom mass can take any shape that is bilaterally symmetric. For simplicity, it is represented as a box in the figure. The top mass m_p is connected to the bottom mass through springs and dampers, and is constrained to move laterally, in a direction parallel to the line defined by the two bottom corners ZY. When the spring is undeformed, the top mass is located at point P. The width of the bottom body is denoted as b, height as h. Its centre of mass is located at height h_b. The centre of mass of the whole body is located at point C when the body is at rest at height h_{cg}. The slenderness of the top mass, the bottom mass and the whole system are described with α_p ($\tan\,\alpha_p = b/(2h)$), α ($\tan\,\alpha = b/(2h_b)$) and α_{cg} ($\tan\,\alpha_{cg} = b/(2h_{cg})$) respectively. R_p, R_{cg} and R is the distance from points P, C, B to the either of the bottom corners. The vertical contact is modelled with tensionless springs and dampers. The horizontal contact is modelled to follow the Coulomb's friction law with frictional springs and dampers. k_v and c_v are the stiffness and damping coefficient of the vertical springs and dampers, k_f is the stiffness of the frictional spring, and c_f is the damping coefficient of the horizontal damper.

The FRMCS has five states: x, y, θ, u and $\boldsymbol{F_{fs}}$. x and y are the $\vec{I}\vec{J}$ coordinates of the centre of mass of the bottom body with respect to an absolute frame with origin, O, located on the undeformed ground surface. u is elongation of the lateral spring and describes the $\vec{i}$ coordinate of the body in the rotating $\vec{i}\vec{j}$ coordinate system with the origin at B. The rotation of the bottom body is described by θ. $\boldsymbol{F_{fs}}$ is the frictional spring force that has to be tracked to describe current states of the model. The sum of the tracked frictional spring force and the horizontal damper force is the horizontal contact force (F_{Z1} and F_{Y1}). The states (i.e., the degrees of freedom) and contact forces are shown in Figure 5.6(b).

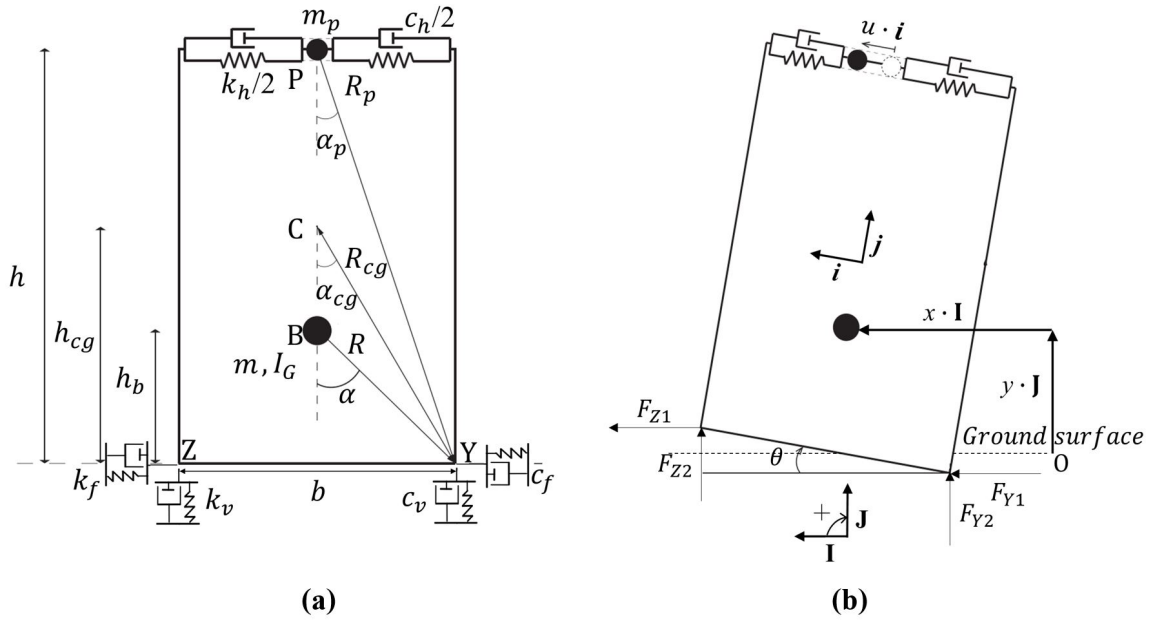


Figure 5.6: (a) Schematic drawing showing the parameters and (b) states and contact forces of FRMCS.

5.6.2 Generation of benchmark states

The synthetic data test was designed to numerically replicate the experimental pulse test using the experiment configuration (3) as described in **Section** 5.4.1, which represents a stocky, flexible body rocking on a stiff support with a rough surface (i.e., specimen configuration 2 with support condition A). The 8 Hz single-cycle sinusoidal pulse acceleration with an amplitude of 2.249 g was used. Accordingly, the FRMCS parameters listed in Table 5.5 were adopted to model the specimen configuration 2.

Table 5.5: FRMCS parameters for the synthetic data test.

Parameter	**Value**	**Parameter**	**Value**	**Parameter**	**Value**
h (m)	0.0944	h_b (m)	0.1966	h_{cg} (m)	0.1648
R_p (m)	0.1163	R (m)	0.2082	α_p (rad)	0.6245
α (rad)	0.3353	α_{cg} (rad)	0.3939	p (s^{-1})	7.2803
b (m)	0.1370	I_G (kg·m^2)	0.0766	k_h (N/mm)	4.51
m_p (kg)	6.0245	m (kg)	13.3581	c_h (N·s/mm)	0.0185

To model the support condition A, the vertical spring stiffness (k_v) and damping coefficient (c_v) were set to 5.5×10^6 (N/m) and 2.34×10^4 (N·s/m), which corresponds to a vertical vibration frequency of 120 Hz. The frictional spring stiffness (k_f) and damping coefficient (c_f) were assigned values of 1.0×10^{11} (N/m) and 1.56×10^6

(N·s/m), respectively. The static coefficient of friction (μ) was measured to be 0.67. Numerical integration was performed using a modified Runge–Kutta (4,5) pair solver, with both relative and absolute tolerances set to 10^{-8}.

5.6.3 Generation of benchmark measurements

As described in **Section** 5.3 and indicated in Figure 5.4, five regions of interest on the specimen will be monitored using the high-speed DIC system, and the displacement of the centroid of each region will be used for state determination. In addition, acceleration data from nine points instrumented with accelerometers will be used in these analyses. Because these measurement points are located at positions different from the centre of mass of the shelf structure, kinematic relationships need to be determined to compute model estimates at measurement locations using the state variables obtained in the previous time step.

The following equations express the total displacements of any point on the bottom mass ($\boldsymbol{\delta}_{p_i}$) and at the top mass ($\boldsymbol{\delta}_u$) in the fixed $\vec{I}\vec{J}$ coordinate directions as a function of the state variables:

$$\boldsymbol{\delta}_{p_i} = (x + x_{\text{ground}} + a_i \cos\theta - a_i - b_i \sin\theta)\,\hat{\mathbf{I}} + (y + y_{\text{ground}} + a_i \sin\theta + b_i \cos\theta - b_i)\,\hat{\mathbf{J}} \tag{5.10}$$

$$\boldsymbol{\delta}_u = (x + x_{\text{ground}} + u \cos\theta - d \sin\theta)\,\hat{\mathbf{I}} + (y + y_{\text{ground}} + u \sin\theta + d \cos\theta - d)\,\hat{\mathbf{J}} \tag{5.11}$$

where x_{ground} and y_{ground} are the displacement of the ground surface in $\vec{I}\vec{J}$ direction, respectively; a_i and b_i are the $\vec{i}\vec{j}$ coordinates of points of interest on the bottom mass with respect to a frame with origin located at point B; d is the $\vec{j}$ coordinate of the top mass with respect to the same frame.

The following equations are used to obtain the total acceleration at specific locations on the bottom mass($\ddot{\boldsymbol{\delta}}_{p_i}$) and at the top mass ($\ddot{\boldsymbol{\delta}}_u$) in the $\vec{i}\vec{j}$ rotating frame:

$$\begin{aligned}\ddot{\boldsymbol{\delta}}_{p_i} = &\Big((\ddot{x} + \ddot{x}_{ground})\cos\theta + (\ddot{y} + \ddot{y}_{ground})\sin\theta - a_i\dot{\theta}^2 - b_i\ddot{\theta}\Big)\,\hat{\mathbf{i}} \\ &+ \Big(-(\ddot{x} + \ddot{x}_{ground})\sin\theta + (\ddot{y} + \ddot{y}_{ground})\cos\theta + a_i\ddot{\theta} - b_i\dot{\theta}^2\Big)\,\hat{\mathbf{j}}\end{aligned} \tag{5.12}$$

$$\begin{aligned}\ddot{\boldsymbol{\delta}}_u = &\Big((\ddot{x} + \ddot{x}_{\text{ground}})\cos\theta + (\ddot{y} + \ddot{y}_{\text{ground}})\sin\theta + \ddot{u} - (d + d_o)\ddot{\theta} - (u + u_o)\dot{\theta}^2\Big)\,\hat{\mathbf{i}} \\ &+ \Big(-(\ddot{x} + \ddot{x}_{\text{ground}})\sin\theta + (\ddot{y} + \ddot{y}_{\text{ground}})\cos\theta + (u + u_o)\ddot{\theta} + 2\dot{u}\dot{\theta} - (d + d_o)\dot{\theta}^2\Big)\,\hat{\mathbf{j}}\end{aligned} \tag{5.13}$$

where $\ddot{x}_{\text{ground}}$ and $\ddot{y}_{\text{ground}}$ are the acceleration of the ground surface in $\vec{I}\vec{J}$ direction, respectivel; u_o and d_o are the $\vec{i}\vec{j}$ coordinates of the position vector pointing from the top mass centre to the accelerometer attached to the top mass.

The computed displacements and accelerations are contaminated next with noise to simulate the experimental measurements.

5.6.4 Generation of sampled noise measurements

The benchmark measurements obtained in the previous step were noise-free, and their time steps differed from the sampling rates of the DIC system and the accelerometers. Therefore, additional processing was required to generate the synthetic data that will be used to test the filter. First, the benchmark signals were resampled at frequencies corresponding to those of the respective measurement devices. In the physical experiments, the accelerometers operated at 18000 Hz, whereas the DIC system operated at 3000 Hz. Next, the displacement data from the DIC system were linearly interpolated from 3000 Hz to 18000 Hz to achieve temporal synchronization with the accelerometer data. Finally, the measurement noise, quantified in **Section** 5.3.4, of the DIC system and the accelerometers was added to the resampled measurements.

5.6.5 Filter setup

The model used for time update is a simplified version of the FRMCS: it resembles the FRMCS model, but the contact springs and dampers are replaced by three external forces applied at the contact interface. The states and the free body diagram of the simplified model are shown in Figure 5.7. This model does not have the discrete contact elements at each corner, therefore the parameters of the model are the same as those of the FRMCS's but without k_f, k_v, c_v and c_f. The simplified model treats the contact forces at the two corners of FRMCS (i.e., F_{Z1}, F_{Z2}, F_{Y1} and F_{Y2} in Figure 5.6(b)) as three external input forces (F_x, F_y and M in Figure 5.7(b)) applied at the middle point of the bottom face. The filter aims to identify these input forces (which represent the sum of the contact forces and the base moment during the experiment) from the measurements. There are four DoFs in the model: x_c, y_c, θ and u; while θ and u are defined the same as in the FRMCS model, x_c and y_c are the total displacement relative to an inertial reference frame that originates at the initial position of the centre of mass of the bottom mass.

The governing equations of the model are given by:

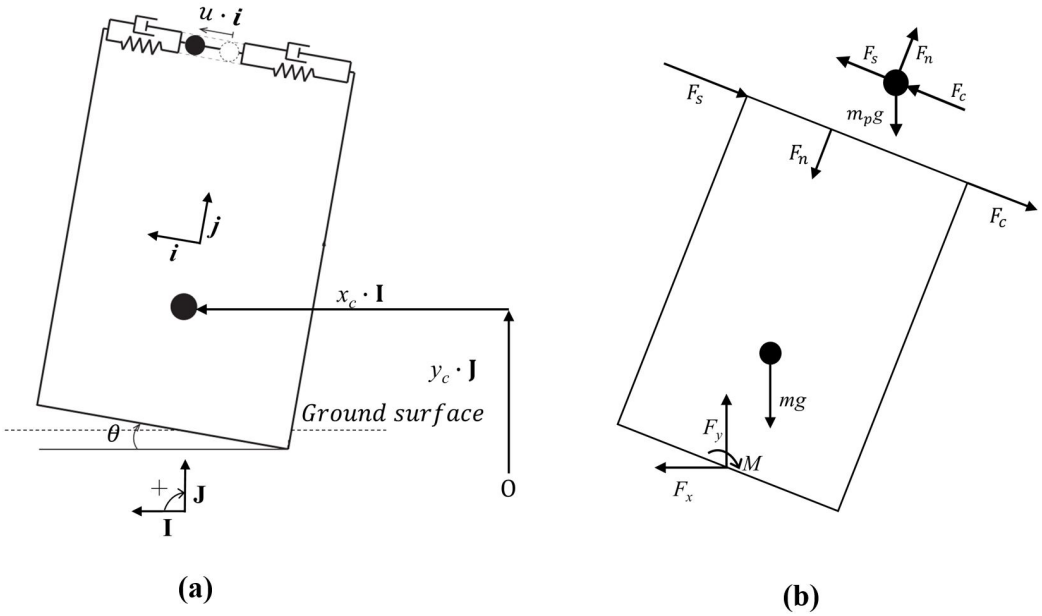


Figure 5.7: (a) Schematic drawing showing the states and (b) the free body diagram of the simplified model for time update.

$$m_p(\ddot{x}_c\cos\theta + \ddot{y}_c\sin\theta + \ddot{u} - u\dot{\theta}^2 - (h-h_b)\ddot{\theta}) = F_s + F_c - m_p g\sin\theta \quad (5.14)$$

$$m_p(-\ddot{x}_c\sin\theta + \ddot{y}_c\cos\theta + u\ddot{\theta} + 2\dot{u}\dot{\theta} - (h-h_b)\dot{\theta}^2) = F_n - m_p g\cos\theta \quad (5.15)$$

$$m\ddot{x}_c = F_x + (-F_s - F_c)\cos\theta + F_n\sin\theta \quad (5.16)$$

$$m\ddot{y}_c = -mg + F_y + (-F_s - F_c)\sin\theta - F_n\cos\theta \quad (5.17)$$

$$I_G\ddot{\theta} = M - F_n u + (F_s + F_c)(h-h_b) + F_x h_b\cos\theta + F_y h_b\sin\theta \quad (5.18)$$

The output equations that relate the states to the measurements are the same as Equations (5.10) to (5.13), except that $x + x_{ground}$ and its corresponding acceleration term need to be replaced by x_c and $\ddot{x}_c$, respectively. A similar substitution is applied to $y + y_{ground}$ and the associated acceleration terms.

In total, there are 11 states to be estimated: four displacement states corresponding to the four DoFs, four velocity states corresponding to the first derivatives of the four DoFs, and three total contact forces (i.e., F_x, F_y, and M). The initial estimates

of all 11 states are assumed to be zero. The initial state variances for x_c, y_c, θ, u, and their first derivatives are set to small values of 1×10^{-8} to reflect the very low uncertainty associated with their initial estimates. In contrast, the initial state variances for F_x, F_y, and M are set to 3.6×10^6, 1×10^6, and 2.5×10^5, respectively, to account for the substantially greater uncertainty in the initial estimates of the contact forces. These values are selected to cover the squared magnitudes of the maximum expected contact forces. For example, for F_y, the self-weight of the specimen is 190.143 N, and the maximum vertical force during impact may reach ten to thirty times this value, yielding a magnitude on the order of 10^3. Therefore, the corresponding variance is chosen as the square of 10^3.

The observation noise used in the filter equations is defined to be identical to the noise added to the benchmark measurements in the previous step (i.e., the noise characteristics of the measurement devices quantified in **Section** 5.3.4). After trial-and-error tuning, the process noise is assumed to have zero mean and an independent variance of 2.75×10^{-5} for each state, which provides the best estimation performance. The parameters α, β, and κ used for sigma point generation are set to 0.5, 2, and 0, respectively. The parameter L is set to 10, as the rocking specimen is relatively rigid. Numerical integration is performed using the forward Euler method with a time step of 1/18000, matching the measurement sampling frequency.

5.6.6 Filter performance with only DIC and DIC with accelerometer data

The sampled noisy measurements were processed using the Kalman filter. Two estimation cases were considered: one utilizing displacement measurements only, and another incorporating both displacement and acceleration measurements. The estimated states and forces were compared with the benchmark results, as shown in Figures 5.8, 5.9, and 5.10.

As shown in Figure 5.8, the estimation using only displacement measurements exhibited excellent agreement with the benchmark displacement response. However, the agreement with benchmarks degrades slightly for the velocity state, and is completed dominated by high-frequency noise for the acceleration dependent force state (Figure 5.10). This reduction in accuracy is expected since the high-frequency noise present in the estimated force is attenuated during numerical integration. It has little influence on the estimated displacement and the filter does not receive corrective feedback to suppress its influence on the velocity and force estimates.

In contrast, the estimation incorporating both displacement and acceleration measurements showed excellent agreement with the benchmark results across the displacement, velocity, and force responses. These findings numerically demonstrate the importance of combining accelerometer data with high-speed DIC measurements for filter applications. This approach is therefore adopted when dealing with experimental data in the ensuing sections.

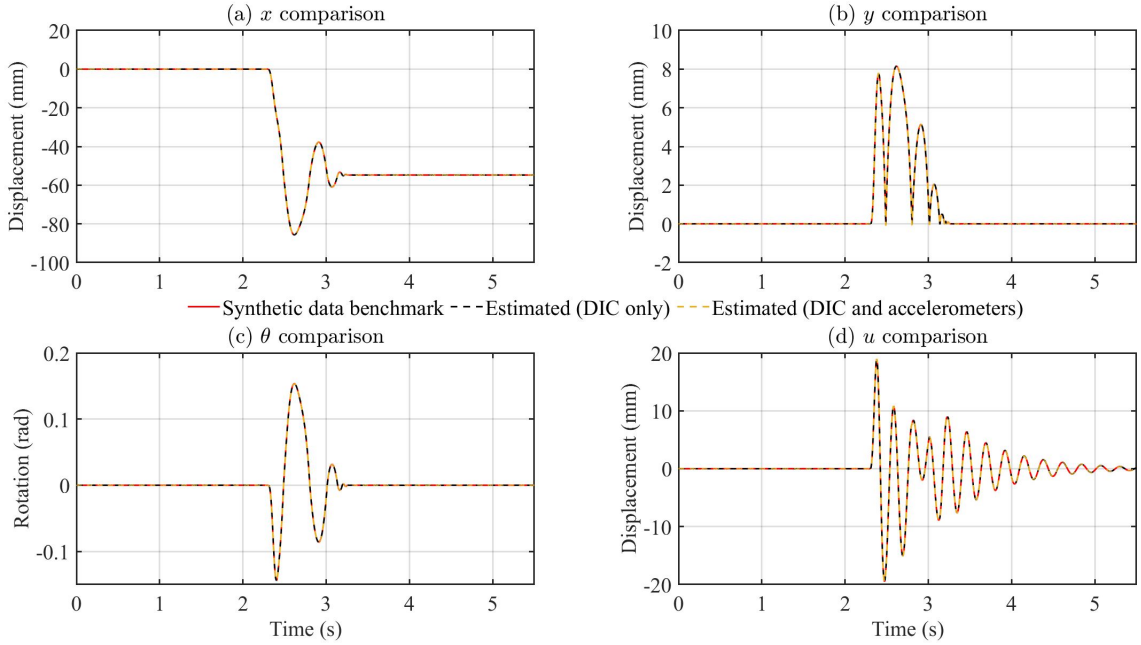


Figure 5.8: Comparison between the estimated displacement states and the benchmark.

5.7 Experimental stability test results

Three experimental configurations were examined in the stability tests, as described in **Section** 5.4.2. For clarity, they are referred to as Soft–Stiff–Rough, Soft–Soft–Rough, and Soft–Soft–Slippery in the following discussion. In this naming convention, the first term (Soft) denotes the lateral flexibility of the top-mass oscillator, which does not change amongst the investigated configurations. The second term describes the deformability of the support medium (either soft rubber or stiff MDF board), while the third term indicates the surface grip condition, either rough (high friction) or slippery (low friction). The results are shown in Figure 5.11. As demonstrated in the figure, the Soft-Soft-Slippery curve becomes coincident with the shake table stroke

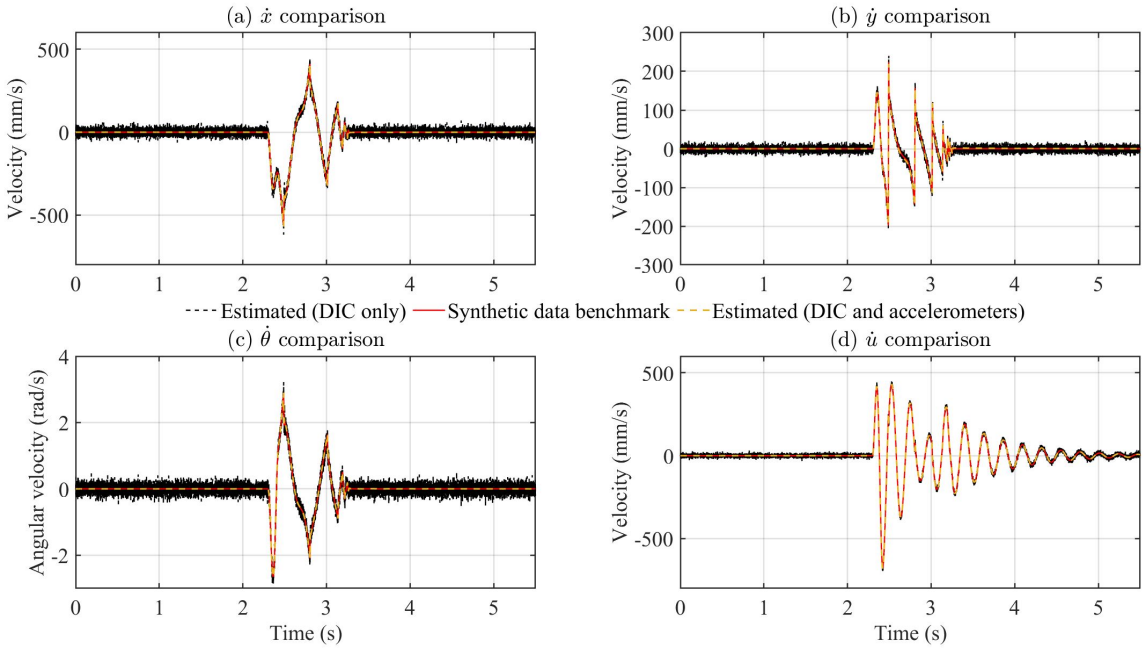


Figure 5.9: Comparison between the estimated velocity states and the benchmark.

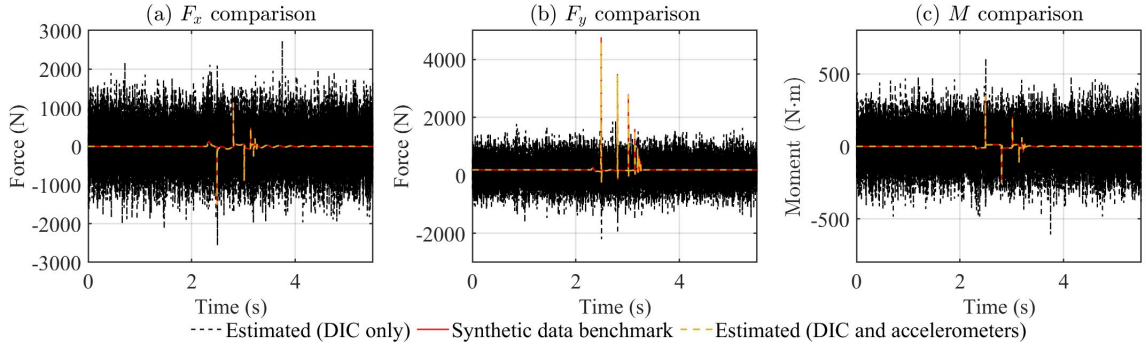


Figure 5.10: Comparison between the estimated force states and the benchmark.

limit at high frequencies, indicating that the stroke limit was reached before any overturning could occur.

Firstly, all instances of overturning occurred following impact during the test. It was observed that the pre-impact rocking angle increased progressively with pulse amplitude after reaching the overturning-with-impact threshold. This suggests that overturning without impact could occur if the shake table were capable of delivering higher acceleration amplitudes; however, the stroke length limit constrained the maximum attainable acceleration amplitude at each frequency during the test.

Secondly, by comparing the Soft–Stiff–Rough overturning boundary with that of the Soft–Soft–Rough configuration, it can be seen that the soft support medium

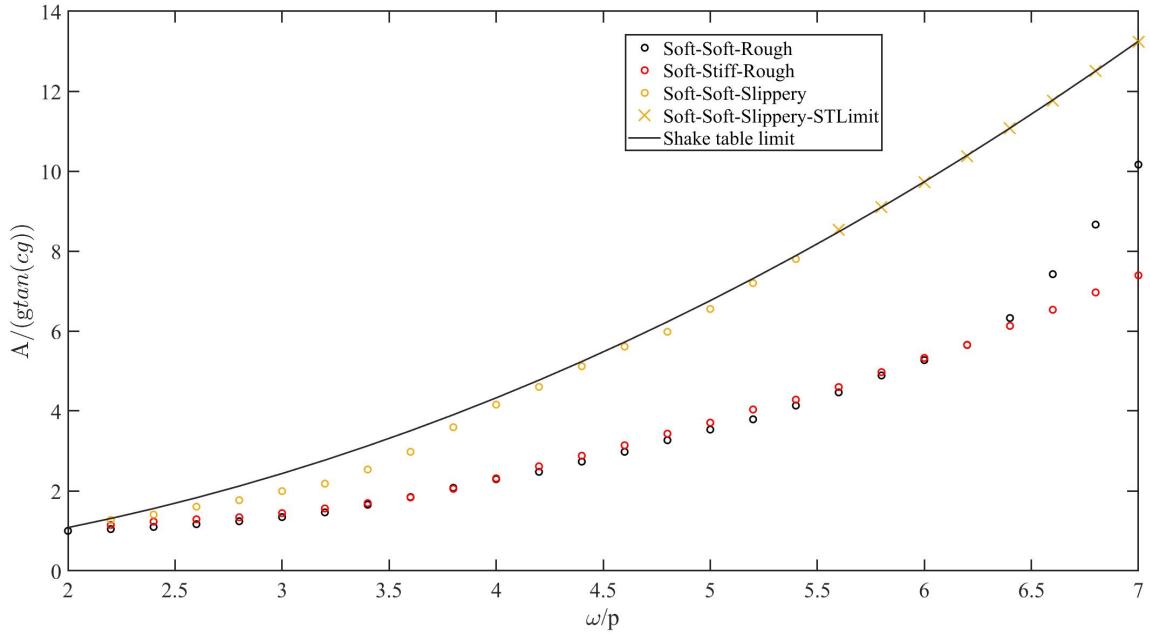


Figure 5.11: Experimental stability test results with the shake table acceleration limit.

slightly reduced the stability of the rocking specimen within the frequency ratio range of 2–6 (ω/p), but noticeably enhanced stability beyond this range. This finding highlights the significant influence of support deformability on the stability of flexible rocking bodies. Moreover, this observation qualitatively validates the numerical stability trends observed model in a previous study [78], which used the FRMCS model to investigate the influence of support deformability.

Finally, by comparing the Soft-Soft-Rough overturning boundary with that of the Soft-Soft-Slippery configuration, it can be seen that the low surface coefficient of friction improved the stability of the rocking specimen, with the improvement becoming increasingly pronounced at higher frequency ratios. From $\omega/p = 5.6$ onward, the overturning amplitude was not reached for the Soft-Soft-Slippery case since the shake table reached its stroke limit. Although the stability improved with the low-friction surface, significant sliding was also observed during the tests. In practical applications, high levels of sliding may violate separate performance criteria [37], which need to be carefully considered. However, this study did not explore this aspect and the extent of sliding was not measured.

5.8 Experimental pulse test results

Nine pulse tests were conducted, as described in the experimental procedure in **Section** 5.4.1. For consistency, the same naming convention used in the stability tests is adopted here to describe the experimental configurations. It should be noted, however, that the stability analysis was performed on a slender rocking specimen, in which the top-mass oscillator was placed on the third shelf, whereas the pulse tests were conducted on a stocky specimen, with the top-mass oscillator positioned on the first shelf. Therefore, although the configuration names could be identical in both the stability and pulse tests, they refer to specimens with the same lateral flexibility and support conditions but different slenderness.

5.8.1 Results of Soft-Stiff-Rough under 8 Hz pulse

Comparisons between the estimated and measured displacements and accelerations at various points on the rocking specimen are presented in Figures 5.12–5.14.

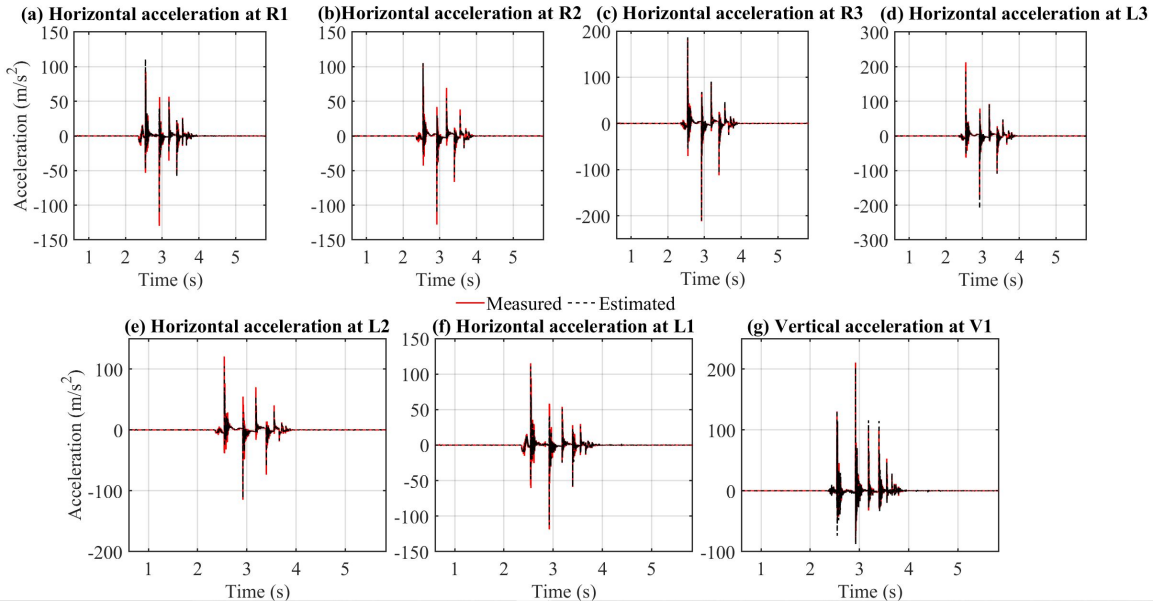


Figure 5.12: Specimen 2 on support condition A: Comparison between the estimated accelerations and the measurements at different points, indicated in Figure 5.5, on the bottom mass.

The estimations were in excellent agreement with the measurements, except for the horizontal acceleration of the top mass (P1 in Figure 5.5). Around the time of impact, the accelerometer mounted on the oscillator recorded high-frequency horizontal accelerations that were not captured by the filter estimation. Similar observations

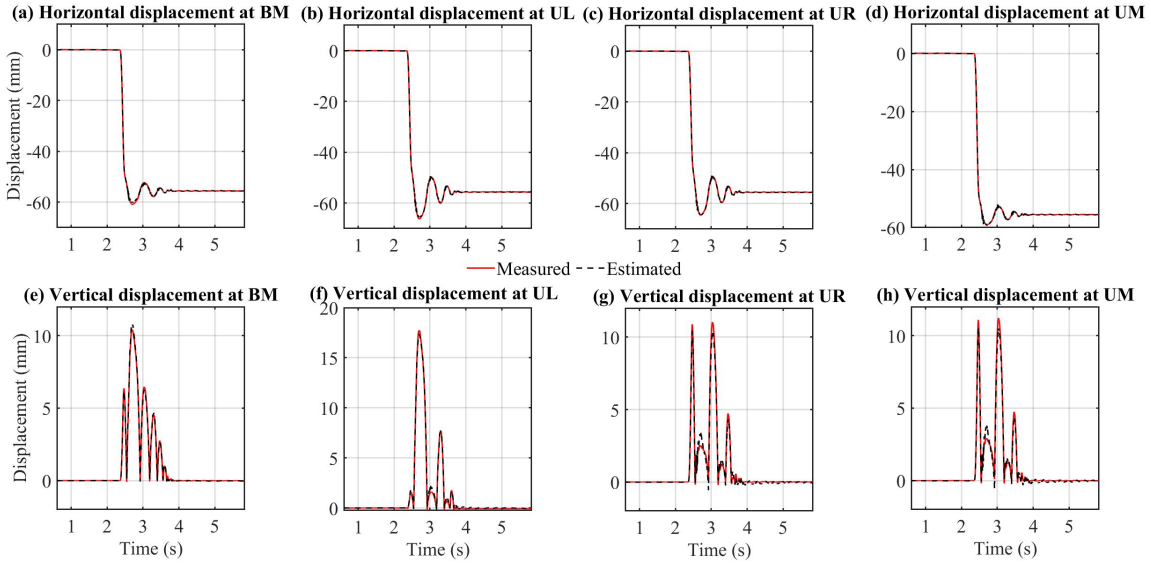


Figure 5.13: Specimen 2 on support condition A: Comparison between the estimated displacements and the measurements at different points on the bottom mass.

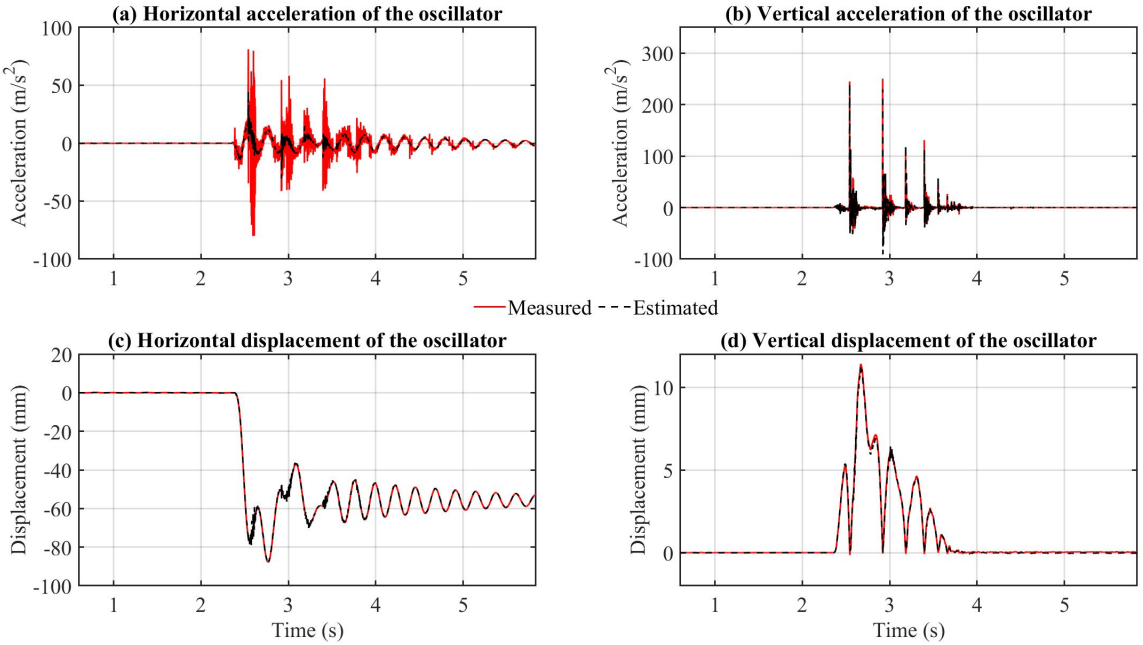


Figure 5.14: Specimen 2 on support condition A: Comparison of the estimated accelerations and displacements with the measurements of the top oscillator.

were made for other configurations of flexible rocking specimens. In contrast, for the stiff rocking specimens, these high-frequency oscillations were absent, and the estimations agreed closely with the measurements as shown in the Appendix A, which includes the comparison of experimental measurements and measurement estimations for all other cases.

An inspection of the top mass–spring–rail system revealed that the rail, designed to allow frictionless sliding of the top mass on the shelf, had been slightly deformed. As a result, instead of sliding smoothly, the top mass occasionally collided with the roller bearings within the rail, with these collisions becoming more pronounced at higher sliding velocities. This behaviour explains the appearance of high-frequency accelerations near impact: the top-mass velocity reached peak values around impact, causing the collisions to become more noticeable in the acceleration records. It also clarifies why such high-frequency accelerations did not occur in the stiff rocking specimen configuration (specimen configuration 1): because a stiff rod, rather than a soft spring, was used in the top mass–spring–rail system, the top mass $\dot{u}$ velocities reduce around impact, and high frequency impulses due to collisions are less noticeable. The filter fails to capture this behaviour due to model error: the top mass–spring–rail assembly is idealised as a point mass connected by linear springs and dampers. This idealised model cannot reproduce the sliding–colliding interaction observed in the experiments. However, this aspect is not considered an issue since the damage to the rail was incidental and did not notably alter the behavioural trends.

The estimated displacement states and forces are summarised in Figure 5.15. Although the numerical example in **Section** 5.6 demonstrated the reliability of the filter, several basic checks were performed to further verify the accuracy of the experimental estimations. First, the total vertical contact force should equal the self-weight of the rocking specimen before the external excitation is applied. Inspection of the estimated F_y response shows that the total vertical contact force prior to excitation was 190.143 N, matching the self-weight of the specimen. This value was derived entirely from the measured data, as the initial contact force provided to the filter was set to zero. Secondly, because the contact surface in this test was highly frictional (60-grit sandpaper), no noticeable sliding was expected or observed. Consequently, the final total horizontal displacement of the centre of mass of the bottom shelf, x, should closely match that of the shake table, which was 55.412 mm. Examination of the estimated x response shows a value of 55.441 mm—very close to the shake table displacement, apart from small oscillations caused by the moving point mass. Thirdly, the free vibration period of the top-mass oscillator was theoretically 0.218 s, while the estimated u response indicated a period of 0.225 s, in close agreement with the theoretical value.

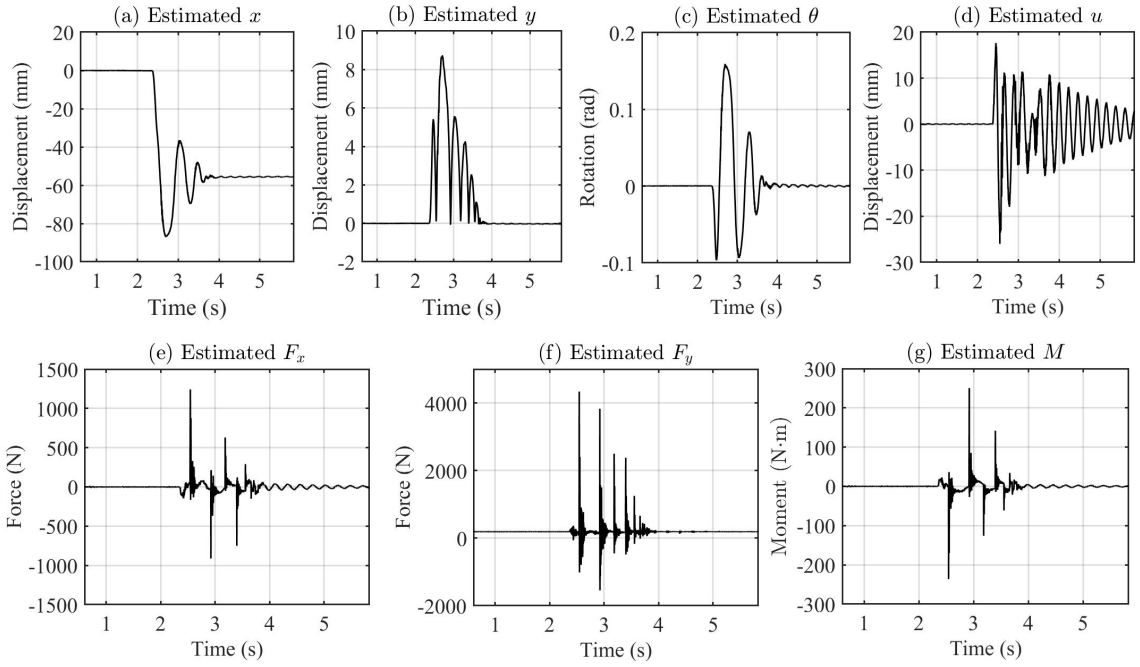


Figure 5.15: Estimated displacement states and forces.

5.8.2 State and force comparisons between all rough surface configurations under 8 Hz pulse

The comparisons of the estimated state and contact force responses for all rough-surface configurations are shown in Figures 5.16 and 5.17.

By comparing the dotted and solid lines of the same colour in Figure 5.16, it can be seen that, for a given level of lateral flexibility, a softer support did not cause a noticeable change in the maximum rocking angle. The estimated u response further showed that the maximum lateral deformation was only marginally affected by changes in support deformability. In contrast, by comparing the solid or dotted lines of the same colour, it is evident that, for a given support deformability, a more flexible oscillator resulted in a clear increase in the maximum rocking angle. Specifically, the maximum rocking angle increased by 26% for the stiff-support cases and by 24 % for the soft-support cases.

Figure 5.17 presents the total contact force responses, and the insets show the maximum force of the soft support cases. Each row compares configurations with the same level of lateral flexibility but different support deformability. Examination of these plots shows that, when the support consisted of a stiff MDF board, the maximum vertical contact force (F_y) was significantly greater than the self-weight of the rocking specimen. Specifically, the self-weight of the specimen was 190.143 N,

while the maximum vertical contact force reached 4470.82 N for the stiff oscillator and 4338.2 N for the flexible oscillator, exceeding 23 times the self-weight.

When the support was replaced by rubber, all peak force responses decreased substantially. For the nearly rigid oscillator, the maximum horizontal contact force (F_x) decreased from 1054.71 N to 191.25 N, the maximum vertical force (F_y) from 4470.82 N to 785.25 N, and the maximum base moment (M) from 203.74 N·m to 28.65 N·m. For the flexible oscillator, the corresponding reductions were from 1242.06 N to 231.02 N for F_x, from 4338.2 N to 749.90 N for F_y, and from 246.20 N·m to 36.86 N·m for M. On the other hand, given the same level of support deformability, changing from a nearly rigid to a flexible oscillator did not result in a noticeable variation in any of the maximum contact force responses.

These observations demonstrate that using a soft support medium significantly reduces the contact forces without adversely affecting the maximum rocking angle or lateral deformation capacity. This finding suggests that incorporating a more deformable support material can be an effective strategy to mitigate contact forces while maintaining rocking stability and allowable deformation.

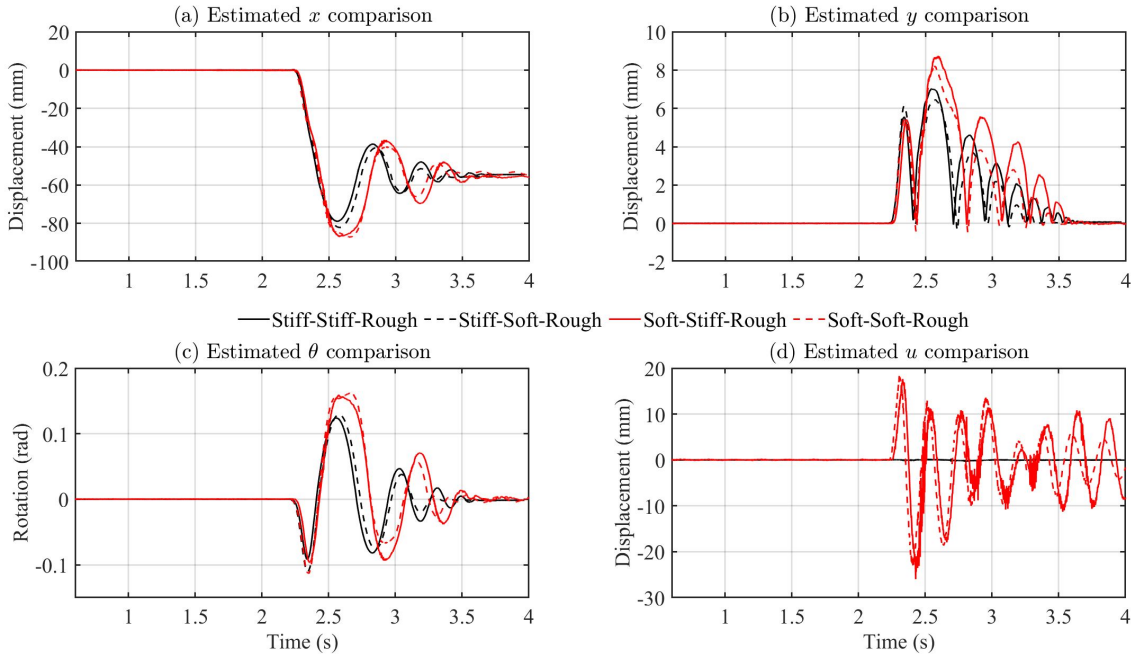


Figure 5.16: Comparison of estimated displacement responses across all cases under 8 Hz pulse.

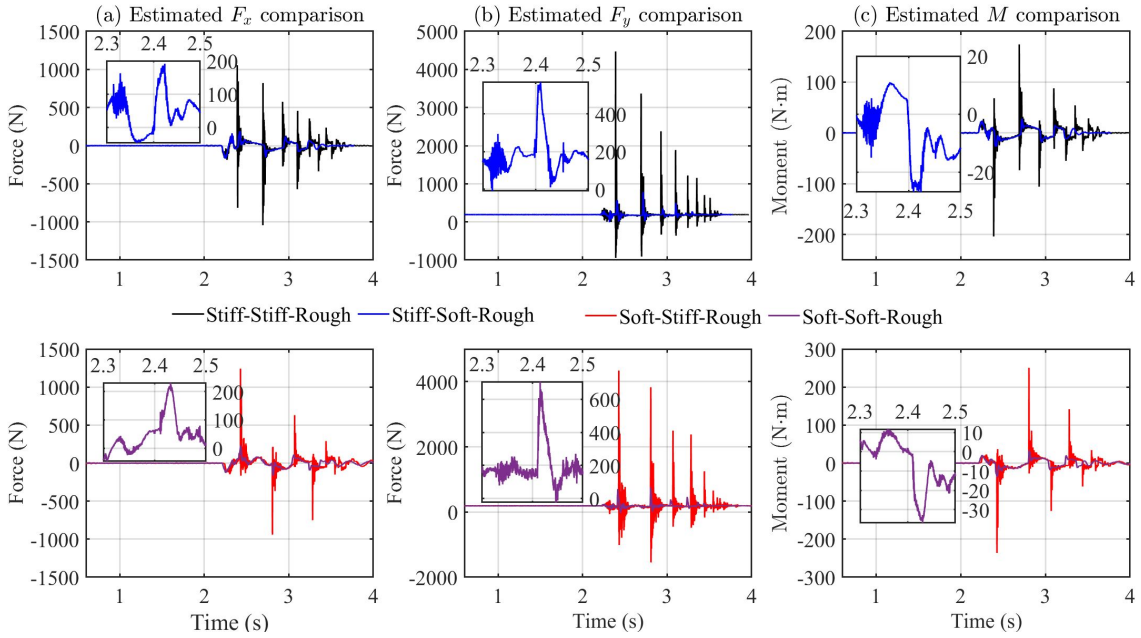


Figure 5.17: Comparison of estimated contact force responses across all cases under 8 Hz pulse.

5.8.3 State and force comparisons between all rough surface configurations under 3 Hz pulse

Experimental measurements and corresponding estimations for all test cases are presented in Appendix A. These estimations exhibited a similar or even higher level of agreement with the measurements discussed in **Section** 5.8.1. The comparisons of the estimated state and total contact force responses for all rough-surface configurations are shown in Figures 5.18 and 5.19.

By comparing the solid and dotted lines of the same colour in Figure 5.18, it is evident that, for a given support deformability, a more flexible oscillator produced a clear increase in the maximum rocking angle, which is also observed in the 8 Hz excitation cases. Furthermore, by comparing the dotted and solid lines of the same colour, it can be seen that, for a given level of lateral flexibility, a softer support also resulted in a larger maximum rocking angle. This behaviour is opposite to that observed in the 8 Hz excitation cases, where changes in support deformability had little influence on the rocking angle. More specifically, the maximum rocking angle increased from 0.05 rad for the stiff–stiff configuration to 0.25 rad for the soft–soft configuration, an increase by a factor of five.

Figure 5.19 presents the total contact force responses. The maximum vertical contact force (F_y) was much greater than the self-weight of the rocking specimen

when the support was a stiff MDF board, reaching 2006 N for the stiff oscillator and 4919.15 N for the flexible oscillator, up to 25 times the self-weight. For a given support deformability, the effect of oscillator flexibility was variable. Under the soft support condition, the change was marginal: the maximum F_y decreased slightly from 1052.22 N to 992.31 N. In contrast, under the stiff support condition, a more flexible oscillator caused a substantial increase in maximum F_y, from 2006 N to 4919.15 N. This may be attributed to the increase in the maximum rocking angle, which led to a larger pre-impact angular velocity. The investigations in **Chapter** 3 using FRMCS demonstrated that this pre-impact angular velocity is proportional to the magnitude of the contact force.

Replacing the stiff support with rubber consistently reduced all peak force responses. For the stiff oscillator, the maximum horizontal force (F_x) decreased from 813.59 N to 188.56 N, the maximum vertical force (F_y) from 2006 N to 1052 N, and the maximum base moment (M) from 91.52 N·m to 34.44 N·m. For the flexible oscillator, the corresponding reductions were from 786.12 N to 198.44 N for F_x, from 4919.15 N to 992.31 N for F_y, and from 119.36 N·m to 36.30 N·m for M.

These observations demonstrate that, although a softer support medium reduces contact forces, it also may lead to larger rocking motion, an effect not seen under the 8 Hz excitation. In addition, the influence of lateral flexibility becomes significant as it can noticeably alter the force responses, which again differs from the results under 8 Hz excitation.

In summary, both support deformability and lateral flexibility play critical roles in the rocking response. The mitigating effect of a soft support on contact forces, as well as the increase in maximum rocking angle induced by a more flexible oscillator, were consistently observed across all tests. However, the influence of support deformability on rocking angle amplitudes was found to vary with excitation frequency, while the influence of oscillator flexibility on the contact force response depended on both the excitation frequency and the support condition.

5.8.4 State and force comparison between rough and semi-slippery surface configurations

Experimental measurements and corresponding estimations for the semi-slippery surface case are presented in Appendix A. These estimations exhibited a similar or even higher level of agreement with the measurements discussed in **Section** 5.8.1. Comparisons of the estimated state and total contact force responses between the rough and semi-slippery surface cases are shown in Figures 5.20 and 5.21.

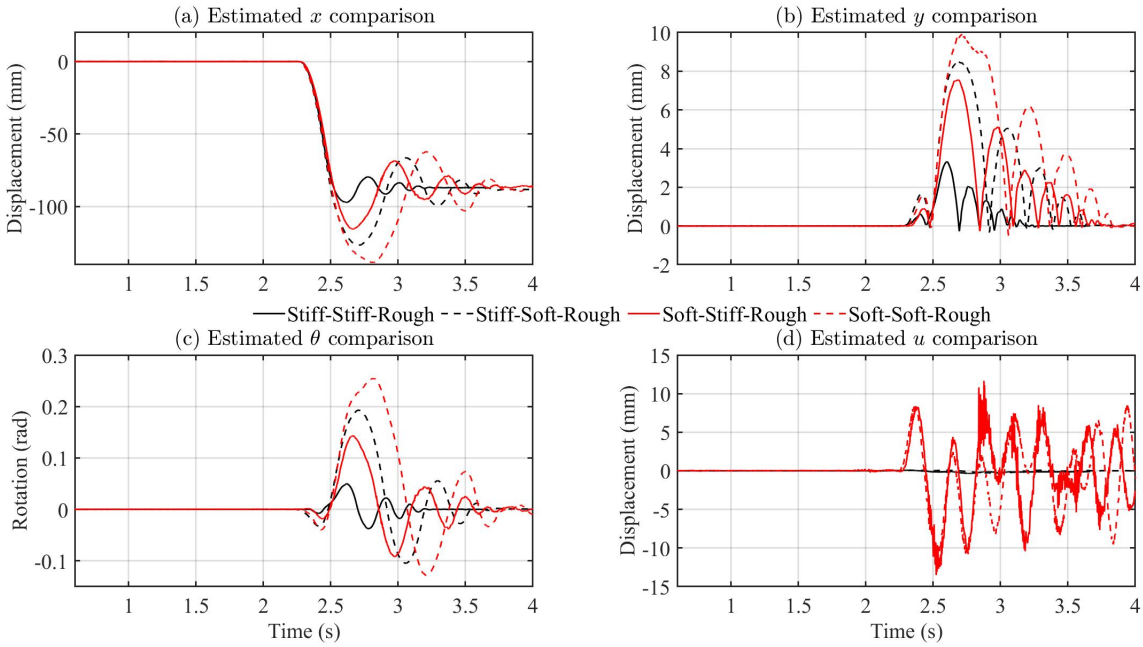


Figure 5.18: Comparison of estimated displacement responses across all cases under 3 Hz pulse.

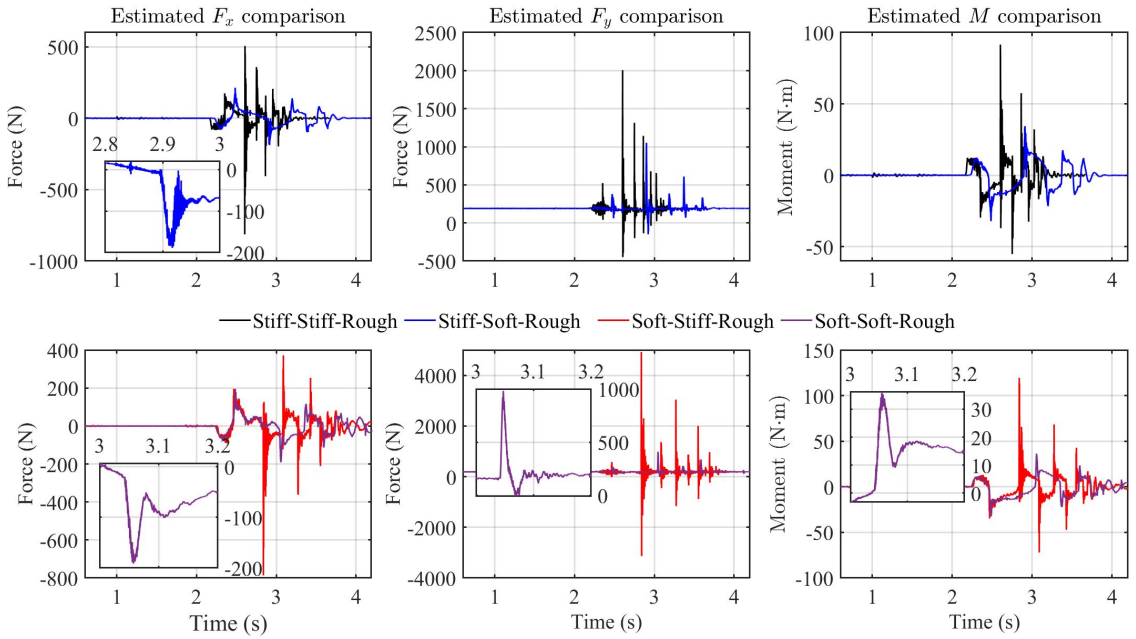


Figure 5.19: Comparison of estimated contact force responses across all cases under 3 Hz pulse.

The estimated x comparison plot indicates that the final horizontal displacement was similar for both cases and closely matched the shake table displacement. While this result is expected for the rough-surface case, in which no observable sliding

occurred, noticeable sliding was observed for the semi-slippery surface case. The comparable final displacement therefore suggests that the sliding at the two rocking corners effectively cancelled each other out.

Furthermore, the estimated θ and u comparison plots show that sliding noticeably reduced the maximum rocking angle while slightly increasing the maximum lateral deformation. Figure 5.21 demonstrates that sliding also reduced both the maximum horizontal (F_x) and vertical (F_y) contact force responses.

These observations indicate that the influence of sliding on the rocking response cannot be neglected. For the case studied, sliding effectively reduced rocking amplitudes and mitigated large contact forces.

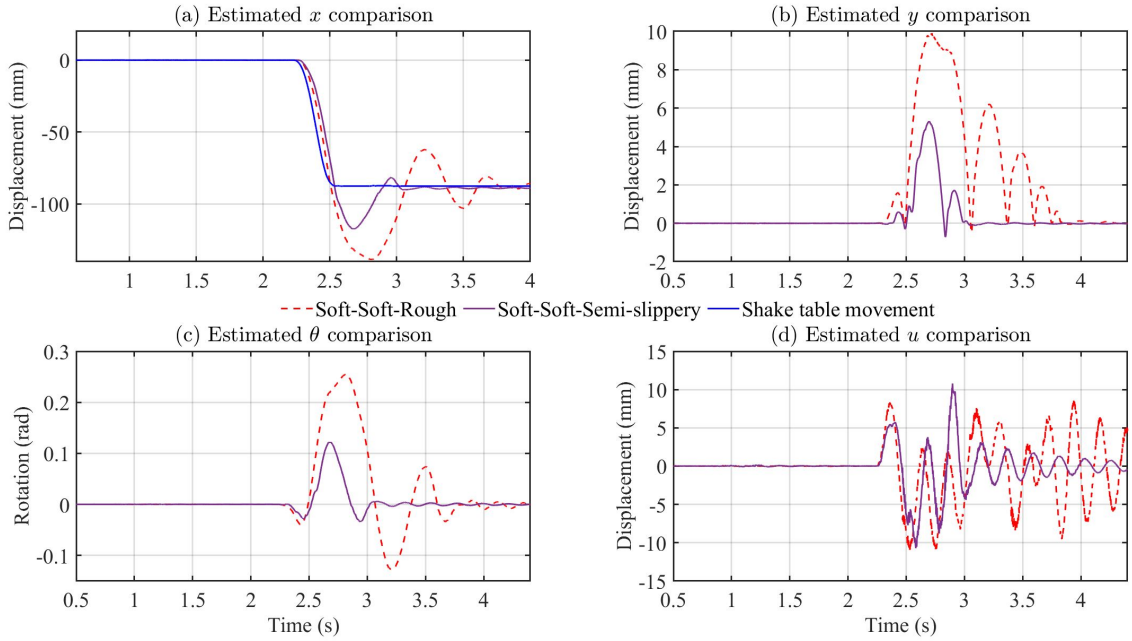


Figure 5.20: Comparison of estimated displacement responses between rough and semi-slippery surface cases under 3 Hz pulse.

5.8.5 Sliding amount estimation for the semi-slippery surface test

During the test of the soft-soft-semi-slippery configuration, sliding motion was observed. However, because no dedicated measurements were taken for the sliding motion, this section attempts to estimate the sliding from the recorded data.

Sliding amount can be estimated as the change in the horizontal relative displacement between the shake table and the corner, when either of or both of the corners are in contact with the support. Therefore, it is necessary to know where the free contact

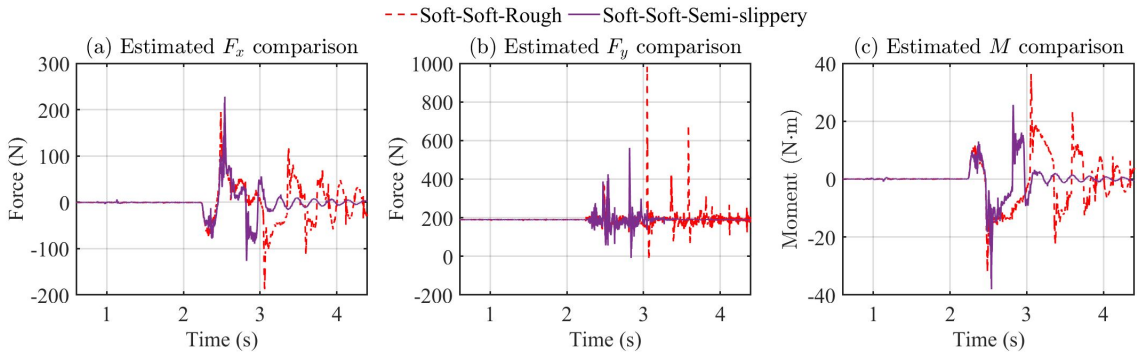


Figure 5.21: Comparison of estimated contact force responses between rough and semi-slippery surface cases under 3 Hz pulse.

surface is. However, this information is not available since the DIC measurements are relative to the first picture frame, where the support medium is already deformed and in static equilibrium with the self-weight of the specimen.

To find how much the support medium deforms due to self-weight of the rocking specimen, it is necessary to know the vertical stiffness of the support medium. The vertical stiffness can be estimated using the free vibration response before the vibration completely stops. The measured vertical acceleration at P for the stiff-soft-rough case during the end free vibration was used for this purpose. The corresponding free vibration time history is shown in Figure 5.22.

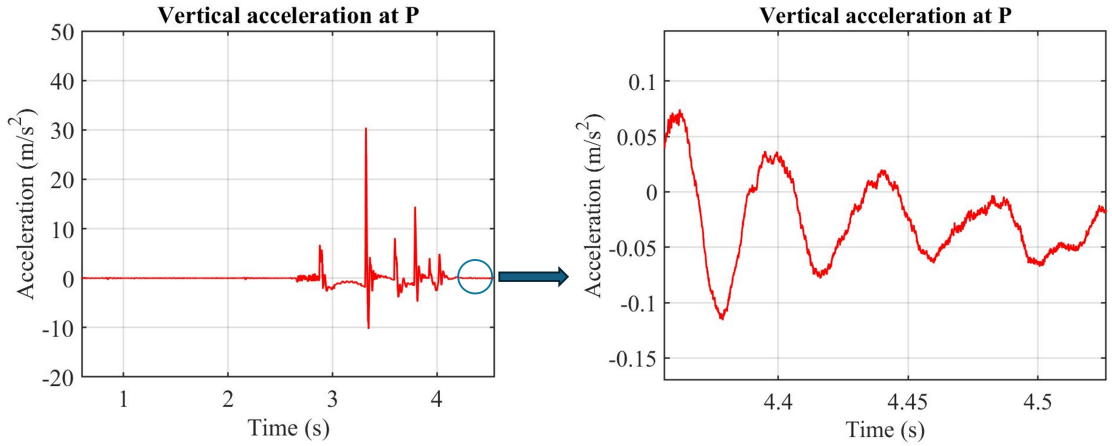


Figure 5.22: Measured vertical acceleration at P for stiff-soft-rough configuration under 3 Hz excitation.

Because the stiff rocking specimen can be regarded as nearly rigid and the rocking angle is very small during the free vibration, the system can be approximated by a

rigid body standing on vertical springs and dampers. The linearised equation of motion for this system is given by:

$$\begin{bmatrix} m+m_p & 0 \\ 0 & I_G \end{bmatrix} \begin{bmatrix} \ddot{y} \\ \ddot{\theta} \end{bmatrix} + \begin{bmatrix} 2c_v & 0 \\ 0 & \frac{1}{2}b^2c_v \end{bmatrix} \begin{bmatrix} \dot{y} \\ \dot{\theta} \end{bmatrix} + \begin{bmatrix} 2k_v & 0 \\ 0 & \frac{1}{2}b^2k_v \end{bmatrix} \begin{bmatrix} y \\ \theta \end{bmatrix} = \begin{bmatrix} F_y(t) \\ M(t) \end{bmatrix} \tag{5.19}$$

It can be seen that the two states are already uncoupled, therefore the first mode is pure vertical translation and the second mode is pure rotation about the centre of mass. The period of the second mode is given by:

$$T_2 = \frac{2\pi}{\sqrt{\frac{k_v b^2}{2I_G}\left(1-\zeta_2^2\right)}} \tag{5.20}$$

where ζ_2 is the second mode damping ratio.

The free vibration immediately before all motion ceased was primarily rotational and therefore dominated by the second mode. Inspections of Figure 5.22 show a vibration period of 0.0391 s (T_2). The logarithmic decrement method was used to calculate the damping ratio using peak amplitudes four cycles apart, and it was found to be 8.7% (ζ_2). Accordingly, the vertical spring stiffness, k_v, was determined to be 2.12×10^5 N/m using Equation (5.20). This corresponds to an undamped first-mode frequency of 23.6 Hz, which is close to the manufacturer's estimated value of 30.41 Hz assuming a uniformly distributed weight throughout the rubber surface area.

The static deformation of the rubber due to the specimen self-weight is therefore determined to be 0.4478 mm. Figure 5.23 (a) shows the vertical displacements of the right and left corners, as well as the position of the contact surface, which is located 0.4478 mm above the initial zero position. This figure indicates when a corner loses or re-establishes contact with the rubber: when the vertical displacement exceeds the contact surface position, the corner loses contact with the rubber, whereas when it becomes smaller, the corner re-establishes contact. Three distinct time windows, A, B, and C, are identified in the figure for calculating the sliding amount.

In time window A, Figure 5.23(a) shows that both corners were initially in contact with the support. The right corner lost contact at approximately 2.33 s, whereas the left corner remained in contact until the end of the time window. More specifically, Figure 5.23(b) shows the sliding amount at the left corner before it lost contact. Prior to the onset of shake-table motion at about 2.2 s, no sliding occurred; after the table began to move, the sliding increased to 10 mm and subsequently decreased to a final value of 5.43 mm.

In time window B, Figure 5.23(a) shows that the right corner re-established contact and remained in contact with the support until it lifted off again, while the left corner remained in the air for the entire duration. Figure 5.23(c) further identifies the instants at which the right corner re-established and lost contact. When contact was re-gained, the right corner slid rapidly by approximately −9.12 mm, after which it oscillated around the same position due to the oscillator vibration.

In time window C, the left corner re-established contact and remained in contact with the support until the end of the test. Figure 5.23(d) shows that upon re-establishing contact, the left corner experienced an initial rapid sliding of 5.8 mm, followed by a reversal of −2.08 mm, before settling near 4.12 mm, around which it vibrated due to the oscillator motion. In addition, Figure 5.23(a) shows that in time window C the right corner re-gained contact with the support at 2.95 s, which coincides with the onset of the rapid reversal sliding of −2.08 mm observed in Figure 5.23(d).

In conclusion, time window A clearly indicates that sliding occurred as a direct result of the external excitation, which was applied from 2.22 s to 2.54 s. Time windows B and C suggest that the most pronounced sliding occurred when a corner re-established contact with the support. This is qualitatively similar to the findings from the FRMCS model in a previous numerical study [78]. Furthermore, the total sliding displacement, obtained by summing 5.43 mm, −9.12 mm, and 4.12 mm, equals −0.43 mm. This small net value explains why, despite noticeable sliding during the test, the difference between the estimated x and the horizontal displacement of the shake table remained minimal at the end, as shown in Figure 5.20.

5.9 Comparisons between FRMCS predictions and experimental results

Since the identified vertical stiffness yielded a first mode frequency comparable to the manufacturer's estimate, and the sliding quantification based on this stiffness accurately explained the experimental observations, the estimated vertical stiffness of the rubber and consequently the damping coefficient are considered reliable. Therefore, these parameters were adopted in the FRMCS model to predict the experimental results and validate the model, and idealised pulse acceleration was used.

The predictions were performed for all configurations with a soft support and rough surface. The transition position of the coefficient of friction for the semi-slippery surface was not recorded; hence, FRMCS modelling could not be conducted for that

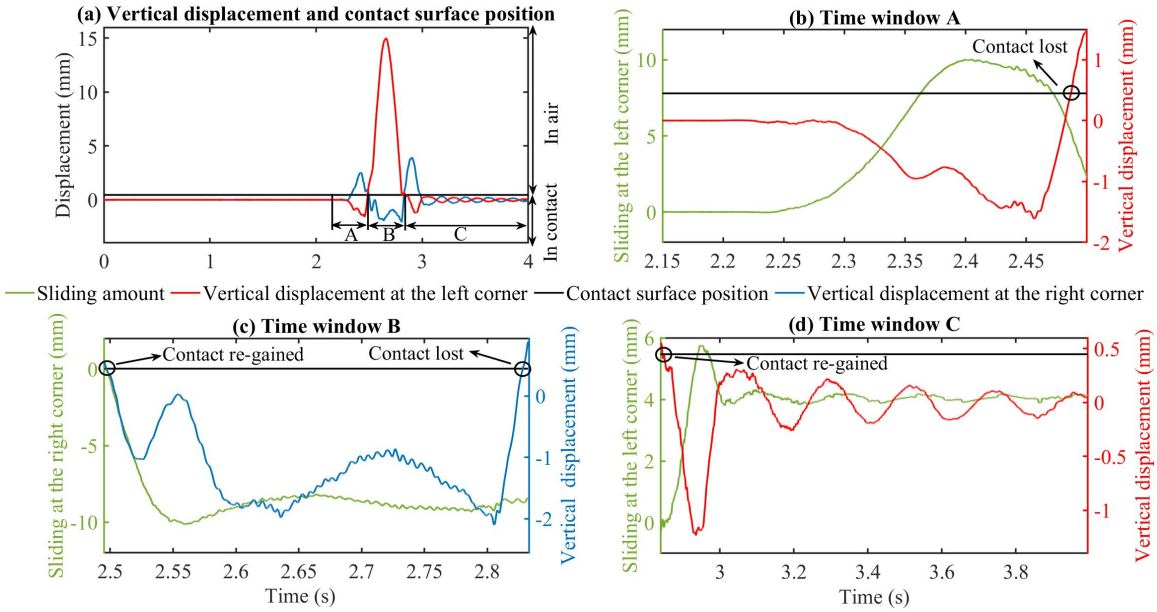


Figure 5.23: Time windows for calculating sliding amount at different corners.

case. Figure 5.24 compares the experimentally estimated and FRMCS-predicted displacements for the soft–soft–rough configuration under the 8 Hz pulse. By comparing the solid black and dotted blue lines, it can be seen that the model reproduced the maximum response with good accuracy. However, the predicted response decayed noticeably faster than the experimental result, indicating excessive energy loss during impact.

Figure 5.25 presents the corresponding comparison of the contact force responses. The FRMCS model overpredicted the maximum contact force by almost a factor of two. The combination of larger predicted contact forces and faster decay suggests that the estimated damping coefficient was too high to represent the actual damping. A subsequent prediction was therefore conducted with the same stiffness but a reduced damping coefficient. As shown by the dotted red lines in Figures 5.24 and 5.25, the modified model produced a much closer agreement between the predicted and experimental displacement and force responses.

Similar patterns of rapid decay of motions and overpredicted contact forces were observed in other configurations, with improved agreement achieved after reducing the damping coefficient. However, it was noticed that the damping coefficient that provided good predictions for one configuration did not yield satisfactory results for others, even though the support material remained the same. This may not be surprising considering that the stiffness and damping in the rubber are rate and strain-magnitude dependent [85]. These findings suggest that modelling energy dissipation

in rocking systems using a linear spring and a viscous damper could be insufficient, and that a more detailed constitutive model may need to be adopted for higher fidelity simulations.

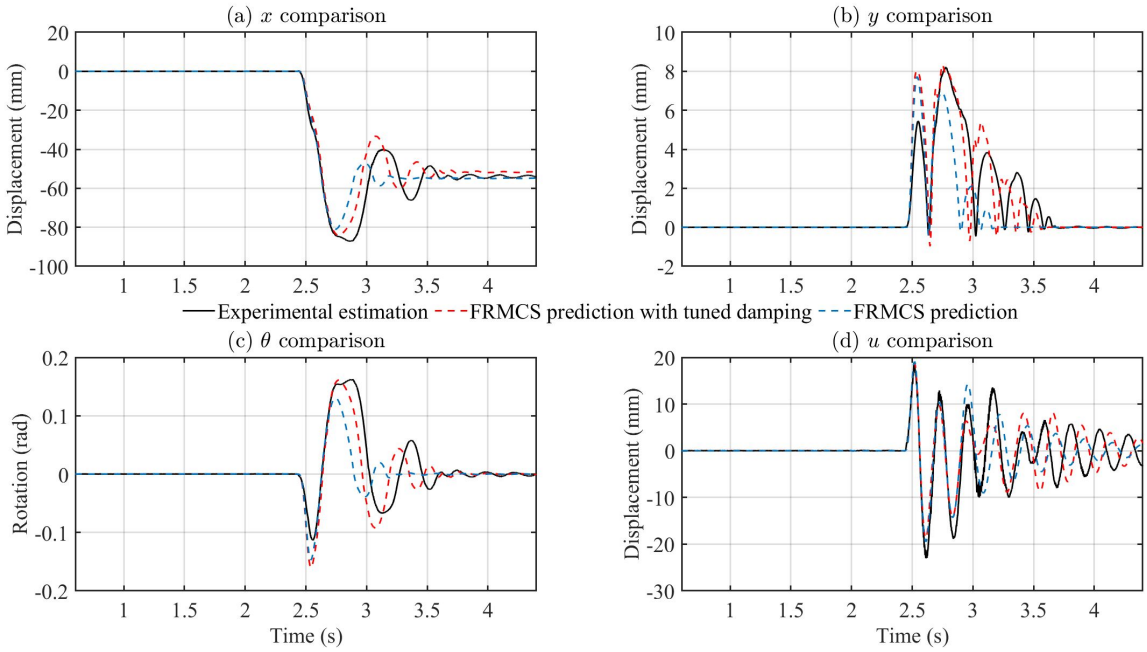


Figure 5.24: Comparison between experimental displacement estimations and FRMCS predictions for the soft–soft–rough case under the 8 Hz pulse.

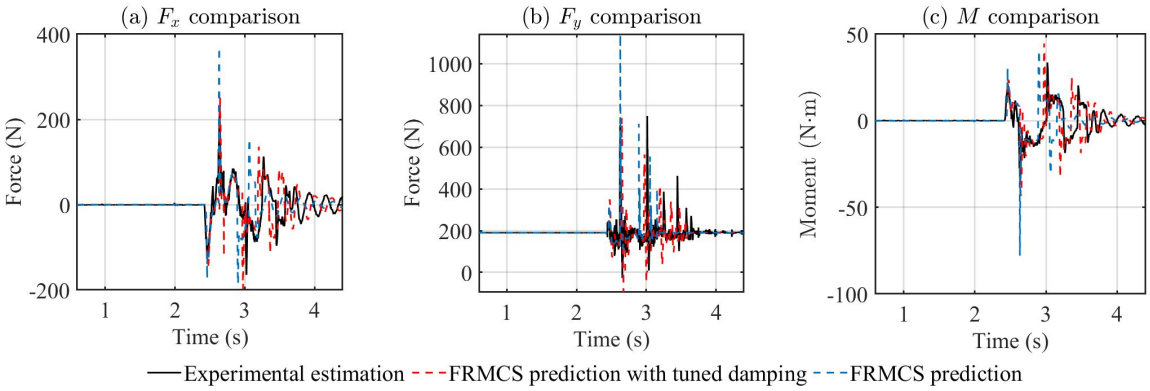


Figure 5.25: Comparison between experimental force estimations and FRMCS predictions for the soft–soft–rough case under an 8 Hz pulse.

5.10 Conclusion

This chapter presented an experimental investigation into the coupled effects of support deformability, rocking-body flexibility, and sliding on the rocking response, us-

ing a modified high-speed testing setup. The new system combined a 3000 Hz digital image correlation (DIC) system with 18,000 Hz accelerometers, providing accurate high-frequency measurements of rocking motion. A novel non-contact method employing an unscented Kalman filter was developed to estimate total contact forces without altering interface properties. Numerical verification confirmed the filter's accuracy and demonstrated the necessity of combining DIC and accelerometer data for reliable state and force estimation. This approach represents the first successful experimental measurement of total contact forces in rocking systems without direct interface instrumentation.

Experimental stability tests showed that a soft support slightly reduces stability for flexible rocking body at low frequency ratios but enhances it at higher ones, while lower surface friction consistently improves stability despite noticeable sliding. These observations are consistent with numerical trends from the authors' previous studies. Pulse excitation tests revealed that impacts can generate contact forces exceeding 25 times the specimen's self-weight, and soft supports can reduce these forces by up to sixfold. Sliding was found to lower contact forces, while flexible oscillators could increase the contact force and the rocking amplitude. Comparisons with FRMCS predictions showed good agreement, validating the model.

Chapter 6

Conclusions

6.1 Research contributions

This thesis has presented a unified analytical, numerical, and experimental study on the dynamic behaviour of flexible structures rocking and sliding on deformable media. Through the development of new theoretical, computational, and experimental tools, it establishes a comprehensive framework for understanding how structural flexibility, support deformability, and surface friction interact to govern rocking stability and force response, thereby advancing both the fundamental understanding and the practical analysis of rocking-induced forces and stability in flexible structures.

- **Analytical Modelling:** Introduced the *Flexible Rocking Model on Concentrated Springs (FRMCS)*, which:
  - Considers geometric nonlinearity, lateral flexibility, friction, and deformable supports within a unified analytical model.
  - Captures contact behaviour through discrete spring–damper elements, providing both physical interpretability and computational efficiency.
  - Enables systematic exploration of how lateral flexibility, support deformability and surface grip affect rocking stability and contact forces.
- **Numerical Modelling:** Developed a *generalised numerical framework* for flexible rocking structures that:
  - Models sliding and deformable supports using discrete elements, and represents the flexible rocking body with finite elements.

  - Applies the Craig–Bampton model reduction technique to the finite element model, achieving computational efficiency while capturing the concentrated stress near contact regions.
  - Demonstrates that Euler–Bernoulli beam models substantially underestimate local stress demands, highlighting the necessity of reduced-order finite element modelling for contact-dominated problems.

- **Experimental Methodology:** Proposed and implemented a *non-contact experimental method* that represents a first-of-its-kind approach for measuring rocking forces. This methodology:
  - Combines high-speed Digital Image Correlation (DIC) and accelerometers to synchronously capture high-frequency displacements and accelerations data.
  - Integrates a modified Unscented Kalman Filter (UKF) to estimate total contact forces and states indirectly, preserving the contact interface property.
  - Enables, for the first time, experimental quantification of the coupled effects of support deformability, structural flexibility, and sliding on the dynamic force response of rocking systems.

- **Integrated Understanding:** By linking the analytical, numerical, and experimental developments, this work establishes a unified framework that:
  - Predicts and explains the complex interplay between support deformability, superstructure flexibility, and surface grip in determining stability and force demands.
  - Provides numerical tools for examining both local stress concentrations and global rocking motion across a range of structural configurations.
  - Establishes experimental method for estimating the contact forces during rocking experiments and verifies numerical findings.

6.2 Summary of findings

The main findings of this thesis, organised by research component, are summarised below.

Chapter 3 — Analytical Investigation (FRMCS Model)

- The FRMCS model successfully incorporates both superstructure flexibility and support deformability, accounting for sliding and free-flight effects through physically consistent contact mechanics.
- Comparison with the existing Flexible Rocking Model (FRM) under nearly rigid support conditions demonstrated that FRMCS reproduces FRM behaviour, confirming its robustness under limiting conditions and validating the FRM.
- Analytical studies across five configurations revealed that:
  - Softer supports substantially reduce peak base forces.
  - Lateral flexibility has a smaller influence on contact forces than vertical support stiffness.
  - Sliding can improve the rocking stability but excessive displacement could occur.
- The analysis identified the "shrinking and sinking'' trend of Mode I overturning with increasing flexibility and deformability, a noticeable feature of flexible rocking stability.

Chapter 4 — Numerical Framework and Investigation

- The proposed numerical framework, implemented in Simulink, combined discrete contact elements, floating frame of reference formulation, and reduced-order finite elements through Craig–Bampton reduction for efficient yet high-fidelity modelling.
- The framework produced responses consistent with FRMCS predictions in appropriate cases, confirming numerical reliability and theoretical consistency.
- Key observations include:
  - While the beam element model produces a stability diagram almost identical to that of the reduced-order tetrahedral element model, it significantly underestimates stresses near the contact zones.
  - Structural deformability reduces stresses due to contact during free vibration but increases pre-impact velocity during pulse excitation, creating a competing effect on maximum stress magnitudes.

  - Small sliding motions markedly reduce horizontal frictional demands without affecting vertical forces, consistent with analytical trends.

- The framework successfully modelled column-like structures and accurately reproduced the experimental response of an uplifting steel frame, demonstrating its versatility, reliability, and ability to simulate fully three-dimensional rocking behaviour.

Chapter 5 — Experimental Investigation

- A comprehensive experimental programme was conducted to investigate, for the first time, the coupled influence of support deformability, superstructure lateral flexibility, and surface grip on the rocking response, with particular focus on the contact force response.

- The developed hybrid system (DIC + accelerometers + UKF) enabled non-contact force estimation—the first experimental approach of its kind for rocking systems.

- Numerical verification of the filter confirmed its accuracy when displacement and acceleration data were used jointly.

- The experimental findings revealed that:

  - Soft supports slightly reduce rocking stability for flexible rocking body at low frequency but enhance it at higher frequency, consistent with analytical trends.

  - Vertical contact forces can exceed 25 times the self-weight of the specimen, yet soft supports reduce these forces by up to sixfold.

  - Lateral flexibility could reduce stability and increase the contact force.

  - Sliding mitigates contact force magnitudes and improves rocking stability.

- Comparisons between experiments and FRMCS simulations showed good agreement, confirming that the analytical model captures the essential rocking physics.

6.3 Recommendations for future work

- Develop experimental methods to identify the energy loss during impact for different support media, and assess the feasibility of modelling it using nonlinear discrete springs and dampers. This will further improve the discrete contact elements.
- Develop methods to identify the contact properties in existing structural or non-structural components that may exhibit rocking behavior during earthquakes. This will support a more accurate seismic assessment of such components.
- Investigate the differences between the predicted contact force responses obtained using the proposed nonlinear numerical framework and a corresponding linearized model. This will clarify the influence of neglecting geometric nonlinearity, which is a common assumption in the current design of rocking structures.
- Investigate the feasibility to use a series of discrete contact elements to represent continuous contact interface, as this study is limited to rocking on feet.
- Apply the proposed framework to three-dimensional rocking studies, as two-dimensional rocking scenarios are not necessarily the most conservative cases. An ongoing investigation using a chimney-like structure subjected to actual earthquake motions is addressing this aspect.
- Apply the proposed framework to reproduce experiments that resulted in crushed concrete corners, to evaluate how well the reduced-order elements can capture the concentrated stresses during impact. This will contribute to the improved design of rocking corners.
- Conduct experiments involving constant sliding, and evaluate how accurately the discrete contact elements can predict the amount of sliding. This will pave the way for designing sliding motion as an intentional mechanism.
- The contact forces developed during impacts, in addition to their large magnitudes, exhibit high-frequency characteristics. Therefore, the corners may fail due to fatigue during an earthquake; however, no research has yet investigated this aspect.

Appendix A

Supplementary Results

This appendix presents the experimental measurements and measurement estimations for all the other cases.

A.1 Stiff-Stiff-Rough under 8 Hz pulse

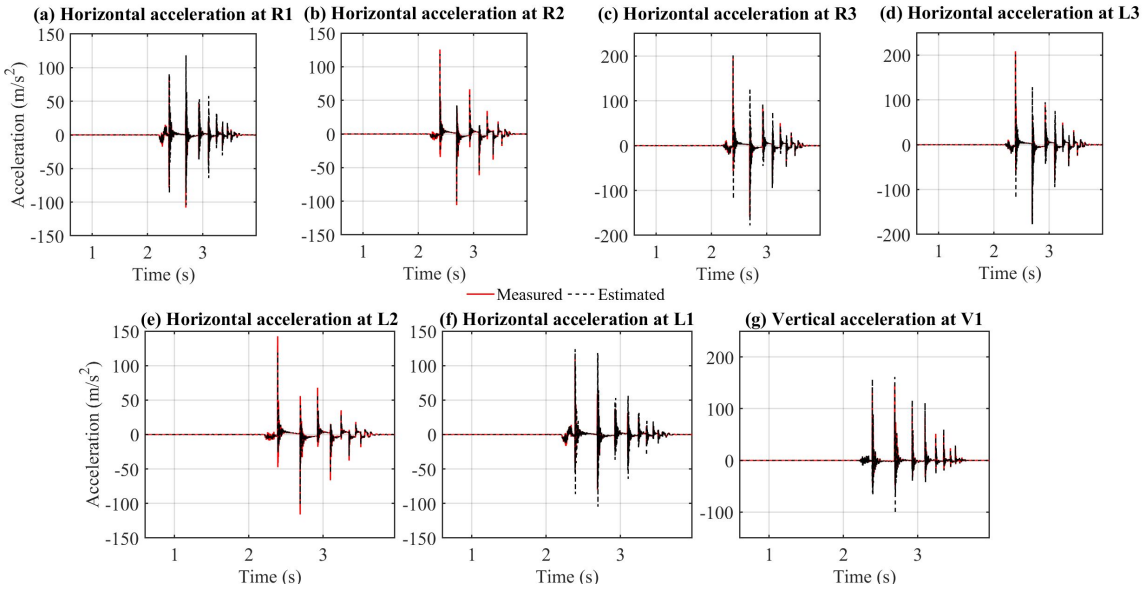


Figure A.1: Comparison between the estimated accelerations and the measurements at various points on the bottom mass.

.

.

.

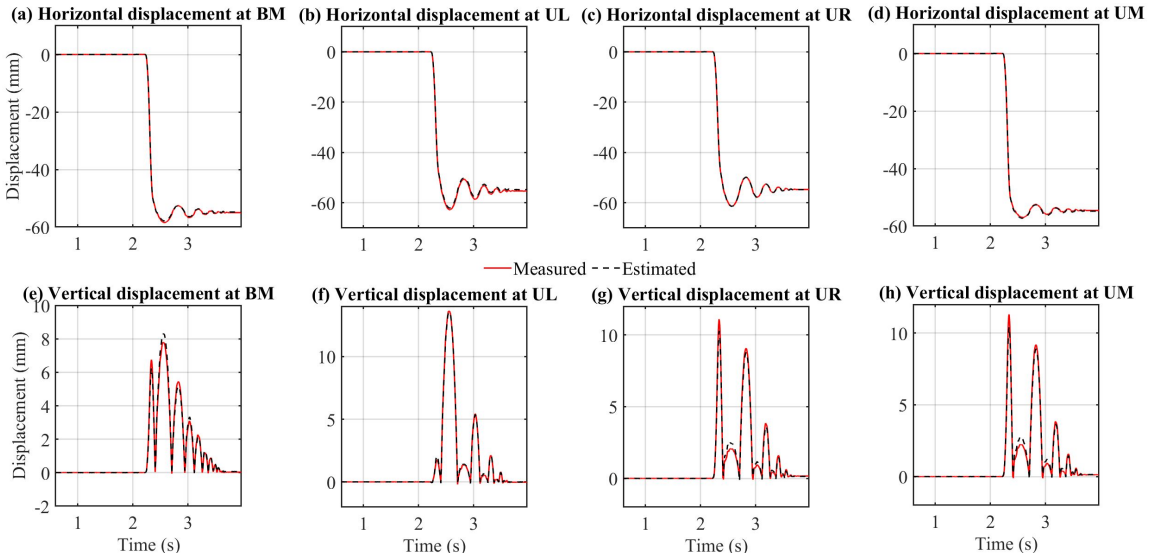


Figure A.2: Comparison between the estimated displacements and the measurements at various points on the bottom mass.

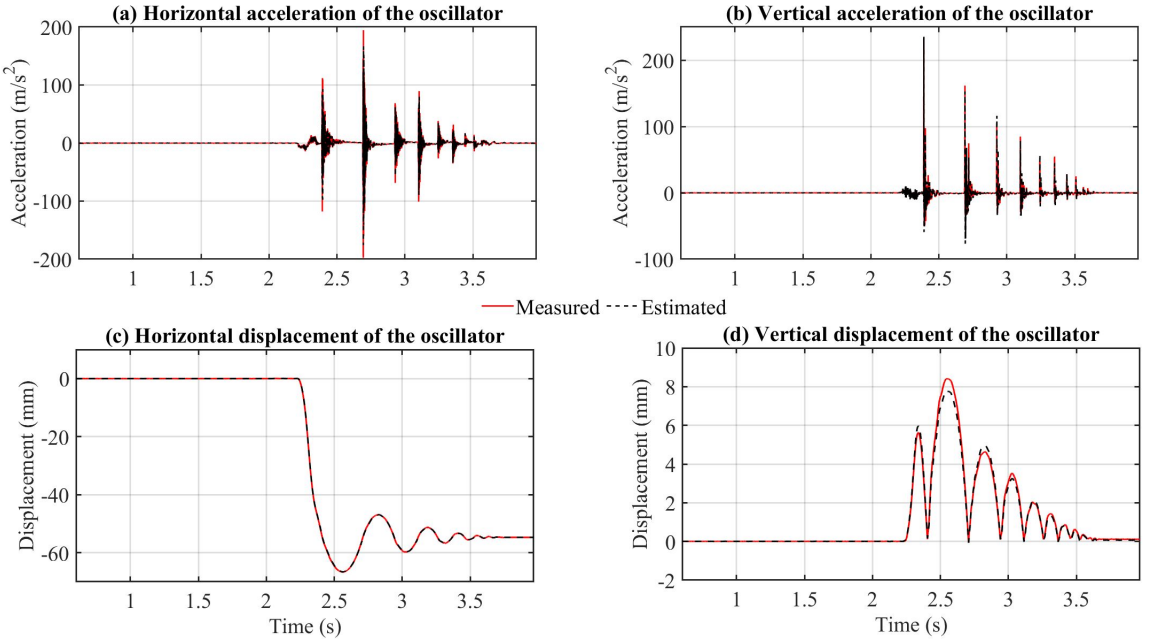


Figure A.3: Comparison of the estimated accelerations and displacements with the measurements of the top oscillator.

A.2 Stiff-Soft-Rough under 8 Hz pulse

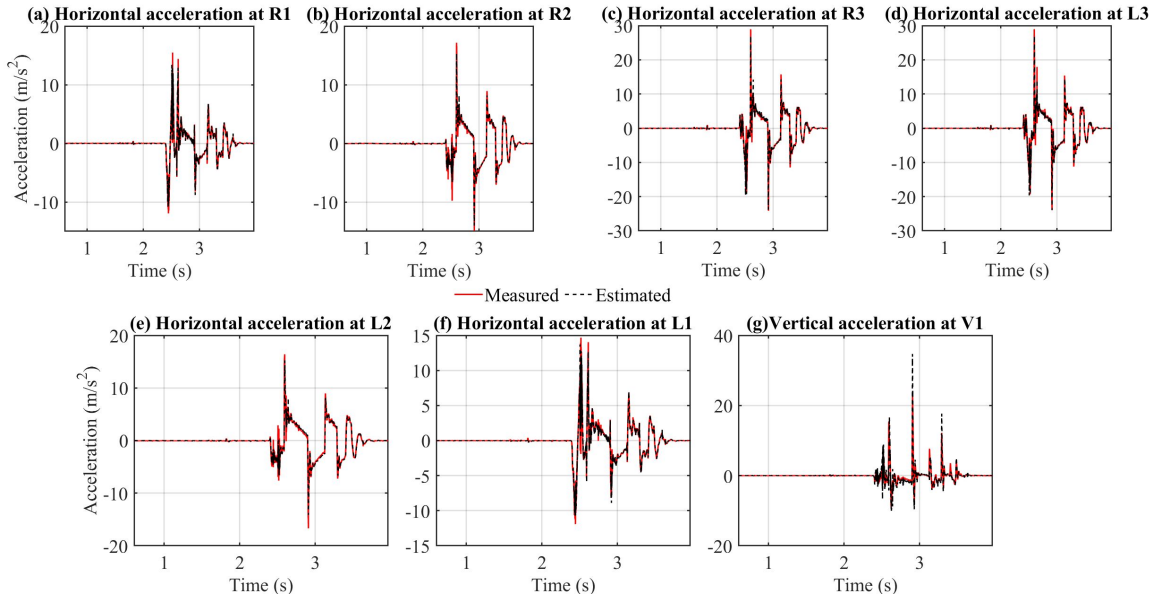


Figure A.4: Comparison between the estimated accelerations and the measurements at various points on the bottom mass.

.

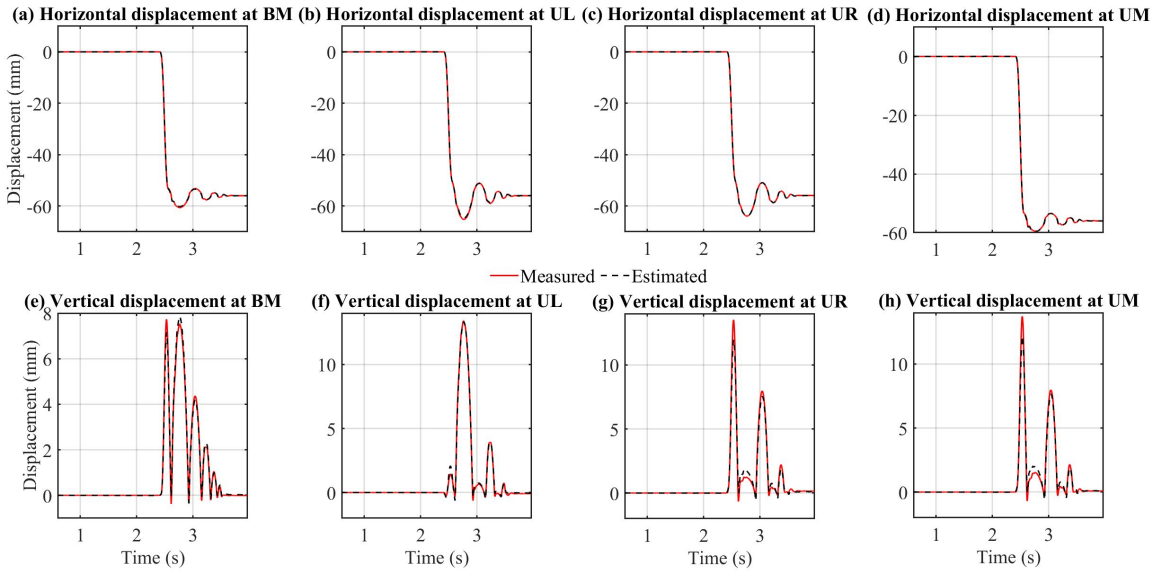


Figure A.5: Comparison between the estimated displacements and the measurements at various points on the bottom mass.

.

.

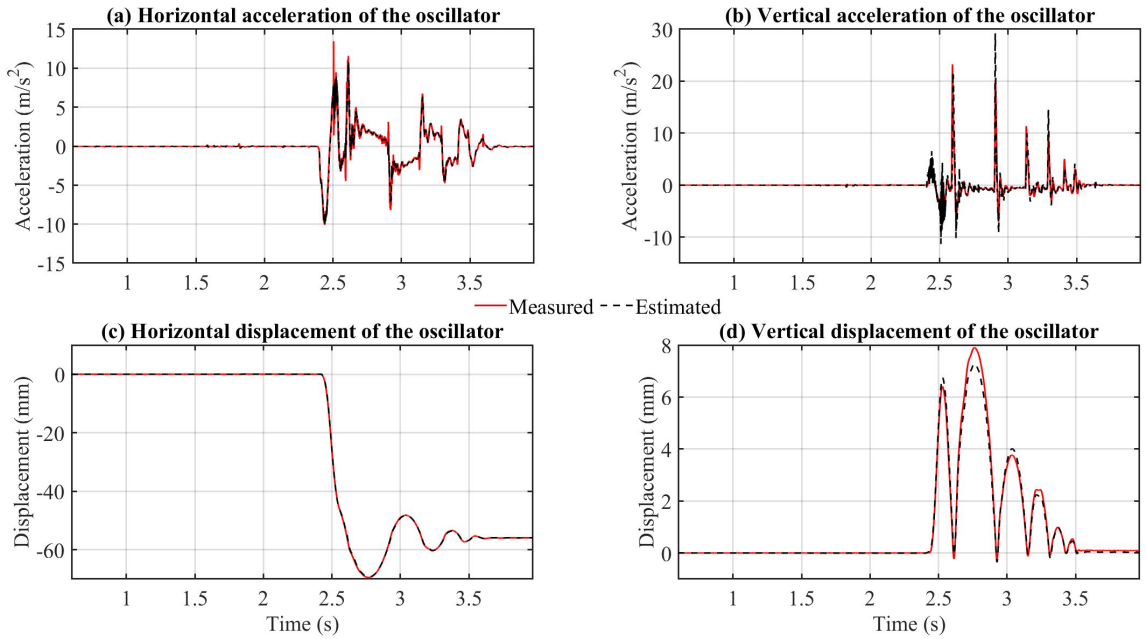


Figure A.6: Comparison of the estimated accelerations and displacements with the measurements of the top oscillator.

A.3 Soft-Soft-Rough under 8 Hz pulse

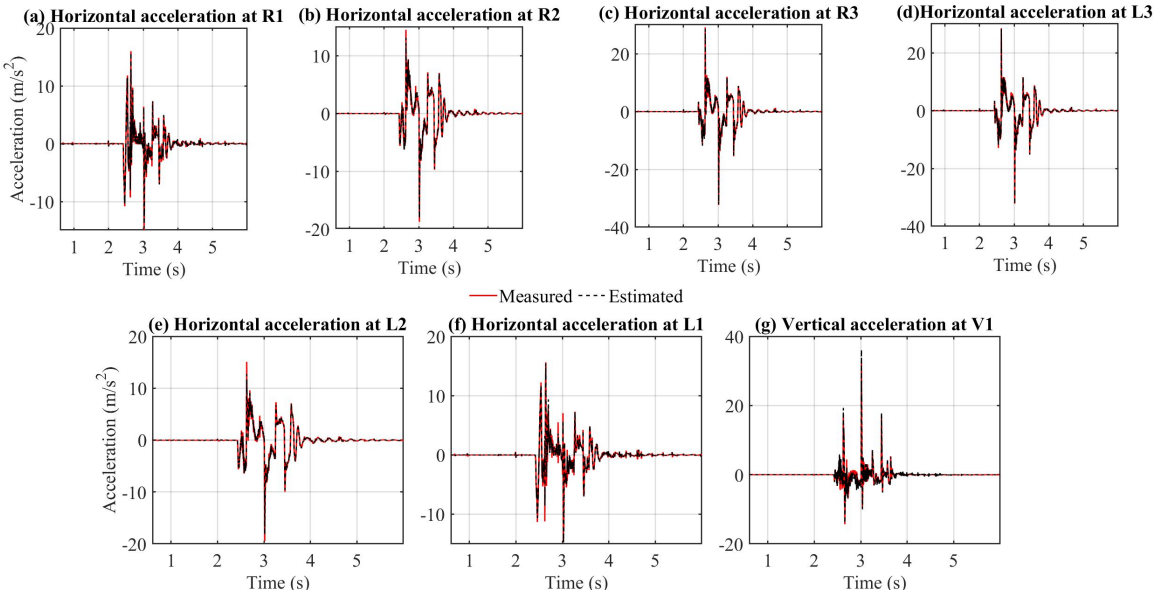


Figure A.7: Comparison between the estimated accelerations and the measurements at various points on the bottom mass.

.

.

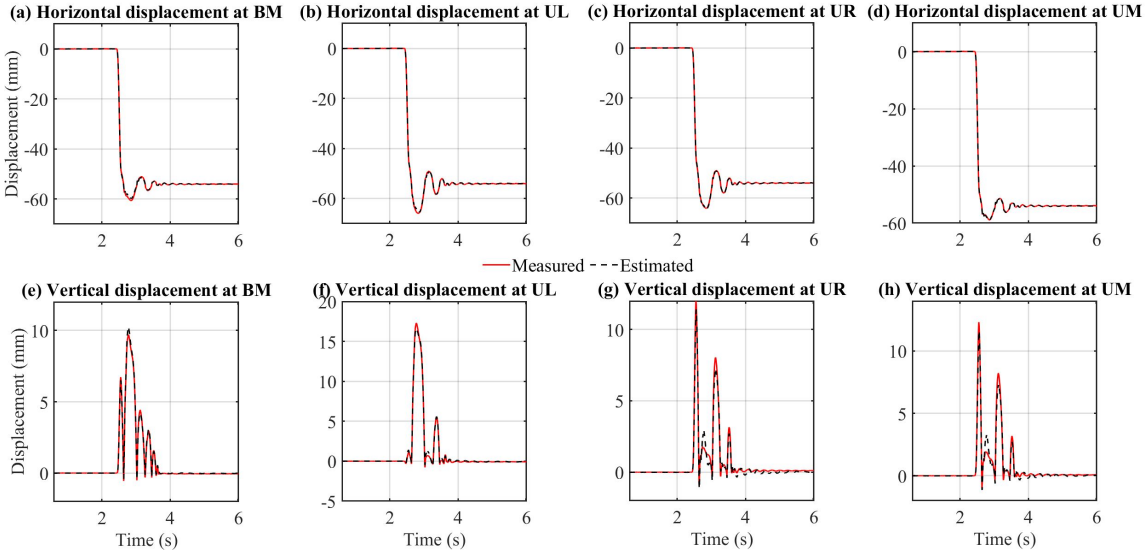


Figure A.8: Comparison between the estimated displacements and the measurements at various points on the bottom mass.

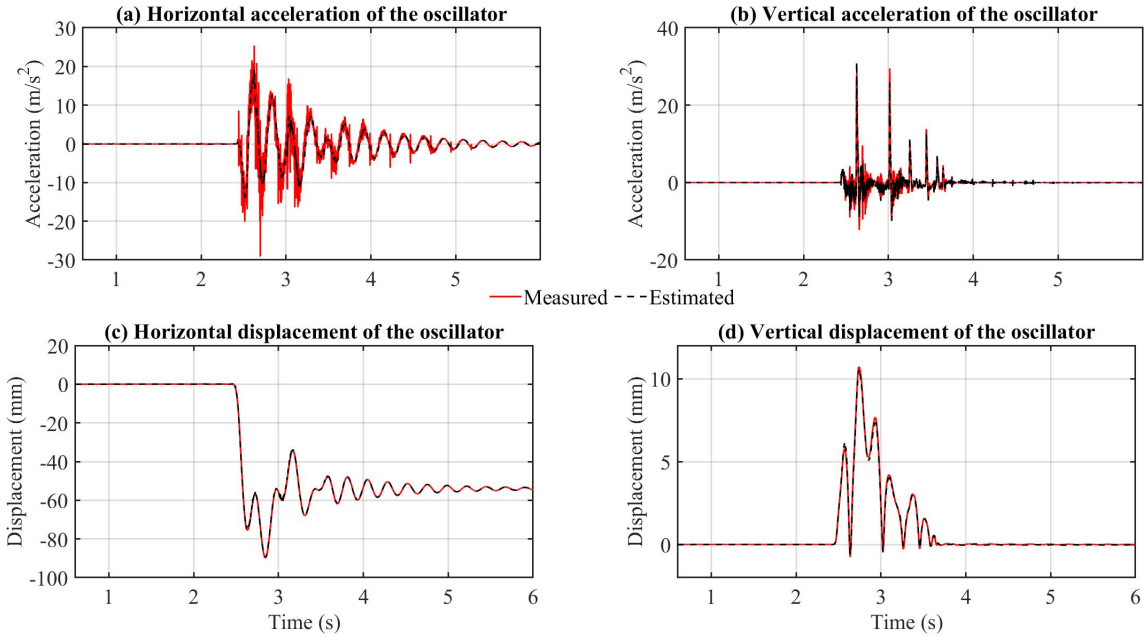


Figure A.9: Comparison of the estimated accelerations and displacements with the measurements of the top oscillator.

.

A.4 Stiff-Stiff-Rough under 3 Hz pulse

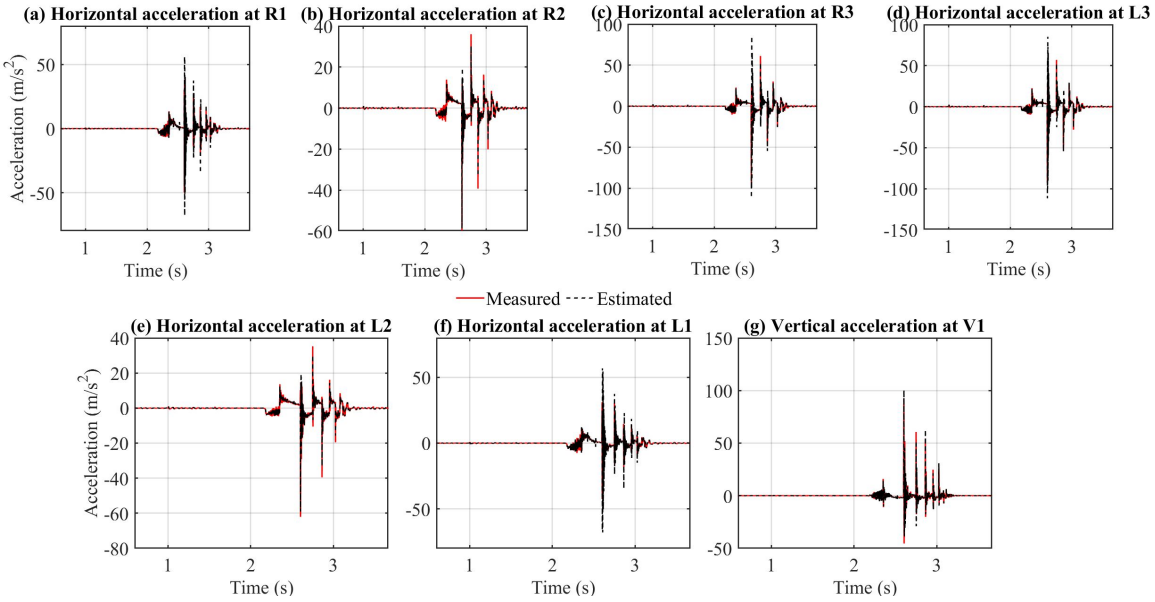


Figure A.10: Comparison between the estimated accelerations and the measurements at various points on the bottom mass.

.

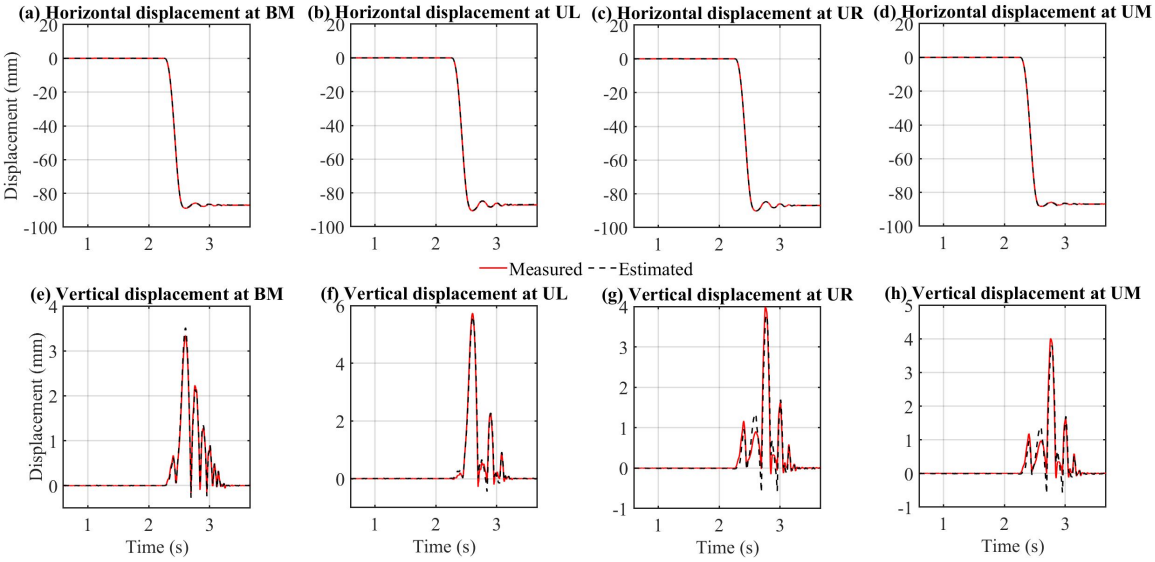


Figure A.11: Comparison between the estimated displacements and the measurements at various points on the bottom mass.

.

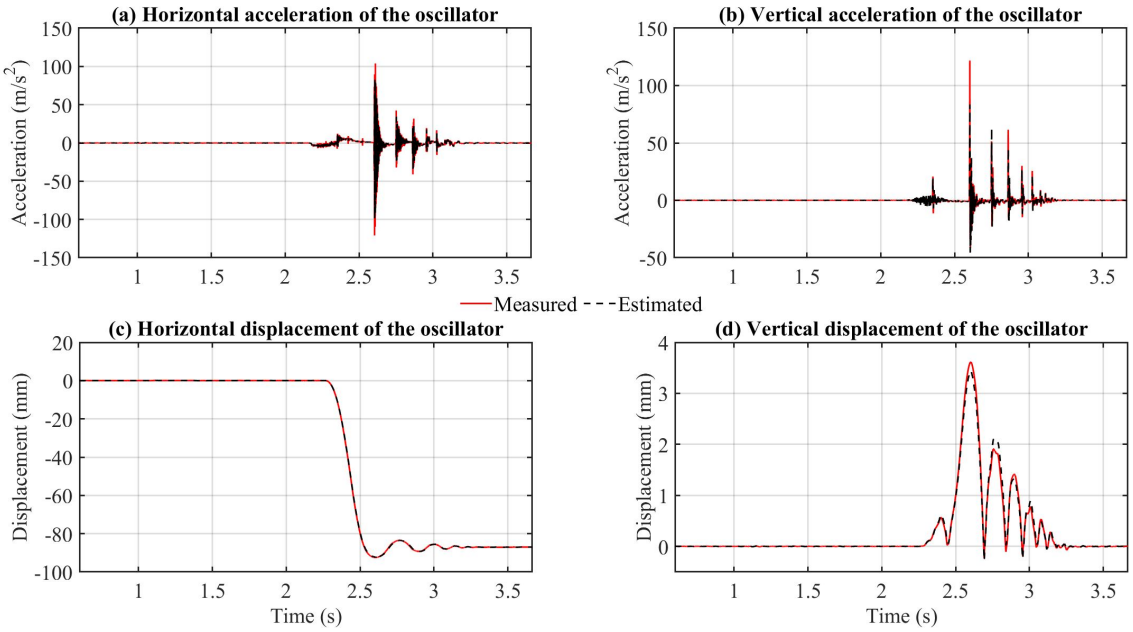


Figure A.12: Comparison of the estimated accelerations and displacements with the measurements of the top oscillator.

.

A.5 Stiff-Soft-Rough under 3 Hz pulse

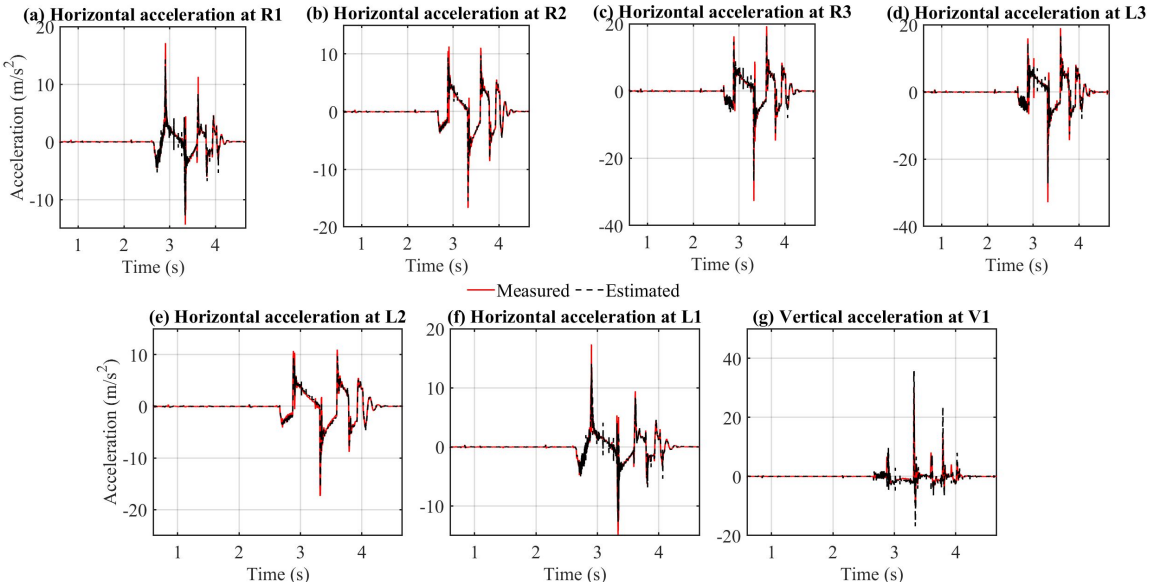


Figure A.13: Comparison between the estimated accelerations and the measurements at various points on the bottom mass.

.

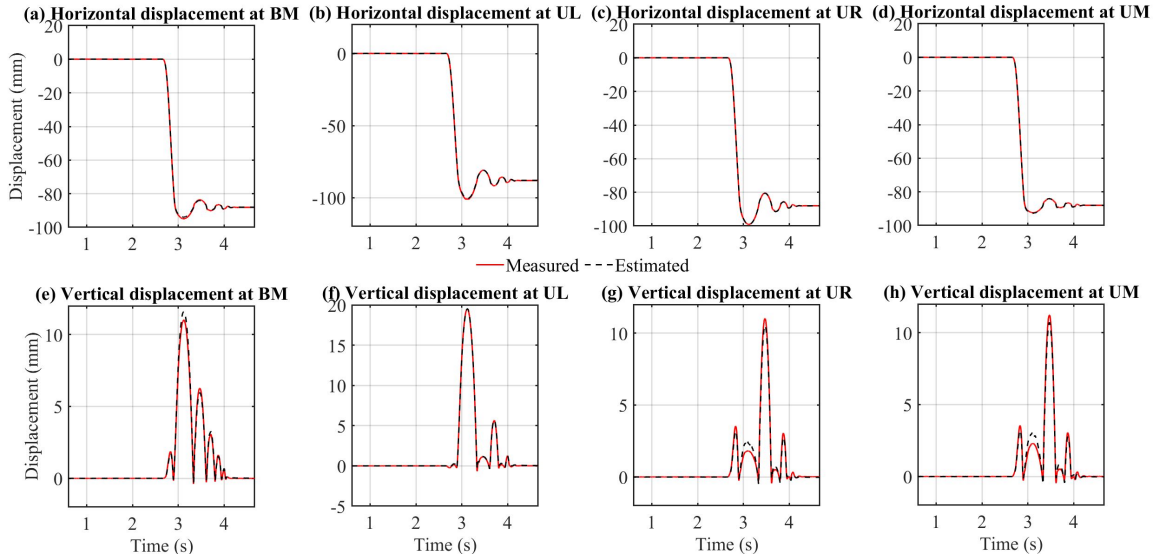


Figure A.14: Comparison between the estimated displacements and the measurements at various points on the bottom mass.

.

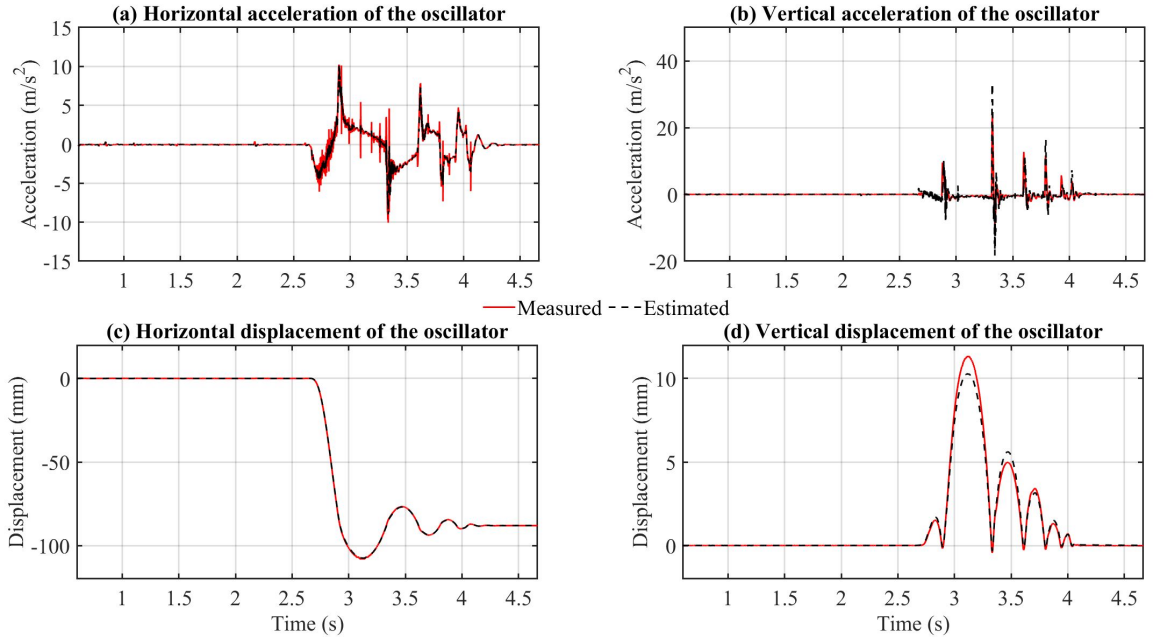


Figure A.15: Comparison of the estimated accelerations and displacements with the measurements of the top oscillator.

.

A.6 Soft-Stiff-Rough under 3 Hz pulse

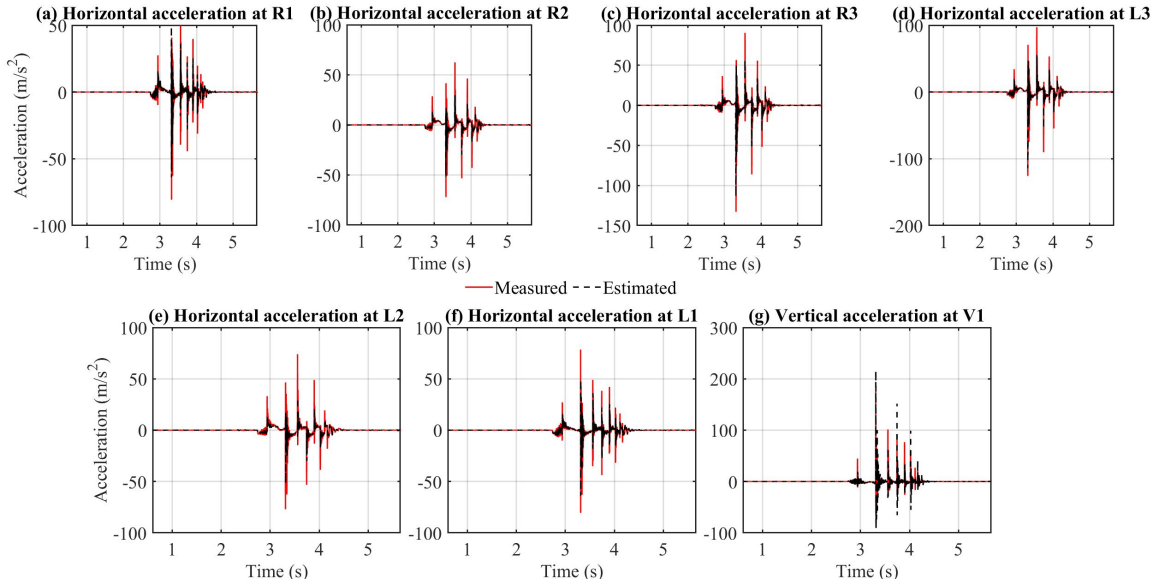


Figure A.16: Comparison between the estimated accelerations and the measurements at various points on the bottom mass.

.

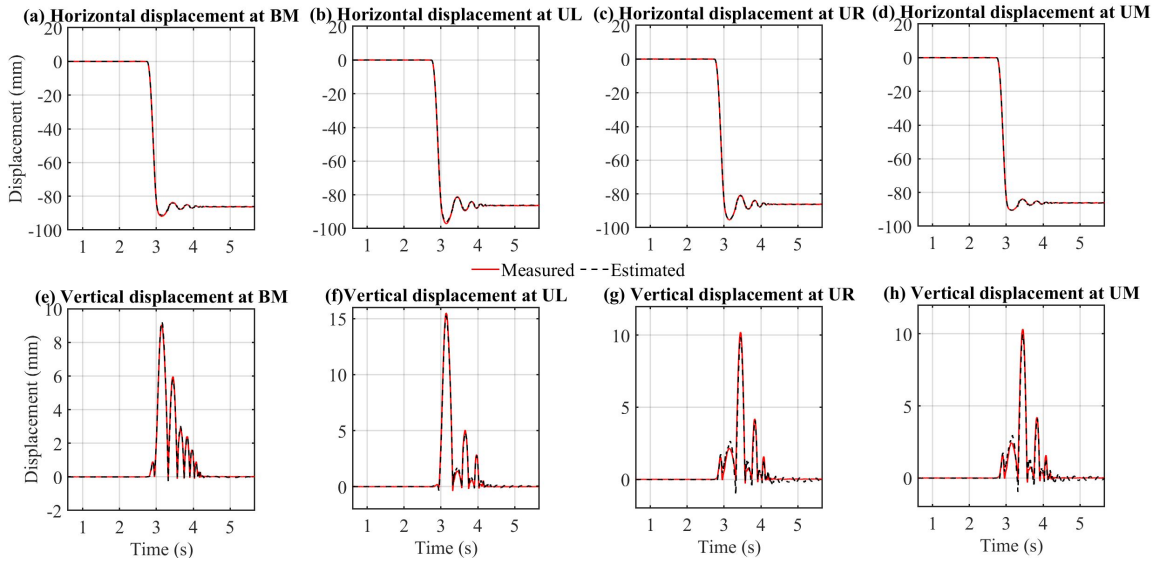


Figure A.17: Comparison between the estimated displacements and the measurements at various points on the bottom mass.

.

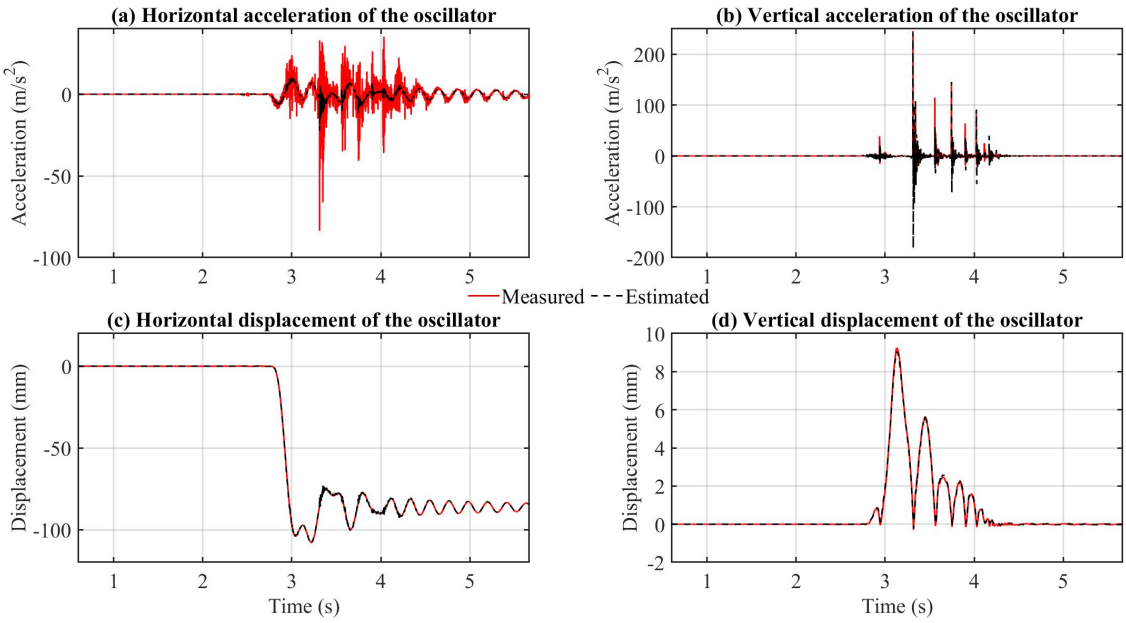


Figure A.18: Comparison of the estimated accelerations and displacements with the measurements of the top oscillator.

.

A.7 Soft-Soft-Rough under 3 Hz pulse

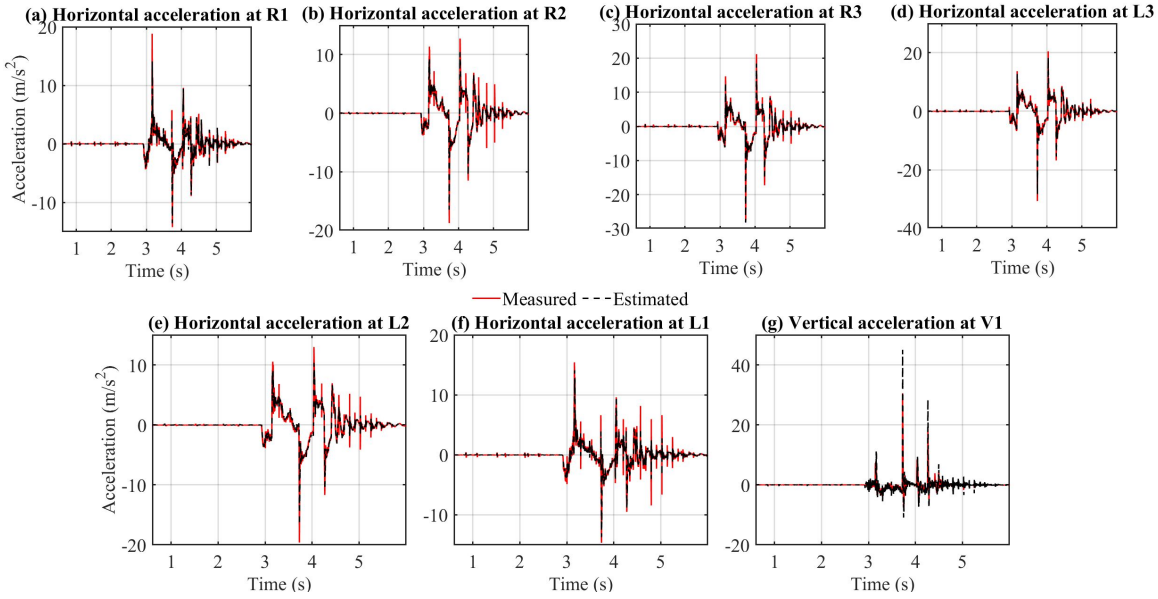


Figure A.19: Comparison between the estimated accelerations and the measurements at various points on the bottom mass.

.

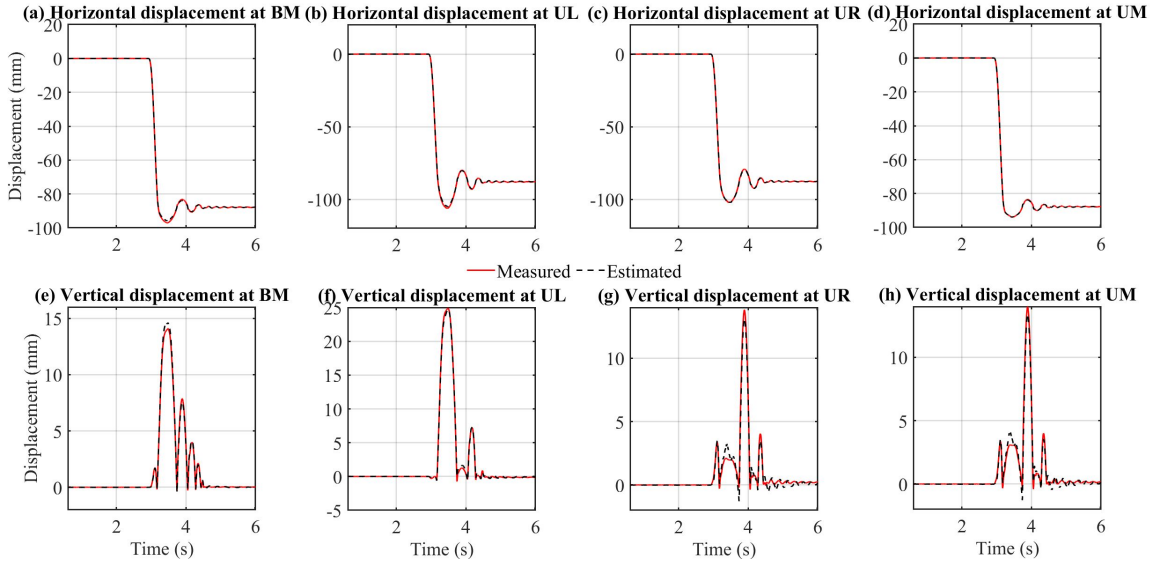


Figure A.20: Comparison between the estimated displacements and the measurements at various points on the bottom mass.

.

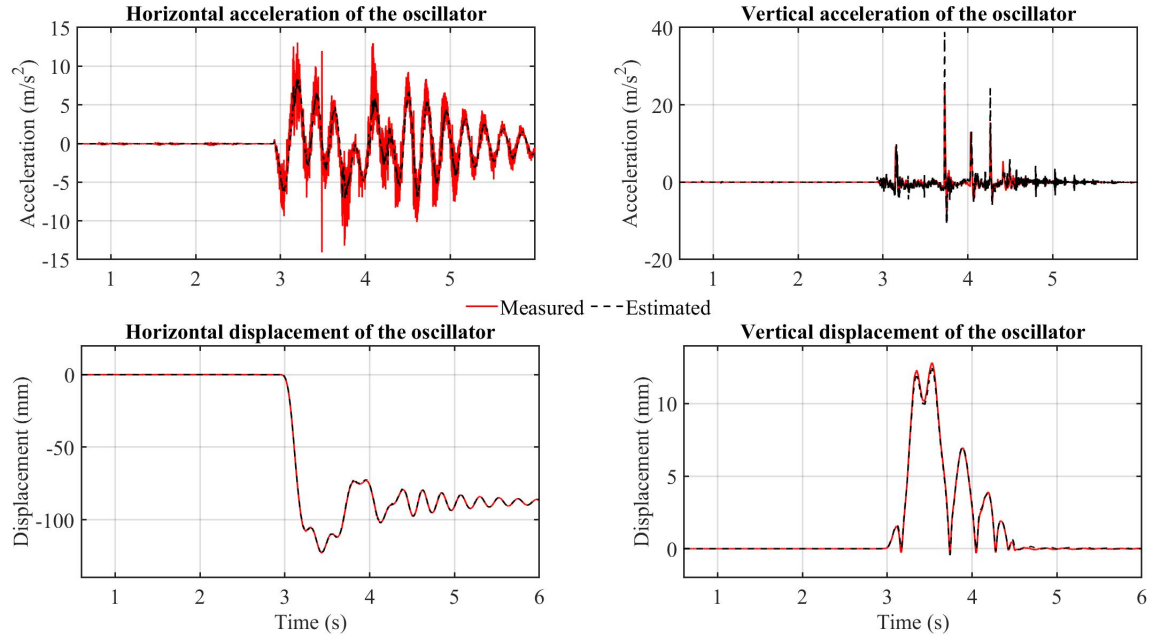


Figure A.21: Comparison of the estimated accelerations and displacements with the measurements of the top oscillator.

.

A.8 Soft-Soft-Semi-slippery under 3 Hz pulse

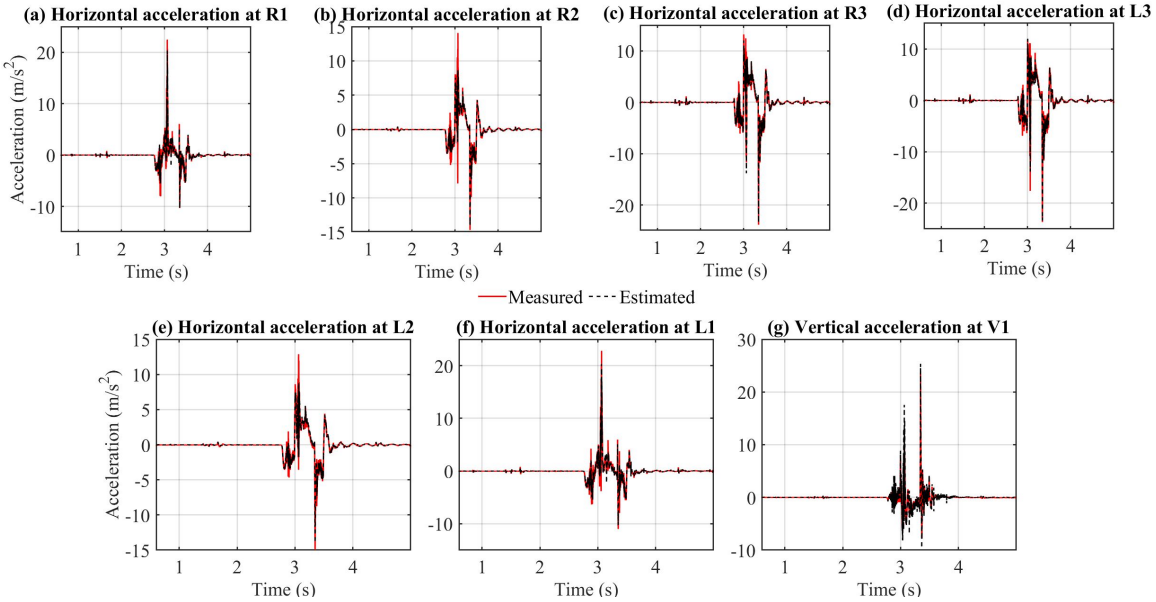


Figure A.22: Comparison between the estimated accelerations and the measurements at various points on the bottom mass.

.

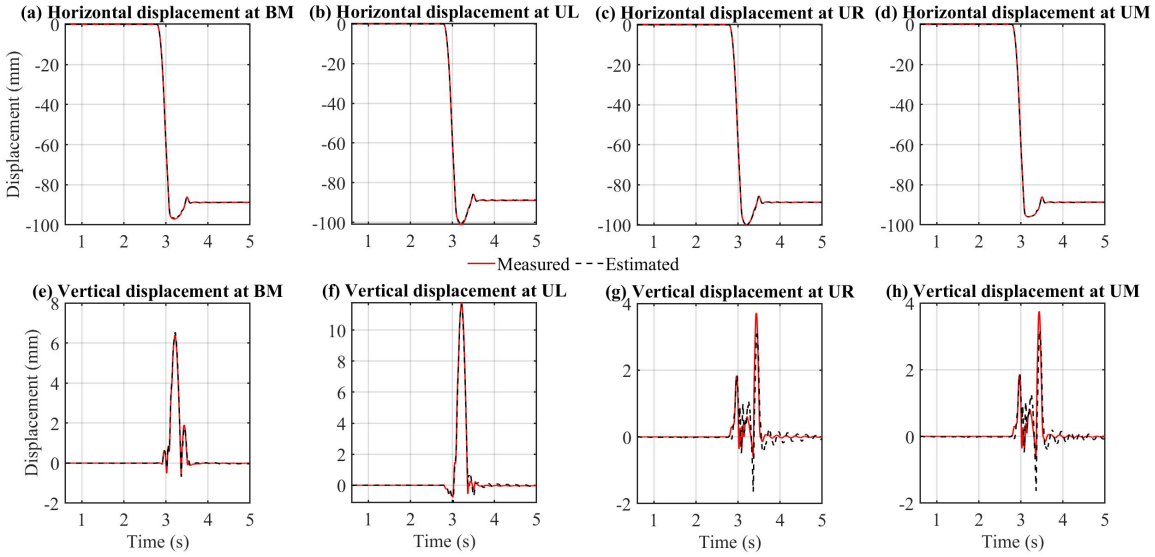


Figure A.23: Comparison between the estimated displacements and the measurements at various points on the bottom mass.

.

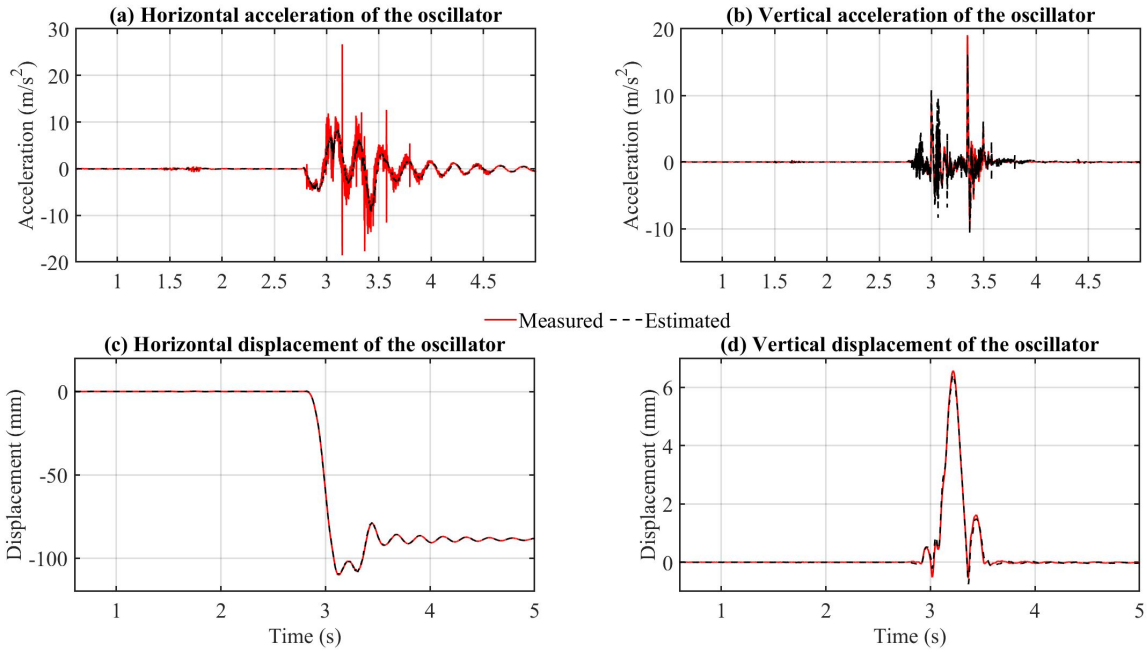


Figure A.24: Comparison of the estimated accelerations and displacements with the measurements of the top oscillator.

.

Bibliography

[1] George W Housner. "THE BEHAVIOR OF INVERTED PENDULUM STRUCTURES DURING EARTHQUAKES". In: *Bulletin of the Seismological Society of America* 53.2 (Dec. 1963), pp. 403–417. URL: http://pubs.geoscienceworld.org/ssa/bssa/article-pdf/53/2/403/5348002/bssa0530020403.pdf.

[2] John B Mander and Chin-Tung Cheng. *Seismic resistance of bridge piers based on damage avoidance design*. Tech. rep. New York: University at Buffalo, Dec. 1997.

[3] A Palermo, S Pampanin, and GM Calvi. "Concept and development of hybrid solutions for seismic resistant bridge systems". eng. In: *Journal of earthquake engineering : JEE* 9.6 (2005), pp. 899–921. ISSN: 1363-2469. DOI: 10.1142/S1363246905002328.

[4] Michael Pollino and Michel Bruneau. "Analytical and experimental investigation of a controlled rocking approach for seismic protection of bridge steel truss piers". In: MCEER, 2008. URL: https://api.semanticscholar.org/CorpusID:112314891.

[5] A A Huckelbridge and R W Clough. *Earthquake simulator tests of a nine-story steel frame with columns allowed to uplift*. Tech. rep. BEERC 7723. Berkeley, CA: Earthquake Engineering Research Center, University of California, 1977.

[6] Matthew R Eatherton et al. "Design Concepts for Controlled Rocking of Self-Centering Steel-Braced Frames". eng. In: *Journal of structural engineering (New York, N.Y.)* 140.11 (2014). ISSN: 0733-9445. DOI: 10.1061/(ASCE)ST.1943-541X.0001047.

[7] Matthew Roy Eatherton. "Large-scale cyclic and hybrid simulation testing and development of a controlled-rocking steel building system with replaceable fuses". eng. PhD thesis. 2010. ISBN: 1124583424.

[8] M J N Priestley et al. "Preliminary results and conclusions from the PRESSS five-story precast concrete test-building". In: *PCI National Bridge Conference*. Chicago, IL, 1999.

[9] Jack J Ajrab, Gokhan Pekcan, and John B Mander. "Rocking Wall-Frame Structures with Supplemental Tendon Systems". eng. In: *Journal of structural engineering (New York, N.Y.)* 130.6 (2004), pp. 895–903. ISSN: 0733-9445. DOI: 10.1061/(ASCE)0733-9445(2004)130:6(895).

[10] Xilin Lu and Hao Wu. "Study on seismic performance of prestressed precast concrete walls through cyclic lateral loading test". eng. In: *Magazine of concrete research* 69.17 (2017), pp. 878–891. ISSN: 0024-9831. DOI: 10.1680/jmacr.16.00363.

[11] M. Preti and A. Meda. "RC structural wall with unbonded tendons strengthened with high-performance fiber-reinforced concrete". eng. In: *Materials and structures* 48.1-2 (2015), pp. 249–260. ISSN: 1359-5997. DOI: 10.1617/s11527-013-0180-8.

[12] K Solberg et al. "Performance of a Damage-Protected Highway Bridge Pier Subjected to Bidirectional Earthquake Attack". eng. In: *Journal of structural engineering (New York, N.Y.)* 135.5 (2009), pp. 469–478. ISSN: 0733-9445. DOI: 10.1061/(ASCE)0733-9445(2009)135:5(469).

[13] Matthew R. Eatherton and Jerome F. Hajjar. "Hybrid simulation testing of a self-centering rocking steel braced frame system". eng. In: *Earthquake engineering & structural dynamics* 43.11 (2014), pp. 1725–1742. ISSN: 0098-8847. DOI: 10.1002/eqe.2419.

[14] Dimitrios Konstantinidis and Nicos Makris. "Experimental and analytical studies on the response of 1/4-scale models of freestanding laboratory equipment subjected to strong earthquake shaking". eng. In: *Bulletin of earthquake engineering* 8.6 (2010), pp. 1457–1477. ISSN: 1570-761X. DOI: 10.1007/s10518-010-9192-8.

[15] Parth Patel, Abhinav Gupta, and Yangsoo Kwon. "Rocking stiffness of electrical cabinets with tubular base in nuclear power plants". eng. In: *Nuclear engineering and design* 414 (2023), p. 112603. ISSN: 0029-5493. DOI: 10.1016/j.nucengdes.2023.112603.

[16] J.V. Lemos, C.S. Oliveira, and M. Navarro. *3-D nonlinear behavior of an obelisk subjected to the Lorca May 11, 2011 strong motion record*. eng. 2015. DOI: 10.1016/j.engfailanal.2015.09.001.

[17] Anthony N. Kounadis. "Rocking instability of free-standing statues atop slender cantilevers under ground motion". eng. In: *Soil dynamics and earthquake engineering (1984)* 48 (2013), pp. 294–305. ISSN: 0267-7261. DOI: 10.1016/j.soildyn.2011.12.002.

[18] Mohamed A. ElGawady et al. "Effects of interface material on the performance of free rocking blocks". eng. In: *Earthquake engineering & structural dynamics* 40.4 (2011), pp. 375–392. ISSN: 0098-8847. DOI: 10.1002/eqe.1025.

[19] Hongjian Zhang, Bernard Brogliato, and Caishan Liu. "Dynamics of planar rocking-blocks with Coulomb friction and unilateral constraints: comparisons between experimental and numerical data". eng. In: *Multibody system dynamics* 32.1 (2014), pp. 1–25. ISSN: 1384-5640. DOI: 10.1007/s11044-013-9356-9.

[20] Lundström Peter. *Obelisk of Hatshepsut at Karnak*. eng. 2011. URL: https://pharaoh.se/ancient-egypt/curiosities/hatshepsut-obelisk/.

[21] Aphrodisias Excavations Project. *Blue Horse*. eng. 2023. URL: https://aphrodisias-excavations.com/bluehorse/.

[22] Federal Emergency Management Agency (FEMA). *Reducing the Risks of Nonstructural Earthquake Damage: A Practical Guide*. 3rd. FEMA 74. Washington, D.C.: FEMA, 2005.

[23] Sergio Lagomarsino. "Seismic assessment of rocking masonry structures". eng. In: *Bulletin of earthquake engineering* 13.1 (2015). Ed. by Sergio Lagomarsino and Dina D'Ayala, pp. 97–128. ISSN: 1570-761X. DOI: 10.1007/s10518-014-9609-x.

[24] C. Casapulla and L.U. Argiento. *The comparative role of friction in local out-of-plane mechanisms of masonry buildings. Pushover analysis and experimental investigation*. eng. 2016. DOI: 10.1016/j.engstruct.2016.07.036.

[25] Claudia Casapulla et al. "Nonlinear Static and Dynamic Analysis of Rocking Masonry Corners Using Rigid Macro-Block Modeling". In: *International Journal of Structural Stability and Dynamics* 19.11 (2019), p. 1950137. DOI: 10.1142/S0219455419501372. URL: https://doi.org/10.1142/S0219455419501372.

[26] C. Casapulla and F. Portioli. *Experimental and analytical investigation on the frictional contact behavior of 3D masonry block assemblages*. eng. 2015. DOI: 10.1016/j.conbuildmat.2014.12.100.

[27] Omar Al Shawa et al. "Out-of-plane seismic behaviour of rocking masonry walls". eng. In: *Earthquake engineering & structural dynamics* 41.5 (2012), pp. 949–968. ISSN: 0098-8847. DOI: 10.1002/eqe.1168.

[28] Arun Menon and Guido Magenes. "Definition of Seismic Input for Out-of-Plane Response of Masonry Walls: I. Parametric Study". eng. In: *Journal of earthquake engineering : JEE* 15.2 (2011), pp. 165–194. ISSN: 1363-2469. DOI: 10.1080/13632460903456981.

[29] Resat Oyguc and Evrim Oyguc. "2011 Van Earthquakes: Lessons from Damaged Masonry Structures". eng. In: *Journal of performance of constructed facilities* 31.5 (2017). ISSN: 0887-3828. DOI: 10.1061/(ASCE)CF.1943-5509.0001057.

[30] Yuji Ishiyama. "MOTIONS OF RIGID BODIES AND CRITERIA FOR OVERTURNING BY EARTHQUAKE EXCITATIONS". In: *EARTHQUAKE ENGINEERING AND STRUCTURAL DYNAMICS* 10 (1982), pp. 635–650.

[31] HW SHENTON and NP JONES. "BASE EXCITATION OF RIGID BODIES .1. FORMULATION". eng. In: *Journal of engineering mechanics* 117.10 (1991), pp. 2286–2306. ISSN: 0733-9399. DOI: 10.1061/(ASCE)0733-9399(1991)117:10(2286).

[32] A Pompei, A Scalia, and M. A Sumbatyan. "Dynamics of Rigid Block due to Horizontal Ground Motion". eng. In: *Journal of engineering mechanics* 124.7 (1998), pp. 713–717. ISSN: 0733-9399. DOI: 10.1061/(ASCE)0733-9399(1998)124:7(713).

[33] Chik-Sing Yim, Anil K. Chopra, and Joseph Penzien. “Rocking response of rigid blocks to earthquakes”. eng. In: *Earthquake engineering & structural dynamics* 8.6 (1980), pp. 565–587. ISSN: 0098-8847. DOI: 10.1002/eqe.4290080606.

[34] P. R Lipscombe and S Pellegrino. “Free Rocking of Prismatic Blocks”. eng. In: *Journal of engineering mechanics* 119.7 (1991), pp. 1387–1410. ISSN: 0733-9399. DOI: 10.1061/(ASCE)0733-9399(1993)119:7(1387).

[35] M. N. Chatzis and A. W. Smyth. “Robust Modeling of the Rocking Problem”. In: *Journal of Engineering Mechanics* 138.3 (Mar. 2012), pp. 247–262. ISSN: 0733-9399. DOI: 10.1061/(asce)em.1943-7889.0000329.

[36] Sinan Acikgoz and Matthew J. Dejong. “The interaction of elasticity and rocking in flexible structures allowed to uplift”. In: *Earthquake Engineering and Structural Dynamics* 41.15 (2012), pp. 2177–2194. ISSN: 10969845. DOI: 10.1002/eqe.2181.

[37] Huanian Zhu, Manolis N. Chatzis, and Sinan Acikgoz. “A New Model for the Sliding Flexible Rocking Oscillator”. eng. In: *Earthquake engineering & structural dynamics* 54.11 (2025), pp. 2882–2899. ISSN: 1096-9845. DOI: https://doi.org/10.1002/eqe.70006.

[38] J. L. Beck and R. I. Skinner. “The seismic response of a reinforced concrete bridge pier designed to step”. eng. In: *Earthquake engineering & structural dynamics* 2.4 (1973), pp. 343–358. ISSN: 0098-8847. DOI: 10.1002/eqe.4290020405.

[39] Chik-Sing Yim and Anil K. Chopra. “Earthquake response of structures with partial uplift on winkler foundation”. eng. In: *Earthquake Engineering & Structural Dynamics* 12.2 (1984), pp. 263–281. ISSN: 0098-8847. DOI: 10.1002/eqe.4290120209.

[40] Ioannis N. Psycharis. “Dynamics of flexible systems with partial lift-off”. eng. In: *Earthquake Engineering & Structural Dynamics* 11.4 (1983), pp. 501–521. ISSN: 0098-8847. DOI: 10.1002/eqe.4290110405.

[41] Giuseppe Oliveto, Ivo Caliò, and Annalisa Greco. “Large displacement behaviour of a structural model with foundation uplift under impulsive and earthquake excitations”. eng. In: *Earthquake engineering & structural dynamics* 32.3 (2003), pp. 369–393. ISSN: 0098-8847. DOI: 10.1002/eqe.229.

[42] Huanian Zhu, Manolis N. Chatzis, and Sinan Acikgoz. “A new impact model for the flexible rocking oscillator”. In: *Earthquake Engineering and Structural Dynamics* 51.8 (July 2022), pp. 1819–1839. ISSN: 10969845. DOI: 10.1002/eqe.3639.

[43] Haitham Dawood, Mohamed ElGawady, and Joshua Hewes. “Behavior of Segmental Precast Posttensioned Bridge Piers under Lateral Loads”. eng. In: *Journal of bridge engineering* 17.5 (2012), pp. 735–746. ISSN: 1084-0702. DOI: 10.1061/(ASCE)BE.1943-5592.0000252.

[44] H A Spieth et al. “Modelling of Post-Tensioned Precast Reinforced Concrete Frame Structures with Rocking Beam-Column Connections”. In: *New Zealand Society for Earthquake Engineering (NZSEE) Conference*. Christchurch, New Zealand, 2004.

[45] Dion Marriott, Stefano Pampanin, and Alessandro Palermo. “Quasi-static and pseudo-dynamic testing of unbonded post-tensioned rocking bridge piers with external replaceable dissipaters”. eng. In: *Earthquake engineering & structural dynamics* 38.3 (2009), pp. 331–354. ISSN: 0098-8847. DOI: 10.1002/eqe.857.

[46] Zhiqiang Wang et al. “Numerical Analytical Model for Seismic Behavior of Prestressing Concrete Bridge Column Systems”. eng. In: *Procedia engineering* 14 (2011). Ed. by LH Fai, pp. 2333–2340. ISSN: 1877-7058. DOI: 10.1016/j.proeng.2011.07.294.

[47] Michalis F. Vassiliou, Kevin R. Mackie, and Božidar Stojadinović. “Dynamic response analysis of solitary flexible rocking bodies: modeling and behavior under pulse-like ground excitation”. eng. In: *Earthquake engineering & structural dynamics* 43.10 (2014), pp. 1463–1481. ISSN: 0098-8847. DOI: 10.1002/eqe.2406.

[48] M J N Priestley et al. “Seismic Behavior and Design of Unbonded Post-Tensioned Precast Concrete Walls”. In: *PCI Journal* 44.3 (1999), pp. 42–68. URL: https://www.pci.org/PCI_Docs/Publications/PCI%20Journal/1999/May-June/Seismic%20Behavior%20and%20Design%20of%20Unbonded%20Post-Tensioned%20Precast%20Concrete%20Walls.pdf.

[49] Felipe J Pérez, Richard Sause, and Stephen Pessiki. “Analytical and Experimental Lateral Load Behavior of Unbonded Post-Tensioned Precast Concrete Walls”. In: *Journal of Structural Engineering* 133.11 (2007), pp. 1531–1540. DOI: 10.1061/(ASCE)0733-9445(2007)133:11(1531).

[50] W Lee et al. “Post-Tensioned Structural Concrete Bridge Piers with Self-Centering Characteristics”. In: *Structures Congress 2007*. Reston, VA: American Society of Civil Engineers (ASCE), 2007, pp. 1–15. DOI: 10.1061/40944(249)42.

[51] Mohammad Salehi, Petros Sideris, and Abbie B Liel. “Numerical Simulation of Hybrid Sliding-Rocking Columns Subjected to Earthquake Excitation”. eng. In: *Journal of structural engineering (New York, N.Y.)* 143.11 (2017). ISSN: 0733-9445. DOI: 10.1061/(ASCE)ST.1943-541X.0001878.

[52] Hwasung Roh and Andrei M. Reinhorn. “Analytical modeling of rocking elements”. eng. In: *Engineering structures* 31.5 (2009), pp. 1179–1189. ISSN: 0141-0296. DOI: 10.1016/j.engstruct.2009.01.014.

[53] Evangelos Avgenakis and Ioannis N. Psycharis. “An integrated macroelement formulation for the dynamic response of inelastic deformable rocking bodies”. eng. In: *Earthquake engineering & structural dynamics* 49.11 (2020), pp. 1072–1094. ISSN: 0098-8847. DOI: 10.1002/eqe.3279.

[54] Triantafyllou Savvas Kakouris Emmanouil Chatzis Manolis. "A MATERIAL POINT METHOD FOR STUDYING ROCKING SYSTEMS". In: *16th European Conference on Earthquake Engineering*. 2018. URL: https://www.researchgate.net/publication/352736037_A_material_point_method_for_studying_rocking_systems.

[55] Clement Benjamin Barthes. "Design of Earthquake Resistant Bridges Using Rocking Columns". eng. PhD thesis. 2012.

[56] M J N Priestley, R J Evison, and A J Carr. "Seismic Response of Structures Free to Rock on Their Foundations". In: *Bulletin of the New Zealand National Society for Earthquake Engineering* 11.3 (1978), pp. 141–150.

[57] J M Ingham, Q T Ma, and M A ElGawady. "Three-Dimensional Rocking of Rigid Blocks on Different Interfaces". In: *Bulletin of the New Zealand Society for Earthquake Engineering* 42.3 (2009), pp. 161–172. URL: https://www.nzsee.org.nz/db/Bulletin/Archive/42(3)0161.pdf.

[58] Alessandro Baratta, Ileana Corbi, and Ottavia Corbi. "Towards a seismic worst scenario approach for rocking systems: analytical and experimental set-up for dynamic response". eng. In: *Acta mechanica* 224.4 (2013), pp. 691–705. ISSN: 0001-5970. DOI: 10.1007/s00707-012-0787-9.

[59] Raphael Judah Yakir Greenbaum. "Experimental Study of Rocking Motion of Rigid Bodies on Deformable Medium via Monocular Videogrammetry". eng. PhD thesis. New York: Columbia University, 2014. ISBN: 132133219X.

[60] Tomoyo TANIGUCHI. "Experimental and analytical study of free lift-off motion induced slip behavior of rectangular rigid bodies: Special Issue on Seismic Engineering". eng. In: *Journal of pressure vessel technology* 126.1 (2004), pp. 53–58. ISSN: 0094-9930.

[61] M A ElGawady et al. "Experimental Investigation of Rigid Body Rocking". In: *Proceedings of the 2005 New Zealand Society for Earthquake Engineering Conference*. Wairakei, New Zealand: New Zealand Society for Earthquake Engineering, 2005, Paper 7.4. URL: https://cdn.ymaws.com/concretenz.org.nz/resource/resmgr/docs/conf/2005/s7_p4_-_elgawadymainghambutt.pdf.

[62] Rico Truniger, Michalis F. Vassiliou, and Božidar Stojadinović. "An analytical model of a deformable cantilever structure rocking on a rigid surface: experimental validation". eng. In: *Earthquake engineering & structural dynamics* 44.15 (2015), pp. 2795–2815. ISSN: 0098-8847. DOI: 10.1002/eqe.2609.

[63] Sinan Acikgoz et al. "Experimental Identification of the Dynamic Characteristics of a Flexible Rocking Structure". eng. In: *Journal of earthquake engineering : JEE* 20.8 (2016), pp. 1199–1221. ISSN: 1363-2469. DOI: 10.1080/13632469.2016.1138169.

[64] Huanian Zhu, Manolis Chatzis, and Sinan Acikgoz. "Experimental investigation of flexible rocking structures". In: *Mechanical Systems and Signal Processing* (2025).

[65] Mohammad Froozanfar et al. “Review of self-centering rocking systems for earthquake-resistant building structures: State of the art”. eng. In: *Journal of Building Engineering* 84 (2024), p. 108607. ISSN: 2352-7102. DOI: 10.1016/j.jobe.2024.108607.

[66] M J N Priestley et al. *Preliminary Test Results from the PRESSS Five-Story Precast Concrete Building*. Tech. rep. PRESSS Report No. 3-3. Chicago, IL: Precast/Prestressed Concrete Institute (PCI), 1999. URL: https://datacenterhub.org/resources/20834/download/PRESSS_Building_Report_Phase_3c.pdf.

[67] Maryam Nazari, Sri Sritharan, and Sriram Aaleti. “An Experimental Evaluation of Unbonded Post-Tensioned Precast Rocking Walls”. In: *Proceedings of the PCI Convention and National Bridge Conference* (2014). URL: https://www.pci.org/PCI_Docs/Papers/2014/An-Experimental-Evaluation-of-Unbonded-Post-Tensioned-Precast-Rocking-Walls.pdf.

[68] Shiling Pei et al. “Shake-Table Testing of a Full-Scale 10-Story Resilient Mass Timber Building”. eng. In: *Journal of structural engineering (New York, N.Y.)* 150.12 (2024). ISSN: 0733-9445. DOI: 10.1061/JSENDH.STENG-13752.

[69] Yuanzhi Chen, Tam Larkin, and Nawawi Chouw. “Experimental assessment of contact forces on a rigid base following footing uplift”. eng. In: *Earthquake engineering & structural dynamics* 46.11 (2017), pp. 1835–1854. ISSN: 0098-8847. DOI: 10.1002/eqe.2885.

[70] Jian Zhang and Nicos Makris. “Rocking Response of Free-Standing Blocks under Cycloidal Pulses”. eng. In: *Journal of engineering mechanics* 127.5 (2001), pp. 473–483. ISSN: 0733-9399. DOI: 10.1061/(ASCE)0733-9399(2001)127:5(473).

[71] Marios Apostolou, G. Gazetas, and Evangelia Garini. “Seismic response of slender rigid structures with foundation uplifting”. eng. In: *Soil dynamics and earthquake engineering (1984)* 27.7 (2007), pp. 642–654. ISSN: 0267-7261. DOI: 10.1016/j.soildyn.2006.12.002.

[72] Sinan Acikgoz and Matthew J. DeJong. “The rocking response of large flexible structures to earthquakes”. In: *Bulletin of Earthquake Engineering* 12.2 (2014), pp. 875–908. ISSN: 15731456. DOI: 10.1007/s10518-013-9538-0.

[73] Matthew J. DeJong. “Amplification of rocking due to horizontal ground motion”. eng. In: *Earthquake spectra* 28.4 (2012), pp. 1405–1421. ISSN: 8755-2930. DOI: 10.1193/1.4000085.

[74] Solomon C.-S Yim and Anil K Chopra. “Simplified Earthquake Analysis of Multistory Structures With Foundation Uplift”. eng. In: *Journal of structural engineering (New York, N.Y.)* 111.12 (1985), pp. 2708–2731. ISSN: 0733-9445. DOI: 10.1061/(ASCE)0733-9445(1985)111:12(2708).

[75] Ioannis N Psycharis. “Effect of Base Uplift on Dynamic Response of SDOF Structures”. eng. In: *Journal of structural engineering (New York, N.Y.)* 117.3 (1991), pp. 733–754. ISSN: 0733-9445. DOI: 10.1061/(ASCE)0733-9445(1991)117:3(733).

[76] Sinan Acikgoz and MJ Dejong. "Vibration modes and equivalent models for flexible rocking structures". eng. In: *Bulletin of earthquake engineering* 15 (Oct. 2017), pp. 4427–4452. DOI: https://doi.org/10.1007/s10518-017-0128-4.

[77] R.W Clough and A.A Huckelbridge. *Preliminary experimental study of seismic uplift of a steel frame*. Tech. rep. Berkeley: Earthquake Engineering Research Center (EERC), 1977.

[78] Zheng-You Zhang, Manolis N. Chatzis, and Sinan Acikgoz. "The dynamic behaviour of flexible oscillators rocking and sliding on concentrated springs". eng. In: *Earthquake engineering & structural dynamics* 53.11 (2024), pp. 3405–3426. ISSN: 0098-8847. DOI: 10.1002/eqe.4178.

[79] Ahmed A. Shabana. *Dynamics of Multibody Systems*. Cambridge University Press, Mar. 2020. ISBN: 9781108757553. DOI: 10.1017/9781108757553.

[80] WALTER C HURTY. "Dynamic analysis of structural systems using component modes". eng. In: *AIAA journal* 3.4 (1965), pp. 678–685. ISSN: 0001-1452. DOI: 10.2514/3.2947.

[81] ROY R. CRAIG and MERVYN C. C. BAMPTON. "Coupling of substructures for dynamic analyses". eng. In: *AIAA journal* 6.7 (1968), pp. 1313–1319. ISSN: 0001-1452. DOI: 10.2514/3.4741.

[82] ROBERT J GUYAN. "Reduction of stiffness and mass matrices". eng. In: *AIAA journal* 3.2 (1965), pp. 380–380. ISSN: 0001-1452. DOI: 10.2514/3.2874.

[83] F. J. Serón et al. "Finite-element method for elastic wave propagation". In: *Communications in Applied Numerical Methods* 6.5 (1990), pp. 359–368. URL: https://doi.org/10.1002/cnm.1630060505.

[84] Manolis Chatzis, Kristof Maes, and Geert Lombaert. "Observability of nonlinear discrete-time systems with unmeasured inputs". eng. In: *Mechanical systems and signal processing* 238 (2025), pp. 113–142. ISSN: 0888-3270. DOI: 10.1016/j.ymssp.2025.113142.

[85] Inc. Sorbothane. *EDG Isolation Pad — Technical Data Sheet*. Tech. rep. URL: https://www.sorbothane.com/wp-content/uploads/Sorbothane-EDG.pdf.